Copolyelectrolyte monolayers: organisation and surface wave dynamics

Andrew Simon Brown

Copolyelectrolyte Monolayers: Organisation and Surface Wave Dynamics

September 1999

Andrew Simon Brown

Trevelyan College,

University of Durham

A thesis submitted to the University of Durham in partial fulfilment of the regulations for the degree of Doctor of Philosophy

ABSTRACT

The organisation and dynamic behaviour of a copolyelectrolyte monolayer is discussed. A linear diblock copolymer of poly(methyl methacrylate) (PMMA) and poly(4-vinyl ethylpyridinium bromide) (QP4VP) has been the main focus of the study, although films of both the unquaternised copolymer, PMMA-P4VP and a PMMA homopolymer have also been examined for comparative purposes. The polymers were spread on subphases of water and potassium chloride solutions of varying concentrations to determine changes in structure and dynamics with polymer surface concentration and subphase salt concentration.

Monolayer behaviour has been characterised from surface pressure isotherms and the use of Brewster angle microscopy. It has been demonstrated that the shape of the isotherm is dependent on the potassium chloride concentration of the subphase.

Information on the organisation of the system has been determined by neutron reflectometry. A systematic variation in organisation occurs as both polymer surface concentration and subphase potassium chloride concentration change. The polyelectrolytic QP4VP block stretches more into the subphase with increasing surface concentration or decreasing salt concentration. The results have been compared to scaling laws for polymer brushes.

Dynamic behaviour has been studied by the use of surface quasi-elastic light scattering (SQELS) and resonance between the capillary and dilational waves of the system is observed. The phenomenon of mode mixing and the application of viscoelastic models to the system have also been examined. It has been discovered that an accurate description of the surface viscoelastic properties of the system could not be obtained by the use of standard viscoelastic models. Mode mixing was not observed, even in those systems where negative dilational viscosities were found.

DECLARATION

All work in this thesis has been carried out at the Interdisciplinary Research Centre in Polymer Science and Technology, Department of Chemistry, University of Durham and the Rutherford – Appleton Laboratory, Chilton, Oxfordshire between October 1996 and September 1999. This work has not been submitted for any other qualification and, unless otherwise stated, is the original work of the author.

STATEMENT OF COPYRIGHT

ACKNOWLEDGEMENTS

I would like to thank a number of people who all played their part (in a wide variety of ways) in the production of this thesis. Firstly, many thanks to Randal for all his help, guidance and tireless enthusiasm over the last three years. Outside 'the office', his willingness to be the first at the bar never wavered, whether it be a group meeting in the Vic or a conference in the antipodes.

My thanks also go to the many people in both the IRC and the Department of Chemistry who have helped me along the way. The initial polymer synthesis was the work of Tom Kiff, who also proved to be a saviour on the numerous occasions when I was lost in the synthetic lab. Thanks also to Alan Kenwright and Julia Say downstairs in NMR for their help with characterisation.

The SQELS experiments reported here could not have been carried out and analysed without the immense help and patience of Stella Peace, Mark Taylor and Andrew Milling. Likewise, the neutron reflectometry work relied heavily on the expertise of the staff at the Rutherford – Appleton laboratory (John Webster, Dave Bucknall, Jeff Penfold and Sean Langridge), who made the long weekends and nights down there pass much more smoothly. Thanks also to my 'able assistants' Aline Miller, Mike Lovell and Gavin Bown, as well as the chefs at the Crown & Horns, Kingsbrook Hotel, Wheatsheaf, Cherry Tree, etc., etc., who made the trips that little bit more palatable.

Thanks to Andy Beeby, whose Brewster angle microscope, expertly designed and constructed by Allison Wigman, was used to collect the pretty pictures in chapter five, Richard Thompson for his proof reading skills and everyone else who been on the receiving end of one (or more) of my questions.

During my six years in Durham, I've encountered a huge number of people, a select few of whom warrant a special mention here. First of all, the eclectic mix of people in the IRC who all contributed to make it such an enjoyable place to work. Special mentions go to Foggy for helping me on the 'wheels of steel', Rich for being Rich,

Helen T, whose devotion to 'The Boro' defies all known logic and Ian & Andreas for looking after me on our around-the-world jaunt.

Outside the hallowed corridor leading to CG156, I must mention the people in Trevs who made my undergraduate days so enjoyable. In addition, Mark and the rest of Aidan's SCR for cricket, formal dinners, the drinks cabinet and our three glorious victories at the Wednesday night Elm Tree pub quiz. Thanks also to all the people with whom I've shared number 43A, especially Allison J, for putting up with me for two years, Phil, for his help in 'emptying' quiz machines and Carrie for seven letter words and being a very special friend.

Finally, thanks to my parents and close family for all of their support. Without you, I would never have got this far.

ABBREVIATIONS AND SYMBOLS USED

ABBREVIATIONS

All non-standard abbreviations used are expressed in their complete form at least once in the text. For ease of reference a full list is given here:

$ampu_{lim}$	Limiting area per monomer unit
BAM	Brewster angle microscopy
FT	Fourier transform
NR	Neutron reflectometry
NRW	Null reflecting water
PEO	Poly(ethylene oxide)
PM	Photomultiplier [tube]
PMMA*	Poly(methyl methacrylate)
P4VP*	Poly(4-vinly pyridine)
QP4VP*	Quaternised poly(4-vinly pyridine)
SCF	Self consistent field [theory]
SQELS	Surface quasi-elastic light scattering

* In some cases H or D, either as a prefix or in parentheses, is used to indicate hydrogenous and deuterated forms respectively.

SYMBOLS

The list below gives all symbols used during the course of this work. Inevitably, some repetition of symbols is unavoidable and the field of study in which each symbol occurs is therefore indicated in parentheses. Common symbols and those encountered in multiple chapters are not specified in such a manner.

Roman Symbols – Upper Case

A	Amplitude factor (SQELS)
$\bar{A}$	Mean tilt azimuth (BAM)
A_2	Second order viral coefficient (theory)
$A_{2,d}$	Second order viral coefficient of dimensionality d (theory)
A_o	Close-packed area (isotherms)
B	Spring constant (theory)
B	Instrumental background (SQELS)
B_n	Basis function (NR)
$D(Q)$	Distribution of scattering vector (NR)
$D(\omega)$	Dispersion equation (SQELS)
E_i^p	Amplitude of incident electric field of p-polarised light (BAM)
E_r^p	Amplitude of reflected electric field of p-polarised light (BAM)
$G(\tau)$	Correlation function (SQELS)
$G^*(\omega)$	Complex modulus (SQELS)
$G'(\omega)$	Storage modulus (SQELS)
$G''(\omega)$	Loss modulus (SQELS)
G_e	Zero frequency modulus (SQELS)
G_i	Strength of relaxation process (SQELS)
H	Height of polymer brush (NR)
I	Reflectivity of light (BAM)
I_r	Intensity of reflected light (SQELS)
I_s	Intensity of scattered light (SQELS)
L_c	Contour length of polymer chain (theory)
M	Molecular weight of monomer unit (theory)
M	Matrix (NR)
M_n	Number average molecular weight
M_w	Weight average molecular weight
N	Number of monomer units per chain / degree of polymerisation
N	Atomic number density (NR)
N_A	Avagadro's number
$P(\omega)$	Power spectrum (SQELS)

Q	Scattering vector (NR)
R	Gas constant
R	Reflectivity (NR)
R	Radius of curvature (BAM)
R_f	Fresnel reflectivity
R_g	Radius of gyration
R_p	p-component of light (BAM)
T	Absolute temperature
V_s	Segment volume (NR)
ΔV	Surface potential (BAM)

Roman Symbols – Lower Case

a	Length of monomer unit (theory)
b	Scattering length (NR)
b	Statistical step length (SQELS)
c	Concentration (theory)
c^*	Concentration at transition from semi-dilute to dilute regime (theory)
c_s	Salt concentration of subphase (theory)
d	Film thickness
d	Layer thickness (NR)
e	Charge on a monomer unit (theory)
g	Number of monomer units per 'blob' (theory)
$g(\tau)$	Correlation function in the time domain (SQELS)
h, h_o	Polymer brush height
h^*	Equilibrium brush height
$h_{ii}(Q)$	Self partial structure factor (NR)
$h_{ij}(Q)$	Cross partial structure factor (NR)
k	Wave vector
k_B	Boltzmann's constant
l_B	Bjerrum length (theory)
l_k	Kuhn length (theory)
m	Scattering mass per unit area of film (NR)

n	Refractive index
n	Number density (NR)
q	Wavenumber (SQELS)
r	Fresnel coefficient
$r_s(\theta_B)$	Reflectivity from a Fresnel interface at the Brewster angle (BAM)
s	Molecular area of coil (theory)
s	Gradient of slope (isotherms)
t	Time
w	Interaction strength (theory)
w	Potential energy (BAM)
z	Height from grafting surface (theory)
z	Depth (NR)

Greek Symbols – Upper Case

Γ	Wave damping (SQELS)
Γ_C	Capillary wave damping (SQELS)
Γ_D	Dilational wave damping (SQELS)
Γ_{norm}	Normalised capillary wave damping (SQELS)
Γ_s	Surface concentration
$\Gamma_{s,i}$	Surface concentration of component i
Γ_s^*	Surface concentration of transition from dilute to semi-dilute regime (theory)
Γ_s^{**}	Surface concentration of transition from semi-dilute to concentrated regime (theory)
Λ	Wavelength (SQELS)
Π	Surface pressure
Π_e	Electrostatic surface pressure (isotherms)
Π_i	Surface pressure of component i
Φ	Polymer fraction (theory)
Φ^*	Polymer fraction at transition from dilute to semi-dilute regime (theory)
Φ^{**}	Polymer fraction at transition from semi-dilute to concentrated regime (theory)
Ω	Frequency of free oscillator (SQELS)

Greek Symbols – Lower Case

β	Optical path length (NR)
β	Instrumental line broadening (SQELS)
γ, γ_o	Surface tension
γ'	Transverse shear viscosity (SQELS)
δ	Layer separation (NR)
ε	Dielectric constant of water (theory)
$\varepsilon, \varepsilon_o$	Dilational modulus
ε'	Dilational viscosity (SQELS)
η	Viscosity
θ	Angle
θ_B	Brewster angle (BAM)
θ_c	Critical angle
θ_i	Angle of incidence
θ_r	Angle of reflection
ϑ	Tilt angle (BAM)
κ	Coupling constant (SQELS)
κ, κ_o	Bending modulus (SQELS)
κ'	Bending viscosity (SQELS)
κ_s	Debye screening length
λ	Lagrangian multiplier (NR)
λ	Neutron wavelength (NR)
λ, λ_o	Coupling constant (SQELS)
λ'	Coupling viscosity (SQELS)
λ_B	Line tension (BAM)
ν	Scaling exponent (theory)
ξ	Radius of 'blob' (theory)
ξ	Interfacial disturbance (SQELS)
π	Osmotic pressure (theory)
ρ	Density
ρ, ρ_d	Scattering length density (NR)

$\overline{\rho}_B$	Ellipticity (BAM)
ϕ	Monomer density
ϕ	Volume fraction (NR)
σ, σ_o	Grafting density / number of chains per unit area
σ	Thickness of a hyperbolic tangent layer (NR)
σ	Standard deviation of rate of change of scattering length density (NR)
τ	Reduced temperature (theory)
τ	Relaxation time (SQELS)
χ	Interaction parameter (NR)
χ^2	'Goodness' of fit
ψ_θ	Critical exponent in theta solvent case (theory)
ω, ω_o	Wave frequency (SQELS)
ω_C	Capillary wave frequency (SQELS)
ω_D	Dilational wave frequency (SQELS)
ω_{norm}	Normalised capillary wave frequency (SQELS)

CONTENTS

CHAPTER FIVE: SURFACE PRESSURE ISOTHERMS & BREWSTER ANGLE MICROSCOPY

CHAPTER ONE

INTRODUCTION

1.1. POLYMERS AT INTERFACES

Polymers at surfaces and interfaces have been the subject of extensive scientific research.[1] An enormous range of such systems have been studied, examining polymers at air-liquid, liquid-liquid, solid-liquid, air-solid and polymer-polymer interfaces. Due to the nature of the research described in this thesis, the following discussion will concentrate on polymers at the air-liquid interface.

In addition to the scientific curiosity evoked by such systems, polymers at interfaces have industrial applications, one major use being the stabilisation of colloid dispersions.[2] This stabilisation is usually steric (where the polymer is attached, by grafting or physical absorption, to the surface of particles) or depletion (where the polymer molecules are free in solution) in nature. A combination of these two effects is electrosteric stabilisation, which is particularly applicable to polyelectrolytes. Copolymers are predominately used in these stabilisation processes. Diblock copolymers are effectively two polymer chains attached end-to-end, resulting in a single chain with vastly differing properties at each extremity. At the air-liquid interface, the copolymers of specific interest are those that are amphiphilic in nature, one block of the polymer being hydrophilic and the other hydrophobic. An example of such a polymer is the system used in this work, a diblock copolymer of poly(methyl methacrylate) and poly(4-vinyl ethylpyridinium bromide) ('PMMA-QP4VP'). The PMMA block is hydrophobic, whereas the polyelectrolytic QP4VP block extends into the subphase and forms the hydrophilic component of the system.

The air-liquid interface (where the liquid is usually aqueous in nature) provides a convenient medium for the study of interfacial phenomena. Such an interface is naturally flat and relatively smooth in nature, although the surface is perturbed by thermal fluctuations of *ca.* 2Å in magnitude. By the use of a Langmuir-Adams trough with a movable barrier, compression of the film to explore a range of surface concentrations is straightforward. Monolayer films of polymers can be produced, either by absorption at the interface or by the spreading of a film, usually from a solution of the polymer in a volatile solvent.

Historically, cultural and religious interest in monolayers dates back four millennia to the Babylonians, who practised lecanomancy, divination by the observation of oil on water.[3] The scientific interest in such systems is much more recent, the first reported experiment dating back two and a quarter centuries.[4] In this, Benjamin Franklin reported than one teaspoon of oil spread on a pond in Clapham Common spread "with surprising swiftness" to cover an area of over half an acre. Earlier this century, the main pioneers in the field were Irwin Langmuir and Katherine Blodgett. Langmuir studied the relationship between the surface pressure and area of such monolayers[5] and Blodgett developed the process of transferring monolayers onto solid substrates,[6] allowing the production of multi-layer films.

Polymer monolayers can be investigated by a myriad of techniques including surface pressure isotherms, neutron reflectometry, surface quasi-elastic light scattering (SQELS), Brewster angle microscopy (BAM), fluorescence microscopy, X-ray reflectivity, Fourier transform infra-red (FTIR) spectroscopy and ellipsometry. These techniques are discussed below, with emphasis being placed on the first four methods that were used in this work.

The simplest technique used in the characterisation of monolayer films is the recording of surface pressure isotherms, where surface pressure is measured as a function of either surface area or surface concentration. The isotherms obtained for polymer molecules (which are usually classified as liquid expanded or liquid condensed films) are relatively featureless compared to those for low molecular weight compounds.[7]

A vast quantity of literature reporting surface pressure isotherms of polymeric molecules has been published. Examples of work more pertinent to the current experimental study are the PMMA studies of Brinkhuis and Schouten, which compare the isotherms obtained for syndiotactic and isotactic PMMA[8] with that from a mixture of these stereotactic forms.[9] Isotherms have been recorded for polymers of poly(4-vinyl pyridine)s quaternised with alkyl chains of varying lengths and differing counterions.[10,11] In addition to this work, where the films are spread on on water, the liquid expanded – liquid condensed phase transition of such

monolayers spread on KBr solution has also been investigated.[12,13] The surface pressure behaviour of low concentration films of PMMA-QP4VP on subphases of both water and KCl solutions has been studied by Rondelez.[14] A combination of surface pressure measurement and transmission electron microscope imaging was used by Eisenberg[15] to observe micelle formation in a monolayer of a diblock copolymer of polystyrene and poly(4-vinyl pyridine)quaternised with decyl iodide.
Scaling laws developed by de Gennes[16] can be applied to surface pressure isotherms. These have been developed further by des Cloizeaux[17] and Daoud and Jannink,[18] who generated scaling expressions for multi-dimensional systems. The scaling exponents obtained have been verified by numerous computer simulations.[19,20,21,22,23,24]
Other physical data extractable from surface pressure isotherms are phase transition points, polymer molecular weights, viral coefficients and dilational moduli. These are discussed at the appropriate points in chapter five.

Surface quasi-elastic light scattering (SQELS) is a relatively new technique that provides information on the parameters of the capillary waves of the liquid surface. These capillary waves scatter light, the extent of such scattering being determined by the viscoelastic parameters of the surface film. An experimental set-up similar to that used today was first developed by Hård[25] who used a diffraction grating to generate a reference beam, producing a heterodyne signal when mixed with scattered light from the detector. Recent modification of the experimental technique was carried out by Earnshaw.[26]

The majority of the SQELS experiments on polymer systems reported in the literature fall into three categories. Firstly, a bulk of work was published by Yu and co-workers, who studied a host of polymer systems, predominantly at the air-liquid interface. Examples of such work are the studies of films of poly(vinyl acetate),[27] poly(vinyl stearate),[28] a poly(ethylene oxide)-polystyrene block copolymer,[29] poly(ethylene oxide) homopolymer,[30] poly(*n*-butyl methacrylate)[31] and linear[32] and branched[33] poly(dimethylsiloxane)s. However, the data fitting method used in these studies is open to debate because the frequency and damping of the capillary waves were obtained by the fitting of a true (rather than skewed) Lorentzian curve to the power spectrum. Furthermore, the four viscoelastic parameters were not determined

unequivocally, the transverse shear viscosity was assumed to be zero and the dynamic surface tension to be equal to the static surface tension.

An improved method of data analysis, the spectral fitting technique, was developed by Earnshaw.[34] This allowed the simultaneous extraction of all four viscoelastic parameters (surface tension, γ_o; transverse shear viscosity, γ'; dilational modulus, ε_o and dilational viscosity, ε') without making any prior assumptions. The fitting procedure has now been used to a wide extent, predominantly by Earnshaw[35,36,37] to study a wide range of systems at the air-water interface and by Richards and co-workers, to examine polymeric systems. The latter study has investigated the dynamic properties of spread films of poly(methyl methacrylate),[38] poly(ethylene oxide),[38,39] block[40] and graft[41,42] copolymers with these two components and aqueous solutions of poly(ethylene oxide).[43] This work, and that of other groups[44,45] included the observation that one of the viscoelastic parameters, dilational viscosity, regularly recorded negative values. This phenomenon was generally assigned to be due to inadequacies in the dispersion equation used to describe the experimental data and it was suggested that the expression required modification.

To this end, Buzza[46] re-derived the dispersion equation with the emphasis on adsorbed polymers. It was found that transverse shear viscosity, γ', was equal to zero and that two new parameters, a bending modulus and a coupling constant, were introduced. These latter two quantities are not applicable in the case of polymers spread at the air-water interface, but the constraining of γ' to zero represents a marked difference to previous studies. The results of this theoretical study are now being applied to experimental studies,[47,48,49] where the data is analysed for only the remaining three viscoelastic parameters, γ_o, ε_o and ε'. In some cases, negative dilational moduli are still observed, perhaps implying that the dispersion equation requires yet further modification.

The above three data analysis techniques make use of two different data analysis techniques to obtain either three or four viscoelastic parameters. Direct comparison of the results obtained between any two of these methods is therefore impossible, a problem which is unavoidable as the theory of the interfacial dynamics of polymer monolayers continues to be developed.

Another recently developed technique is that of neutron reflectometry, which allows the complete determination of the organisation of a polymer at the interface. Neutron reflection was first reported by Fermi[50] over fifty years ago, but it is only in the last two decades that the technique has been applied to polymeric systems at 'wet' interfaces. Such advancement has been due largely to the building of the CRISP[51] and SURF[52] reflectometers at the Rutherford – Appleton Laboratory, Oxfordshire. The technique of hydrogen – deuterium isotopic substitution is used to provide sufficient contrast between the species, allowing a complete description of the interfacial region to be obtained.

The first techniques used to extract such information initially involved modelling profiles to the raw reflectivity data. More recently, the kinematic approximation developed by Thomas[53] has allowed the contribution of each component to the total reflectivity to be determined. From this, the organisation of each species can be found, along with the separations between them. By combining these two sets of data, a full number density profile of the interfacial region can be generated.

An extensive review[52] of the recent use of neutron reflection to study chemical surfaces and interfaces (both polymeric and non-polymeric) is available in the literature. More pertinent to the work here, neutron reflectometry has been used to obtain the surface structure of monolayers of PMMA of various tacticities,[54] and films of PMMA spread on both water[55,56] and aqueous solutions of poly(ethylene oxide).[57] Further work on similar materials includes films of a PEO homopolymer[56,58] and both linear diblock[56,59] and graft[60] copolymers of PMMA and PEO. Other examples of studied of monolayers spread at the air-water interface are poly(lauryl methacrylate)[61] and poly(dimethylsiloxane)[62] homopolymers and a diblock copolymer of poly(ethylene oxide) and polystyrene.[63] Examples of more recent work are the study of a copolymer of poly(2-(dimethylamino)ethyl methacrylate) and PMMA adsorbed both at the air-water interface[64] and on a water subphase with varying pH and electrolyte content.[65]

The final experimental technique used, Brewster angle microscopy (BAM) was developed at the beginning of the decade.[66,67] The technique uses p-polarised light at the Brewster angle (53.1° for an air-water interface), where light is not reflected at a clean interface. The introduction of a monolayer causes a small quantity of the

incident light to be reflected, which can be recorded and imaged to provide a direct visualisation of the morphology and structural organisation of the monolayer. For examples of some of the systems studied by BAM, see the recent review[68] by Möbius. In addition to providing images of the system being studied, BAM can also be used in a qualitative fashion to give information on physical parameters such as hydrocarbon chain tilt,[69] interfacial line tension[70] and film thickness.[71] BAM is an advancement of the technique of fluorescent microscopy,[72] in which a fluorescent amphiphilic molecule is added to the monolayer to allow the visualisation of domains of different phases (e.g. the liquid expanded – liquid condensed phase transition). However, the technique has its drawbacks as the introduction of such species into the system may in some way affect the transition under study, a problem avoided with BAM.

Other techniques used to study polymers at interfaces include ellipsometry, which exploits the changes in the ellipticity of light after reflection to study systems such as PMMA.[73] Fourier transform infra-red (FTIR) spectroscopy has been used to determine the orientational characteristics of a Langmuir-Blodgett film of PMMA[74] and X-ray reflectivity has also been used to study polymer monolayers on water.[75] The latter of these techniques suffers from lack of contrast at the interfacial region, a problem that is overcome in neutron reflectometry by the use of selective deuteration.

1.2. Aims & Outline

The aim of this work is to investigate the organisation and surface wave dynamics of a copolyelectrolyte monolayer at the air – liquid interface. The system studied is a diblock copolyelectrolyte of PMMA and poly(4-vinyl pyridine) quaternised with bromoethane, a continuation of the work on PMMA homopolymers[38] and copolymers[40] and the surface pressure studies of the specific copolymer used here.[14] The inclusion of the QP4VP block in the copolymer introduces polyelectrolyte character to the system. The spreading of a film on water and salt solution subphases therefore allows the study of the behaviour of this charged species with changing subphase salt concentration.

Following the synthesis and characterisation of the polymer (and three partially deuterated analogues), the objectives were the determination of the surface organisation of the system by a combination of surface pressure isotherms, neutron reflectometry and Brewster angle microscopy. SQELS experiments were then used to determine the dynamic behaviour.

The results from each technique have been correlated with each other, to gain an understanding of any link between the structural organisation and surface dynamics of the system. The experimental results are also compared to theory wherever appropriate.

Following this brief introduction to the field, chapter two of this thesis covers the background theory of polymers at interfaces and the experimental procedures used in this work. Chapter three describes the mechanics of carrying out such experiments, before chapter four details the synthesis and characterisation of the polymers. The main bulk of the work then concentrates on the experimental results obtained, along with their analysis and discussion. The results from surface pressure isotherm and Brewster angle microscopy experiments are presented in chapter five, followed by those from neutron reflectometry and SQELS in chapters six and seven respectively. Finally, chapter eight summarises and concludes the results obtained and makes suggestions for further studies.

1.3. REFERENCES

1 R. A. L. Jones and R. W. Richards, *Polymers at Surfaces and Interfaces*, Cambridge University Press, Cambridge, UK, 1999.

2 D. H. Napper, *Polymeric Stabilization of Colloidal Dispersions,* Academic Press, London, UK, 1993.

3 A. L. Oppenheim, *Ancient Mesopotamia: Portrait of a Dead Civilisation*, University of Chicago Press, Chicago, USA, 1964.

4 B. Franklin, *Phil. Trans. Roy. Soc.*, 1774, **64**, 445.

5 I. Langmuir, *J. Am. Chem. Soc.*, 1917, **39**, 1848.

6 K. B. Blodgett, *Phys. Rev.*, 1939, **55**, 391.

7 A. W. Adamson, *Physical Chemistry of Surfaces*, 4/e, Wiley-Interscience, New York, USA, 1982.

8 R. H. G. Brinkhuis and A. J. Schouten, *Macromolecules*, 1991, **24**, 1487.

9 R. H. G. Brinkhuis and A. J. Schouten, *Macromolecules*, 1992, **25**, 2725.

10 F. Davis, P. Hodge, X.-H. Liu and Z. Ali-Adib, *Macromolecules*, 1994, **27**, 1957.

11 J. Wagner, T. Michel and W. Nitsch, *Langmuir*, 1996, **12**, 2807.

12 M. Kawaguchi, S. Itoh and A. Takahashi, *Macromolecules*, 1987, **20**, 1052.

13 M. Kawaguchi, S. Itoh and A. Takahashi, *Macromolecules*, 1987, **20**, 1056.

14 E. Bringuier, R. Vilanove, Y. Gallot, J. Selb and F. Rondelez, *J. Colloid Interface Sci.*, 1985, **104**, 95.

15 J. Zhu, A. Eisenbers and R. B. Lennox, *J. Am. Chem. Soc.*, 1991, **113**, 5583.

16 P.-G. de Gennes, *Scaling Concept in Polymer Physics*, Cornell University Press, New York, USA, 1979.

17 J. des Cloizeaux, *J. Phys. (Paris) Lett.*, 1980, **41**, L-151.

18 M. Daoud and G. Jannink, *J. Phys. (Paris)*, 1976, **37**, 973.

19 R. Derrida, *J. Phys. A: Math. Gen.,* 1981, **14**, L-5.

20 S. Havlin and D. Ben-Avraham, *Phys. Rev. A,* 1983, **27**, 2759.

21 R. Vilanove, D. Poupinet and F. Rondelez, *Macromolecules*, 1989, **22**, 2491.

22 R. Derrida and H. Saleur, *J. Phys. A: Math. Gen.,* 1985, **18**, L-1075.

23 J. A. Marqusee and J.M. Deutch, *J. Chem. Phys.*, 1981, **75**, 5179.

24 K. Kremer and J.W. Lyklema, *Phys. Rev. Lett.*, 1985, **54**, 267.

25 S. Hård, Y. Hamnerius and O. Nilsson, *J. App. Phys.*, 1976, **47**, 2433.

26 C. J. Hughes and J. C. Earnshaw, *J. Phys. E: Rev. Sci. Instrum.*, 1993, **64**, 2789.

27 M. Kawaguchi, M. Sano, Y.-L. Chen, G. Zografi and H. Yu, *Macromolecules,* 1986, **19**, 2606.

28 Y.-L. Chen, M. Kawaguchi, H. Yu and G. Zografi, *Langmuir,* 1987, **3**, 31.

29 B. B. Sauer, H. Yu, C.-F. Tien and D. F. Hager, *Macromolecules,* 1987, **20**, 393.

30 B. B. Sauer, M. Kawaguchi and H. Yu, *Macromolecules*, 1987, **20**, 2732.

31 K.-H. Yoo and H. Yu, *Macromolecules*, 1989, **22**, 4019.

32 F. E. Runge and H. Yu, *Langmuir*, 1993, **9**, 3191.

33 F. E. Runge, H. Yu and D. Woermann, *Ber. Bunsenges. Phys. Chem.*, 1994, **98**, 1046.

34 J. C. Earnshaw, R. C. McGivern, A. C. McLaughlin and P. J. Winch, *Langmuir*, 1990, **6**, 649.

35 J. C. Earnshaw and P. J. Winch, *Thin Solid Films*, 1988, **159**, 159.

36 J. C. Earnshaw and D. J. Sharpe, *J. Chem. Soc., Faraday Trans.*, 1996, **92(4)**, 611.

37 J. C. Earnshaw, C. P. Nugent, K. Lunkenheimer and R. Hirte, *J. Phys. Chem.*, 1996, **100**, 5004.

38 R. W. Richards and M. R. Taylor, *J. Chem. Soc., Faraday Trans.*, 1996, **92(4)**, 601.

39 C. Booth, R. W. Richards, M. R. Taylor and G.-E. Yu, *J. Phys. Chem. B*, 1998, **102**, 2001.

40 R. W. Richards, B. R. Rochford and M. R. Taylor, *Macromolecules*, 1996, **29**, 1980.

41 S. K. Peace and R. W. Richards, *Polymer*, 1996, **37**, 4945.

42 S. K. Peace and R. W. Richards, *Langmuir*, 1998, **14**, 667.

43 R. W. Richards and M. R. Taylor, *Macromolecules*, 1997, **30**, 3892.

44 D. J. Sharpe and J. Eastoe, *Langmuir*, 1995, **11**, 4636.

45 D. J. Sharpe and J. Eastoe, *Langmuir*, 1996, **12**, 2303.

46 D. M. A. Buzza, J. L. Jones, T. C. B. McLeish and R. W. Richards, *J. Chem. Phys.*, 1998, **109**, 5008.

47 F. Monroy, F. Ortega and R. G. Rubio, *J. Phys. Chem. B*, 1999, **103**, 2061.

48 A. S. Brown, R. W. Richards, D. M. A. Buzza, and T. C. B. McLeish, *Farad. Discuss.*, 1999, **112**, 309.

49 A. J. Milling, R. W. Richards, R. C. Hiorns and R. G. Jones, *Submitted for publication.*

50 E. Fermi and L. Marshall, *Phys. Rev.*, 1947, **71**, 666.

51 J. Penfold, R.C. Ward and W. G. Williams, *J. Phys. E: Sci. Instrum.*, 1987, **20**, 1411.

52 J. Penfold, R. M. Richardson, A. Zarbakhsh, J. R. P. Webster, D. G. Bucknall, A. R. Rennie, R. A. L. Jones, T. Cosgrove, R. K. Thomas, J. S. Higgins, P. D. I. Fletcher, E. Dickinson, S. J. Roser, I. A. McLure, A. R. Hillman, R. W. Richards, E. J. Staples, A. N. Burgess, E. A. Simister and J. W. White, *J. Chem. Soc. Faraday Trans.*, 1997, **93(22)**, 3899.

53 T. L. Crowley, E. M. Lee, E. A. Simister and R. K. Thomas, *Physica B*, 1991, **173**, 143.

54 J. A. Henderson, R. W. Richards, J. Penfold, C. Shackleton and R. K. Thomas, *Polymer*, 1991, **32**, 3284.

55 J. A. Henderson, R. W. Richards, J. Penfold and R. K. Thomas, *Macromolecules*, 1993, **26**, 65.

56 S. K. Gissing, R. W. Richards and B. R. Rochford, *Colloids and Surfaces A: Physiochem. Eng. Asp.*, 1994, **86**, 171.

57 S. K. Peace, R. W. Richards, F. T. Kiff, J. Penfold and N. Williams, *Polymer*, 1999, **40**, 207.

58 J. A. Henderson, R. W. Richards, J. Penfold R. K. Thomas and J. R. Lu, *Macromolecules*, 1993, **26**, 4591.

59 R. W. Richards, B. R. Rochford and J. R. P. Webster, *J. Chem. Soc. Farad. Discuss.*, 1994, **98**, 263.

60 S. K. Peace, R. W. Richards, M. R. Taylor J. R. P. Webster and N. Williams, *Macromolecules*, 1998, **31**, 1261.

61 I. Reynolds, R. W. Richards and J. R. P. Webster, *Macromolecules*, 1995, **28**, 7845.

62 L. T. Lee, E. K. Mann, D. Lanevin and B. Farnoux, *Langmuir*, 1991, **7**, 3076.

63 H. D. Bijsterbosch, V. O. de Haan, A. W. de Graaf, M. Mellema, F. A. M. Leermakers, M. A. Cohen Stuart and A. A. van Well, *Langmuir*, 1995, **11**, 4467.

64 S. W. An, R. K. Thomas, F. L. Baines, N. C. Billingham, S. P. Armes and J. Penfold, *Macromolecules*, 1998, **31**, 7877.

65 S. W. An, R. K. Thomas, F. L. Baines, N. C. Billingham, S. P. Armes and J. Penfold, *J. Phys. Chem. B*, 1998, **102**, 5120.

66 S. Hénon and J. Meunier, *Rev. Sci. Instrum.*, 1991, **62(4)**, 936.

67 D. Hönig and D. Möbius, *J. Phys. Chem.*, 1991, **95**, 4590.

68 D. Möbius, *Curr. Opin. Colloid Interface Sci.*, 1998, **3**, 137.

69 C. Lautz, Th. M. Fischer and J. Kildea, *J. Chem. Phys.*, 1997, **107**, 7448.

70 S. Riviére, S. Hénon, J. Meunier, G. Albrecht, M. M. Boissonnade and A. Baszkin, *Phys. Rev. Lett.*, 1995, **75**, 2506.

71 J. M. Rodríguez Patino, C. Carrera and M^{a}. R. Rodríguez Niño, *Langmuir*, 1999, **15**, 2484.

72 B. Moore, C. M. Knobler, D. Broseta and F. Rondelez, *J. Chem. Soc. Faraday Trans.*, 1986, **82(10)**, 1753.

73 B. B. Sauer, H. Yu, M. Yazdanain, G. Zografi and M. W. Kim, *Macromolecules*, 1989, **22**, 2332.

74 R. H. G. Brinkhuis and A. J. Schouten, *Macromolecules*, 1991, **24**, 1496.

75 D. A. Styrkas, R. K. Thomas, Z. A. Adib, F. Davies, P. Hodge and X. H. Liu, *Macromolecules*, 1994, **27**, 5504.

CHAPTER TWO

THEORY

2.1. POLYMER MONOLAYERS

2.1.1. SURFACE PRESSURE ISOTHERMS

When a monolayer is spread at the air-water interface, the surface tension of the system may be reduced. The surface pressure, Π, is simply defined as this reduction in surface tension:

$$\Pi = \gamma_{o,wat} - \gamma_o \qquad \textbf{Equation 2.1.1.}$$

Where $\gamma_{o,wat}$ is the surface tension of the pure water surface and γ_o that of the film covered surface.

By recording the change in surface pressure with surface concentration, information regarding the conformation of the molecules on the surface can be obtained. Plotting such data as surface pressure against surface concentration, Γ_s, results in a surface pressure isotherm. An example of an idealised isotherm is given below:

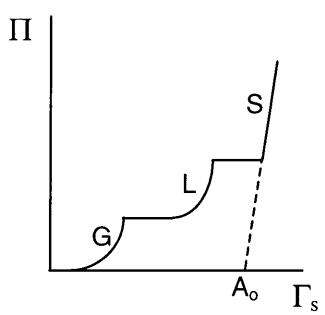

Figure 2.1.1. An idealised surface pressure isotherm. G, L and S are the gaseous, liquid and solid states respectively. A_o is the close-packed area.

The isotherm above is typical of that produced by stearic acid, $CH_3(CH_2)_{16}COOH$. In general, isotherms produced by polymeric molecules tend to be more featureless.

The differing states in which a monolayer may exist[1] are shown in figure 2.1.1. G is the gaseous state which, as is the case with bulk matter, should always be attainable at sufficiently low surface concentrations. S is the solid state, a region (usually

linear) of low compressibility, shown by molecules such as fatty acids. Occurring between these is the liquid state, L. In this regime, the film is coherent (some co-operative interaction between molecules is present). This state is more commonly sub-divided into liquid expanded (LE) and liquid condensed (LC) states, the liquid condensed state being the closer packed of the two.

The point on the x-axis marked A_0 corresponds to the surface concentration at which the zero-pressure (or close packed, or minimum) area occurs. This can be easily obtained by the extrapolation of the solid phase of the isotherm back to zero pressure. However, a certain amount of care has to be taken when quoting this value for polymeric systems. If the polymer exists in a non-uniform configuration (e.g. coils on the liquid surface), the results obtained may be invalid.

2.1.2. Equations of State

A breakthrough in providing a mathematical description of molecular interactions in polymer monolayers was obtained by Singer.[2] In this work, Huggins' theory of polymer solutions[3] was used to formulate an expression relating the surface pressure to the degree of polymerisation and surface area. This has since been refined by workers such as Frisch[4] who introduced terms to deal with chain looping and Motomura[5] who took into account cohesive forces. More recently, de Gennes[6] has made great developments in the field of scaling concepts.

2.1.3. Scaling Concepts

The use of scaling concepts in polymer science was developed by de Gennes, a full treatment of the subject being given in his classic text.[6] The more relevant points of 3-dimensional scaling theory are given below, followed by its application to monolayers, which are assumed to be 2-dimensional systems.

2.1.3.1. Scaling Concepts in 3-Dimensions

In three dimensions, for a polymer in a good solvent, three distinct regimes can be defined; dilute, onset of overlap and semi-dilute. These are shown schematically and discussed in turn:

(a) (b) (c)

Figure 2.1.2. Schematic representation of the three regimes: (a) dilute, (b) onset of overlap, (c) semi-dilute.

The Dilute Regime

The dilute regime is defined as the region where $c < c^*$, where c is the solution concentration and c^* the overlap threshold where the coils begin to be closely packed. At this point, the imaginary spheres containing the polymer chains begin to overlap. The radius of gyration, R_g, is related to the number of monomers in a chain, N, by a scaling exponent, ν:

$$R_g \approx N^{\nu} \qquad \textbf{Equation 2.1.2.}$$

The osmotic pressure, π of the system is defined by the following equation of state:

$$\frac{\pi}{T} = \frac{c}{N} + A_2 c^2 + \ldots \qquad \textbf{Equation 2.1.3.}$$

Where A_2 is the second virial coefficient which has a dependence on the value of N (the degree of polymerisation) of:

$$A_2 \approx R_g^3 N^{-2} \approx N^{-1/5} \qquad \textbf{Equation 2.1.4.}$$

The Overlap Regime

The overlap threshold is not sharp, and is simply defined as the region of cross-over between the dilute and semi-dilute regions. It is in this region where chain overlap

initially occurs. If the overlap threshold, c^*, is deemed to be comparable with the local concentration inside a single coil, it can be related to R_g by:

$$c^* \approx N/R_g^3 = a^{-3}N^{1-3\nu} = a^{-3}N^{-4/5} \qquad \textbf{Equation 2.1.5.}$$

Where a is the monomer length and ν the critical exponent. The corresponding threshold for the polymer fraction Φ^* is $\Phi^* \approx N^{-4/5}$.

The Semi-dilute Regime

In the semi-dilute region, the coils now overlap but the polymer fraction is still low ($\Phi^* < \Phi < \Phi^{**}$ where Φ^{**} is the value of the polymer fraction where transition to concentrated solution behaviour occurs). The thermodynamic properties are predicted by the scaling law for the osmotic pressure:

$$\frac{\pi}{T} = \frac{c}{N} f_\pi\left(\frac{cR_g^3}{N}\right) = \frac{c}{N} f_\pi\left(\frac{c}{c^*}\right) \qquad \textbf{Equation 2.1.6.}$$

Where $f_\pi(x)$ is a dimensionless property which has the following limiting properties:

$$\lim_{x\to\infty} f_\pi(x) = \text{constant}\, x^m = \text{constant}\left(\frac{\Phi}{\Phi^*}\right)^m = \text{constant}\,\Phi^m N^{4m/5}$$

Equation 2.1.7.

The osmotic pressure can also be related to Φ by:

$$\frac{a^3\pi}{T} = \text{constant}\,\Phi^{m+1}N^{(4m-5)-1} \qquad \textbf{Equation 2.1.8.}$$

To express π in terms independent of N, we let m = 5/4, yielding an expression relating osmotic pressure with polymer fraction:

$$\frac{\pi a^3}{T} = \text{constant}\,\Phi^{9/4} \qquad \textbf{Equation 2.1.9.}$$

2.1.3.2. Scaling Concepts in 2-Dimensions

Des Cloizeaux[7] and Daoud and Jannink[8] generated general scaling expressions for systems of dimensionality d. The expression for such a second order virial coefficient $A_{2,d}$ is:

$$A_{2,d} = N^{\nu d}\tau^{d(\nu-\nu_\theta)\psi_\theta} \qquad \textbf{Equation 2.1.10.}$$

Where τ is the reduced temperature and ν, ν_θ and ψ_θ are the critical exponents in the good, theta, and two-dimensional solvent cases respectively. The dimensionality implicit in scaling theory renders it applicable to polymer monolayers, which are assumed to be 2-dimensional systems.

The Dilute Regime

In the dilute regime, the relationship between the osmotic pressure and the second virial coefficient is:

$$\frac{\pi}{RT} = \frac{\Gamma_s}{M_n} + \Gamma_s^2 A_{2,2} + \ldots \qquad \textbf{Equation 2.1.11.}$$

Where M_n is the number average molecular weight of the polymer, Γ_s the surface concentration and $A_{2,2}$ the two-dimensional second virial coefficient.

Numerous simulations have been undertaken to obtain the value of the exponent ν. For good solvent conditions, mean field theory predicts the value of ν to be 0.75. Values of 0.7503 ± 0.0002[9] and 0.753 ± 0.004[10] have been calculated by matrix transfer and Monte Carlo methods respectively.

In theta solvent conditions, a wide range of ν_θ values have been obtained,[11] varying between 1/2 (the ideal random walk value) and 2/3 (the mean field value when only ternary interactions are considered). Examples of such values are 0.55 for transfer matrix data,[12] 0.567 ± 0.003 for an indefinitely growing self-avoiding walk method[13] and 0.59 for real space normalisation.[14]

The Overlap Regime

In the overlap regime, the general definition of c^* is given by the equation:

$$c^* \approx N/R_{g,d}^{d} \approx N^{1-\nu d}\tau^{-d(\nu-\nu_\theta)\psi_\theta} \qquad \textbf{Equation 2.1.12.}$$

And the osmotic pressure expression is:

$$\pi/T \approx c^{\nu d(\nu d-1)}\tau^{(\nu-\nu_\theta)d/\psi_\theta(\nu d-1)} \qquad \textbf{Equation 2.1.13.}$$

The Semi-dilute Regime

In the semi-dilute regime, a two-dimensional analogue of this is difficult to envisage as it is impossible for an entangled monolayer system to have anything less than three dimensions. However, the following equation for osmotic pressure is still valid:

$$\pi/T = c^{\nu_\theta d/(\nu_\theta d-1)} \qquad \textbf{Equation 2.1.14.}$$

2.1.4. Polymer Brushes

2.1.4.1. Uncharged Polymer Brushes

The conformation of polymers end-grafted at interfaces has also been defined by the use of scaling laws. As surface concentration increases, the steric interaction between the polymer chains leads to a stretching of the chains, resulting in what is termed a 'brush' conformation.

Alexander[15] and de Gennes[16] used a scaling approach to investigate such a system. They represented the polymer chain as a series of blobs, each of radius $\xi \sim \sigma^{1/2}$ and containing $g \sim \xi^{1/\nu}$ monomer units. Using the exponent $\nu \approx 3/5$, it was found that the height of a polymer brush scales as $h \sim N\sigma^{1/3}$ and the surface pressure scales as $\Pi \sim N\sigma^{11/6}$. N is the length of the polymer and σ is the number of chains per unit area. Such an scaling approach yields a step-function density profile.

An alternative approach to polymer brush theory was that taken by Milner, Witten and Cates,[17] who used a self consistent field (SCF) approximation model. Such a

model makes no assumption regarding the density profile of the monolayer. For a grafted polymer, this theory finds that the concentration profile is parabolic in nature, a significant departure from the step-function profile in the above work. The parabolic density profile is defined as:

$$\phi = \frac{B}{w}\left[(h^*)^2 - z^2\right] \qquad \textbf{Equation 2.1.15.}$$

Where ϕ is the monomer density, h^* the equilibrium brush height, z the height from the grafting surface, B the spring constant and w the interaction strength.
Such a parabolic profile results in the free ends of the polymer being distributed throughout the entire length of the brush, rather than in a confined region at the extremities of the system. For the scaling relationships, SCF finds the same scaling for brush height as the Alexander – de Gennes model ($h \sim N\sigma^{1/3}$). A small difference in the scaling of surface pressure is observed, the relationship in this case being given as $\Pi \sim N\sigma^{5/3}$ as opposed to $\Pi \sim N\sigma^{11/6}$

2.1.4.2. Polyelectrolyte Brushes

An outline of the theoretical investigations into polyelectrolyte brushes in both water and salt solutions is given below. For consistency, some parameters are assigned different symbols than in the original text.
Early work by Bringuier[18] studied a theoretical diblock copolymer at the air-liquid interface. In the semi-dilute regime, the polyelectrolyte sequence remained fully stretched and therefore only one characteristic length was observed. The brush height is scaled as:

$$h \sim Nl_B \qquad \textbf{Equation 2.1.16.}$$

Where N is the number of ionisable monomers (each of charge e) and l_B the Bjerrum length (the electrostatic separation length), which is defined as:

$$l_B = \frac{e^2}{\varepsilon k_B T}$$ **Equation 2.1.17.**

Where ε is the dielectric constant of water. A free energy study revealed that surface pressure, Π, could be expressed as:

$$\Pi = \frac{1}{2} k_B T c$$ **Equation 2.1.18.**

Surface pressure thus being linear with polymer concentration, c, but independent of N.

To examine the conformation of a charged polymer brush in salt solution, Pincus[19] studied a densely grafted brush by the use of mean-field theory. For simplicity, only the electrostatic interactions were considered. The Kuhn (or segment) length, l_k, could then simply be expressed as l, the Kuhn length for an uncharged chain. In salt solution, the osmotic pressure was found to be:

$$\pi = \frac{c^2 T}{2c_s}$$ **Equation 2.1.19.**

Where c_s is the salt concentration. The excluded volume parameter is:

$$\nu = \frac{4\pi l}{\kappa_s^2} \qquad \text{i.e.:} \qquad \nu \sim \frac{1}{\kappa_s^2}$$ **Equation 2.1.20.**

Where κ_s^{-1} is the Debye screening length.

When the salt concentration falls below the brush counterion concentration, the swelling of the layer reaches an asymptotic value, independent of both c_s and σ (grafting density).

A similar mean-field method is used by Argillier and Tirrell.[20] In this instance, a diblock copolymer consisting of a collapsed layer and a stretched polyelectrolyte

layer is studied. Local chain stiffening was included in the model and the excluded volume parameter was found to scale as:

$$\nu \sim l_k^3 \qquad \textbf{Equation 2.1.21.}$$

The length of the polyelectrolyte chain is given by the expression:

$$h = aM\sigma^{1/3}c_s^{-2/3} \qquad \text{i.e.:} \quad h \sim c_s^{-2/3} \qquad \textbf{Equation 2.1.22.}$$

Where a is the length and M the molecular weight of a monomer unit receptively. A high scaling factor is reported in this case, where h is not independent of σ.

A Monte Carlo simulation method was utilised by Muthukumar.[21] A linearised Poisson - Boltzmann distribution function was used, balancing the osmotic pressure of the counterions with the force due to the entropy of the brush. A series of regimes of differing electrostatic interactions were identified. In the high salt concentration regime, the brush layer thickness was expressed as:

$$h \approx \left(\frac{\sigma}{2l_k c_s}\right)^{1/3} l_k N \qquad \text{i.e.:} \quad h \sim c_s^{-1/3} \qquad \textbf{Equation 2.1.23.}$$

Theoretical investigations using Milner, Witten and Cates' self consistent field theory[17] were carried out by both Miklavic[22] and Misra.[23] These expansions to Milner, Witten and Cates' approach reveal that the polyelectrolyte brush height no longer scales to $\sigma^{1/3}$, as is the case with neutral polymer brushes. However, a parabolic segment density profile is again reported. Such a brush is found to exist in a more extended conformation as salt concentration decreases or charge density increases.

A self consistent field method was also applied by Zhulina.[24] For the salted brush, if salt concentration exceeds counterion concentration, it is reported that:

$$h \sim L_c\sigma^{1/3}c_s^{-1/3} \qquad \textbf{Equation 2.1.24.}$$

Where L_c is the contour length of the polymer chains.

Further investigations by the same group[25,26] resulted in the production of a phase diagram of the states of a grafted polyelectrolyte layer. The two states most relevant to this work are the osmotically swollen brush and the salted brush. Expressions are generated for the dimensions of the brush, both perpendicular and parallel to the grafting interface and in both theta and good solvent environments.
For the osmotically swollen brush, the layer brush thickness is given by:

$$h \approx l_k (eN)^{1/3} \qquad \textbf{Equation 2.1.25.}$$

In the salted brush region, the thickness of the film decreases and is now given by:

$$h \approx N(N/e)^{-2/3}(sc_s)^{-1/3} \qquad \text{i.e.:} \quad h \sim c_s^{-1/3} \qquad \textbf{Equation 2.1.26.}$$

Where s in the molecular area of the coil.

From the above, it can clearly be seen that, at sufficiently high salt concentrations, the majority of theoretical studies have found the length of a polyelectrolyte brush to scale with salt concentration as $c_s^{-1/3}$.

2.2. NEUTRON REFLECTOMETRY

In general, the laws governing the specular reflection of neutrons at interfaces[27] bear great similarities to those of light.

When a wave is incident upon an interface between two components of refractive indices n_0 and n_1 (figure 2.2.1), the incident beam (I) emerges in two components, reflected (R) and transmitted (T), where R + T = I.

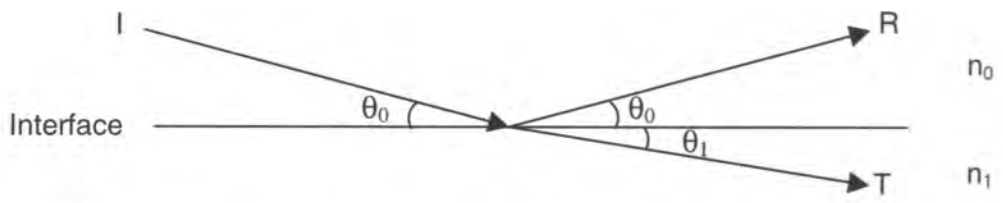

Figure 2.2.1. Reflection and transmission at an interface

Snell's law states:

$$n_0 \cos\theta_0 = n_1 \cos\theta_1 \qquad \textbf{Equation 2.2.1.}$$

At the critical angle, θ_c, $\theta_1 = 0$ and all neutrons incident upon the surface are externally reflected. From Snell's law, this angle can be defined as:

$$\cos\theta_c = n_1 / n_0 \qquad \textbf{Equation 2.2.2.}$$

The refractive index for neutrons, n, can be defined as:

$$n = 1 - \frac{\lambda^2 N b}{2\pi} \qquad \textbf{Equation 2.2.3.}$$

Where λ is the wavelength of the neutron, N the atomic number density and b the scattering length of the atom (see section 2.2.1). For neutrons at the air-liquid interface, θ_c is small, allowing a cosine series expansion to be used, thus obtaining the following expression:

$$\theta_c/\lambda = (\rho_d/\pi)^{1/2}$$ **Equation 2.2.4.**

Where ρ_d is the scattering length density of the subphase. For an air - D_2O interface, the critical angle occurs at a momentum transfer (Q) value of $0.00179Å^{-1}$ (see section 2.2.2). With the instrumental set-up used in this work, the lowest experimentally obtainable value of Q is approximately $0.025Å^{-1}$, therefore the critical angle is not encountered during experimental studies.

2.2.1. Scattering Length and Scattering Length Density

The scattering length of an atom (defined in equation 2.2.3) determines the amplitude of the reflected wave. The values of scattering length for some of the nuclei most frequently encountered in polymer chemistry are given in table 2.2.1.
The negative scattering length observed for hydrogen indicates that neutrons undergo a phase change following interaction with a hydrogen nucleus. Such a value, compared to the positive scattering length of deuterium, is of fundamental importance in neutron reflectometry. It allows the practice of deuterium labelling to be used, where hydrogenated and deuterated analogues of the same polymer are produced. Such compounds, although chemically identical, have substantially differing scattering lengths, giving the contrast that is vital for neutron reflectometry experiments.

Nucleus	b / 10^{-4}Å
H	-0.374
D	0.667
C	0.665
O	0.580
N	0.937

Table 2.2.1. Scattering lengths of some common nuclei

The scattering length density of a molecule, ρ_d, is related to the scattering length by:

$$\rho_d = \sum_i n_i b_i$$ **Equation 2.2.5.**

Where n is the number density and i the number of nuclei in the molecular system (or monomer unit in the case of a polymer). Table 2.2.2 gives the sum of scattering lengths and the scattering length densities for the monomer units and subphases used in this work:

Monomer unit	$\Sigma b_i / 10^{-4}$ Å	$\rho / 10^{-6}$ Å^{-2}
H-MMA	1.493	0.902
D-MMA	9.821	6.023
H-Q4VP	2.434	1.157
D-Q4VP	7.639	2.991
H_2O	-0.168	-0.560
D_2O	1.917	6.347

Table 2.2.2. Sum of scattering lengths and scattering length units of monomer units and subphases

The differing signs of the scattering length densities of D_2O and H_2O can be used to prepare null reflecting water (NRW), a solution with zero scattering length density. Such a solution is produced by the mixing of a 91.06 : 8.94 mass ratio of H_2O : D_2O and acts as a subphase which is 'invisible' to neutrons.

2.2.2. The Scattering Vector, Q

The scattering of neutrons can be represented in terms of neutron wave vectors in the following manner:

Figure 2.2.2. Relationship between wave vectors and Q for neutron scattering

The neutron does not exchange energy during the scattering process and so the magnitudes of the two vectors k_i and k_f are identical:

$$k_i = k_f = 2\pi/\lambda \qquad \textbf{Equation 2.2.6.}$$

The change in wave vector is defined as Q (the scattering vector) and is expressed as:

$$Q = \frac{4\pi}{\lambda}\sin(\theta/2) \qquad \textbf{Equation 2.2.7.}$$

2.2.3. Reflection and Reflectivity Profiles

Reflection of neutrons from a thin film can be schematically shown as follows:

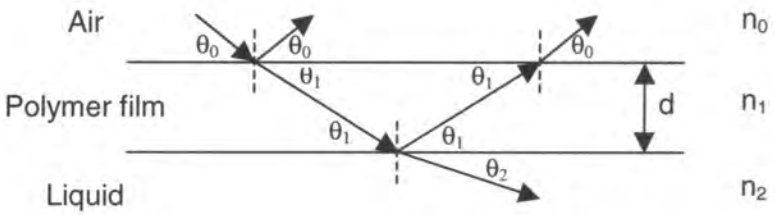

Figure 2.2.3. Reflection of neutrons from a thin film at the air-liquid interface.

Where, in this case, layers 0, 1 and 2 are air, the thin film (which has a thickness d) and the liquid respectively. n_i is the refractive index of a specific layer.
The reflectivity from an interface between two media with refractive indices n_0 and n_1 (figure 2.2.1) is given by:

$$R = \left|\frac{n_0\sin\theta_0 - n_1\sin\theta_1}{n_0\sin\theta_0 + n_1\sin\theta_1}\right|^2 \qquad \textbf{Equation 2.2.8.}$$

The corresponding expression for the thin layer case such (as outlined in figure 2.2.3) is:

$$R = \left|\frac{r_{01} + r_{12}\exp(2i\beta)}{1 + r_{01}r_{12}\exp(2i\beta)}\right|^2 \qquad \textbf{Equation 2.2.9.}$$

Where r_{ij} is the Fresnel coefficient which is defined as:

$$r_{ij} = \frac{n_i \sin\theta_i - n_j \sin\theta_{ji}}{n_i \sin\theta_i + n_{ji} \sin\theta_j}$$ **Equation 2.2.10.**

And β, the optical path length in the film is given by:

$$\beta = (2\pi/\lambda) n_1 d_1 \sin\theta$$ **Equation 2.2.11.**

2.2.4. Data Fitting Techniques

Three approaches have been used to fit reflectivity data. These are outlined in turn:

2.2.4.1. The Optical Matrix Approach

A reflectivity profile can be approximated by a series of layers. A general solution for the reflectivity relies upon the condition that the wave function of a neutron is continuous across each boundary. Each layer can be represented by a characteristic matrix:

$$M_i = \begin{bmatrix} \cos\beta_i & -(i/\kappa_i)\sin\beta_i \\ -i\kappa_i \sin\beta_i & \cos\beta_i \end{bmatrix}$$ **Equation 2.2.12.**

Where $\kappa_i = n_i \sin\theta_i$.

The total reflectivity in the system given by the sum of all the matrices, M, is:

$$M = [M_1][M_2][M_3]...[M_n]$$ **Equation 2.2.13.**

Which results in a 2x2 matrix:

$$M = \begin{bmatrix} M_{11} & M_{12} \\ M_{21} & M_{22} \end{bmatrix}$$ **Equation 2.2.14.**

And the reflectivity is given by:

$$R = \left| \frac{(M_{11} + M_{12}\kappa_s)\kappa_a - (M_{21} + M_{22})\kappa_a}{(M_{11} + M_{12}\kappa_s)\kappa_a - (M_{21} + M_{22})\kappa_a} \right|^2$$ **Equation 2.2.15.**

Where the subscripts s and a represent subphase and air respectively.

The most efficient method for calculating reflectivity is that used by Abelès.[28] In this approach, the optical matrix is defined as:

$$M_i = \begin{vmatrix} \exp(i\beta_{i-1}) & r_i \exp(i\beta_{i-1}) \\ r_i \exp(-i\beta_{i-1}) & \exp(-i\beta_{i-1}) \end{vmatrix}$$ **Equation 2.2.16.**

The resulting matrix is identical to that of equation 2.2.14 and the specular reflectivity is given by:

$$R(Q) = \frac{M_{21} M_{21}^*}{M_{11} M_{11}^*}$$ **Equation 2.2.17.**

The optical matrix method uses this approach to calculate the reflectivity profile of a system from a set of inputted parameters. This profile is then compared to the experimental data and the parameters varied until the generated and experimental profiles show the best agreement.

One major drawback with this method is that experimental data may be fitted by more than one set of parameters. However, these ambiguities can usually be overcome by ruling out the majority of the obtained fits by the use of external evidence. Once such method is the calculation of the surface concentration of each component, which should correspond to the quantity of polymer known to have been spread upon the liquid surface.

A data analysis method that results in fewer ambiguities is the kinematic approximation method:

2.2.4.2. The Kinematic Approximation

The kinematic approximation[29] is also a model dependent technique, but subtle differences in polymer organisation are more apparent, meaning that ambiguities are less inherent than in the previous method.

Assuming that reflectivity is weak, the kinematic approximation can be defined as:

$$R(Q)=\frac{16\pi^2}{Q^2}|\rho(Q)|^2 \qquad \textbf{Equation 2.2.18.}$$

Where $\rho(Q)$ is the one-dimensional Fourier transform of $\rho(z)$, where $\rho(z) = \Sigma b_i n_i(z)$ and:

$$\rho(Q)=\int_{-\infty}^{\infty}\exp(-iQz)\rho(z)dz \qquad \textbf{Equation 2.2.19.}$$

The total reflectivity of the system can be expressed as:

$$R(Q)=\frac{16\pi^2}{Q^2}\sum_i\sum_j b_i b_j h_{ij}(Q) \qquad \textbf{Equation 2.2.20.}$$

Where $h_{ij}(Q)$ is the partial structure factor.

When i = j, $h_{ii}(Q)$, the self partial structure is obtained. This describes the distribution of each of the components of the system and is given by:

$$h_{ii}(Q)=|n_i(Q)|^2 \qquad \textbf{Equation 2.2.21.}$$

The cross partial structure factor, h_{ij}, occurs when $i \neq j$. This provides details about the relative positions of the components to each other and is defined as:

$$h_{ij}(Q)=\mathrm{Re}[n_i(Q)n_j^*(Q)] \qquad \textbf{Equation 2.2.22.}$$

For a three component system (for example a diblock copolymer spread upon a liquid surface), the scattering length density dependence is given by:

$$\rho(z) = b_A n_A(z) + b_B n_B(z) + b_W n_W(z) \qquad \textbf{Equation 2.2.23.}$$

Which, by substitution into equation 2.2.18 gives:

$$R(Q) = \frac{16\pi^2}{Q^2}\begin{pmatrix} b_A^2 h_{AA}(Q) + b_B^2 h_{BB}(Q) + b_W^2 h_{WW}(Q) + b_A b_B h_{AB}(Q) \\ + b_A b_W h_{AW}(Q) + b_B b_W h_{BW}(Q) \end{pmatrix}$$

Equation 2.2.24.

In the above two equations, the subscripts A and B refer to the blocks of the polymer and W the subphase. Due to the format of the data ($R(Q)Q^4/16\pi^2$), equation 2.2.24 is actually expressed as:

$$R(Q) = \frac{Q^2 16\pi^2}{Q^4}\begin{pmatrix} b_A^2 h_{AA}(Q) + b_B^2 h_{BB}(Q) + b_W^2 h_{WW}(Q) + b_A b_B h_{AB}(Q) \\ + b_A b_W h_{AW}(Q) + b_B b_W h_{BW}(Q) \end{pmatrix}$$

Equation 2.2.25.

To utilise such an equation in its full form, a set of six experimental contrasts are required. These are obtained by the deuteration of various blocks of the copolymer and using D_2O and NRW subphases. The six contrasts required, along with the partial structure factor to which each contrast primarily contributes are given in table 2.2.3:

Contrast	Block A	Block B	Subphase	Partial Structure Factor
1	D	H	NRW	A-A self term
2	H	D	NRW	B-B self term
3	H	H	D_2O	W-W self term
4	D	D	NRW	A-B cross term
5	D	H	D_2O	A-W cross term
6	H	D	D_2O	B-W cross term

Table 2.2.3. The six contrasts required for the kinematic approximation

The reflectivity profiles are corrected for values of $Q < 0.07\text{Å}^{-1}$ to take into account multiple scattering events that limit the application of the kinematic approximation. The correction, obtained by Crowley[30] is given by:

$$R(Q)=\left[\frac{1+\left(1-Q_c^2/Q^2\right)}{2}\right]\frac{R_o-R_f}{1-R_f}+R_k \qquad \textbf{Equation 2.2.26.}$$

Where R_o is the experimentally measured reflectivity and R_f and R_k are the exact and kinematic reflectivities for a perfectly smooth interface between the two bulk media. Only data obtained on high reflecting subphases (D_2O in this case), undergo such a correction.

To generate the six partial structure factors, these corrected reflectivity curves are converted into the form $R(Q)Q^4/16\pi^2$. A matrix of scattering lengths, A, is then set up (equation 2.2.27).

Each element in the matrix is simply the product of the appropriate scattering lengths from equation 2.2.24. For example, a_{11} is the product of the scattering lengths relating to h_{ww}, namely (from equation 2.2.24) b_w^2. For this contrast (H-H on D_2O), the scattering length of the subphase is $1.917\text{x}10^{-4}\text{Å}^{-4}$, therefore $b_w^2 = a_{11} = 3.675\text{x}10^{-8}\text{Å}^{-8}$. The same process is repeated to calculate the remaining elements.

$$\begin{array}{r} \\ H-H/D_2O \\ D-H/D_2O \\ H-D/D_2O \\ D-D/NRW \\ D-H/NRW \\ H-D/NRW \end{array}\begin{array}{c} \begin{array}{cccccc} h_{WW} & h_{AA} & h_{BB} & h_{WA} & h_{WB} & h_{AB} \end{array} \\ \begin{bmatrix} a_{11} & a_{12} & a_{13} & a_{14} & a_{15} & a_{16} \\ a_{21} & a_{22} & a_{23} & a_{24} & a_{25} & a_{26} \\ a_{31} & a_{32} & a_{33} & a_{34} & a_{35} & a_{36} \\ a_{41} & a_{42} & a_{43} & a_{44} & a_{45} & a_{46} \\ a_{51} & a_{52} & a_{53} & a_{54} & a_{55} & a_{56} \\ a_{61} & a_{62} & a_{63} & a_{64} & a_{65} & a_{66} \end{bmatrix} \end{array} = A \qquad \textbf{Equation 2.2.27.}$$

A second matrix, Y is constructed from the values of $R(Q)Q^4/16\pi^2$ obtained for each contrast at a specific Q value:

$$\begin{matrix} H-H/D_2O \\ D-H/D_2O \\ H-D/D_2O \\ D-D/NRW \\ D-H/NRW \\ H-D/NRW \end{matrix} \begin{bmatrix} y_{11} \\ y_{21} \\ y_{31} \\ y_{41} \\ y_{51} \\ y_{61} \end{bmatrix} = Y$$

Equation 2.2.28.

$A \cdot Z = Y$ where Z is a matrix containing the values of Q^2h_{ij}:

$$Z = \begin{bmatrix} Q^2h_{WW} \\ Q^2h_{AA} \\ Q^2h_{BB} \\ Q^2h_{WA} \\ Q^2h_{WB} \\ Q^2h_{AB} \end{bmatrix}$$

Equation 2.2.29.

The above matrix, containing the partial structure factors, can simply be calculated by $Z = A^{-1} \cdot Y$, where A^{-1} is the inverse of matrix A. This process is repeated for every Q value for which data is obtained, resulting in a series of matrices Z and therefore data sets of Q against Q^2h_{ij}, the partial structure factors to be used in the data analysis.

Self partial structure factors are fitted by the application of a series of models. As an example, the simplest of these, the single uniform layer model has a polymer distribution of:

$n(z) = n_i$ for $0 < z < 1$

$n(z) = 0$ for all other z.

This gives the self partial structure factor:

$$Q^2h_{ii}(Q) = 4n_i{}^2\sin^2\left(\frac{Qd}{2}\right)$$

Equation 2.2.30.

A variety of further models have been utilised in the fitting of neutron reflectometry data and these are outlined where appropriate in chapter 6.

The cross partial structure factor between the two distributions can be generated by:

$$h_{ij}(Q) = \pm \mathrm{Re}\left[n_i(Q) n_j^*(Q) \exp(-iQ\delta)\right] \qquad \textbf{Equation 2.2.31.}$$

Where δ is the distance between the origins of the two polymer distributions.
When n(z) is even (which occurs with a symmetrical distribution such as a uniform of Gaussian model), the Fourier transform n(Q) is real. When n(z) is odd (for an asymmetrical distribution, such as a hyperbolic tangent model), the Fourier transform is imaginary.

For two even functions (common in polymer – polymer cross terms), the cross partial structure factor can be simplified to:

$$h_{ij}(Q) = \pm\left(h_{ii} h_{ij}\right) \sin(Q\delta) \qquad \textbf{Equation 2.2.32.}$$

For one even and one odd distribution (usually the case for a polymer – solvent cross term), the cross term is given by:

$$h_{ij}(Q) = \pm\left(h_{ii} h_{ij}\right) \cos(Q\delta) \qquad \textbf{Equation 2.2.33.}$$

Again, expressions for specific cross terms will be given where appropriate.

2.2.4.3. Model Independent Fitting

The third data fitting technique, usually used as a supplementary method to the preceding two, is model independent fitting.[31] This kinematic method expresses the distributions to be determined as a set of basis functions. Such functions can, in principle, describe any function and are therefore termed 'model independent'. The process involves two distinct steps, indirect Fourier transform[32] and square root deconvolution,[33] which are discussed in turn below:

Indirect Fourier Transform

The indirect Fourier Transform simultaneously transforms the data into a profile correlation function, $\rho(z)$, and an ideal reflectivity curve. $\rho(z)$ can be written as:

$$\rho(z) = \sum_{n=1}^{N} a_n B_n(z) \qquad \textbf{Equation 2.2.34.}$$

When $B_n(z)$ are a series of basis functions (in this case cubic *b* splines) and a_n are the coefficients to be determined. The reflectivity, as a ratio of the Fresnel (ideal) reflectivity, R_F, can be expressed as:

$$R(Q)/R_F(Q) = \sum_{n=1}^{N} a_n B_n(Q) \qquad \textbf{Equation 2.2.35.}$$

where:

$$B_n(Q) = 2\int_0^{\infty} B_n(z)\cos(Qz)dz \qquad \textbf{Equation 2.2.36.}$$

The above expression can be modified to include the instrumental resolution, which smears the basis function in the expression. The final ideal reflectivity expression becomes:

$$R(\langle Q\rangle)/R_F(\langle Q\rangle) = \sum_{n=1}^{N} a_n \int_{-\infty}^{\infty} B_n(Q)R_F(Q)D(\langle Q\rangle, Q)dQ \qquad \textbf{Equation 2.2.37.}$$

Where $D(\langle Q\rangle, Q)$ is the distribution of scattering vector Q probed when the instrument is at the normal scattering vector, $\langle Q\rangle$.

Square Root Deconvolution

Square root deconvolution takes the profile correlation function and produces the derivative of the scattering profile, $d\rho(z)/dz$ and the scattering length density profile, $\rho(z)$ as output. It is the latter of these which the ultimate aim of this analysis procedure.

The scattering length density profile can be expressed as:

$$\rho(z) = \sum_{j=1}^{P} b_j B_j(z)$$ **Equation 2.2.38.**

Where P is the number of functions in the square-root deconvolution. The derivative of this profile, $d\rho(z)/dz$, is:

$$d\rho(z)/dz = \sum_{j=1}^{P} b_j dB_j(z)/dz$$ **Equation 2.2.39.**

2.3. Surface Quasi-Elastic Light Scattering (SQELS)

The surface of a liquid is not uniformly flat, but is in fact continually roughened by random thermal fluctuations. Such fluctuations, approximately 2-3Å in magnitude, are predominantly transverse to the surface and are referred to as capillary waves. These microscopic waves scatter light and this fact is exploited by the use of surface quasi-elastic light scattering (SQELS) to gain information on the interfacial system.

2.3.1. Light Scattering from a Liquid Surface

If the air-liquid interface is defined as a x-y plane, a two-dimensional wave propagating in the x-direction results in an interfacial disturbance, ξ:

$$\xi(x,t) = \xi_o \exp\, i(qx + \omega t) \qquad \textbf{Equation 2.3.1.}$$

Where q is the wavenumber of a capillary wave which propagates in the x-direction. q is related to the wavelength, Λ, by:

$$q = 2\pi/\Lambda \qquad \textbf{Equation 2.3.2.}$$

In equation 2.3.1, ω is the propagation frequency, a complex quantity consisting of a real term (wave frequency, ω_o) and an imaginary term (wave damping, Γ):

$$\omega = \omega_o + i\Gamma \qquad \textbf{Equation 2.3.3.}$$

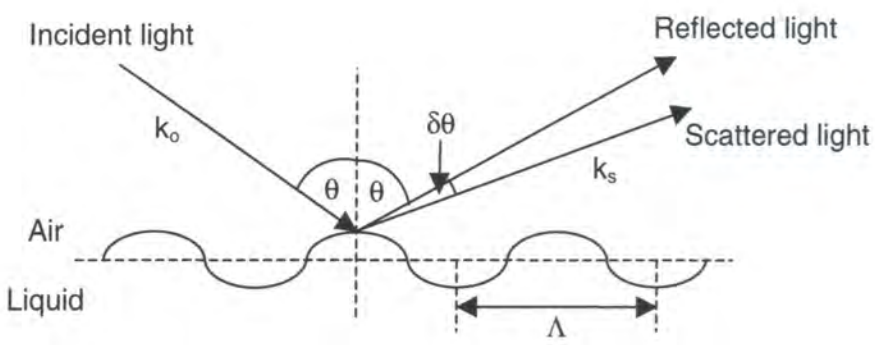

Figure 2.3.1. Scattering of light by a capillary wave

The interfacial perturbation acts in a similar manner to a diffraction grating, reflecting some of the incident light by an angle $\delta\theta$ (figure 2.3.1). For such a small angle of scatter, the wavenumber can be expressed in terms of θ:

$$q = 2k_o \sin(\delta\theta/2)\cos\theta \qquad \textbf{Equation 2.3.4.}$$

The vector diagram relating q to k_o is given in figure 2.3.2.

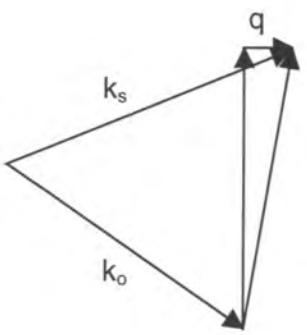

Figure 2.3.2. Vector diagram relating the wavenumber, q, to the incident wavevector, k_o, and the scattering vector, k_s.

2.3.2. Light Scattering From A Monolayer Covered Surface

The introduction of a monolayer onto a liquid surface introduces up to five modes of motion to the system. Of these modes, only two, transverse shear and surface dilation are of relevance to SQELS experiments. These are shown schematically in figure 2.3.3.

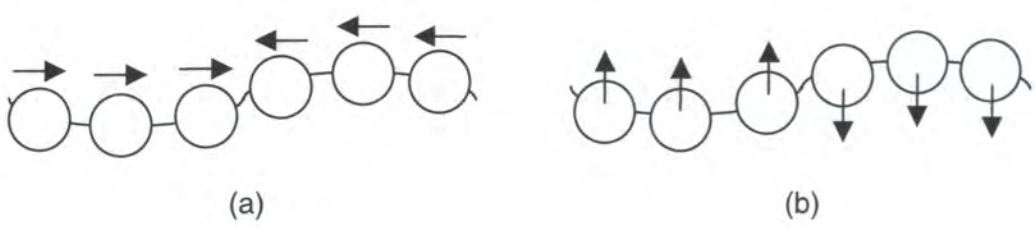

Figure 2.3.3. Schematic representation of (a) surface dilation and (b) transverse shear of a film at the air-liquid interface

2.3.3. SQELS THEORY

2.3.3.1. The Dispersion Equation

The dispersion equation relates the surface modes to the bulk properties of the fluids and the wavenumber and frequency of the capillary waves. At the air-liquid interface, the classical dispersion equation for capillary waves[34] is given by:

$$D(\omega)=\left[\varepsilon q^2+i\omega\eta(q+m)\right]\left[\gamma q^2+i\omega\eta(q+m)-\omega^2\rho/q\right]-\left[i\omega\eta(q-m)\right]^2=0$$

Equation 2.3.5.

Where γ and ε are the surface tension and dilational modulus of the surface film and η and ρ are the viscosity and density of the bulk liquid. The viscosity and density of air are assumed to be zero. m is given by the relationship:

$$m=\sqrt{q^2+i\omega\rho/\eta} \qquad \text{For } Re(m) > 0 \qquad \textbf{Equation 2.3.6.}$$

The dispersion equation has two physically realistic roots, relating to the capillary and dilational modes of the system. A first order estimation of the frequency of each of these modes may be obtained. For the capillary waves:

$$\omega_C=\sqrt{\frac{\gamma_o q^3}{\rho}}+i\frac{2\eta q^2}{\rho} \qquad \textbf{Equation 2.3.7.}$$

Whereas for the dilational waves:

$$\omega_D=\frac{1}{2}\left(\sqrt{3}+i\right)\left(\frac{\varepsilon_o^2 q^4}{\eta\rho}\right)^{1/3} \qquad \textbf{Equation 2.3.8.}$$

The two surface film moduli in equation 2.3.5 are complex terms and can be expanded as follows:

$$\gamma = \gamma_o + i\omega_o\gamma' \qquad \textbf{Equation 2.3.9.}$$

$$\varepsilon = \varepsilon_o + i\omega_o\varepsilon' \qquad \textbf{Equation 2.3.10.}$$

The subscript o indicates an elastic term and the prime a viscosity term. The two viscosity terms, γ' and ε' are the transverse shear viscosity and dilational viscosity respectively.

The capillary waves are predominantly influenced by the surface tension, whereas the behaviour of the dilational waves is driven by the dilational modulus. However, the dilational properties ε_o and ε' do have an effect upon the capillary waves and, similarly, the transverse shear parameters affect the dilational frequency. Such a phenomenon is due to coupling between the two modes. The strength of this coupling, κ, can be defined as:

$$\kappa = \eta(q - m) \qquad \textbf{Equation 2.3.11.}$$

The values of the viscoelastic parameters therefore have a significant effect upon the frequency and damping of the surface waves. If γ_o remains constant and ε_o is increased, resonance can occur between the capillary and dilational modes. This takes place when the frequencies of the two modes are equivalent, i.e. $\omega_C = \omega_D$. Such a resonance condition occurs when the ratio of the two viscoelastic parameters, $\varepsilon_o/\gamma_o \approx 0.16$ and is often denoted by a maximum in the value of damping (and sometimes frequency) of the capillary waves.

When the dampings of each mode converge, Earnshaw[35] has reported that the modes become mixed and the frequencies of the capillary and dilational modes deconverge. This phenomenon has been found to occur when either a large positive value of transverse shear viscosity or a large negative value of dilational viscosity is observed.

2.3.3.2. The Power Spectrum

The relationship between the dispersion equation and the spectrum of scattered light, $P(\omega)$, is given by the power spectrum:

$$P(\omega) = \frac{-k_B T}{\pi\omega} \mathrm{Im}\left[\frac{i\omega\eta(q+m)+\varepsilon q^2}{D(\omega)}\right] \qquad \textbf{Equation 2.3.12.}$$

Where k_B is the Boltzmann constant, T the temperature and $D(\omega)$ the dispersion equation (equation 2.3.2).

The power spectrum is approximately Lorentzian in form and is characterised by a central frequency, ω_0, and a line width (full width at half peak height), Γ.
It is possible to recorded the power spectrum directly, but in the SQELS experiments carried out here, it is the Fourier transform of the spectrum $g(\tau)$, rather than the spectrum itself, which is measured:

$$g(\tau) = FT(P(\omega)) \qquad \textbf{Equation 2.3.13.}$$

To enable the detection of the small frequency shifts resulting from the light scattering, a technique of heterodyne correlation is used, where the diffracted reference beams are mixed with scattered light. The difference in the frequency of the light of the two beams results in a beat pattern and it is this that is detected by the photomultiplier tube. The correlation function obtained is given by:

$$G_H(\tau) \propto (I_s + I_r)^2 + 2I_s I_r g^{(1)}(\tau) + I_s^2 \left[g^{(2)}(\tau) - 1\right] \qquad \textbf{Equation 2.3.14.}$$

Where I_s and I_r are the intensities of the scattered and reference beams respectively, $g^{(1)}(\tau)$ and $g^{(2)}(\tau)$ are the field and intensity correlation functions and τ is the delay time. To ensure that only heterodyne detection takes place, an experimental I_s/I_r ratio of approximately 10^{-4} is used.

2.3.4. Data Fitting

2.3.4.1. The Damped Cosine Fit

As previously stated, the power spectrum obtained is only approximately Lorentzian in shape. The Fourier transform of a true Lorentzian function is:

$$G(\tau) = B + A\cos(\omega_o \tau)\exp(-\Gamma\tau)$$ **Equation 2.3.15.**

Attempting to fit SQELS data using the above expression[36] results in fits of low quality, characterised by highly correlated residuals. To obtain a reasonable fitting function, equation 2.3.15 had to be expanded and it was Earnshaw[37,38] who developed the function used:

$$G(\tau) = B + A\cos(\omega_o \tau + \phi) + \exp(-\beta^2\tau^2/4) + C\exp(-\alpha\tau) + D\tau^2$$

Equation 2.3.16.

Where A is an amplitude factor, B is the instrumental background, ϕ takes into account non-Lorentzian behaviour (the power spectrum is in fact a skewed Lorentzian) and the term $\exp(-\beta^2\tau^2/4)$ accounts for instrumental line broadening. The first point of a correlation function is dropped as it is affected by an exponential decay due to afterpulsing in the photomultiplier.[39] At very short sample times, subsequent points are also affected and the term $C\exp(-\alpha\tau)$ accounts for this. $D\tau^2$ accounts for the presence of other external vibrations, which it is impossible to eliminate completely. This is normally exhibited as 'droop' in the correlation function.

2.3.4.2. The Spectral Fit

The spectral fitting procedure is used to obtain values of the four viscoelastic parameters, γ_o, γ', ε_o and ε'. To extract these parameters without making any prior assumptions requires a much more powerful technique than that described above. Such a method, the spectral fit, involves the generation of a theoretical correlation function from initial values inputted for the surface parameters. This takes place by the generation of a theoretical power spectrum, which is Fourier transformed to give a theoretical correlation function, $\hat{g}(\tau_i)$. The theoretical function is then compared to the experimental correlation function, $g(\tau_i)$ and non-linear least squares fitted, by a process of varying the starting parameters and repeating the cycle until the best fit is obtained. The best fit is characterised by the attainment of the minimum value of F, defined below:

$$F = \sum_{i=2}^{i=n} [g(\tau_i) - \hat{g}(\tau_i)]^2$$ **Equation 2.3.17.**

Where n is the total number of channels (excluding delay channels). The fitted form of the correlation function is given by the expression:

$$G(\tau) = B + A \times FT(P(\omega)) + \exp(-\beta^2\tau^2/4) + C\exp(-\alpha\tau) + D\tau^2$$

Equation 2.3.18.

2.3.5. Recent Developments: Copolymers at a Fluid – Fluid Interface

Recent theoretical developments[40] have resulted in a modified theory for a diblock copolymer at the fluid – fluid interface (figure 2.3.4).

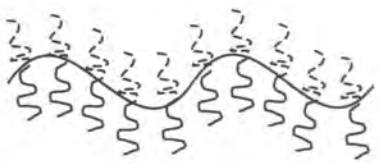

Figure 2.3.4. Representation of a diblock copolymer at the (perturbed) fluid - fluid interface

Perturbation of such a system by the capillary waves is described by the curvature of the surface, and scaling expressions for the surface viscoelastic moduli have been obtained using the Alexander – de Gennes model.[15,16] The four parameters obtained are γ, ε, κ and λ. In section 2.3.3.1, it is stated that γ consists of surface tension, γ_o and transverse shear viscosity, γ' and the components of ε are dilational modulus, ε_o and dilational viscosity, ε'. However, microscopic calculations have established that $\gamma' \equiv 0$, a significant departure from the initial theory outlined above.

The third term, λ, is a coupling constant and is related to the asymmetry of the polymer brush layer. This can be expanded as a complex term:

$$\lambda = \lambda_o + i\omega_o\lambda'$$ **Equation 2.3.19.**

Finally, κ, the bending modulus, can be expressed similarly:

$$\kappa = \kappa_o + i\omega_o\kappa' \qquad \textbf{Equation 2.3.20.}$$

The viscous terms arise from the permeation of solvent through the polymer brush, which can be treated as a porous medium.

2.3.5.1. Copolymers at the Air – Liquid Interface

The above theory applies to a polymer brush system at a general fluid – fluid interface. A more specific discussion can be applied to a diblock polymer at an air – liquid interface, which can be treated as a 'one-sided brush'. The viscosity and density of the air can again be assumed to be zero, giving the following dispersion equation:

$$D(q,\omega) = \left[\eta\omega(q-m)+i\lambda q^3\right]^2+\left[\varepsilon q^2+i\eta\omega(q+m)\right] \times\left[\left(\gamma+\kappa q^2\right)q^2+i\eta\omega(q+m)+-\omega^2\rho/q\right]=0 \qquad \textbf{Equation 2.3.21.}$$

And the associated power spectrum becomes:

$$P(\omega)=\frac{-2k_BT}{\omega}\,\mathrm{Im}\left[\frac{i\eta\omega(q+m)+\varepsilon q^2}{D(\omega)}\right] \qquad \textbf{Equation 2.3.22.}$$

The bending modulus, κ, is only applicable to systems where the surface tension is ultra-low (approximately zero). This is obviously not the case for a water subphase where $\gamma_o \approx 72\mathrm{mNm}^{-1}$, resulting in the term being negligible for such a system.
The scaling relationships for surface pressure, Π, dilational modulus, ε_o, dilational viscosity, ε' and the two components of the coupling constant, λ_o and λ' are given below:

$$\Pi \approx \sigma_o^{11/6} b^{5/3} N_A k_B T \qquad \textbf{Equation 2.3.23.}$$

$$\varepsilon_o \approx \sigma_o^{11/6} b^{5/3} N_A k_B T \qquad \textbf{Equation 2.3.24.}$$

$$\varepsilon' \approx \sigma_o^2 b^5 \eta_1 N_A^3 \qquad \textbf{Equation 2.3.25.}$$

$$\lambda_o \approx \sigma_o^{13/6} b^{10/3} N_A^2 k_B T \qquad \textbf{Equation 2.3.26.}$$

$$\lambda' \approx \sigma_o^{7/3} b^{20/3} \eta_l N_A^4$$ **Equation 2.3.27.**

Where N_A is the degree of polymerisation of block A (and statistical step length b) immersed in the subphase with a grafting density of σ_o and η_l is the viscosity of the subphase.

The coupling constant, λ, is related to the capillary wavenumber and the brush length, h_o as $\lambda = qh_o$. For λ to exert a significant contribution, its value has to be approximately 0.1. For the values of q used in SQELS experiments, this would require h_o to be of the order of micrometres, which is 2 to 3 orders of magnitude greater than the experimentally observed values.
Neglecting the terms κ and λ gives the dispersion equation for a thin film at the air-water interface:

$$D(q,\omega) = [\eta\omega(q-m)]^2 + [\varepsilon q^2 + i\eta\omega(q+m)] \times [\gamma_o q^2 + i\eta\omega(q+m) + -\rho\omega^2/q] = 0$$

Equation 2.3.28.

As expected, the above expression bears a great similarity to the original dispersion equation (equation 2.3.5), the only differences between the two being due to the lack of a transverse shear viscosity, γ', in the latter expression.

2.4. BREWSTER ANGLE MICROSCOPY (BAM)

Brewster angle microscopy (BAM) is a recently developed technique[41,42] that allows direct visualisation of the organisation of a polymer film on an air-liquid interface. Before the introduction of the technique, such systems were generally studied by fluorescence microscopy, where a fluorescent amphiphilic molecule is added to the monolayer. However, such a technique has more than one drawback. Firstly, such molecules may affect the phase transition which it is being attempted to study. Due to the low solubility of the fluorescent molecule in both phases, such transitions may be difficult to study at high surface concentrations. Furthermore, photochemical transitions in the fluorescent probes may occur, the products from such reactions acting as impurities in the system.

Due to the direct nature of the process, BAM circumvents these problems, but is not without its drawbacks. Early apparatus suffered form poor resolution and long image acquisition times, thus rendering it difficult to observe very small or rapidly moving monolayer domains. However, recent improvements in experimental design have resolved most of these difficulties.

2.4.1. BACKGROUND THEORY

Brewster angle microscopy exploits the fact that at a specific angle of incidence, no reflection occurs when p-polarised light is incident upon a liquid interface. The reflectivity of such light is dependent upon the angle of incidence and is given by the Fresnel equation:

$$E_r^p = \left[\frac{\tan(\theta_i - \theta_r)}{\tan(\theta_i + \theta_r)}\right] E_i^p \qquad \textbf{Equation 2.4.1.}$$

Where θ_i and θ_r are the incident and reflected angles respectively and E_r^p and E_i^p are the amplitudes of the electric field for the p-polarised light.

When p-polarised light is incident upon an interface between two media (figure 2.4.1), Snell's law states that:

$$n_1 \sin\theta_i = n_2 \sin\theta_r$$ **Equation 2.4.2.**

Where n_1 and n_2 are the refractive indices of the two media. When the incident and reflected waves are perpendicular to each other, $\theta_i + \theta_r = 90°$ giving:

$$n_1 \sin\theta_i = n_2 \sin(90 - \theta_i) = n_2 \cos\theta_i$$ **Equation 2.4.3.**

Therefore:

$$\tan\theta_B = \frac{n_2}{n_1}$$ **Equation 2.4.4.**

Where θ_B is the Brewster angle, where the reflectivity vanishes for p-polarised light.

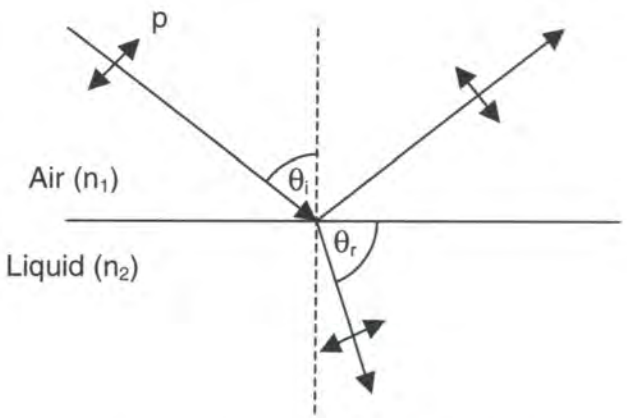

Figure 2.4.1. p-polarised light incident upon an air-liquid interface

At the air-water interface, n_1 = 1.000 and n_2 = 1.333 (at 20°C), giving a Brewster angle of 53.12°. For the two highest salt concentrations studied (0.1M and 1M, see section 5.5.2.2), the values of n_2 are 1.334 and 1.343, giving Brewster angles of 53.14° and 53.32°.

For a real interface, the reflected light goes through a minimum at the Brewster angle, but does not disappear completely, as the theory suggests. This finite reflectivity is due to the interfacial properties of the system, the real reflectivity being governed by three major factors:

1. Interfacial thickness

Real interfaces do not follow Fresnel's theoretical stipulation of changing steeply from n_1 to n_2 at z = 0. The interfacial region is given a refractive index of $n(z) \neq n_1 \neq n_2$ and a thickness l. The reflectivity for the amplitude of a p-polarised wave has been given by Drude[43] to be:

$$r_{pp}(\theta_B) = ir_s(\theta_B)\overline{\rho}_B \qquad \textbf{Equation 2.4.5.}$$

Where $r_s(\theta_B)$ is the reflectivity of a Fresnel interface for the amplitude of a wave of s-polarisation (normal to the interface), i indicates a $\pi/2$ increase between the phase difference of the waves after reflection and $\overline{\rho}_B$ is the ellipticity which is given by:

$$\overline{\rho}_B = \frac{\pi}{\lambda}\frac{\sqrt{n_1^2 + n_2^2}}{n_1^2 - n_2^2}\int_{-\infty}^{+\infty}\frac{\left[n(z)^2 - n_1^2\right]\left[n(z)^2 - n_2^2\right]}{n(z)^2}dz \qquad \textbf{Equation 2.4.6.}$$

2. Interfacial Roughness

As stated earlier, thermal fluctuations of a liquid surface result in an interfacial roughness of approximately 2-3Å. This roughness results in a small amount of reflectivity from the surface.

3. Monolayer Anisotropy

In some cases, phase in monolayers can be optically anisotropic,[44] which can greatly influence the reflected intensity. If such an optically anisotropic monolayer does not have a vertical axis z of symmetry, the reflected light is a function of the orientation of the monolayer in its plane.

2.4.2. QUANTITATIVE USE OF BAM

In addition to the visualisation of a monolayer on a liquid surface, the quantity of light reflected from the surface can be measured and used to obtain a number of physical parameters. Three examples of this follow:

1. *Monolayer Thickness*[45]

The recorded light intensity is dependent upon the thickness and the optical properties of the film. At the Brewster angle, the relative reflectivity of light, I, is defined as:

$$I = |R_p|^2 = C \cdot d^2 \qquad \textbf{Equation 2.4.7.}$$

Where C is a constant, d the film thickness and R_p the p-component of the light, which is defined as:

$$R_p = \frac{r_{01} + r_{12} \times e^{-i2b}}{1 + r_{01} \times r_{12} \times e^{-i2b}} \qquad \textbf{Equation 2.4.8.}$$

Where:

$$b = 2\pi n_1 \cos\theta_1 \cdot (d/\lambda), \qquad \textbf{Equation 2.4.9.}$$

$$r_{01} = \frac{n_1 \times \cos\theta_0 - n_0 \times \cos\theta_1}{n_1 \times \cos\theta_0 + n_0 \times \cos\theta_1} \text{ and} \qquad \textbf{Equation 2.4.10.}$$

$$r_{12} = \frac{n_2 \times \cos\theta_1 - n_1 \times \cos\theta_2}{n_2 \times \cos\theta_1 + n_1 \times \cos\theta_2}. \qquad \textbf{Equation 2.4.11.}$$

Where λ is the wavelength of light and n_i and θ_i are the refractive index and incident angle for each layer. The subscripts 0, 1 and 2 refer to air, monolayer and water respectively.

R is therefore dependent upon d^2 and it is this relationship which can be used to obtain information regarding the film thickness. The camera used is calibrated to obtain a relationship between grey scale and relative reflectivity. From this, the relative thickness of the monolayer can be calculated

2. *Tilt of Hydrocarbon Chains*[46]

The tilt angle of hydrocarbon chain of a monolayer can be obtained from Brewster angle autocorrelation spectroscopy.

As domains of the monolayer flow through the laser spot, the intensity of the reflected light fluctuates. The autocorrelation function is given by:

$$g_2 = \frac{\langle I(t)I(t+\tau)\rangle}{\langle I(t)\rangle^2}$$ **Equation 2.4.12.**

Where the quantities in triangular brackets donate time average values. The correlation function shows a decay as a function of time and the decay height is given by:

$$g_2(\tau = 0) - g_2(\tau \to \infty) = \Delta g_2 = \frac{\left\langle (I - \langle I\rangle)^2 \right\rangle}{\langle I\rangle^2}$$ **Equation 2.4.13.**

All tilt azimuth directions have the same free energy and therefore Δg_2 can be expressed in terms of an average tilt azimuth direction:

$$\Delta g_2 = \frac{\overline{(I - \bar{I})^2}}{\bar{I}^2}$$ **Equation 2.4.14.**

Where the bar donates the tilt azimuth average ($\bar{A} = (1/2\pi)\int A(\varphi)d\varphi$) The reflectivity at the Brewster angle can be expressed as:

$$I_\alpha(\varphi) = (A\cos^2\varphi + B + C\sin\varphi + D\sin\varphi\cos\varphi)^2$$ **Equation 2.4.15.**

A, B, C and D can be expressed in terms of, ϑ, the tilt angle. Insertion of equation 2.4.15 into equation 2.4.14 yields a lengthy expression relating Δg_2 to ϑ, thus allowing the tilt angle to be determined.

3. Monolayer Line Tension[47]

BAM can also be used to study line tension in a monolayer. In the specific example referenced, the line tension between a liquid expanded (L_1) and a liquid condensed

(L_2) phase was studied. The line tension, λ_B, between two such phases can be expressed as:

$$\lambda_b\left(\frac{1}{R_A}-\frac{1}{R_B}\right)=(\Delta V_{L1}-\Delta V_{L2})[w_b(A)-w_b(B)] \qquad \textbf{Equation 2.4.16.}$$

Where R_A and R_B are the radii of curvature at two points, A and B, on the domain border, ΔV_{L1} and ΔV_{L2} are the surface potentials of the two phases and $w_b(A)$ and $w_b(B)$ are the potential energies at the two points. Therefore, using BAM to measure the radius of curvature of the domains can result in the line tension being obtained.

2.5. REFERENCES

1 A. W. Adamson, *Physical Chemistry of Surfaces*, Wiley, New York, USA, pp.124-7, 4 ed., 1982.

2 S. J. Singer, *J. Chem. Phys.*, 1948, **16**, 872.

3 M. L. Huggins, *J. Phys. Chem.*, 1942, **46**, 151.

4 H. L. Frisch and R. Simha, *J. Chem. Phys.*, 1957, **27**, 702.

5 K. Motomura and R. Matuura, *J. Coll. Sci.*, 1963, **18**, 52.

6 P.-G. de Gennes, *Scaling Concepts in Polymer Physics*, Cornell University, New York, USA, 1991.

7 M. Daoud and G. Jannink, *J. Phys. (Paris)*, 1976, **37**, 973.

8 J. des Cloizeaux, *J. Phys. (Paris) Lettres*, 1980, **41**, L-151.

9 R. Derrida, *J. Phys. A: Math. Gen.*, 1981, **14**, L-5.

10 S. Havlin and D. Ben-Avraham, *Phys. Rev. A*, 1983, **27**, 2759.

11 R. Vilanove, D. Poupinet and F. Rondelez, *Macromolecules*, 1988, **21**, 2491.

12 R. Derrida and H. Saleur, *J. Phys. A: Math. Gen.*, 1985, **18**, L-1075.

13 J. A. Marqusee and J.M. Deutch, *J. Chem. Phys.*, 1981, **75**, 5179.

14 K. Kremer and J.W. Lyklema, *Phys. Rev. Lett.*, 1985, **54**, 267.

15 S. Alexander, *J. Phys. (Paris)*, 1977, **38**, 983.

16 P.-G. de Gennes, *Macromolecules*, 1980, **13**, 1069.

17 S. T. Milner, T. A. Witten and M. E. Cates, *Macromolecules*, 1988, **21**, 2610.

18 E. Bringuier, *J. Phys. (Paris) Lettres*, 1984, **45**, L-107.

19 P. Pincus, *Macromolecules*, 1991, **24**, 2912.

20 J.-F. Argillier and M. Tirrell, *Theor. Chim. Acta.*, 1992, **82**, 343.

21 F. von Goeler and M. Muthukumar, *Macromolecules*, 1995, **28**, 6617.

22 S. J. Miklavic and S. Marčelja, *J. Phys. Chem.*, 1988, **92**, 6718.

23 S. Misra, S. Varanasi and P. P. Varanasi, *Macromolecules*, 1989, **22**, 4173.

24 E. B. Zhulina, O. V. Borisov and T. M. Birshtein, *J. Phys. (France) II*, 1992, **2**, 63.

25 O. V. Borisov, E. B. Zhulina and T. M. Birshtein, *Macromolecules*, 1994, **27**, 4795.

26 E. B. Zhulina, T. M. Birshtein and O. V. Borisov, *Macromolecules*, 1995, **28**, 1491.

27 J. S. Higgins and H. C. Benôit, *Polymers and Neutron Scattering*, Oxford University Press, Oxford, UK, 1994.

28 F. Abelès, *Ann. de Physique*, 1948, **3**, 504.

29 T. L. Crowley, E. M. Lee, E. A. Simister and R. K. Thomas, *Physica B*, 1991, **173**, 143.

30 T. L. Crowley, *Physica A*, 1993, **195**, 354.

31 J. K. Pederson, *J. Appl. Cryst.*, 1992, **25**, 129.

32 O. Glatter, *J. Appl. Cryst.*, 1977, **10**, 415.

33 O. Glatter, *J. Appl. Cryst.*, 1981, **14**, 101.

34 D. Langvin (ed.), *Light Scattering by Liquid Surfaces and Complimentary Techniques*, Dekker, New York, USA, 1992.

35 J. C. Earnshaw and E. McCoo, *Langmuir*, 1995, **11**, 1087.

36 J. C. Earnshaw and R. C. McGivern, *J. Colloid Interface Sci.*, 1988, **123**, 36.

37 J. C. Earnshaw and R. C. McGivern, *J. Phys. D: Appl. Phys.*, 1987, **20**, 82.

38 J. F. Crilly and J. C. Earnshaw, *J. Phys. D: Appl. Phys.*, 1985, **18**, 609.

39 J. C. Earnshaw, R. C. McGivern, A. C. McLaughlin and P. J. Winch, *Langmuir*, 1990, **6**, 649.

40 D. M. A. Buzza, J. L. Jones, T. C. B. McLeish and R. W. Richards, *J. Chem. Phys.*, 1998, **109**, 5008.

41 S. Hènon and J. Meunier, *Rev. Sci. Instrum.*, 1991, **62**, 936.

42 D. Hönig and D. Möbius, *J. Phys. Chem.*, 1991, **95**, 4590.

43 P. Drude, *Ann. Phys. Chem. (Leipzig)*, 1891, **43**, 126.

44 H. Berceyol, F. Gallet, D. Langevin, J. Meunier, *J. Phys. (France)*, 1989, **50**, 2277.

45 J. M. Rodríguez Patino, C. Carrera and M^{a}. R. Rodríguez Niño, *Langmuir*, 1999, **15**, 2484.

46 C. Lautz, Th. M. Fischer and J. Kildea, *J. Chem. Phys.*, 1997, **107**, 7448.

47 S. Riviére, S. Hénon, J. Meunier, G. Albrecht, M. M. Boissonnade and A. Baszkin, *Phys. Rev. Lett.*, 1995, **75**, 2506.

CHAPTER THREE

EXPERIMENTAL TECHNIQUES

3.1. Surface Pressure Isotherm Measurements

All surface pressure measurements were carried out on a circular Langmuir trough (NIMA Technology, Coventry, UK, figure 3.1.1). The trough consists of a Teflon base with two movable Teflon barriers, which could be opened and closed to give areas between $50cm^2$ and $980cm^2$. The volume of subphase required to fill the through was approximately $900cm^3$.

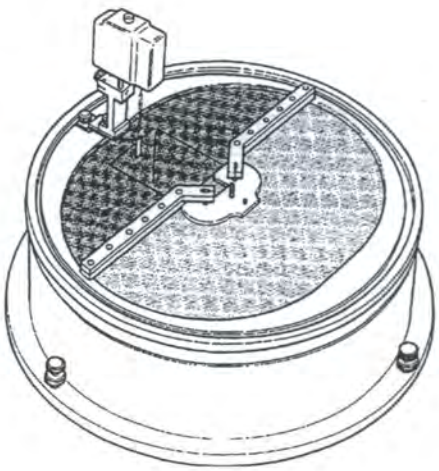

Figure 3.1.1. Circular Langmuir trough (reproduced with permission of NIMA Technology Limited)

The trough was placed on a heavy optical table to reduce the effects of external vibrations. All isotherms were recorded at a subphase temperature of 298K, such conditions being maintained by circulation of water underneath the trough using a Haake water circulator.

3.1.1. Surface Pressure Measurement

Surface pressure values were read using a Wilhelmy plate, a rectangular piece of high quality filter paper with dimensions of 10mm x 20mm, obtained directly from NIMA Technology. The plate was connected to a pressure sensor,[1] consisting of an electromagnetic coil, the moving arm of which was illuminated by an infrared diode. This created a shadow, the position of which was adjusted by the apparatus until it fell equally upon two detectors. The force required to do this was measured by the current passing through the electromagnetic coil and converted into a reading of

surface pressure. Calibration of the pressure sensor involved the use of a weighing pan, a 100mg weight and the automatic calibration program in the trough software.

3.1.2. Sample Preparation

For surface pressure isotherm determination, and all the other experimental techniques undertaken, polymer solutions with concentrations of approximately 1mg ml^{-1} were utilised. The glassware to be used, usually a 10ml volumetric flask, was thoroughly cleaned with permanganic acid. This solution of concentrated sulphuric acid and potassium permanganate was generally left to stand in the flask overnight. The flask was then thoroughly rinsed with pure water and left to dry. A sufficient quantity of polymer was then dissolved in the correct volume of solvent. For the quaternised block copolymer, a solvent mixture of 20:80 (v/v) methanol and chloroform (both spectrophotometric grade, Aldrich) was used. Such a mixture was required because the PMMA block is soluble in chloroform but insoluble in methanol, while the QP4VP block is soluble only in methanol. The other two polymer systems studied, PMMA homopolymer and the unquaternised block copolymer were dissolved in chloroform. Before use, the solutions were allowed to stand overnight to ensure that complete dissolution took place.

3.1.3. Subphase Preparation

Pure water was obtained by passing previously doubly distilled water through an Elgastat UHQ II water purification system (Elga Technology, High Wycombe, UK). The resulting ultra-high quality water had a resistivity of approximately 18MΩ cm.
Subphases of pH3 and pH10 were produced by the addition of a sufficient quantity of high grade NaOH or HCl (Aldrich) to ultra-high quality water until the pH of the solution was either raised or lowered to the desired value. pH measurements were carried out by the use of a Jenway pH meter calibrated using buffer solutions of pH4 and pH10.
Potassium chloride solutions were prepared by dissolving an appropriate quantity of AnalaR KCl (BDH) in ultra-high quality water.

3.1.4. Experimental Procedure

Prior to filling with subphase, the trough was thoroughly cleaned by the use of tissues soaked in chloroform. The trough was then filled with the subphase to be used and the liquid surface aspirated to remove traces of dust and surface particulates. If free of such surface-active agents, water has a surface tension of approximately 73mN m^{-1} and the surface was repeatedly cleaned until such a value was obtained.

A volume of solution of approximately 50µl (accurately known) was spread upon the surface from a gas-tight Hamilton syringe, and a period of approximately 10-15 minutes was allowed for the solvent to evaporate. The barriers were closed under computer control at a speed such that the area decrease was 30cm^2 $minute^{-1}$. The data produced were in the form of surface area against surface pressure. These were converted into the preferred form of surface concentration against surface pressure via knowledge of the volume of material spread upon the surface.

3.1.5. Film Relaxation Studies

Film relaxation studies were carried out by compressing the film to a defined surface concentration and monitoring the change in surface pressure with time after the barriers had become stationary.

3.2. NEUTRON REFLECTOMETRY

All neutron reflectometry experiments were carried out at the ISIS spallation neutron source at the Rutherford-Appleton Laboratory, Chilton, Oxfordshire. Two reflectometers were used, SURF and CRISP. The two instruments are very similar insofar as set-up and operation are concerned, as is outlined below.
The neutrons were produced by the bombardment of a tantalum target by protons from a pulsed source. On collision of protons with the target, neutrons spall off and are guided towards the numerous instruments grouped around the target.

3.2.1. EXPERIMENTAL PRINCIPLES

In all experiments, the reflectivity, R(Q), was recorded as a function of Q, the scattering vector. Q is defined as:

$$Q = \frac{4\pi}{\lambda}\sin\theta \qquad \textbf{Equation 3.2.1.}$$

Where λ is the neutron wavelength and θ is the incident angle.

Both CRISP and SURF are variable wavelength instruments, allowing a range of Q to be explored at each fixed angle. The accessible range of Q was approximately $0.0275 < Å^{-1} < 0.6$ on CRISP and $0.0255 < Å^{-1} < 0.7$ on SURF, which in both cases required the use of two incident angles, 0.8° and 1.5°, to explore the whole Q range. The lower angle was used to explore Q values up to approximately $0.06Å^{-1}$, whereas the higher angle was used for Q values above 0.055 $Å^{-1}$. The slight overlap allowed the two data sets to be combined with minimal error

3.2.2. THE CRISP REFLECTOMETER

As an example of one of the reflectometers used, a description of CRISP is given. A schematic diagram is given below:

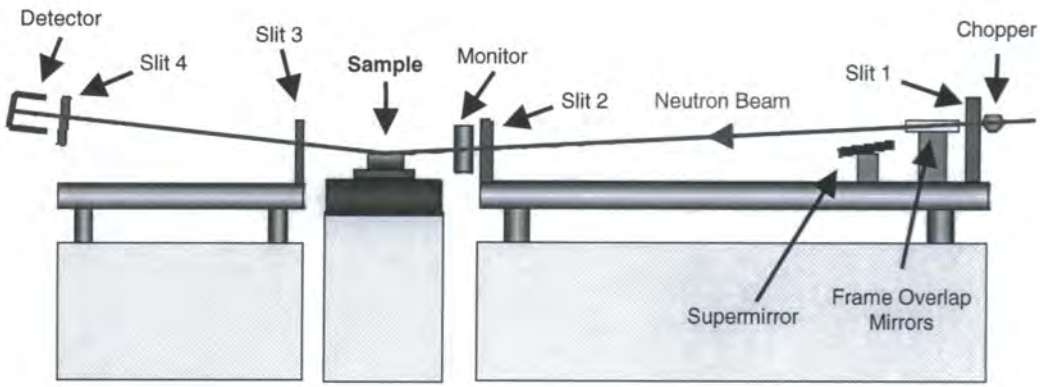

Figure 3.2.1. Schematic representation of the CRISP Reflectometer

The neutrons arrive from the target with a wide range of energies (and therefore a wide range of wavelengths). Any neutrons with energies outside the range of 0.5-6.5Å (with the instrument set up at 1.5°) are excluded by a beam chopper, positioned immediately before the instrument. After passing through slit one, the next components of CRISP are the frame overlap mirrors, a nickel-coated mirror with a very large radius of curvature. These mirrors have the effect of rejecting any neutrons with very long wavelengths (known as 'slow neutrons') which have passed through the chopper. This ensures that only neutrons from a single pulse impinge upon the detector at any one time, with no neutrons from previous or succeeding pulses corrupting the data.

The neutrons then pass through a second slit, are reflected and scattered by the sample, and pass through the two final slits. The four slits collimate the beam, slits one and two collimate the incident beam, while slits three and four collimate the reflected beam. The width of these slits was varied from experiment to experiment, to optimise the configuration of the instrument. An example of one set-up used was slit widths of 2mm, 1.25mm, 4mm and 4mm for slits one to four respectively at 0.8° and 4mm, 2.5mm, 3mm and 4mm at 1.5°.

Finally, the beam is incident upon a time-of-flight detector. The reflectivity, defined as the reflected neutron intensity divided by the incident neutron intensity, was calculated by instrument control and analysis software.

3.2.3. THE SURF REFLECTOMETER

SURF is a second reflectometer specifically designed for the study of surfaces and interfaces. It operates on the same principles as CRISP, the main differences occurring in the physical layout of the apparatus and the fact that a slightly higher neutron flux is available than for CRISP.

3.2.4. EXPERIMENTAL PROCEDURE

Sample preparation was carried out as outlined in section 3.1.2. A rectangular Langmuir trough with two movable barriers was used, this being enclosed in a Perspex box to prevent perturbance by air currents and reduce hydrogen / deuterium exchange between D_2O and H_2O in the subphase. The box had two optical windows, to allow unhindered passage of the neutron beam, and both the trough and box were situated on a vibration isolation table.

A laser beam was used for alignment of the sample, mimicking the neutron path. The height of the sample table was adjusted until the laser beam (and hence the neutron beam) passed through all the slits and was incident on the centre of the detector.

Instrumental operation was automatically controlled by a command file, which, in addition to automatically collecting a pre-determined quantity of data, also controlled the change of incident beam geometry from high to low angle. Experimental durations were dependent on the samples and subphases used, but were generally 30-60 minutes (corresponding to 90-180μA of current) for low angle runs and 2-3 hours (360-550μA of current) for high angle runs.

3.2.5. DATA ANALYSIS

The high angle data set was multiplied by a scaling factor obtained from a calibration run on D_2O. The low angle data was then scaled accordingly to overlap the high angle data. The two sets were then combined to give a single reflectivity

curve for each sample, covering the whole Q range. A number of data analysis methods were employed, as outlined below:

3.2.5.1. Partial Structure Factors: The Kinematic Approximation

Before the kinematic approximation (section 2.2.4.2) could be utilised, further data manipulation was necessary. Initially, the background was subtracted from each of the reflectivity curves by the process of averaging the reflectivity values in the 'background region' ($Q > 0.4\text{Å}^{-1}$). The data obtained on D_2O subphases were Crowley corrected[2] (equation 2.2.25) and then all data converted into the form of $Q^4R(Q)$ against Q, the appropriate form for input into the program PARTIAL3. This program solves the six simultaneous equations relating the reflectivity to Q (via partial structure factors), obtained under different control conditions (section 2.2.4.2). Analysis of the resulting partial structure factors is discussed in chapter six.

3.2.5.2. The Optical Matrix Approach

The program PCMULF was used to fit the reflectivity profiles (without background subtraction) via the optical matrix method (section 2.2.4.1). Initially, a one layer fit was attempted, inputting parameters of layer thickness, scattering length density and interfacial roughness. These parameters were varied by the program and the final values, along with an indication of the goodness of the fit, χ^2, were calculated. This process was repeated until the best (physically realistic) fit was obtained. If a one layer fit proved to be insufficient, further layers were incorporated into the procedure as required.

3.2.5.3. Model Independent Fitting

The model independent fitting method initially required the data files to be converted from a histogram format and to be background subtracted. The fitting program, MODELI), required the inputting of the scattering length density of the subphase and an estimation of the scattering length density of the polymer layer.

For each surface concentration studied, three reflectivity profiles were required, usually the contrasts D-H on NRW, H-D on NRW and H-H on D_2O. In each case, the value of the Lagrangian multiplier, λ, was varied until the best fit to the data was obtained with care being taken not to use too low a value of λ, as this caused the fit to be over-parameterised. The scattering length density profiles obtained by this method could then be used to obtain plots of number density against depth by use of the program NUMB_DEN. This required the values of the scattering length of each component of the system. These plots were in turn converted into plots of volume fraction by the multiplication of the appropriate segment volumes, namely 29.9Å^3 molecule^{-1} for water, 139.4Å^3 molecule^{-1} for PMMA and 267.0Å^3 molecule^{-1} for QP4VP. These values were calculated using the expression:

$$V_s = \frac{M_w \rho}{N_A N} \qquad \textbf{Equation 3.2.1.}$$

Where V_s is the segment volume and M_w, ρ and N are the molecular weight, density and degree of polymerisation of the polymer respectively. In the case of water, M_w/N is replaced by M, the molecular weight of a water molecule.

The final output from the model independent fitting technique gives no information on the relative positions of each of the components as the origin used to define each of the scattering length density profiles is arbitrary. To obtain a complete picture of the system, information on the separations of the three components has to be obtained from another analysis method, such as the kinematic approximation.

3.3 Surface Quasi-Elastic Light Scattering

All surface quasi-elastic light scattering (SQELS) experiments were carried out in Durham, on two sets of light scattering apparatus. The older apparatus used a 100mW diode pumped Nd:YAG laser, λ = 532nm (Adlas) while the second, more recently constructed set-up, has a 400mW solid state diode pumped laser (Coherent).

3.3.1. Experimental Principle

Thermal motion of a liquid results in random fluctuations on the surface, which can be Fourier decomposed into a set of capillary waves, which in turn can be characterised by a surface wave number, q, given by:

$$q = \frac{2\pi}{\Lambda} \qquad \textbf{Equation 3.3.1.}$$

Where Λ is the wavelength of the capillary waves. The range of q that could be explored with our apparatus was approximately $180 < cm^{-1} < 1000$ with the 100mW laser and $400 < cm^{-1} < 2500$ with the 400mW laser.

3.3.2. Experimental Set-up

A schematic representation of the surface light scattering apparatus is given in figure 3.3.1. In an attempt to minimise external vibrations, the apparatus was placed on a heavy optical table and surrounded by Perspex windows, to reduce perturbations caused by air currents.

The laser light (reflected down the main optical rail via a series of mirrors) was first incident upon the half wave-plate, which both rotated the plane of polarised light and attenuated the power of the laser beam. Any remaining horizontally polarised light was removed by the polariser.

Lenses 1 and 2, in conjunction with the diffraction grating, were adjusted to ensure that the beam was focussed on the photomultiplier tube and that the main beam and the diffracted beams (produced by the diffraction grating) coalesced on the liquid surface. The neutral density filter attenuated the reference beam and a variety of

such filters were used, most commonly OD = 2, a filter transmitting only 10^{-2} (1%) of incident light. A neutral density filter was essential to give an I_s/I_r (scattered light intensity : reflected light intensity) ratio of 10^{-3} to 10^{-5}, the optimum conditions for heterodyne correlation to occur.

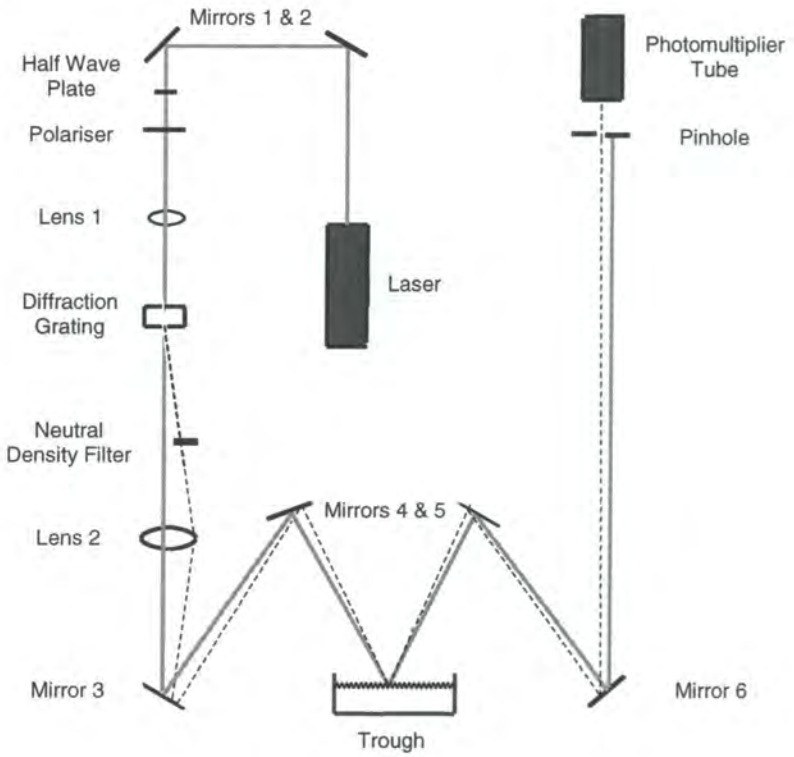

Figure 3.3.1. Schematic Representation of SQELS Apparatus.

The incident light was 'periscoped' onto the liquid surface in a Langmuir trough by mirrors 3 and 4. The trough was again temperature controlled, the exact temperature of the trough being read by a temperature pen.

After scattering and reflection at the liquid surface, the light was reflected by another periscope (mirrors 5 and 6) towards the photomultiplier (PM) tube. Upon arrival at the PM tube, a series of spots were observed, each corresponding to a different wavenumber, q. The central (and most intense) of these spots corresponded to the main beam, the remainder of the spots being the diffracted beams with a contribution from the light scattered by the liquid surface from the main beam. The spot under study was focussed down the PM tube and the response from the tube

analysed by a correlator. Two different PM tube / correlator combinations were used:

1. Malvern – A Malvern PM tube was connected to a Malvern K7025 128 channel correlator with variable channel width. The correlation function obtained was displayed on a cathode ray oscilloscope and control of the correlator took place via a 486 PC.
2. Brookhaven – A Brookhaven PM tube was connected to a Pentium PC containing a Brookhaven 9000AT correlator card and Windows based control program 9KDLSW.

The latter of these two set-ups had the advantage that the PM tube was of a much higher sensitivity (maximum count rate of 22Mcps compared to 7Mcps for the Malvern set-up), allowing much faster collection of the correlation functions with reduced signal to noise ratios. However, the correlator only allowed the selection of a finite series of channel widths (10μs, 5μs, 2μs and 1μs being the more commonly used.) A further disadvantage was the limited number of data channels available. Although 256 channels were available at longer channel widths, this was reduced to 128 channels at 5μs channel widths, 80 at 2μs and 40 at 1μs.

3.3.3. Experimental Procedure

Three different sets of experiments were undertaken and each of these are outlined below.

In all cases, a calibration run was initially required to determine the value of q used in the experiment. This was carried out by collecting a set of ten correlation functions on a pure water surface, analysing the data using the program FITS (see below) and obtaining an average value of the frequency of the capillary waves from FITSUM. The physical properties (surface tension, viscosity and density) of the water for the temperature used were inputted into the CANICE program which solved the dispersion equation and calculated values of capillary wave frequency and damping as a function of q. The value of q could then be obtained by simply reading off the value corresponding to the experimentally obtained value of frequency.

3.3.3.1. Experiment One – Concentration Studies

To study a range of surface concentrations, one diffraction spot was selected to define a particular capillary wavenumber, usually $q \approx 265cm^{-1}$.
Following the calibration procedure outlined above, a polymer film was spread upon the liquid surface and the solvent was allowed to evaporate. The film was compressed to a specific surface concentration, and after a wait of 3-5 minutes (to allow the system to settle), ten correlation functions were recorded. This process was repeated for each required surface concentration.

3.3.3.2. Experiment Two – Frequency Studies

The second series of experiments studied a film of a fixed surface concentration using a series of diffraction spots (and therefore a range of q). Each spot was defined by a calibration run (on a pure water surface) to obtain the q values. Then, the polymer was spread, compressed to the required surface concentration and data collected. As previously, ten correlation functions were recorded for each value of q investigated.

3.3.3.3. Experiment Three – Time Studies

Time dependency studies were used to observe any change in the behaviour of the film with time. One correlation function was collected per minute over a period of approximately ten hours. Each correlation function was analysed individually and the value of the capillary wave damping plotted against time.

3.3.4. Data Analysis

3.3.4.1. Damped Cosine Analysis

The frequency and damping of the capillary waves were obtained by damped cosine analysis (equation 2.3.12) carried out by the use of the programs FITS and BRKFITS, dependent upon the correlator used. These programs automatically read

in the raw data along with initial guesses for frequency and damping. Fitting could be carried out very rapidly.

The ten values of frequency and damping obtained by this fitting procedure were averaged using the program FITSUM.

3.3.4.2. Spectral Fitting

Values of the four viscoelastic parameters (surface tension, transverse shear viscosity, dilational modulus and dilational viscosity – equations 2.3.4 and 2.3.5) were obtained via the use of the programs HERMAN and BRKHERM. From the inputted parameters, the program generated a theoretical power spectrum which was Fourier transformed to produce a theoretical correlation function. This was compared with the experimentally obtained correlation function, the values of the parameters varied and the above process was repeated until the best fit was obtained. Attempts were made to fit the data in two ways, firstly fitting all four viscoelastic parameters and secondly with transverse shear viscosity constrained to zero, fitting only surface tension, dilational modulus and dilation viscosity. Generally, spectral fitting was much more time-consuming and much more dependent upon the initial inputted parameters than the damped cosine analysis. An example of a typical fit, along with the residuals obtained from the fit, is given in figures 3.3.2 and 3.3.3 respectively.

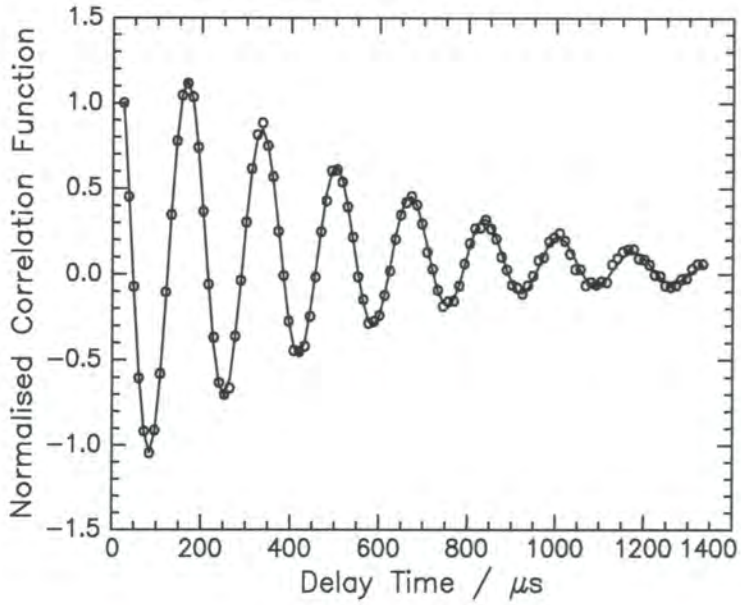

Figure 3.3.2. Example of a typical correlation function (circles) and spectra fit (line). Data obtained for PMMA-QP4VP on water, $\Gamma_s = 0.2 mgm^{-2}$, $q = 269.5 cm^{-1}$

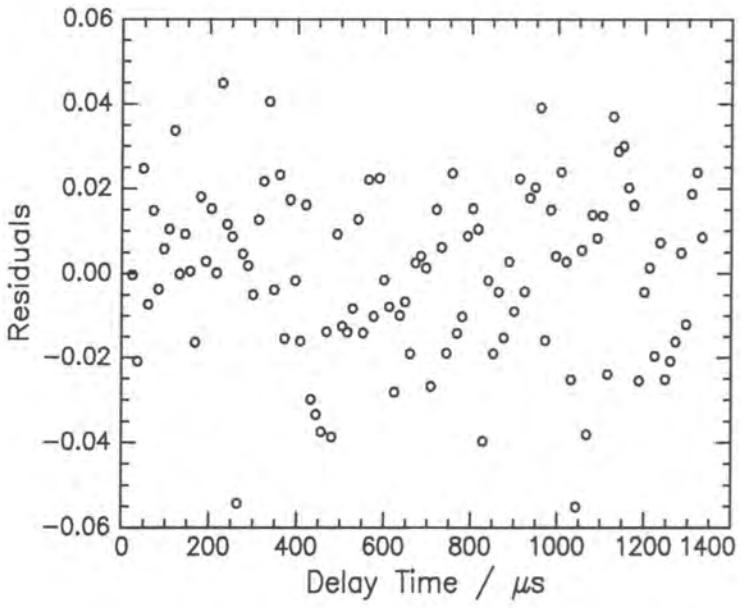

Figure 3.3.3. Residuals for the fit shown in figure 3.3.2.

3.4. Brewster Angle Microscopy

Brewster angle microscopy experiments were carried out at Durham on apparatus belonging to Dr. Andrew Beeby.

3.4.1. Experimental Principle

At the Brewster angle (53.1° for the air-water interface), all light from a vertically polarised laser is transmitted into the subphase (i.e. none is reflected). When a monolayer is present on the liquid surface, the properties of the interface change and a small quantity of the incident light is reflected and recorded by a detector.

3.4.2. Experimental Set-up

The trough used for Brewster angle microscopy studies was a long, rectangular (100cm x 14cm) trough (NIMA Technology). A small glass window was cut into the Teflon base at the point of incidence of the laser beam to reduce scattering from the base of the trough.

A 8mW He-Ne, λ = 632.8nm laser (Melles-Griot) was used. Before being incident upon the trough, the light passed through a polariser (to ensure that all light was p-polarised) and a beam expander, to increase the diameter of the beam to approximately 5mm.

After reflection, a COHU 4910 series CCD camera picked up the image. This was fitted with a zoom lens with a manual focus range of 75-85mm and a resolution of 10μm. A magnification range up to x7 was accessible. The image produced by the camera was displayed in real-time on both a monitor and directly onto a VDU via the use of the software program Paint Shop Pro. Both the laser and the camera were mounted on rotation stages (Ealing), to allow adjustments as small as 0.00001° to be made. The entire set up was situated on a heavy optical table to reduce external vibrations.

3.4.3. EXPERIMENTAL PROCEDURE

The trough was initially filled to the brim with liquid, the surface cleaned and a quantity of liquid removed to allow the image to appear in the centre of the monitor. The film was deposited on the liquid in the manner described above and sufficient time was left for the solvent to evaporate.

Compression of the barriers took place at $30cm^2$ $minute^{-1}$ and a surface pressure isotherm was automatically recorded. Images were collected at predetermined surface concentrations by the use of the computer package Paint Shop Pro. The saved images were initially monochrome, but were converted into colour by the use of a Pascal program, COLORIT, which measured the intensity of light on each pixel and allocated one of sixteen colours.

3.5 References

1 F. Grunfeld, *Rev. Sci. Instrum.*, 1993, **64(2)**, 548

2 T. L. Crowley, *Physica A*, 1993, **195**, 394.

CHAPTER FOUR

POLYMER SYNTHESIS & CHARACTERISATION

4.1. Precursor Polymers

Two linear diblock copolymers of methyl methacrylate and 4-vinyl pyridine, one with a fully hydrogenous, the other with a fully deuterated methyl methacrylate block (denoted HPMMA-P4VP and DPMMA-P4VP respectively), were synthesised in Durham by Mr F. T. Kiff,[1] using the synthetic route of Nugay.[2]

The schematic structures of the two copolymers are shown below:

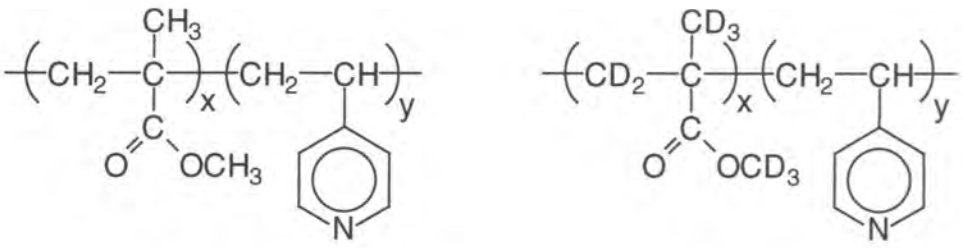

HPMMA-P4VP DPMMA-P4VP

Figure 4.1.1. Structures of HPMMA-P4VP and DPMMA-P4VP

4.1.1. Molecular Weights and Polydispersity Indices

The molecular weights (and polydispersity indices) of the two precursor copolymers were determined by size exclusion chromatography (SEC) using polystyrene calibrants. The results obtained are given in table 4.1.1:

Polymer	M_n	M_w	M_w/M_n
HPMMA-P4VP	54200	56400	1.04
DPMMA-P4VP	56400	58100	1.03

Table 4.1.1. Molecular weights of precusor copolymers

4.1.2. Tacticity of PMMA

In previous work, it has been shown that PMMA samples of differing tacticity produce vastly differing surface pressure isotherms.[3] Determination of the tacticity of the PMMA block is therefore of great importance.

In the isotactic form, each asymmetric chain along the polymer backbone exists in the same steric conformation. Syndiotactic polymers exhibit the opposite conformation around each succesive asymmetric centre, whereas atactic (or heterotactic) polymers have a random stereochemistry (see figure 4.1.2).

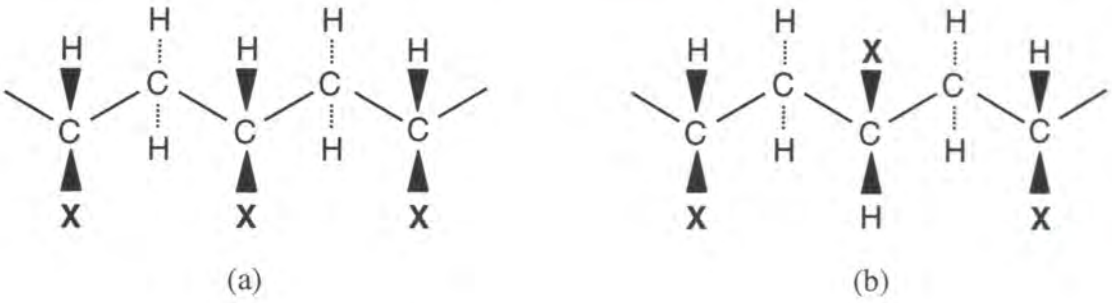

Figure 4.1.2. Schematic representation of (a) isotacticity and (b) syndiotacticity

The degree of stereoregularity can be calculated by ^{13}C NMR spectroscopy. This allows the determination of the conformation of pairs or sets of three monomer units (termed diads and triads respectively). The nomenclature assigned to such sequences are given below:

Sequence	Symbol
Isotactic diads	m
Syndiotactic diads	r
Isotactic triads	mm
Syndiotactic triads	rr
Atactic triads	mr

Table 4.1.2. Diad and triad sequences

A ^{13}C NMR spectrum of the PMMA homopolymer used in the synthesis was obtained (spectrum 1, see appendix), and enlarged (spectrum 2). The spectrum can be separated into four main regions, 15-20ppm (representing α-methyl shifts), 44-45ppm (quaternary carbon shifts), 51-55ppm (CH_2 and O-CH_3 shifts) and 176-179ppm (C=O shifts). It is the last of these which is the optimum region for analysing the tacticity of the polymer as it is the most sensitive to the statistical distribution of neighbouring chain sequences. Assigning pentad sequences to the peaks in this region,[4] we obtain:

Shift/ppm	Sequence(s)	Relative Intensity
176.50	mmmm	0
176.93	rmrr/mmrr + mmrm/rmrm	0.177
177.74	rrrr	0.623
178.04	mrrr	0.200

Table 4.1.3. Assignment of sequences in the carbonyl region of the ^{13}C NMR spectrum of PMMA

From these data, a syndiotacticity of 91.2% is obtained.

4.1.3. Polymer Composition

The composition of the diblock copolymers was determined in a number of ways. An accurate composition determination result is of great importance, as for neutron reflectivity work to be completely valid, it is important that all four polymers used should be as identical in composition as possible. Three methods were used to determine the composition, ^1H NMR spectroscopy, elemental analysis and UV-visible absorption spectroscopy.

^1H NMR Spectroscopy

All proton NMR spectra were obtained on a 400MHz Varian machine. The proton NMR spectra of HPMMA-P4VP solutions in chloroform and DMSO are shown in spectra 3 and 4 respectively (see appendix). In both cases, the peaks at approximately δ = 6.4 and 8.4ppm correspond to the protons of the pyridine ring (two protons per peak), while the peak at δ = 3.6ppm is due to the three protons of the methyl group of the PMMA block. By integrating the areas under these curves and calculating the area per proton, the composition of the polymer could be determined. Interestingly, two quite distinct values arose, 17.9% weight (17.0% molar) P4VP when using chloroform and 24.1% weight (22.9% molar) P4VP in DMSO. The discrepancy between these two results is probably due to the insolubility of the P4VP in chloroform, meaning that a number of protons were undetected by the NMR process. Similar solubility problems were encountered by

Natansohn,[5] who dissolved the polymer in DMSO or benzene, as opposed to chloroform.

Elemental Analysis

Samples of both of the copolymers were submitted for elemental analysis. From the results obtained, the composition of each copolymer could be obtained from the percentage nitrogen content, because this only occurs in the P4VP block of the copolymer. The average carbon, hydrogen and nitrogen percentage compositions for each copolymer and the copolymer compositions calculated from these data, are given in table 4.1.4:

	Weight			Composition (%P4VP)	
Polymer	**%C**	**%H**	**%N**	**Weight**	**Mole**
HPMMA-P4VP	63.16 ± 0.10	7.70 ± 0.06	2.68 ± 0.07	20.1 ± 0.5	19.1 ± 0.5
DPMMA-P4VP	58.14 ± 0.05	7.31 ± 0.04	2.45 ± 0.12	18.4 ± 0.9	19.1 ± 0.9

Table 4.1.4. Results of elemental analyses

UV-Visible Spectroscopy

The third method of composition determination employed was UV-visible spectroscopy. In the UV spectrum of the copolymer, an absorption occurs at 358nm due to the pyridine ring in the P4VP block. By preparing a series of solutions of P4VP homopolymer of known concentrations, the absorbance as a function of concentration was obtained (figure 4.1.3).

A least squares fit to the data gives a gradient of 21.88g l^{-1} (equal to εl in the relationship $A = \varepsilon cl$, where ε is the extinction coefficient and l the path length).

Solutions (of known concentration) of the two copolymers were prepared. The concentration and absorbance of each these solutions and the polymer composition calculated from these are given in table 4.1.5:

Polymer	**Solution conc. / g l^{-1}**	**Relative absorbance**	**% P4VP**
HPMMA-P4VP	0.197	0.837	**19.4**
DPMMA-P4VP	0.196	0.629	**14.7**

Table 4.1.5. Results of UV spectroscopy experiments on block copolymer solutions

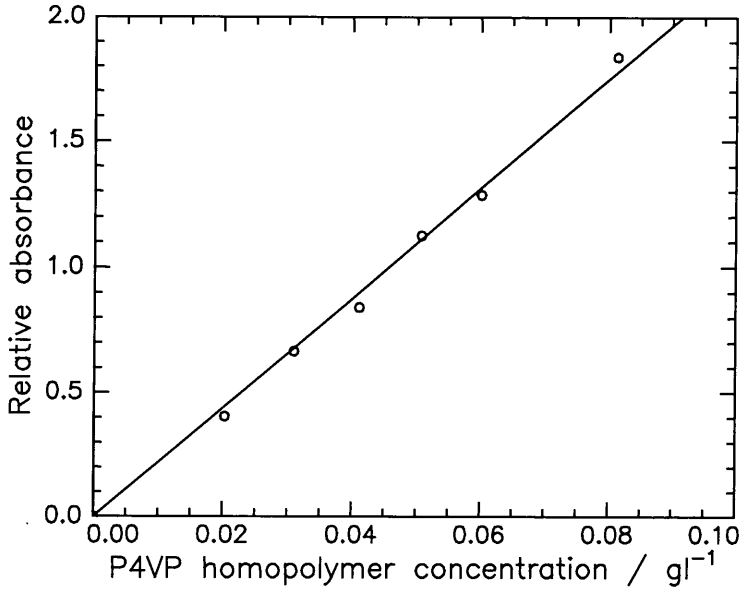

Figure 4.1.3. Plot of concentration against relative absorbance for P4VP homopolymer solutions

Summary

The results obtained for the molar composition of P4VP in each of the diblock copolymers are summarised below:

	Experimental Technique			
Polymer	**^{1}H NMR in $CDCl_3$**	**^{1}H NMR in d-DMSO**	**Elemental Analysis**	**UV-Visible Spectroscopy**
HPMMA-P4VP	17.0 ± 0.8	22.9 ± 0.9	19.1 ± 0.5	19.4 ± 0.9
DPMMA-P4VP	N/A	N/A	19.1 ± 0.9	14.7 ± 0.9

Table 4.1.6. Summary of obtained values of polymer composition (molar % P4VP)

As can be seen, the four results obtained for the ratio of the blocks in the copolymer differ substantially, to an extent greater than the experimental error implicit in any of the techniques.

The results for HPMMA-P4VP give an average value of 19.6% P4VP over the four techniques, which corresponds well with that obtained via both elemental analysis and UV-visible spectroscopy. Due to the inability of ^{1}H NMR spectroscopy to provide qualitative information on a deuterated compound, only two values have been obtained for the DPMMA-P4VP copolymer. These give an average of 17.1%.

Of the two techniques, it is elemental analysis that is deemed to give the more reliable result (19.1% P4VP). Similar values of composition are obtained by more than one technique for the hydrogenous form of the polymer and it is therefore assumed that the UV-visible spectroscopy result from DPMMA-P4VP is erroneous. Using the results from elemental analysis, a polymer composition of 19.1% P4VP is assumed.

4.2. QUATERNISED COPOLYMERS

To give a sufficient number of contrasts for neutron reflectometry work, four separate quaternisation reactions were carried out (outlined in table 4.2.1), to produce the products shown schematically in figure 4.2.1.

Precusor polymer	Reagent	Product
HPMMA-P4VP	C_2H_5Br	HPMMA-Q(H)P4VP
HPMMA-P4VP	C_2D_5Br	HPMMA-Q(D)P4VP
DPMMA-P4VP	C_2H_5Br	DPMMA-Q(H)P4VP
DPMMA-P4VP	C_2D_5Br	DPMMA-Q(D)P4VP

Table 4.2.1. Summary of the four quaternisation reactions

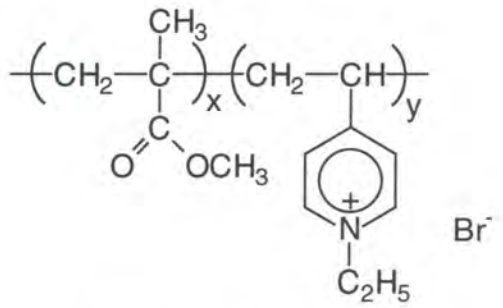

HPMMA-Q(H)P4VP

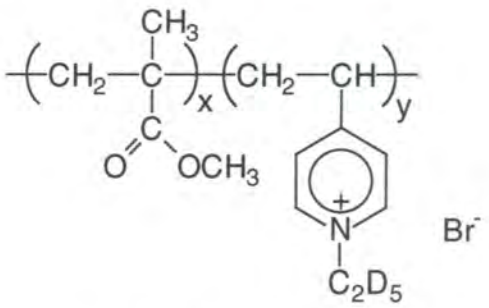

HPMMA-Q(D)P4VP

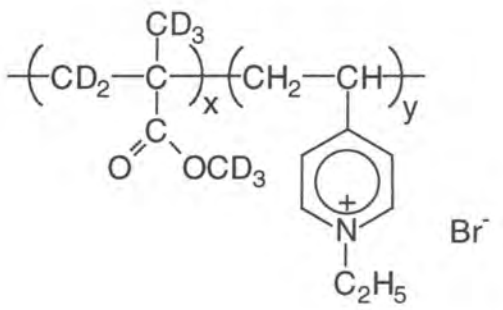

DPMMA-Q(H)P4VP

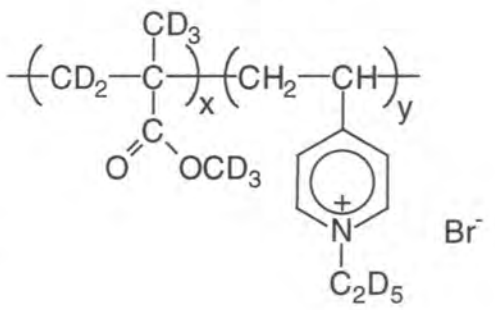

DPMMA-Q(D)P4VP

Figure 4.2.1. Structures of the four quaternised block copolymers

Due to the unavailability of DP4VP, a fully deuterated QP4VP block, which would have provided the maximum contrast with the hydrogenous polymer, could not be synthesised.

4.2.1. SYNTHESIS

An initial attempt at the quaternisation reaction was carried out by using sulphanone (tetramethyl sulphone) as a solvent and refluxing the solution with bromoethane.[6] After refluxing overnight at 35°C, attempts to recover the polymer (a notoriously difficult process for amphiphilic systems) were unsuccessful. Attempts to precipitate the polymer in hexane, methanol, acetone and diethyl ether failed due to their immisciblity with sulphanone, while suspensions were formed in water, methanol and DMF.

Ultimately, the reaction was accomplished by use of the following synthetic route:

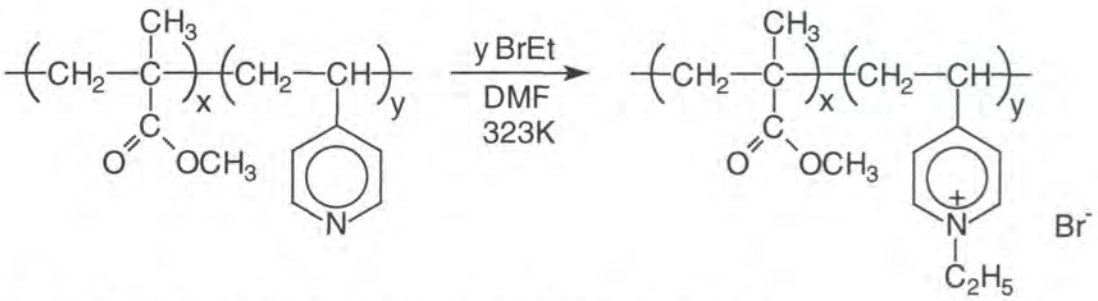

Figure 4.2.2. Route for the synthesis of HPMMA-Q(H)P4VP

Starting Materials

DMF and bromoethane were dried and degassed by the use of freeze-thaw cycles. Both were stored on the vacuum line, DMF over 3Å molecular sieves and bromoethane over CaH_2.

Synthesis

Approximately 3g of the unquaternised polymer was placed in a reaction flask fitted with a Young's tap on a high vacuum line and was dried by heating with a hot air gun and evacuating overnight. To this was added 30-40cm^3 of DMF by vacuum distillation and the solution was stirred for 3-4 hours to allow the polymer to dissolve completely. An excess (1.5cm^3) of bromoethane was added to the polymer solution via vacuum distillation and the mixture then stirred overnight in an oil bath at a temperature of 323K. A pale orange/pink coloured solution resulted.

A small quantity of AnalaR acetone was added to this mixture and the solution was poured into 8-10 volumes of n-hexane. The resulting material was redissolved in acetone (to remove any residual DMF) and reprecipitated into hexane. This process was repeated until a fine, non-sticky polymer was obtained, whereupon the polymer was separated from the precipitant by being filtered through a Büchner funnel and washed with hexane. The product was dried in a vacuum oven and stored in the dark in a desiccator.

4.2.2. CHARACTERISATION

Three techniques were used to determine whether the quaternisation reaction was successful, namely IR spectroscopy, NMR spectroscopy and elemental analysis.

Infra-red Spectroscopy

IR spectra were obtained on a Perkin-Elmer 1600 machine. As an example of the spectra obtained, those for the unquaternised HPMMA-P4VP and the quaternised HPMMA-Q(H)P4VP are shown (spectra 5 and 6 respectively, see appendix). Complete quaternisation is indicated by the replacement of the pyridine band at approximately 1600cm^{-1} by a pyridinium band at around 1640cm^{-1}. This feature was observed in the spectra for all four quaternised polymers, indicating a successful reaction in each case.

NMR Spectroscopy

^{1}H NMR spectra were obtained for all four polymers dissolved in deuterated DMSO at a temperature of 95°C, the increase in temperature increasing the definition in the spectrum. All of the spectra produced indicate that quaternisation has taken place as can be seen in the example given, the fully hydrogenous polymer HPMMA-Q(H)P4VP (spectrum 7, see appendix), the peaks at δ = 4.6 and 1.6ppm corresponding to the CH_2 and CH_3 of the ethyl group on the nitrogen respectively. Furthermore, the aromatic chemical shifts (at δ = 6.6 and 8.2 pmm) shift downfield by approximately 0.8ppm.

An attempt to obtain ^{2}D NMR spectra of the polymers was also made. Theoretically, this should have proved a very valuable tool in the characterisation of the polymers as the small number of deuterium atoms present should have resulted in spectra with relatively few peaks. Unfortunately, when the process was carried out at room temperature, the resulting spectra were impossible to interpret due to the width of some of the peaks, up to 25ppm in one case. Increasing the temperature to 95°C reduced the broadness slightly, but still no information could be gleaned from the spectra. The temperature could not be increased much further due to the proximity of the boiling point of the solvent and uncertainties regarding the thermal stability of the polymer.

Elemental Analysis

Samples of each of the four quaternised copolymers were submitted for experimental analysis. An idea of the completeness of the reaction was obtained from the percentage of bromine observed. The expected and experimentally obtained percentages of bromine in each of the polymers are given in the table below:

Polymer	Theoretical % Bromine	Observed % Bromine
HPMMA-Q(H)P4VP	12.66	11.79
HPMMA-Q(D)P4VP	12.42	12.16
DPMMA-Q(H)P4VP	11.66	11.60
DPMMA-Q(D)P4VP	11.57	10.60

Table 4.2.2. Results of elemental analysis of quaternised copolymers

As can be seen, all of the bromine percentages obtained fall slightly (between 0.5% and 8.7%) short of the expected values. As the IR spectra produced seem to indicate full quaternisation, the discrepancy may be due to the difficulty of combusting the polymer. For elemental analysis, the sample must be completely combusted and this is notoriously difficult with quaternised poly(vinyl pyridine)s.[7]

4.3. REFERENCES

1 F.T.Kiff, *Personal Communication.*

2 N. Nugay, C. Hosotte, T. Nugay and G. Riess, *Eur. Polym. J.*, 1994, **30**, 1187.

3 R. H. G. Brinkhuis and A. J. Shouten, *Macromolecules,* 1991, **24**, 1487.

4 R. C. Ferguson and D. W. Ovenall, *Macromolecules*, 1987, **20**, 1245.

5 A. Natansohn and A. Eisenberg, *Can. J. Chem.*, 1987, **65**, 1873.

6 E. A. Boucher, J. A. Groves, C. C. Mollett and (in part) P. W. Fletcher, *J. Chem. Soc. Faraday I,* 1977, **73**, 1629.

7 E. A. Boucher, E. Khosravi-Babadi and C. C. Mollett, *J. Chem. Soc. Faraday I,* 1979, **75(5)**, 1728.

CHAPTER FIVE

SURFACE PRESSURE ISOTHERMS & BREWSTER ANGLE MICROSCOPY

5.1. INTRODUCTION

Properties of monolayers of spread films of PMMA homopolymer, PMMA-P4VP copolymer and PMMA-QP4VP quaternised copolymer have been investigated by measurement of compressional surface pressure isotherms using a Langmuir trough. Subphases of pure water, KCl solutions of varying concentrations and acidic and alkaline solutions have been used. Film stability, hysteresis and the behaviour of deuterium analogues of the quaternised copolymer have also been explored. As stated in chapter three, all isotherms were recorded using a subphase temperature of 298K and a compression rate of $30cm^2$ $minute^{-1}$.

This chapter outlines the results obtained for the polymers spread upon water, KCl solutions and other subphases. In each case, a discussion of the experimental results is followed by investigation of the thermodynamic properties of the monolayers using scaling laws.

5.2. WATER SUBPHASES

5.2.1. PMMA HOMOPOLYMER

Polymer films containing PMMA generally form monolayers of high rigidity at high surface concentrations. An experimental consequence of this is that at such surface concentrations (generally greater than 3.0mg m^{-2}), the Wilhelmy plate used to measure surface pressure was displaced from the vertical position, leading to erroneous surface pressure readings. This effect could be reduced by the use of the larger, circular trough with two symmetrically closing barriers (figure 3.1.1) as opposed to the rectangular trough. For the latter, uniaxial compression exerts an unequal force on the plate. However, with the round trough, the effect was still observable at the highest surface concentrations studied, signifying that such data should be interpreted with caution.

A typical isotherm obtained from a film of PMMA homopolymer spread on a pure water subphase (in the circular trough) is shown in figure 5.2.1. The reproducibility

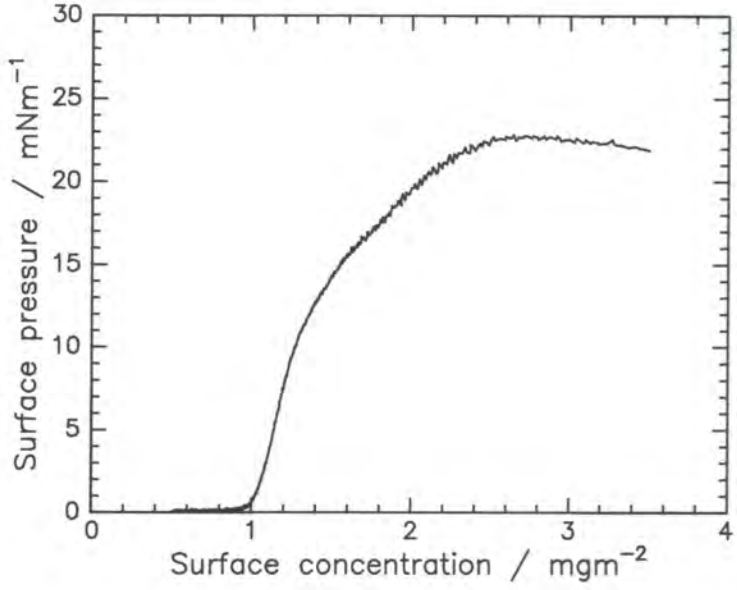

Figure 5.2.1. Surface pressure isotherm for PMMA on water

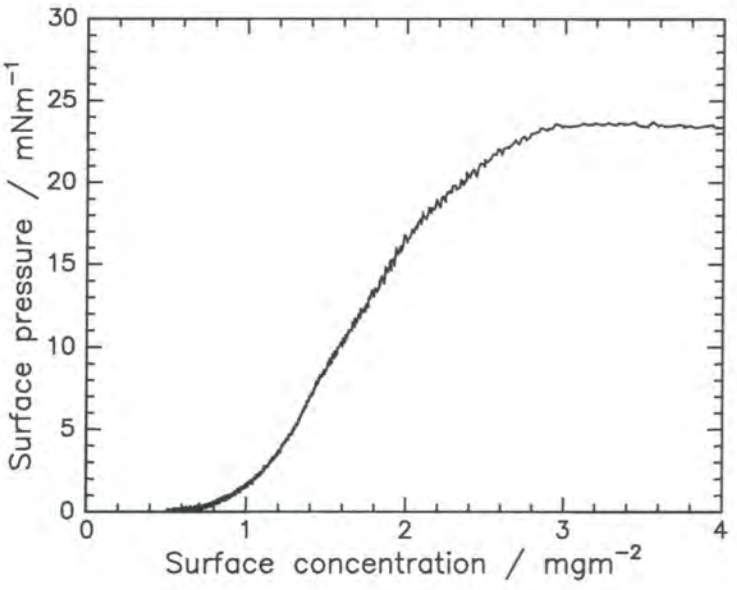

Figure 5.2.2. Surface pressure isotherm for PMMA-P4VP on water

of such an isotherm is high, particularly at lower surface concentrations. In addition to the displacement of the Wilhelmy plate outlined above, discrepancies at higher concentrations can be attributed to effects of subphase contamination. Contaminants, such as dust, are able to nucleate the process of collapse in a monolayer.

The results obtained are characteristic of a liquid condensed film and compare well to those from previous studies of syndiotactic PMMA.[1] The surface pressure remains at zero until a surface concentration of approximately 1.0mg m^{-2} is reached, whereupon a sharp rise is observed. This rise gradually decreases in magnitude and a maximum surface pressure of approximately 25mN m^{-1} is reached at a concentration of 2.5mg m^{-2}.

Previous work comparing the behaviour of PMMA of various tacticities[2] revealed significant differences between the isotherms obtained for the syndiotactic and atactic forms compared to that of the isotactic form. The isotactic form was found to exhibit the characteristics of a liquid expanded film, whereas both syndiotactic and atactic PMMA showed liquid condensed film character. Such a difference in behaviour was attributed to the lateral cohesive forces in the film, due to the dipole interactions between ester groups in the PMMA. It is speculated that for isotactic PMMA, these ester groups penetrate into the subphase, reducing in-plane interactions. For syndiotactic PMMA, the conformation of the polymer precludes such an occurrence.

5.2.2. PMMA-P4VP Unquaternised Copolymer

Surface pressure isotherms for films of the unquaternised block copolymer, PMMA-P4VP were also reproducible at low surface concentrations. A typical isotherm is shown in figure 5.2.2. As can clearly be seen, the shape is significantly different to that obtained from the homopolymer, the initial rise in surface pressure occurring at a substantially lower surface concentration (approximately 0.5mg m^{-2}) than in the case of the homopolymer. This rise, initially very gradual, steepens at $\Gamma_s \approx 1.2$mgm^{-2} and reaches a plateau value of surface pressure similar to that recorded by the homopolymer.

The difference between the two isotherms indicates that the introduction of a P4VP block has a significant effect upon the behaviour of the system. In an attempt to glean more information on such a phenomenon, the data for the PMMA-P4VP polymer was expressed in terms of surface concentration of PMMA, $\Gamma_{s,PMMA}$. A copolymer composition of 80.9% PMMA (as obtained by elemental analysis – see section 4.1.3) was used to calculate $\Gamma_{s,PMMA}$. A comparison of this set of data with the isotherm of the PMMA homopolymer is shown in figure 5.2.3.

The contribution to the surface pressure of the vinyl pyridine block was then calculated. This was carried out in the rather crude fashion of simply subtracting the surface pressure of PMMA at a specific surface concentration from that of the copolymer (i.e. $\Pi_{P4VP} = \Pi_{PMMA\text{-}P4VP} - \Pi_{PMMA}$). The data obtained is shown in figure 5.2.4.

The P4VP contribution to surface pressure rises until $\Gamma_{s,PMMA} = 1.0 mg\ m^{-2}$, where it is suggested that a complete monolayer of PMMA is formed. This calculated surface pressure then decreases to zero at PMMA surface concentrations of approximately $1.3 mg\ m^{-2}$. Here, the two isotherms converge, implying that the influence of the P4VP group on the total surface pressure drops to zero, the chains being forced down into the liquid subphase. At higher concentrations, the P4VP block again appears to have an effect, its contribution to surface pressure rising to $1.6 mN\ m^{-1}$. This may be due to the reorganisation of the chains in the subphase. At the highest surface concentrations, the two polymers produce isotherms of almost identical shape. If these isotherms can, in fact, be assumed to be identical in the region, the implication is that at such concentrations, the monolayer behaviour is again being dominated by the PMMA backbone.

To summarise, at low surface concentrations, subtle differences between the two isotherms are observed, due to the effects of the P4VP block. The PMMA monolayer then becomes a complete film at $\Gamma_{s,PMMA} = 1.0 mg\ m^{-2}$ before a further contribution to the surface pressure by P4VP is recorded at higher concentrations.

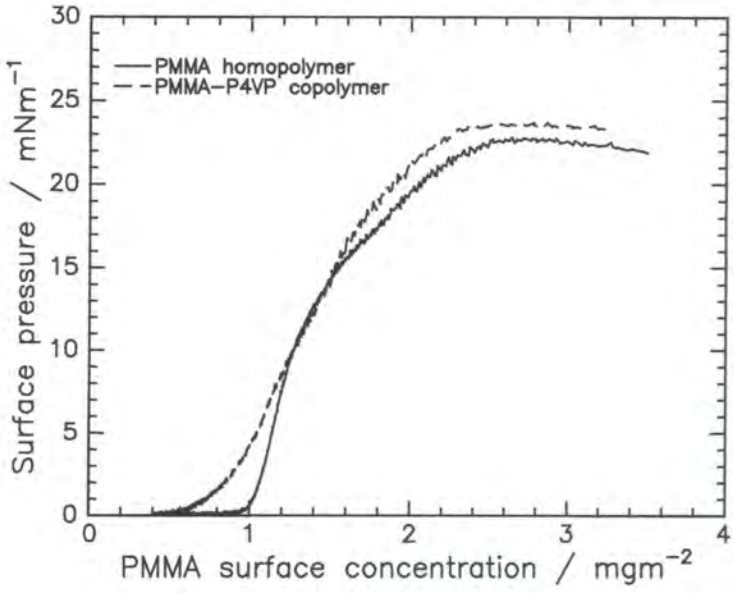

Figure 5.2.3. Comparison of surface pressure isotherms for PMMA (line) and PMMA-P4VP (dashes) on water (expressed in terms of PMMA surface concentration)

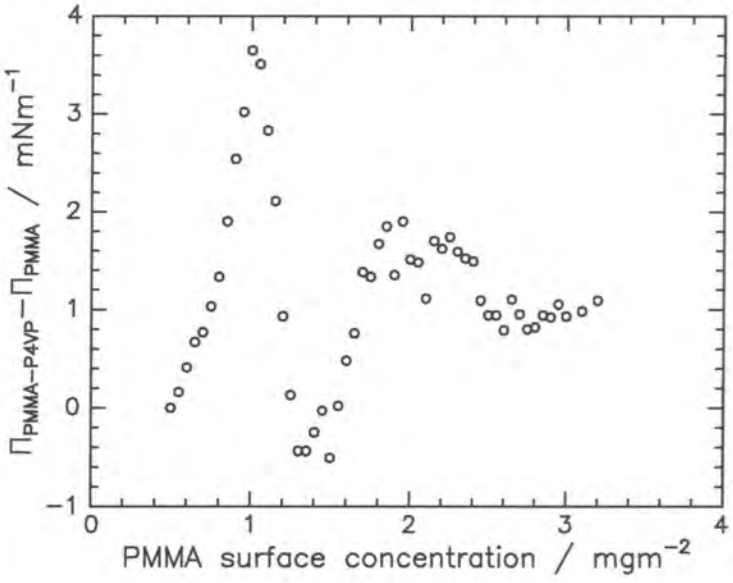

Figure 5.2.4. Plot of P4VP contribution to surface pressure against PMMA surface concentration

5.2.3. PMMA-QP4VP QUATERNISED COPOLYMER

5.2.3.1. Hydrogenous PMMA-QP4VP

Two separate isotherms obtained for the quaternised form of the copolymer spread on water are shown in figure 5.2.5. The two isotherms appear to be indistinguishable up to a surface concentration of approximately 2.0mg m^{-2} and are highly similar in shape thereafter, indicating good reproducibility.

The isotherm exhibits an initial rise in surface pressure at a surface concentration of approximately 1.2mg m^{-2}. From there, the surface pressure increases monotonically, reaching a maximum value of *ca.* 35mN m^{-1}, higher than that for either of the two polymers previously studied. In fact, the shape of the isotherm is significantly different to that of the PMMA-P4VP, implying that the conversion of the P4VP to a strongly polyelectrolytic chain has a significant effect on monolayer organisation.
To investigate this, the electrostatic contribution to the surface pressure has been calculated. Previously, Rondelez[3] defined the electrostatic contribution to the surface pressure as $\Pi_e = \Pi_Q - \Pi_{PMMA}$, where Π_Q is the surface pressure of the quaternised copolymer (at a specific PMMA surface concentration) and Π_{PMMA} is the surface pressure of the PMMA homopolymer at the same concentration. However, this method of calculating Π_e is more likely to give an indication of the contribution of the hydrophilic block as a whole. To obtain a better indication of the contribution to surface pressure caused by the quaternisation of the vinyl pyridine block, we have defined the electrostatic contribution to the surface pressure as $\Pi_e = \Pi_Q - \Pi_{UQ}$. Here, Π_{UQ} is the surface pressure of the unquaternised copolymer. A plot of Π_e (expressed here as $\Delta\Pi$) obtained by both of the methods outlined above is shown in figure 5.2.6.

The results reported by Rondelez were for a range of low surface concentrations (0.2 to 0.8 mg m^{-2}) with surface pressures less than 0.5mN m^{-1}. Such low surface pressures cannot be compared to those obtained here, the values are almost within the experimental uncertainty of our apparatus. Results at higher surface concentrations were not reported by Rondelez.

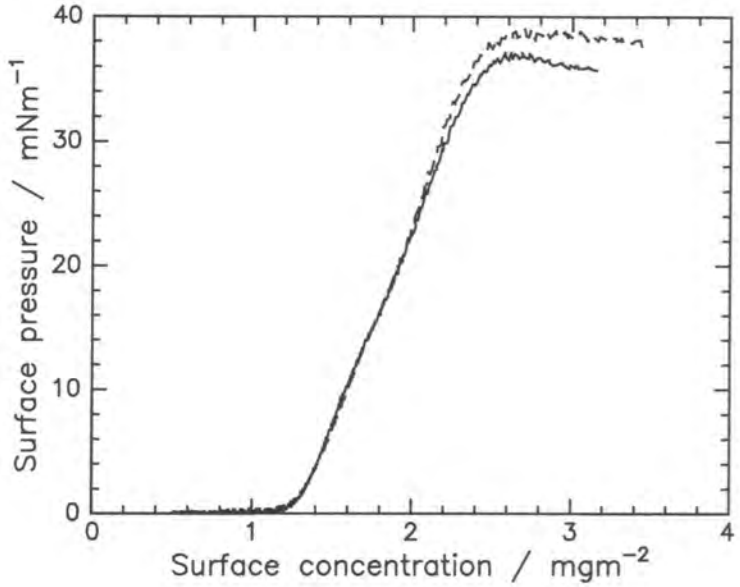

Figure 5.2.5. Examples of two surface pressure isotherms for PMMA-QP4VP

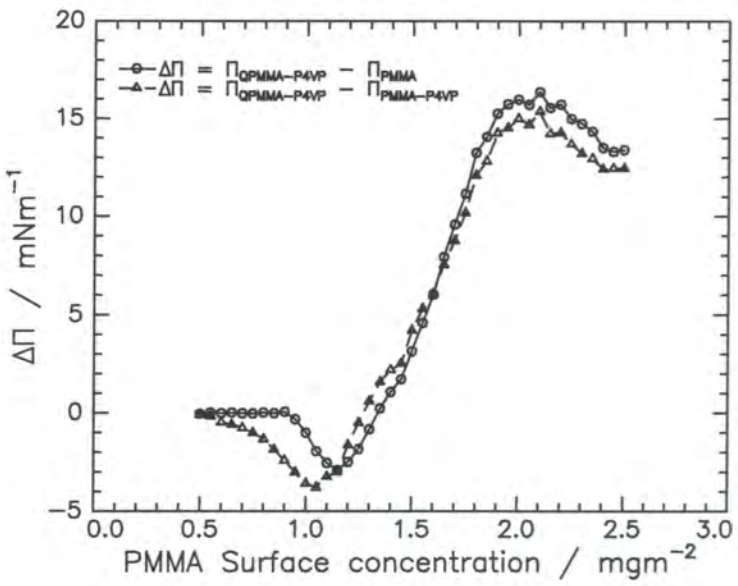

Figure 5.2.6. PMMA surface concentration against electrostatic contribution to surface tension, denoted $\Delta\Pi$. The latter quantity is calculated in two ways: (a) $\Delta\Pi = \Pi_Q - \Pi_{PMMA}$ (shown as circles) and (b) $\Delta\Pi = \Pi_Q - \Pi_{UQ}$ (shown as triangles). The lines connecting the data are guides to the eye only

In our results, the data obtained, using both definitions of the electrostatic surface pressure follow similar, albeit subtly distinct trends. In both cases, an unusual trend is observed. Using our definition of Π_e, from an initial PMMA surface concentration of 0.5mg m^{-2}, the value of Π_e initially falls to a negative value. This indicates that the quaternisation of the vinyl pyridine block has the effect of decreasing the surface pressure in this range. An explanation for this could be that quaternisation causes the QP4VP chains to extend further into the subphase than the PV4P chains. This would mean that less material would be present upon the surface of the liquid at any specific surface concentration, allowing the films to be compressed to a smaller area before any interaction between the polymer chains occurs.

The behaviour of the system at higher surface concentrations is more difficult to explain. The decrease in Π_e comes to an end at $\Gamma_{s,PMMA} \approx 1.0$mg m^{-2}, corresponding to the 'take-off' concentration of the PMMA-QP4VP isotherm. Π_e then rises, becoming positive at $\Gamma_{s,PMMA} \approx 1.25$mg m^{-2} and continuing to increase thereafter, implying that at the highest surface concentrations, it is the QP4VP which dominates the surface pressure. It is highly unlikely that the QP4VP block resides at the liquid surface at higher concentrations. However, the change may be due to a change in the organisation of the PMMA-P4VP. The reluctance of the P4VP chains to extend into the subphase may manifest itself in some other conformation, enabling the system to exist at a lower surface pressure than that the quaternised copolymer. If this is occurring, a similar phenomenon must occur with the PMMA homopolymer, due to the highly similar shapes of the two isotherms (figure 5.2.3).

5.2.3.2. Deuterated PMMA-QP4VP

To assess whether the three partially deuterated quaternised copolymers were suitable for neutron reflectometry studies, surface pressure isotherm were recorded (figure 5.2.7). Clearly, experimental error notwithstanding, there is good agreement between the isotherms obtained. It can therefore be concluded that the four polymers are of similar composition and behave in a similar manner when spread at the air-water interface.

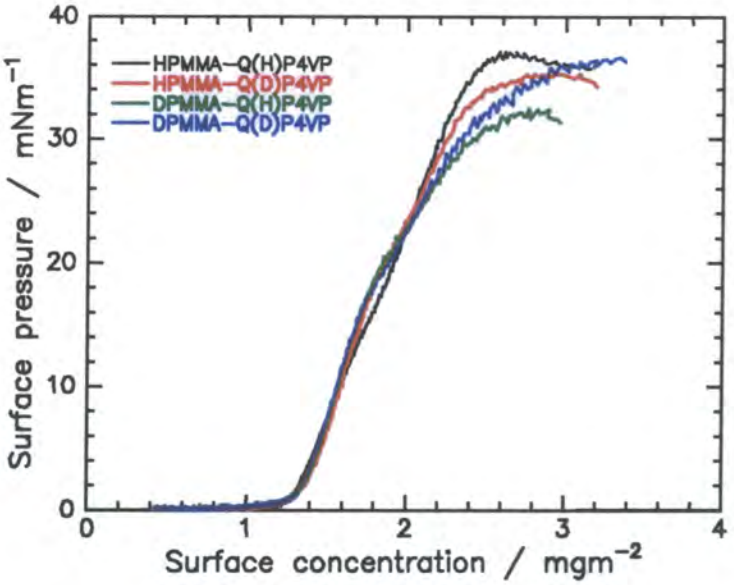

Figure 5.2.7. Comparison of the surface pressure isotherms of the partially deuterated PMMA-QP4VP copolymers

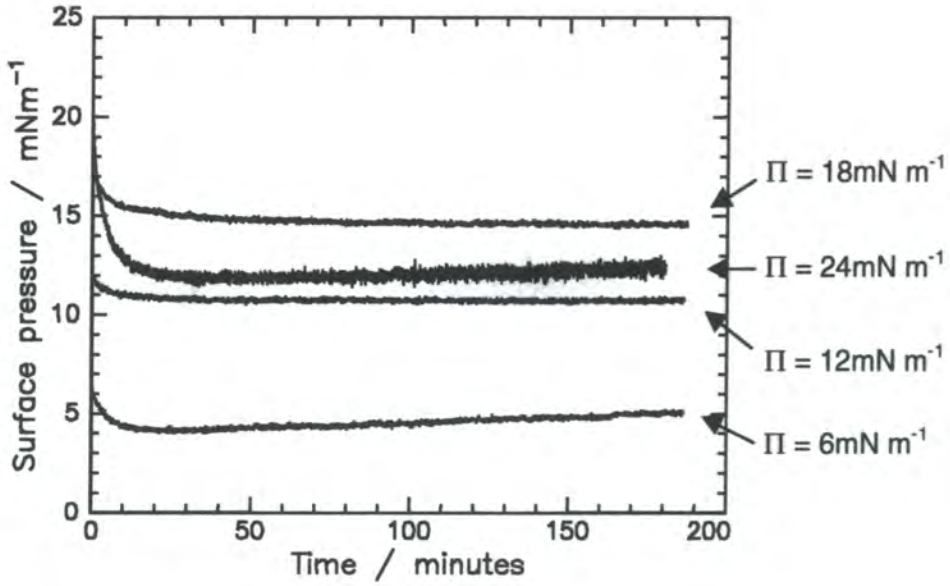

Figure 5.2.8. Film relaxation studies of PMMA-QP4VP

5.2.3.3. Film Stability

Experiments were undertaken to investigate the stability of films of PMMA-QP4VP at a range of surface pressures. Knowledge of this behaviour is of importance, as it enables us to determine the temporal stability of the film. This feature is essential for both SQELS and neutron reflectometry experiments, where a film may remain spread upon the liquid surface for periods of hours. It is also important to quantify such behaviour to allow sufficient time for the film to stabilise before beginning any physical studies of the system.

The film was compressed to initial surface pressures of 6, 12, 18 and 24mN m^{-1}, the barriers stopped and the surface pressure was recorded as a function of time. Any decrease in surface pressure is an indication of relaxation taking place in the film. Figure 5.2.8 shows plots for a range of four surface pressures.

Any decrease in surface pressure observed before 'zero' time is due to the finite period of time (approximately 30s) which elapses between cessation of barrier compression and the collection of recording surface pressure data.

In each of the four cases, an initial drop in surface pressure (indicative of film relaxation) is followed by a flat region. An observation of interest is the sharp drop in surface pressure of the film compressed to approximately 24mN m^{-1} to below that of that compressed to 18mN m^{-1}. This large relaxation is a real effect as repeated experiments reveal an identical phenomenon. The large quantity of noise of the final set of data is simply due to a high margin of error arising when the barriers are closed to a small area. In all cases, film stability is achieved after a time period no greater than 15 minutes.

5.2.3.4. Hysteresis

In an attempt to investigate if hysteresis occurred in the system, a monolayer of PMMA-QP4VP was compressed to a surface pressure of 25mN m^{-1}. The barriers were then stopped, and immediately opened to a surface concentration of 0.5mg m^{-2}. This process was repeated consecutively nine times (figure 5.2.9).

Hysteresis can be seen to occur from the first compression onwards, as the decompression curve does not follow the same path as the compression curve. Upon

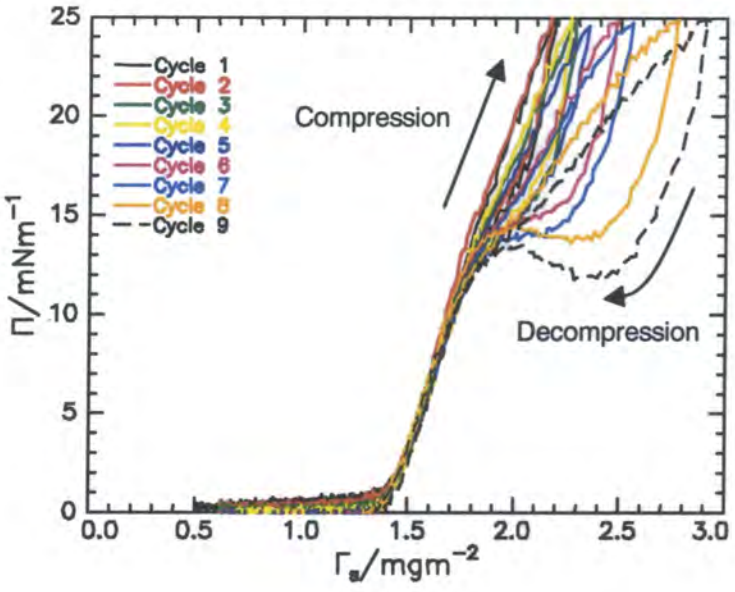

Figure 5.2.9. Hysteresis occurring in a film of PMMA-QP4VP compressed to a surface pressure of 25mN m^{-1}

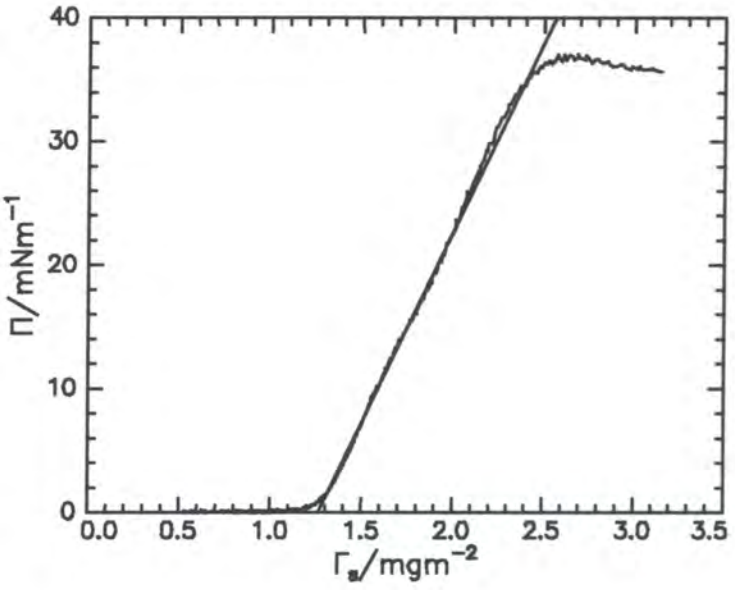

Figure 5.2.10. Straight line fit extrapolating the initial rise in surface pressure back to zero (example given is for PMMA-QP4VP on water)

commencement of decompression, the surface tension drops sharply and only regains the path followed by the compression curve when surface pressure has approximately halved (12mN m^{-1}).
Upon repeating the process, a hysteresis curve of a similar shape is observed for each cycle, although the separation of the two parts (compression and decompression) is increased. Additionally, compression to a higher surface concentration is required to achieve the target pressure of 25mN m^{-1}.

Such an occurrence may imply that a quantity of polymer is being 'lost' from the surface (i.e. extending further into the air or subphase or forming multilayers) at higher concentrations. The film would then require greater compression to achieve the same surface pressure. However, all of the isotherms regain the same path at lower surface concentrations, implying that in this regime, the organisation of the polymer is similar in every case.
The observed hysteresis is not due to barrier leakage, as this would manifest itself as a difference in pressure at all surface concentrations. Furthermore, the 'take-off' point of the isotherm would occur at increasing apparent surface concentrations.

5.2.4. Mathematical Analysis of Isotherms

Further information on the polymer systems can be obtained by the application of scaling laws (outlined in chapter 2). Such expressions have been derived for homopolymer monolayers and therefore the validity of extending their application to diblock copolymers, especially those where one of the blocks extends into the subphase, is uncertain. However, beneficial information can still be obtained if it is borne in mind that there may be some error in the absolute values of the data obtained.

5.2.4.1. Limiting Surface Area Per Monomer Unit

One quantity which is frequently used in the characterisation of surface pressure isotherms is the limiting area per monomer unit, $apmu_{lim}$. It is possible to obtain the limiting surface concentration simply by extrapolating the initial rise in surface

concentration back to zero surface pressure (as an example, see figure 5.2.10). The value of $ampu_{lim}$ may then be determined by a trivial calculation.
The results obtained for the three polymers spread on water are shown in table 5.2.1:

Polymer	$\Gamma_{s,lim}$ / mg m^{-2}	$apmu_{lim}$ / Å^2
PMMA	1.02	16.3
PMMA-P4VP	1.01	16.6
PMMA-QP4VP	1.27	14.0

Table 5.2.1. Values of limiting concentration and area per monomer unit for polymer monolayers on water

These data, along with the observations made in section 5.2.3.1, suggest that the QP4VP block extends into the water subphase, with only the PMMA residing on the liquid surface. The monolayer can therefore be compressed to a greater extent before segment interaction occurs.

5.2.4.2. Scaling Law Exponents

In the semi-dilute regime, the scaling law relationship between surface pressure, Π, and surface concentration, Γ_s, is given by:[4]

$$\Pi \approx \Gamma_s^{2\nu/(2\nu-1)} \qquad \textbf{Equation 5.2.1.}$$

If the data obtained is used to produce a double logarithmic plot, a linear portion is observed for the section of the isotherm corresponding to the semi-dilute regime. The slope of this region has a value of $2\nu/(2\nu-1)$, and application of a linear least squares fitting technique therefore allows the value of ν to be obtained.

As examples, the plots for PMMA-QP4VP on water are given. Figure 5.2.11 shows the whole double logarithmic plot and figure 5.2.12 details the linear portion in the semi-dilute region of the isotherm, along with the least squares fit obtained.
The values of the slopes and scaling exponents obtained from such plots are given in table 5.2.2.

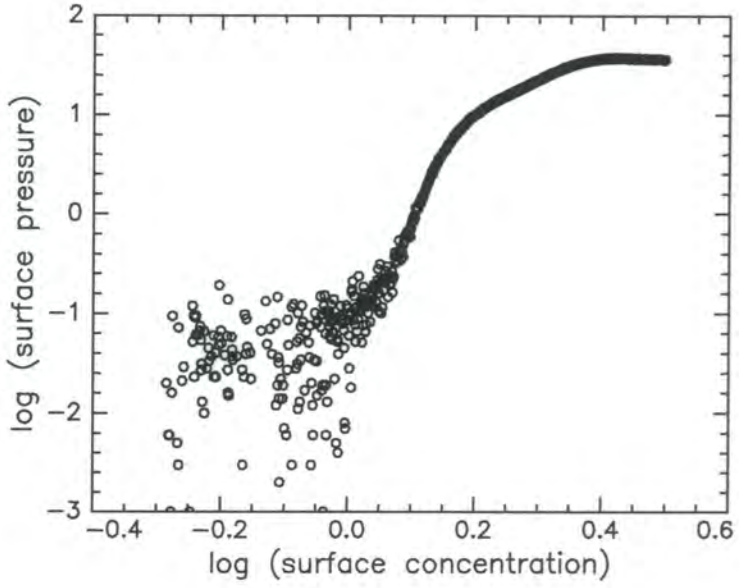

Figure 5.2.11. Double logarithmic plot for PMMA-QP4VP

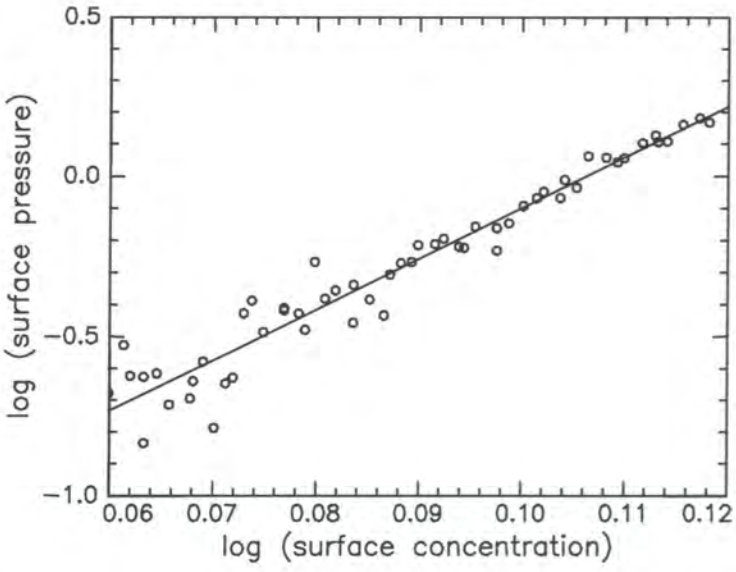

Figure 5.2.12. Double logarithmic plot of the semi-dilute regime of PMMA-QP4VP on water (circles) with least squares fit (line)

Polymer	Slope	ν
PMMA	19.29	0.53
PMMA-P4VP	5.70	0.61
PMMA-QP4VP	15.87	0.53

Table 5.2.2. Values of the slope of the linear portion of the double logarithmic plots and ν, the scaling exponent for polymer monolayers on water

The relationship between the gradient of the slope, s, and the excluded volume parameter, ν, is given in figure 5.2.13. For higher values of s, the value of ν extracted is insensitive to changes in s. An example of this is the data obtained for PMMA and PMMA-QP4VP, which have values of s differing by 18%, but the same values of ν (to two significant figures). Greater variation of ν with s is observed for lower values of s.

Accepting the generally recognised values of $\nu = 0.57$ for a polymer in the theta state and $\nu = 0.75$ for a polymer in thermodynamically good solvent conditions,[5] both PMMA and the quaternised copolymer exists in less than theta states. The value of scaling exponent for PMMA ($\nu = 0.53$) is identical to that found by Rondelez. The unquaternised copolymer has values of ν indicating that it exists in an intermediate state, between theta and good conditions.

5.2.4.3. Phase Transition Points

The points where linearity is lost on the log-log plots correspond to transitions from the dilute to the semi-dilute regions and from the semi-dilute to the concentrated regions (section 2.1.3). These two values, denoted by Γ^* and Γ^{**} respectively, are extractable (albeit with limited accuracy) from such plots and are given in table 5.2.3 below:

Polymer	Γ^* / mg m^{-2}	Γ^{**} / mg m^{-2}
PMMA	1.00	1.07
PMMA-P4VP	0.68	0.97
PMMA-QP4VP	1.15	1.32

Table 5.2.3. Surface concentrations of the phase transitions for polymers spread on water.

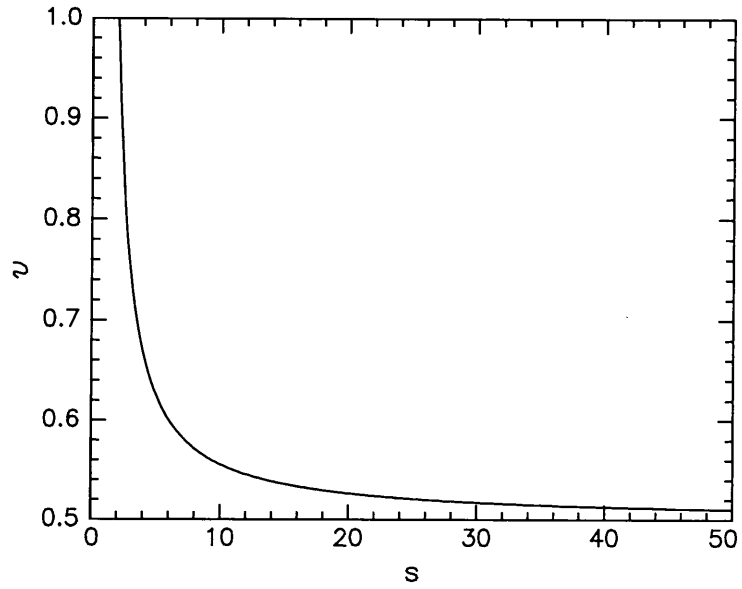

Figure 5.2.13. Plot of the excluded volume parameter, ν, against slope, s

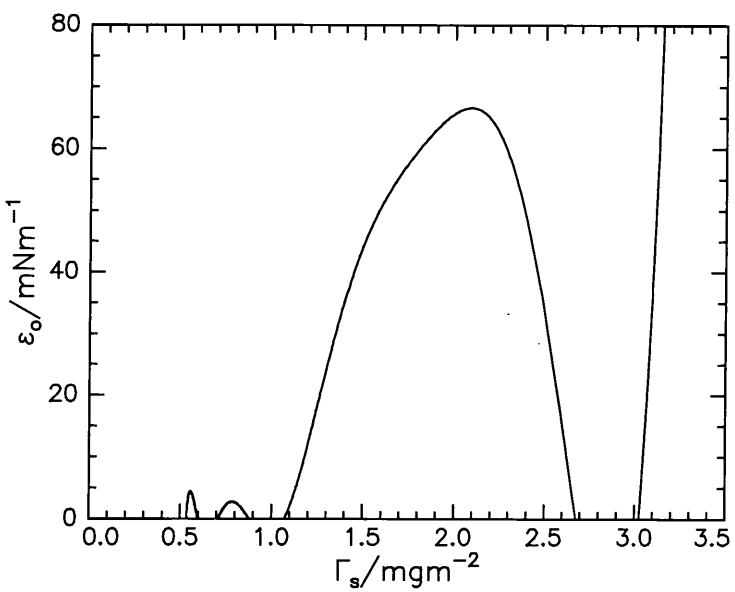

Figure 5.2.14. Plot of surface concentration against dilational modulus obtained from static surface pressure measurements for PMMA-QP4VP on water

These data agree well when compared to the transitions observed from the raw data in the isotherms. It can be seen that PMMA-QP4VP undergoes transitions at higher polymer surface concentrations than PMMA, which in turn has its transitions at higher concentrations than PMMA-P4VP.

5.2.4.4. Dilational Moduli

By utilising the relationship;

$$\varepsilon_o = \Gamma_s \frac{d\Pi}{d\Gamma_s} \qquad \textbf{Equation 5.2.2.}$$

it is also possible to obtain values of dilational modulus from surface pressure isotherms. Such values of ε_o were obtained by fitting a polynomial expression to the isotherm, differentiating this (to obtain values of $d\Pi/d\Gamma_s$ and multiplying by the surface concentration. The results for the system used in SQELS experiments, PMMA-QP4VP are shown in figure 5.2.14.

At surface concentrations below 1mg m^{-2}, the value of dilational modulus can be assumed to be zero, the slightly positive values shown being due to the noise on the surface pressure data. The dilational modulus then rises to a very high value (around 70mN m^{-1}) before falling back to zero. Any values of ε_o obtained at higher concentrations can be ignored, as to the slightly negative slope of the isotherm leads to erroneous results.

5.3. Potassium Chloride Solution Subphases

In addition to the previously reported experiments upon water, a series of isotherms were recorded on solutions of potassium chloride. These results are preceded by measurement of the surface tension of such solutions.

5.3.1. Surface Tensions of Potassium Chloride Solutions

Surface tension measurements were made via the use of a tensiometer and a Wilhelmy plate. Data were obtained for a range of subphases from water to 1M KCl solution. The results are shown in figure 5.3.1.

Each data point is the average of ten individual readings and the errors indicated are the standard deviation of mean calculated from these values. All runs were carried out at 295K. The two lines on the plot are data obtained from literature. Weissenborn[6] (solid line) obtained data for a variety of inorganic electrolyte solutions by use of the maximum bubble pressure method. In that work, only values of $\Delta\gamma/\Delta c$ (change in surface tension with concentration) are given. To plot these data on an absolute scale, the surface tension of pure water is taken from reference 7. The dashed line, which follows an almost identical path, is obtained from the aforementioned literature source.[7]

Although there is significant scatter on the experimental data, it is clear that an increase in salt concentration corresponds to an increase in surface tension. Such an increase is said to be due to a negative surface excess concentration of solute. A similar phenomenon is exhibited for the majority of electrolytes, although a small number (e.g. HCl, HNO_3 and $HClO_4$) show a decrease in surface tension with concentration.

5.3.2. PMMA Homopolymer

To determine if subphase salt concentration had any effect on a monolayer of hydrophobic PMMA, isotherms were recorded on salt subphases of 0.1M and 1M KCl. The results are shown in figure 5.3.2. At low surface concentrations, the

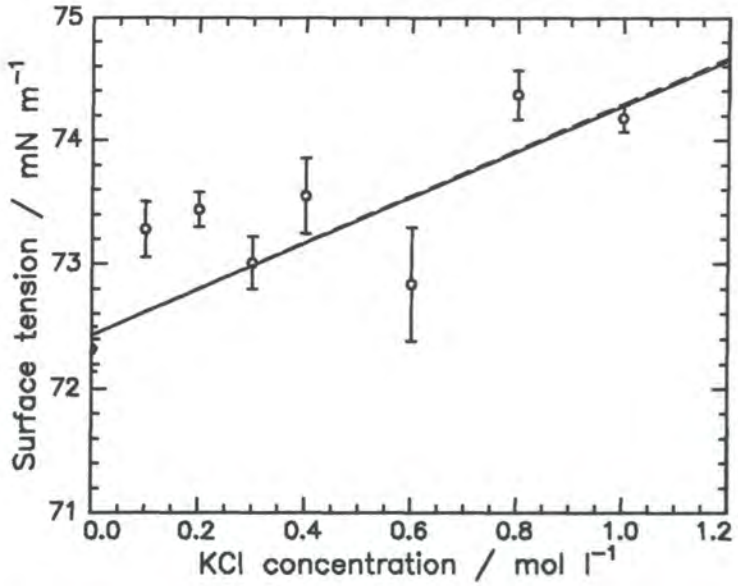

Figure 5.3.1. Surface tension of potassium chloride solutions (circles: experimental data, solid line: data from reference 6, dashed line: data from reference 7)

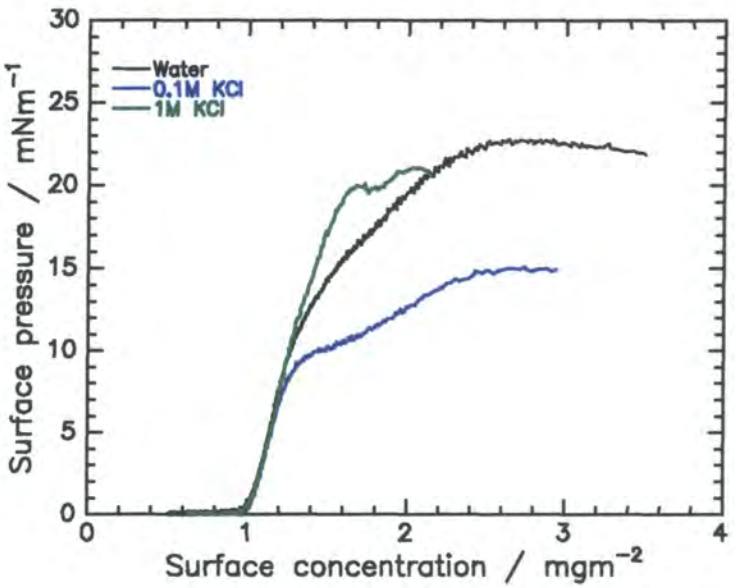

Figure 5.3.2. Surface pressure isotherms of PMMA on subphases of water and 0.1M and 1M salt solutions

isotherms overlay very well, with almost identical 'take–off' concentrations and initial gradients of slope. Although the isotherms diverge at higher surface concentrations, this is assumed to be due to effects caused by any small amounts of impurities in the subphase. It can therefore be assumed that the salt concentration of the subphase has no effect on the organisation of the PMMA film at the air-liquid interface.

5.3.3. PMMA-P4VP UNQUATERNISED COPOLYMER

Isotherms obtained from the unquaternised copolymer spread on a series of salt solutions are shown in figure 5.3.3.

In this case, it is clear that the monolayer behaviour is dependent upon subphase salt concentration. Such data is highly reproducible. At surface concentrations lower than 1.5mgm^{-2}, the isotherms obtained on both the lowest salt concentration subphase (10^{-3}M) and water are similar. A subtle change in the isotherm is observed when the salt concentration of the subphase is increased further. The resulting two isotherms (on 0.3M and 1.0M KCl solution) initially follow similar trends, both distinct from that for water and 10^{-3}M KCl. However, the isotherm on 1M salt solution reaches a plateau at a low surface pressure. The data falls into two groups, each with a similar initial gradient and it can be assumed that a transition occurs at intermediate salt concentration. These isotherms are numerically analysed in the following section.

For any specific surface concentration below 1.5mg m^{-2}, the surface pressure of the film spread on 0.3M or 1M KCl is greater than that of the film spread on water or 10^{-3}M KCl. The lower surface pressure implies that there is less polymer upon the liquid surface, due to the vinyl pyridine chains extending further into the subphase at lower salt concentrations. As even the unquaternised form of the polymer used here is a weak polyelectrolyte, this result follows polyelectrolyte theory (section 2.1.4.2). Such a theory relies on the electrostatic potential decaying with increased salt concentration, which allows the chains to congregate near to the liquid surface. At low salt concentrations however, the charges on the polymer are not screened, results in the brush adopting a more stretched configuration.

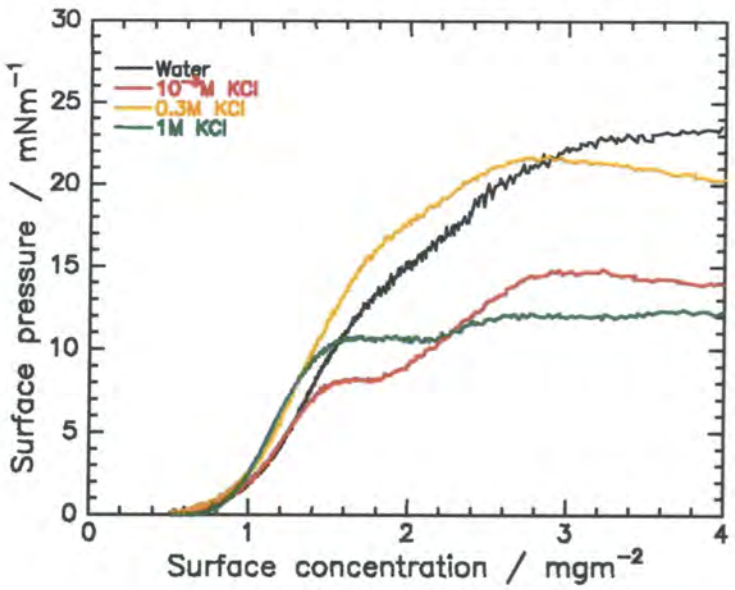

Figure 5.3.3. Surface pressure isotherms of PMMA-P4VP on subphases of water and 10^{-3}M, 0.3M and 1M salt solutions

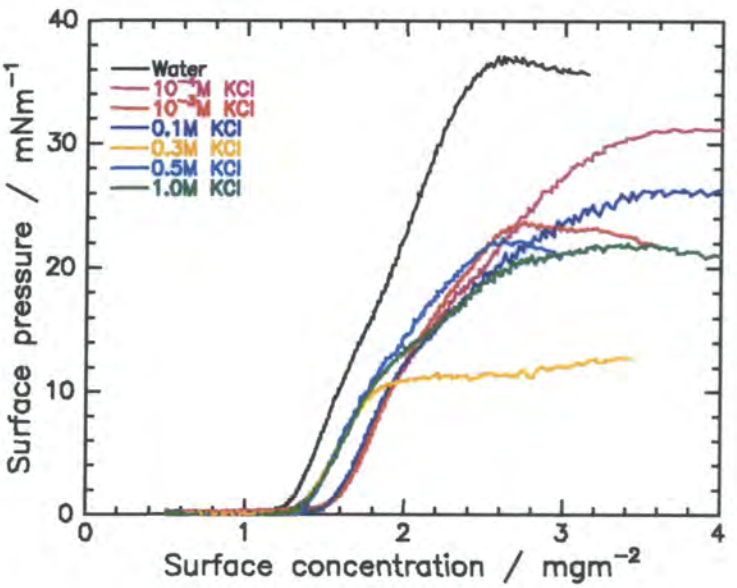

Figure 5.3.4. Surface pressure isotherms of QPMMA-P4VP on subphases of water and 10^{-4}M, 10^{-3}M, 0.1M, 0.3M, 0.5M and 1M salt solutions

5.3.4. PMMA-QP4VP QUATERNISED COPOLYMER

In an attempt to ascertain information on the behaviour of the polyelectrolyte block, isotherms of PMMA-QP4VP were recorded on a number of subphases, exploring a range of KCl concentrations over several orders of magnitude (figure 5.3.4).

Again, a distinct pattern is observed. Addition of small quantities of salt (10^{-4}M, 10^{-3}M and 0.1M KCl) to the subphase sees the isotherm 'shift' along the x-axis, moving the 'take-off' surface concentration from *ca.* 1.2mg m^{-2} to *ca.* 1.5mg m^{-2}. As the salt concentration increases further (to 0.3M, 0.5M and 1.0M KCl), the isotherms 'shift' again, this time in the opposite direction, moving to a take-off surface concentration of *ca.* 1.35mg m^{-2}. The initial gradients of the isotherms appear to be similar.

As for the results obtained for the unquaternised polymer, it is suggested that the inclusion of a small quantity of KCl in the subphase causes the QP4VP block to adopt a stretched brush formation, extending deep into the subphase. Such a conformation is retained until the salt concentration is increased to 0.3M KCl, whereupon the surface pressure rises, indicating coiling of the polyelectrolyte block, a greater proportion of which resides in the near-surface region. This hypothesis is confirmed to some extent by the results obtained from neutron reflectometry experiments (see chapter six).

An attempt was then made to calculate the electrostatic contribution to the overall surface tension exhibited by the quaternised copolymer. This was undertaken in two ways. Firstly, the expression $\Pi_e = \Pi_Q - \Pi_{PMMA}$ of Rondelez was used. Experiments using a film of PMMA on salt solutions (section 5.3.2) reveal that the film behaviour is unaffected by any change in KCl concentration. This is exemplified by the low surface concentrations (which reveal the most detail) where all values of surface pressure are identical. It is only at higher values of surface concentration where the isotherms begin to deviate. As a result of this, the surface tension of PMMA used in the calculation are those obtained on water. As before, the surface pressure data are plotted against the PMMA contribution to surface concentration. The results, giving

a crude indication of the contribution of the QP4VP block to the overall surface pressure, are shown in figure 5.3.5.

The data falls into three distinct sets. Firstly, the results obtained for a water subphase appear to be unique. No change in Π_e is observed until a PMMA surface concentration of approximately 1.0mg m^{-2} is reached. At this point, the PMMA isotherm begins to rise, and this manifests itself as a slight decrease in Π_e. At higher surface concentrations, Π_e attains large, positive values.

The other data fall into two groups. Both of these exhibit similar trends, the absolute values of Π_e being dependent upon the surface concentration where the surface pressure of the quaternised copolymer begins to rise.

The calculated values of Π_e generally decrease between PMMA surface concentrations of 1.0mg m^{-2} and 1.3mg m^{-2}, whereupon the quaternised polymer surface pressure (and therefore the value of Π_e) begins to rise. The data for subphase concentrations of 10^{-4}M KCl to 0.1M KCl show a lengthier decrease in Π_e from $1.0 < \Gamma_{s,PMMA} < 1.3$mg m^{-2} than those of 0.3M to 1M KCl. The drop in Π_e at higher surface concentrations observed for 0.3M KCl is an artefact of the low plateau surface pressure recorded for the quaternised copolymer. Although presumably due to subphase contamination, this low surface pressure was observed persistently. At PMMA surface concentrations of 1.3mg m^{-2}, the rise in $\Pi_{PMMA\text{-}QP4VP}$ is greater than that of Π_{PMMA}, thus causing the value of Π_e to rise and follow a similar path to the remainder of the data.

For all salt concentrations (except 0.3M), the values of Π_e approach zero at the highest surface concentrations. This leads to the assumption that, at these surface concentrations, the behaviour of the monolayer is again dominated by PMMA.

As with the results obtained on water subphases, similar data have been obtained by Rondelez. It was reported that with polymers of similar molecular weights, distinct relationships between Π_e and $\Gamma_{s,PMMA}$ were revealed. The data obtained for water subphases showed a linear relationship between the two parameters, reaching $\Pi_e = 0.5$mN m^{-1} at $\Gamma_{s,PMMA} = 0.6$mg m^{-2}. The data for salt solutions subphases of 10^{-4}M, 10^{-3}M and 0.1M KCl also showed increases in Π_e with $\Gamma_{s,PMMA}$, although in these cases, the rise was not monotonic. The rise in Π_e decreased with increasing subphase

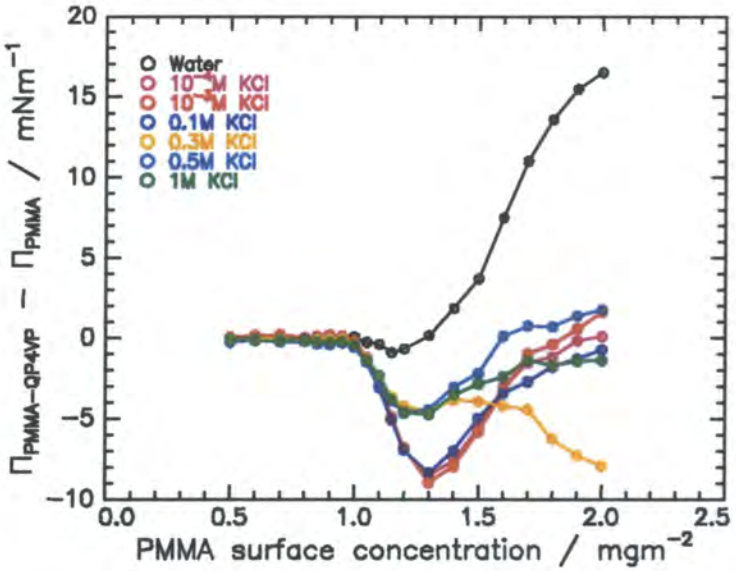

Figure 5.3.5. Electrostatic contribution to surface tension (calculated by $\Pi_e = \Pi_Q - \Pi_{PMMA}$) against PMMA surface concentration for PMMA-QP4VP spread on water and KCl solution subphases. The lines connecting the data act as guides to the eye only

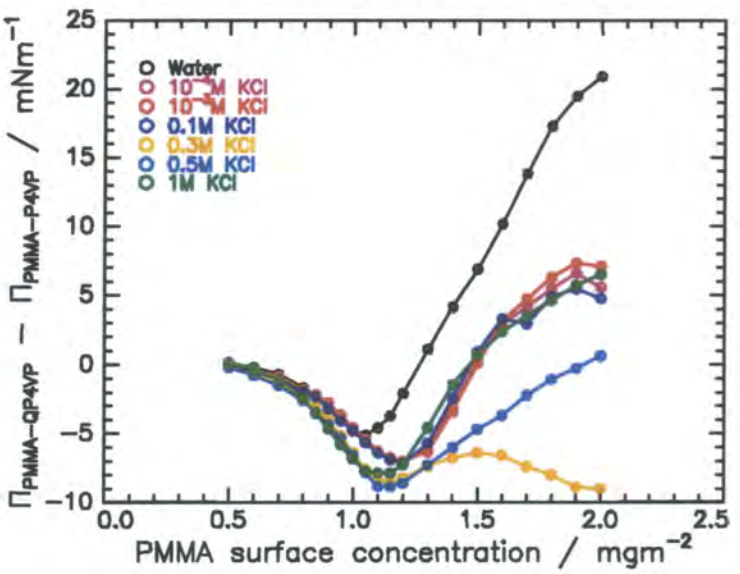

Figure 5.3.6. PMMA surface concentration against electrostatic contribution to surface tension (calculated by $\Pi_e = \Pi_Q - \Pi_{UQ}$) for PMMA-QP4VP spread on water and KCl solution subphases. The lines connecting the data act as guides to the eye only

concentration, down to an increase of approximately 0.15mN m^{-1} for the highest salt concentration studied, 0.1M.

As previously stated, no information was given regarding the behaviour of the system at PMMA surface concentrations above 1.0mg m^{-2}. Consequently no direct comparison with the present data set is possible. However, similarities with this work are found with the work of Henderson,[8] where similar data can be extracted from isotherms of PMMA-QP4VP and PMMA spread on water. In this work, the values of Π_e are initially slightly negative. At higher concentrations, $\Pi_{PMMA\text{-}QP4VP}$ rises rapidly, resulting in positive values of Π_e.

As described earlier, the second method of calculating the contribution of quaternisation to the surface pressure of PMMA-QP4VP is to use the expression $\Pi_e = \Pi_Q - \Pi_{UQ}$. The plots of $\Gamma_{s,PMMA}$ against Π_e obtained in this manner are illustrated in figure 5.3.6 for various salt solution subphases. It was assumed that the isotherms obtained for PMMA-P4VP were in some cases independent of subphase salt concentration (see figure 5.3.3). Although a seemingly crude assumption, the data for the unquaternised polymer do follow quite definite trends, allowing this method to be used as a valid first approximation.

To undertake the calculations, the data obtained for PMMA-P4VP on 10^{-3}M KCl was subtracted from that for the quaternised polymer on 10^{-4}M, 10^{-3}M and 0.1M KCl. Data for PMMA-P4VP on 0.3M KCl was used for the quaternised polymer on 0.3M and 0.5M KCl, whereas water and 1M runs were used exclusively for the quaternised polymer data on the corresponding subphases.

In general, the results obtained are of a similar form to those obtained above, where the original definition of Π_e is utilised. In both cases, an initial decrease in Π_e with increasing $\Gamma_{s,PMMA}$ is followed by an increase to positive values. Again, the data falls into three distinct groups, namely water, subphases of 10^{-4}M to 0.1M KCl and subphases of 0.3M to 1M KCl. However, using this definition of Π_e, the discrepancies between the two latter sets of data are less pronounced.

Due to the 'take-off' point of the PMMA-P4VP isotherms on 0.3M and 1M KCl occurring at lower surface concentrations, values of Π_e for subphases of higher salt concentrations become more negative. The plots for salt concentrations of 0.3M,

0.5M and 1M KCl diverge at higher surface concentrations, due to the low value of surface pressure recorded for the quaternised copolymer on 0.3M KCl.

The data for the lowest three salt concentrations follow very similar paths, reflecting the uniformity of the isotherms. The data recorded on water is again totally unique, Π_e decreasing up to PMMA surface concentrations of 1.0mg m^{-2}, before rising sharply to attain large, positive values.

5.3.5. Mathematical Analysis of Isotherms

The results obtained for the two copolymer systems spread on salt solution were analysed as described in section 5.2.4. The results, along with a brief discussion are presented here, beginning with the limiting area per monomer unit.

Polymer	Subphase	$\Gamma_{s,lim}$ / mg m^{-2}	$apmu_{lim}$ / Å^2
PMMA-P4VP	water	0.95	17.7
	10^{-3}M KCl	0.90	18.6
	0.3M KCl	0.92	18.2
	1M KCl	0.87	19.3
PMMA-QP4VP	water	1.27	14.0
	10^{-4}M KCl	1.54	11.5
	10^{-3}M KCl	1.57	11.3
	0.1M KCl	1.54	11.5
	0.3M KCl	1.35	13.1
	0.5M KCl	1.37	12.9
	1M KCl	1.37	12.9

Table 5.3.1. Values of limiting concentration and area per monomer until for polymer monolayers on potassium chloride solutions

The data (table 5.3.1) appears to confirm the trends observed from the shape of the isotherms, with significant differences in the values obtained. The PMMA-P4VP experiments performed using both water and salt solutions resulted in a larger limiting area per monomer unit than those of PMMA-QP4VP. Again, it is suggested that this is due to deeper penetration of the charged QP4VP chains into the subphase relative to those of PMMA-P4VP, thus depleting a quantity of material from the liquid surface. For the quaternised copolymer, the data form three distinct groups. The film on water has the highest limiting area per monomer unit, 14.0Å^2, whereas the isotherms on salt solutions have values of approximately 11.4Å^2 (10^{-4}M to 0.1M KCl) or 13.0 Å^2 (0.3M to 1M KCl). The differences of the values within each of

these sets of data is due to the difficulty of locating the exact start and end of the linear region of the isotherm.

The scaling law exponents obtained from the semi-dilute region of the isotherms are given in table 5.3.2. For each reported polymer sample, the scaling exponent appears to be independent of subphase. On a water subphase, PMMA-P4VP ($0.60 < \nu < 0.65$) is in a state intermediate of theta and good solvency conditions, whereas the quaternised copolymer ($0.53 < \nu < 0.56$) is in state of poorer solvency.

Polymer	Subphase	Slope	ν
PMMA-P4VP	Water	4.35	0.65
	10^{-3}M KCl	4.72	0.63
	0.3M KCl	5.77	0.60
	1M KCl	5.40	0.61
PMMA-QP4VP	water	15.87	0.53
	10^{-4}M KCl	16.04	0.53
	10^{-3}M KCl	18.45	0.53
	0.1M KCl	19.39	0.53
	0.3M KCl	12.30	0.54
	0.5M KCl	9.36	0.56
	1M KCl	14.07	0.54

Table 5.3.2. Values of the slope of the linear portion of the double logarithmic plots and ν, the scaling exponent for polymer monolayers on potassium chloride solutions

Polymer	Subphase	Γ^* / mg m^{-2}	Γ^{**} / mg m^{-2}
PMMA-P4VP	water	0.89	1.24
	10^{-3}M KCl	0.75	1.23
	0.3M KCl	0.91	1.15
	1M KCl	0.89	1.26
PMMA-QP4VP	water	1.15	1.32
	10^{-4}M KCl	1.44	1.66
	10^{-3}M KCl	1.44	1.65
	0.1M KCl	1.45	1.61
	0.3M KCl	1.39	1.51
	0.5M KCl	1.48	1.62
	1M KCl	1.35	1.49

Table 5.3.3. Values of the surface concentrations of the phase transitions for polymer monolayers on potassium chloride solutions

The phase transition points are given in table 5.3.3. A similar trend is obtained as for the limiting area per monomer unit, as the phase transition concentrations for the unquaternised polymer are less than those for the quaternised polymer. For the quaternised polymer, the film spread on water has phase transitions at the lowest surface concentrations, followed by subphases of 1M KCl, 0.3M KCl and the remainder of the salt solutions.

5.4. Acidic and Alkaline Subphases

Isotherms were also obtained on acidic (pH 3) and alkaline solutions (pH 10) subphases. The results obtained from these experiments are reported in this section and are compared with the isotherms obtained on pure water (pH approximately 5.5).

5.4.1. PMMA Homopolymer

Typical isotherms obtained on each of the subphases are shown in figure 5.4.1. At low surface concentrations, the isotherms appear to be independent of subphase, as all 'take-off' concentrations and initial gradients of the isotherms are similar. At higher surface concentrations, the isotherms diverge somewhat, although the overall trends for $\Gamma_s > 2.0$mg m^{-2} are remarkably similar. This latter observation tends to imply that PMMA behaves similarly on all the subphases investigated, any discrepancies arising from factors such as subphase contamination. It can therefore be concluded that a monolayer of PMMA behaves in a similar manner, independent of pH.

5.4.2. PMMA-P4VP Unquaternised Copolymer

Isotherms of the unquaternised copolymer are shown in figure 5.4.2. A distinct trend is observed. As the pH of the subphase increases, the length of the initial, shallow rise in surface pressure and the value of the final plateau surface pressure decreases. The magnitude of these differences between the isotherms, and the fact that such differences occur at low surface concentrations, implies that this cannot be ascribed to contamination. Implicitly, a change in behaviour of the monolayer is occurring. The surface pressure at any specific low value of surface concentration decreases with decreasing pH. A decrease in Π can be symptomatic of a decrease in the quantity of material being present in the surface region of the system. It is suggested that this is indicative of the P4VP chain existing in a more stretched conformation, due to an attraction between the electron cloud around the pyridine ring and the hydrogen ions in solution. In addition to this, the effect may be at least partially due

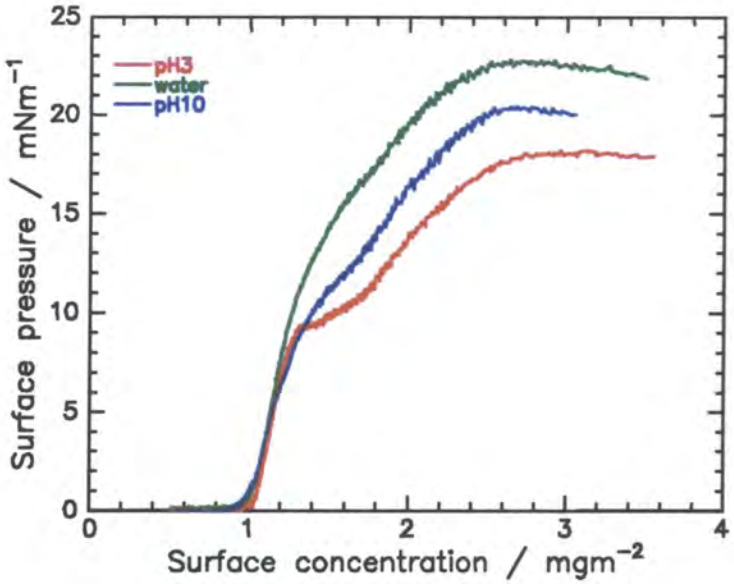

Figure 5.4.1. Surface pressure isotherms of PMMA recorded on subphases of differing pH

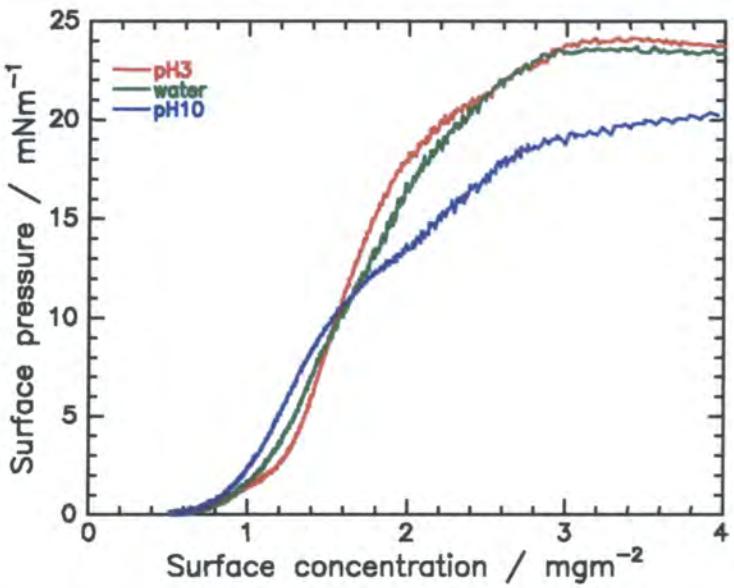

Figure 5.4.2. Surface pressure isotherms of PMMA-P4VP recorded on subphases of differing pH

to the nitrogen on the pyridine ring, which acts as a weak base, and can therefore complex with protons in subphases of low pH.

5.4.3. PMMA-QP4VP Quaternised Copolymer

The isotherms obtained for the quaternised copolymer system are shown in figure 5.4.3. Although there appears to be a slight variation in 'take-off' concentration with pH (pH3 > pH10 > water) and a more significant dissimilarity between the plateau surface pressures (water > pH10 > pH3), the initial gradients of the isotherms are similar, tending to imply that the behaviour of the system is similar on all subphases. It may appear peculiar that only a slight difference is observed between the isotherms produced by this polymer, whereas a significant variation is recorded with the unquaternised copolymer. However, the ionic strengths of the acid and alkali solutions are 10^{-3} and 10^{-4}mol kg^{-1}, which in both cases are rather low. Results presented in section 5.3.4 show that there is little change in the characteristics of the isotherm at very low subphase salt concentration and these two sets of results therefore agree well.

5.4.4. Mathematical Analysis of Isotherms

Analysis of the isotherms again took place as outlined in section 5.2.4. The results on water are included for comparison.

Polymer	Subphase	$\Gamma_{s,lim}$ / mg m^{-2}	$apmu_{lim}$ / $Å^2$
PMMA	pH3	1.00	16.6
	water	1.02	16.3
	pH10	0.95	17.5
PMMA-P4VP	pH3	1.16	14.5
	water	1.01	16.6
	pH10	0.89	18.8
PMMA-QP4VP	pH3	1.33	13.3
	water	1.27	14.0
	pH10	1.30	13.6

Table 5.4.1. Values of limiting concentration and area per monomer unit for polymer monolayers on subphases of differing pH

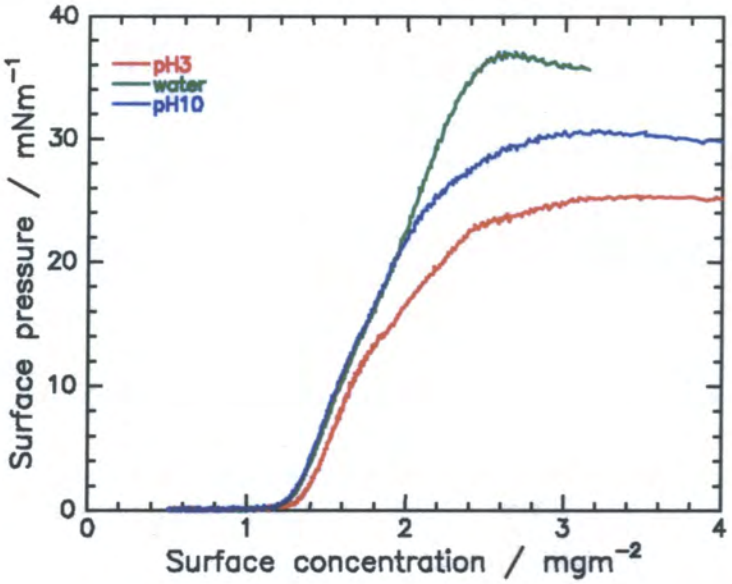

Figure 5.4.3. Surface pressure isotherms of PMMA-QP4VP measured on subphases of differing pH.

The values of limiting area per monomer unit obtained are given in table 5.4.1. The only major difference between subphases is found with PMMA-P4VP, where the values of limiting area follow the discussion in section 5.3.4. The values for PMMA-QP4VP are all quite similar, even allowing for the slight 'shift' in the isotherm observed on an acidic subphase.

The scaling law exponents obtained form the semi-dilute regime are given in table 5.4.2:

Polymer	Subphase	Slope	ν
PMMA	pH3	26.87	0.52
	Water	19.29	0.53
	pH10	11.58	0.55
PMMA-P4VP	pH3	4.49	0.64
	Water	5.70	0.61
	pH10	5.45	0.61
PMMA-QP4VP	pH3	17.71	0.53
	Water	15.87	0.53
	pH10	14.57	0.54

Table 5.4.2. Values of the slope of the linear portion of the double logarithmic plots and ν, the scaling exponent for polymer monolayers on subphases of differing pH

As expected from the shape of the isotherms, the results generally concur with those obtained on a water subphase. The values obtained for PMMA and PMMA-QP4VP fall within a narrow range (ν = 0.52 to 0.55), whereas the PMMA-P4VP system again exhibits higher values, suggesting that it exists in an intermediate state between theta and good solvent conditions.

Polymer	Subphase	Γ^{*} / mg m^{-2}	Γ^{**} / mg m^{-2}
PMMA	pH3	1.00	1.06
	Water	1.00	1.07
	pH10	0.98	1.06
PMMA-P4VP	pH3	0.71	0.95
	Water	0.68	0.97
	pH10	0.69	0.91
HPMMA-QP4VP	pH3	1.27	1.41
	Water	1.15	1.32
	pH10	1.32	1.42

Table 5.4.3. Surface concentrations of the phase transitions for polymer monolayers on subphases of differing pH

The phase transition points are given in table 5.4.3. Here, the transitions occur at different concentrations for each polymer. There is little difference between the transitions points for polymers on water and those on acidic or alkaline solutions.

5.5. BREWSTER ANGLE MICROSCOPY

Brewster angle microscopy (BAM) was used in an attempt to obtain a direct visualisation of the polymer organisation at the air-liquid interface. Firstly, it was attempted to determine whether the polymer existed as a uniform film, or a series of 'islands' floating on the liquid surface. Information regarding the thickness of the polymer films was also desired. Recently, experiments to determine film thicknesses of monolayers have been performed.[9] However, such a method is not feasible on the apparatus used here.

BAM images were recorded whilst compressing a film at a constant rate. These 'snapshot' images of the film were taken at regular intervals, a sample of which are presented in the discussion below. The systems studied were PMMA-QP4VP on water, 0.1M and 1M KCl solutions, and the PMMA homopolymer on water. As outlined in section 3.4.2, the imagines were coloured on a scale from black (minimum light intensity) through to white (maximum light intensity). For convenience, the full colour scale is reproduced with each figure.

5.5.1. PMMA HOMOPOLYMER

A selection of images obtained for the PMMA homopolymer on a water subphase are given in figure 5.5.1. It is immediately evident that the images provide little information on the surface organisation as no structure in the film can be visualised. The maximum light intensity of each image lies in a central circular region, corresponding to the area of the detector illuminated by the laser. The concentric circles in each of the images are simply interference rings.

Images (a) and (b) relate to polymer surface concentrations of 0.5 and 1.0mg m^{-2}, both of which occur on the initial, flat section of the isotherm. These images are quite similar in character and imply that there is little change in the film thickness in this region. It then follows that the full surface coverage does not occur at these low concentrations, as compression of the film seems to bring the polymer chains closer together, rather than increasing the thickness of material on the surface. The concentration range $\Gamma_s = 1.0 - 1.5$ mg m^{-2} corresponds to the initial rise in surface

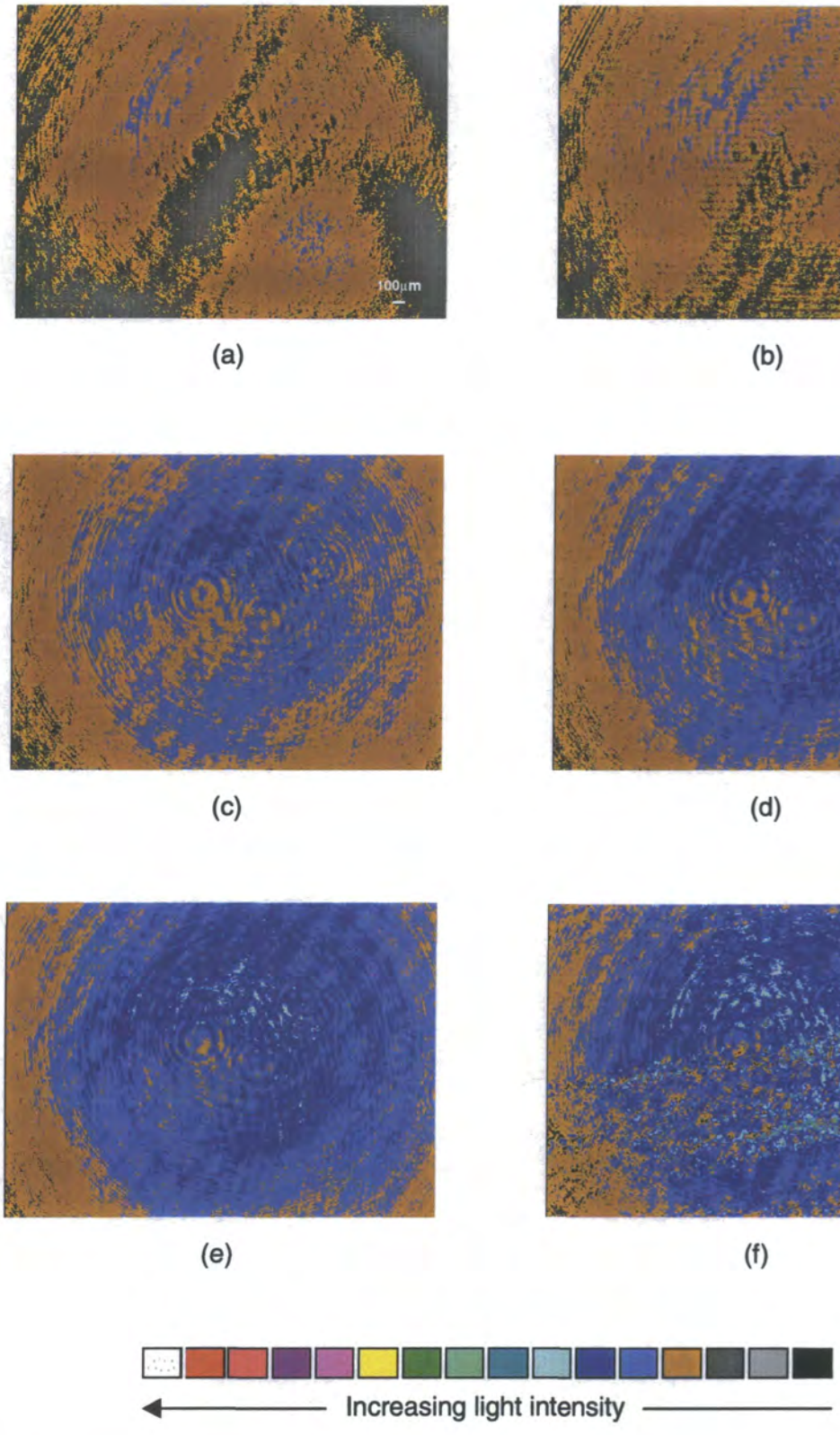

Figure 5.5.1. Brewster Angle Microscopy images (and colour scale) for PMMA on water. Images depict polymer surface concentrations of (a) 0.5mg m^{-2} (b) 1.0mg m^{-2} (c) 1.5mg m^{-2} (d) 2.0mg m^{-2} (e) 2.5mg m^{-2} (f) 7.2mg m^{-2}. All images are x2 magnification. The scale is shown on (a)

pressure of the isotherm, which relates to some interaction between the polymer chains. A significant increase in light intensity is recorded at 1.5mg m^{-2}. Thereafter, there are no further abrupt changes in the images, although there is a constant light intensity increase in this high concentration range, perhaps corresponding to an increase in film thickness. Image (f) was recorded at the highest surface concentration explored, 7.2mg m^{-2}. The thick diagonal band across the image consists of ridges formed as the film buckles due to overcompression.

5.5.2. PMMA-QP4VP QUATERNISED COPOLYMER

5.5.2.1. Water Subphase

Six images are presented for the quaternised polymer (figure 5.5.2), showing the surface at a range of polymer concentrations between 1.0 and 4.0mg m^{-2}. The intensity of light recorded increases quite slowly at low concentrations (images (a) and (b)). A much more abrupt change occurs at a surface concentration of *ca.* 2.0mg m^{-2} (images (c) to (e)). This surface concentration is of no special significance, occurring approximately half way up the initial rise in surface pressure. It is suggested that such an increase in light intensity is due to the film becoming thicker at such surface concentrations. This is discussed further in chapter six.

As discussed earlier, care has to be taken when interpreting data at high surface concentrations. A good illustration of this is given in figure 5.5.3 which shows an image recorded on water at a surface concentration of 3.5mg m^{-2}. Here, film collapse appears to have already occurred (presumably due to a surface contaminant) and a 'lump' of polymer exists on the liquid surface. The polymer film is therefore not monolayer in the instance.

5.5.2.2. Salt Solution Subphases

Images from BAM experiments on subphases of 0.1M KCl solution are shown in figure 5.5.4. For the concentration range shown, 1.0mg m^{-2} to 2.5mg m^{-2}, the recorded light intensity appears to increase quite constantly with surface concentration. At no stage of the compression does there appear to be an abrupt

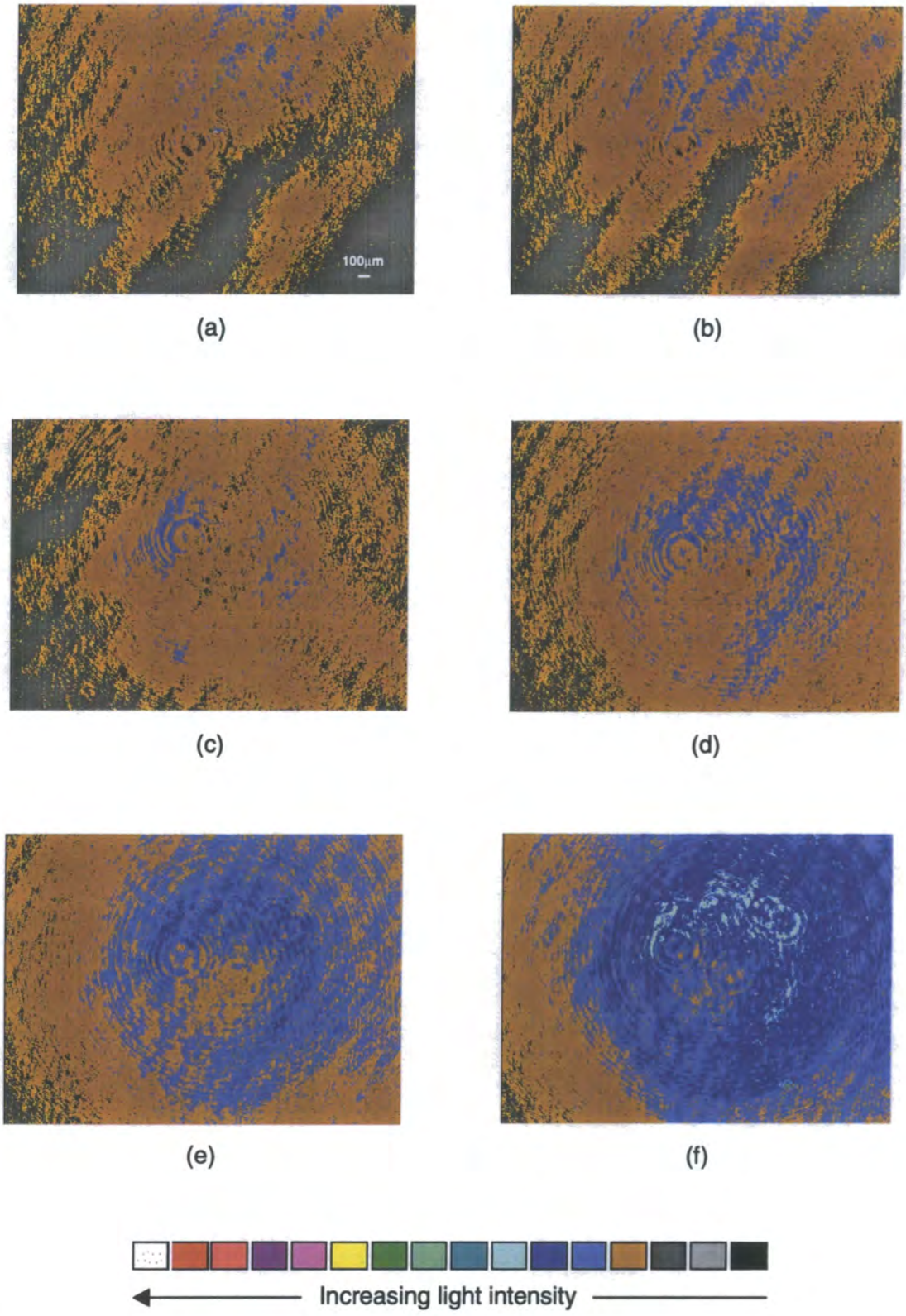

Figure 5.5.2. Brewster Angle Microscopy images (and colour scale) for PMMA-QP4VP on water. Images depict polymer surface concentrations of (a) 0.5mg m^{-2} (b) 1.0mg m^{-2} (c) 1.5mg m^{-2} (d) 2.0mg m^{-2} (e) 2.5mg m^{-2} (f) 7.2mg m^{-2}. All images are x2 magnification, the scale is shown on (a)

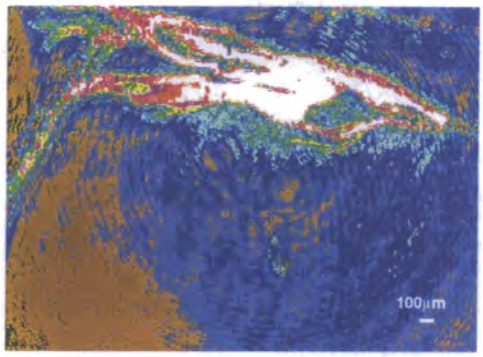

Figure 5.5.3. Example of monolayer collapse. Brewster Angle Microscopy image for PMMA-QP4VP on water, polymer surface concentration = 3.5mg m^{-2}, x2 magnification

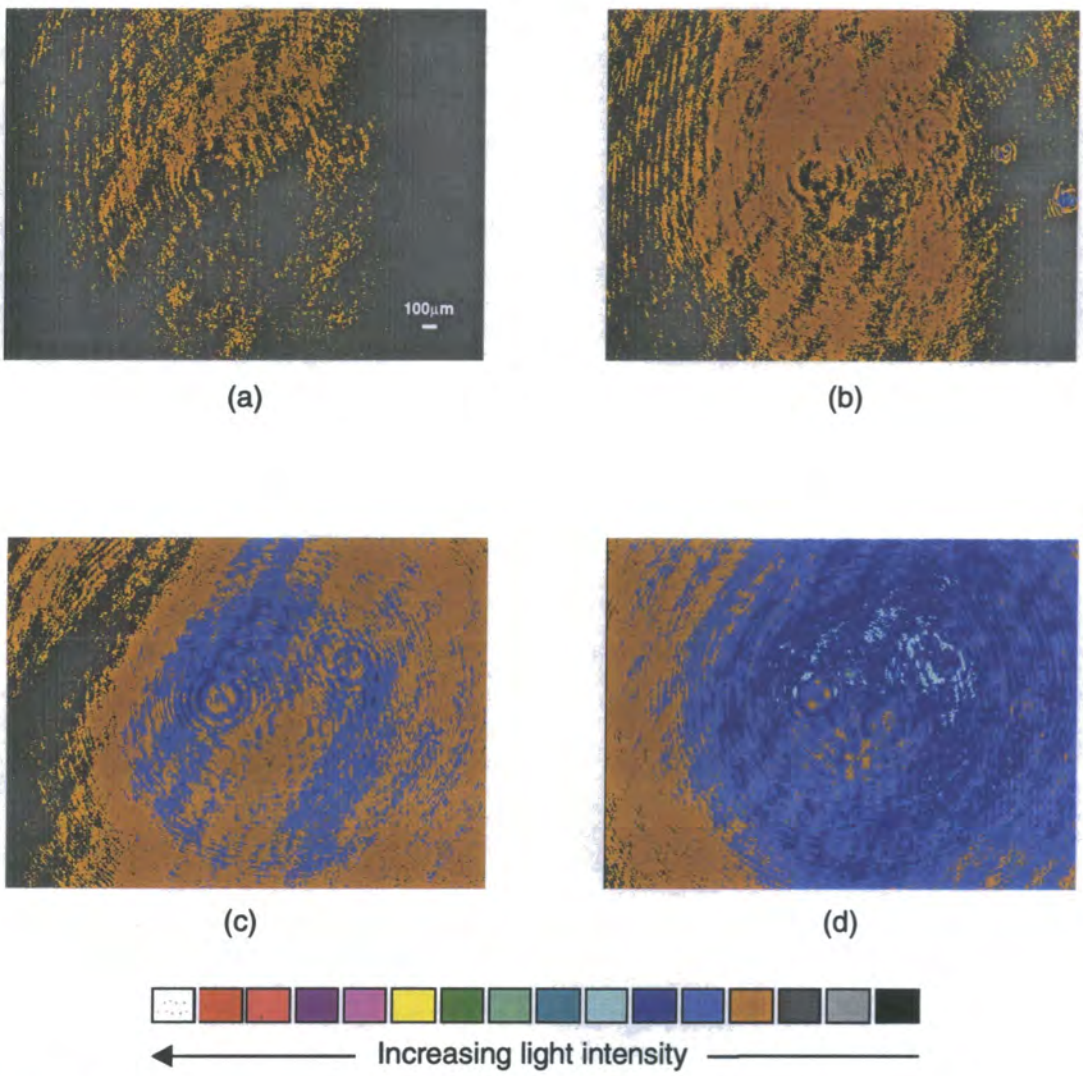

Figure 5.5.4. Brewster Angle Microscopy images (and colour scale) for PMMA-QP4VP on 0.1M KCl solution. Images depict polymer surface concentrations of (a) 1.0mg m^{-2} (b) 1.5mg m^{-2} (c) 2.0mg m^{-2} (d) 2.5mg m^{-2}. All images are x2 magnification, the scale is shown on (a)

change in behaviour. The small area of high intensity on the extreme right hand side of image 5.5.4(b) is a speck on dust on the liquid surface.

Figure 5.5.5 illustrates images for PMMA-QP4VP on 1M KCl solution. Here, there initially appears to be little change in the recorded light intensity, Between 2.0 and 2.5mg m^{-2} (images (c) and (d)) however, the intensity increases dramatically. Thereafter, a smaller increase is again observed.

In an attempt to gain further information, images (figure 5.5.6) were measured for the same system at the maximum magnification available with the apparatus (x7). This gave images of *ca.* 0.8mm width. Those presented here are typical of those obtained at this magnification. The low light ensured that no useful observations could be made. This was also the case with high magnification observations for other subphases.

One phenomenon observable in the presented images is the overall greater light intensity measured for the higher concentration salt solution. As the two sets of data were obtained consecutively, such an effect is not an artefact of the experimental set-up, nor does it necessarily imply the existence a thicker film on 1M KCl solution. Rather, it is due to the differing refractive indices of the subphases.

The refractive indices for water, 0.1M KCl solution and 1M KCl solution (at 20°C) are 1.333, 1.334 and 1.343 respectively and using the relationship below, the Brewster angle for each system can be calculated. These are given in table 5.5.1:

$$\tan\theta_B = \frac{n_2}{n_1}$$ **Equation 5.5.1.**

Interface	Brewster angle
Air - water	53.12°
Air – 0.1M KCl solution	53.14°
Air – 1M KCl solution	53.32°

Table 5.5.1. Values of the Brewster angle for a range of air-liquid systems

All of the above images were obtained with the instrument fixed at 51.12°. The observed increase in light intensity is therefore merely a result of the increased

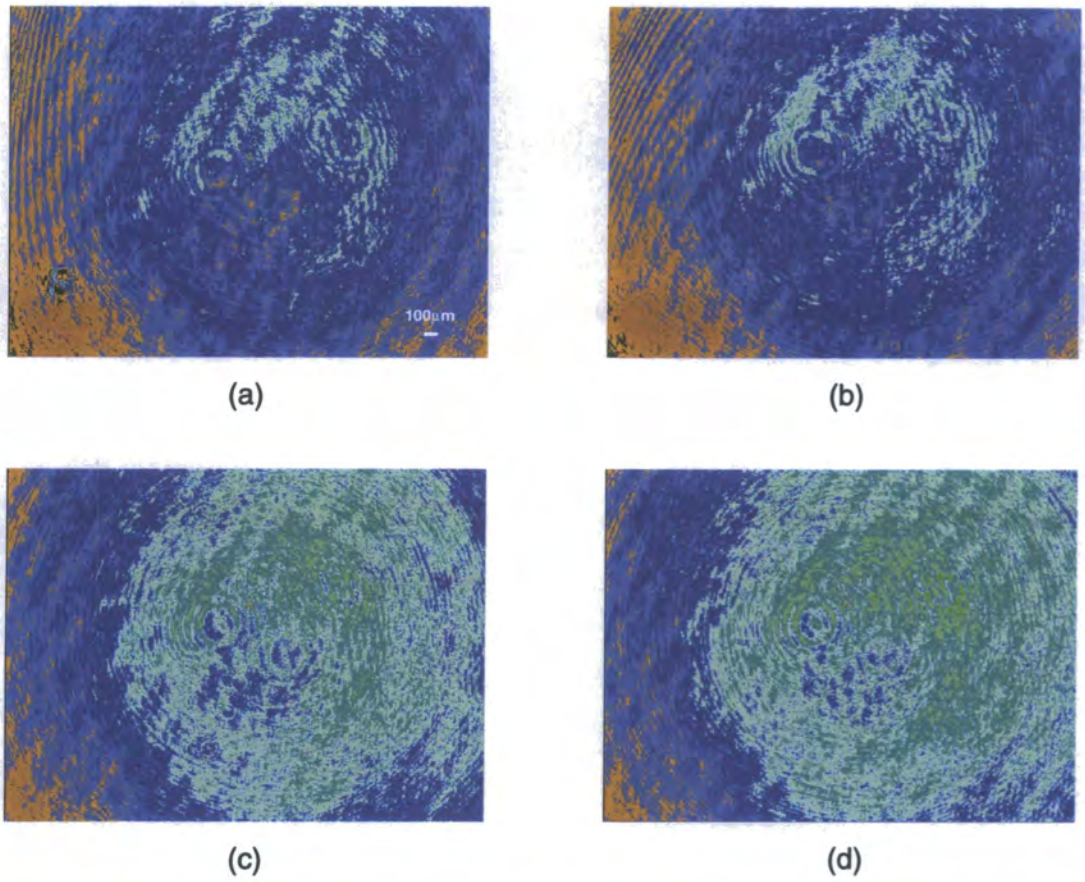

Figure 5.5.5. Brewster Angle Microscopy images for PMMA-QP4VP on 1M KCl solution. Images depict polymer surface concentrations of (a) 1.0mg m^{-2} (b) 2.0mg m^{-2} (c) 2.5mg m^{-2} (d) 3.0mg m^{-2} at x2 magnification, scale shown on (a)

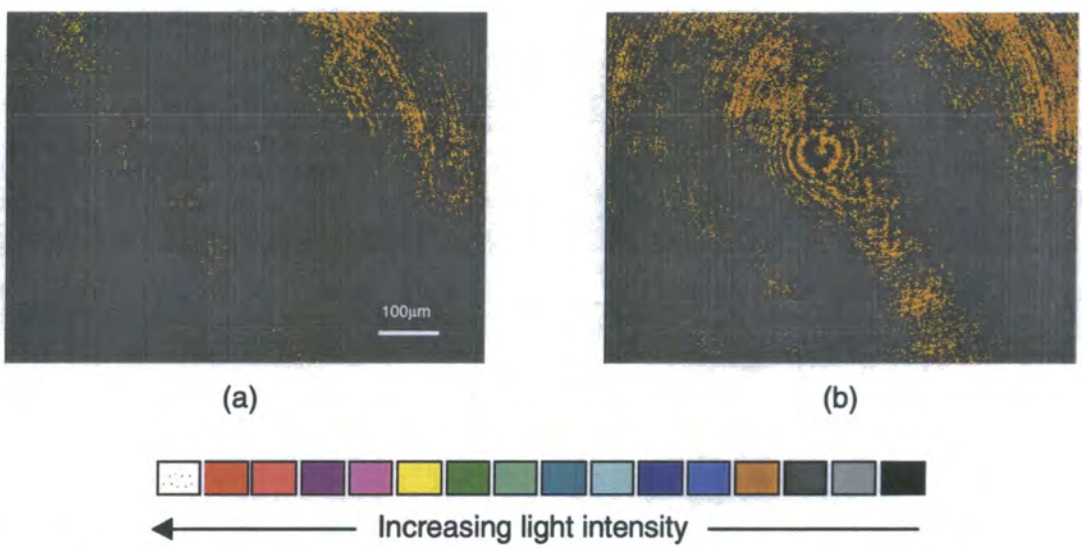

Figure 5.5.6. Brewster Angle Microscopy images (and colour scale) for PMMA-QP4VP on 1M KCl solution. Images depict polymer surface concentrations of (a) 2.0mg m^{-2} (b) 3.0mg m^{-2}. All images are x7 magnification, the scale is shown on (a)

quantity of light reflected from the surface at angles slightly removed from the Brewster angle.

5.5.3. Discussion

From the results obtained, it is difficult to form any firm conclusions regarding the organisation of the system. Three possible explanations for this are:

1. The monolayer exists as a uniform film on the liquid surface. This is probably the case at high surface concentrations. However, results from SQELS experiments (chapter 7), imply that the film exists as islands at low surface concentrations. This cannot be visualised directly by BAM, although, as alluded to in section 5.5.1, the observation that light intensity remains approximately constant at low surface concentrations implies incomplete surface coverage.

2. Any structure in the film exists on a scale too small to be observed by this technique. Details as small 10μm and 50μm should be observable at the highest and lowest magnifications respectively and any domains on the surface would therefore have to be smaller than this to be unobservable. As previously stated, other details (such as dust and monolayer collapse) can be observed, so the resolution of the instrument may not be sufficient to reveal any finer surface structure.

3. The polymer film has a refractive index equal to that of the subphase, thus rendering it 'invisible' to this technique. The refractive index of PMMA[10] (at 20°C) is 1.490. No data is obtainable for the quaternised poly(4-vinyl pyridine) block, but it can be safely assumed that the refractive index is greater than that of water. If this is the case, the block copolymer will have a refractive index distinct from that of the subphase and therefore should be observable by Brewster angle microscopy.

   However, if the polyelectrolyte chains exist in a highly stretched conformation, for example in solutions of low salt concentration, the value of dn/dc, the

refractive index increment, will be small. The refractive index of the polymer in subphase would therefore be similar to that of the subphase, resulting in the QP4VP chains being 'invisible' to BAM. The opposite effect would occur for a coiled QP4VP conformation, namely $n_{QP4VP} \neq n_{water}$, allowing the surface structure to be visualised by BAM.

5.6. CONCLUSIONS

Surface pressure isotherms have been measured for three polymer systems, using subphases of water and salt, acidic and alkaline solutions.

On water, the surface pressure isotherms for the two neutral polymers are distinct at low surface concentrations, but show similar characteristics as the quantity of polymer increases. From this, the PMMA backbone is assumed to dominate the polymer structure at higher surface concentrations. The quaternised copolymer produces a significantly different isotherm, from which it can be implied that the hydrophilic QP4VP block extends into the liquid subphase. Qualitative analysis of such isotherms has been used to obtain a number of physical parameters of each system, which show good agreement with those in the literature.
Surface pressure isotherms measured for the deuterium-containing polymers indicated that these materials are suitable for use in neutron reflectometry experiments, providing a sufficient length of time is allowed for film relaxation to take place.

Studies of KCl solutions over a range of concentrations confirm that surface tension increases monotonically with salt concentration. Isotherms recorded on KCl solution subphases show differing characteristics as salt concentration is varied. From these isotherms, it is deduced that the polyelectrolyte chains become less stretched with increasing salt concentration.

Isotherms recorded on subphases of pH 3 and pH 10 reveal that only one of the polymers studied, the unquaternised PMMA-P4VP, undergoes a significant change of organisation on solutions of differing acidity. A film of the quaternised polymer produced highly similar isotherms on solutions of such low ionic strengths. These results are similar for those observed on subphases of very low salt concentration. Finally, the PMMA homopolymer isotherms appears to be independent of pH.

Brewster angle microscopy experiments failed to yield the detailed structural information that was initially hoped for. However, by analysing the images obtained,

it could be surmised that the polymer film is initially non-uniform across the liquid surface, before forming a complete layer, the thickness of which increases at higher surface concentrations.

5.7. REFERENCES

1 J. A. Henderson, R. W. Richards, J. Penfold, C. Shackleton and R. K. Thomas, *Polymer,* 1991, **32**, 3284.

2 R. H. G. Brinkhuis and A. J. Schouten, *Macromolecules,* 1991, **24**, 1487.

3 E. Bringuier, R. Vilanove, Y. Gallot, J. Selb and F. Rondelez, *J. Colloid and Interface Sci.,* 1985, **104**, 95.

4 D. Poupinet, R. Vilanove and F. Rondelez, *Macromolecules*, 1989, **22**, 2491.

5 R. Vilanove, D. Poupinet and F. Rondelez, *Macromolecules*, 1988, **21**, 2880.

6 P. K. Weissenborn and R. J. Pugh, *J. Colloid and Interface Sci.,* **1996**, 550.

7 R. C. Weast (ed.), *Handbook of Chemistry and Physics*, 68/e, CRC Press, Boca Raton, USA, 1988.

8 J. A. Henderson, *Ph.D. Thesis*, University of Durham, 1992.

9 J. M. Rodríguez Patino, C. Carrera and M^{a}. R. Rodríguez Niño, *Langmuir,* 1999, **15**, 2848.

10 J. Brandrup, E. H. Immergut and E. A. Grulke (editors), *Polymer Handbook*, 4/e, Wiley-Interscience, New York, USA, 1998.

CHAPTER SIX

NEUTRON REFLECTOMETRY

6.1. INTRODUCTION

Neutron reflectometry has been used to study the organisation of spread films of the quaternised diblock copolymer, PMMA-QP4VP at the air – water and air – KCl solution interfaces.

For films spread on water, six surface concentrations have been studied, covering the full range of surface pressure variation in the isotherm (figure 5.2.1). At the air – KCl solution interface, a range of three subphase salt concentrations have been examined, all at the highest surface concentration explored, 3.0mg m^{-2}. These results are presented in section 6.4.

Data analysis has predominantly used the kinematic approximation which, in addition to being sensitive to subtle changes in the organisation, gives a full description of the organisation of the polymer at the interface. Optical matrix and model independent fitting techniques have also been utilised.

This chapter begins with a résumé of the experimental procedure undertaken. The results obtained are then presented and discussed. In both cases, the raw reflectivity data are given, followed by the results of the various fitting processes and their interpretation. To avoid repetition, a full description of the data analysis techniques will only be given in the first of the two discussions.

6.2. EXPERIMENTAL

In chapter four, the use of selective deuteration resulted in the synthesis of one fully hydrogenous and three partially deuterated forms of PMMA-QP4VP. Spreading films of these polymers upon D_2O as well as NRW allowed a full set of six contrasts to be obtained at each surface concentration studied.

The surface concentrations and subphases for which such a full set of contrasts were obtained are given in table 6.2.1, along with the reflectometer on which the data was recorded.

Γ_s / mg m^{-2}	Subphase	Reflectometer
1.0	water	SURF
1.5	water	SURF
2.0	water	CRISP
2.2	water	SURF
2.5	water	SURF
3.0	water	SURF
3.0	10^{-3}M KCl solution	SURF
3.0	0.1M KCl solution	SURF
3.0	1M KCl solution	SURF

Table 6.2.1. Systems studied (and reflectometer used) in neutron reflectometry experiments

Full kinematic approximation analysis of all the data obtained was possible, with the exception of surface concentrations of 2.2 and 2.5mg m^{-2} on water. Incorrect instrumental alignment prevented such analysis in these cases and this will be discussed in section 6.3.6.

6.3. WATER SUBPHASE

6.3.1. REFLECTIVITY DATA

Examples of the reflectivity curves obtained at surface concentrations of 1.0, 1.5, 2.0 and 3.0mg m^{-2} are given in figures 6.3.1 to 6.3.6. A general discussion of the characteristics pertinent to all of the profiles will initially be given.

In all cases, the reflectivity is observed to fall off sharply with increasing scattering vector, Q (section 2.2.1), reaching the incoherent background at $Q \approx 0.20 - 0.25 Å^{-1}$ (for D_2O subphases) and $Q \approx 0.10 Å^{-1}$ (for NRW subphases). The higher background reflectivity observed for the 2.0mg m^{-2} data set is an artefact of the reflectometer used, CRISP, which has a poorer resolution, and therefore higher background reflectivity than SURF, on which the remaining data was recorded. It is also observed that the background occurs at a higher reflectivity for a NRW subphase than for D_2O. Such background reflectivity can be over three times greater for NRW compared to that for D_2O and largely arises from the high incoherent scattering cross-section of the hydrogen nuclei found in NRW.

The surface concentration dependence on reflectivity is shown in figures 6.3.1 to 6.3.4. The reflectivity profile for the fully hydrogenous polymer, HPMMA-Q(H)P4VP is given in figure 6.3.1, along with an expanded region at intermediate values of Q (figure 6.3.2). Data obtained on a clean D_2O surface are included for comparison.

Throughout the Q range (most noticeable in the region highlighted in figure 6.3.2), the addition of the hydrogenous film to the subphase is seen to depress the reflectivity. These data fall into two categories: The profiles recorded for surface concentrations of 1.0, 1.5 and 2.0mg m^{-2} appear to be relatively coincident, whereas increasing the polymer surface concentration to 3.0mg m^{-2} results in a further depression in reflectivity. Such an overall decrease in reflectivity is indicative of a reduction in the deuterium content of the near-surface region. This is consistent with the increasing quantity of hydrogenous polymer spread upon the subphase.

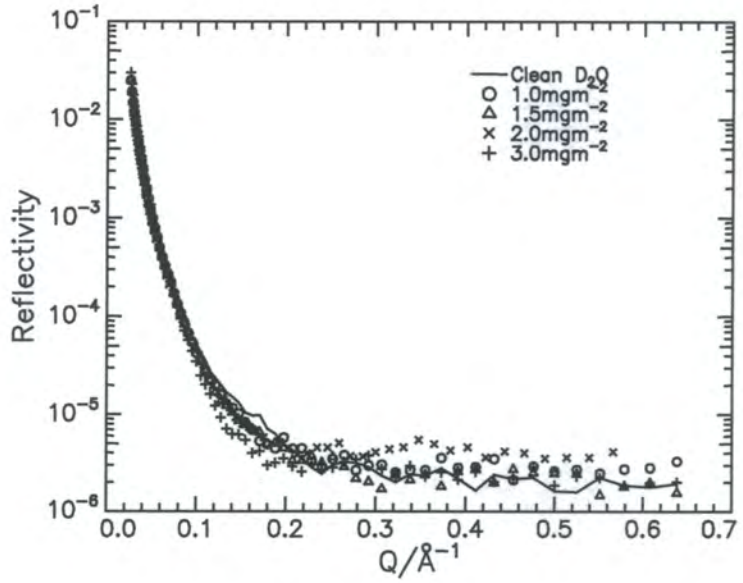

Figure 6.3.1. Reflectivity profiles for HPMMA-Q(H)P4VP on D_2O

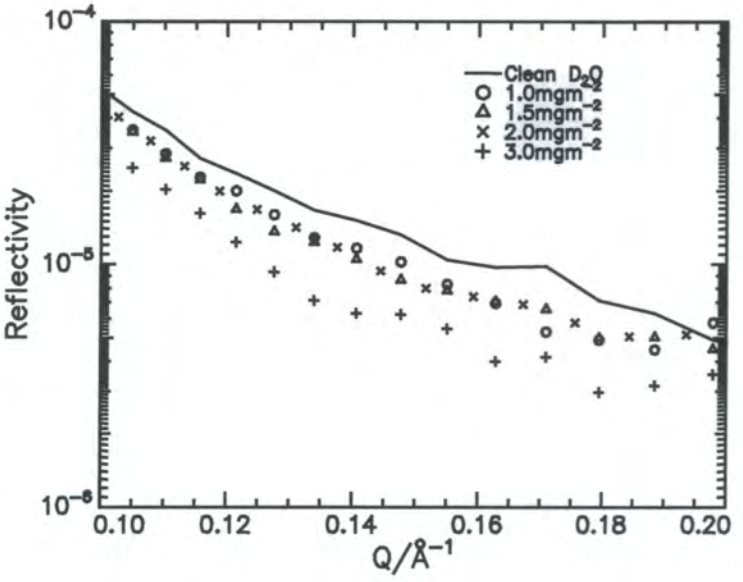

Figure 6.3.2. Expansion of the Q range $0.10 \leq Q/Å^{-1} \leq 0.20$ in figure 6.3.1

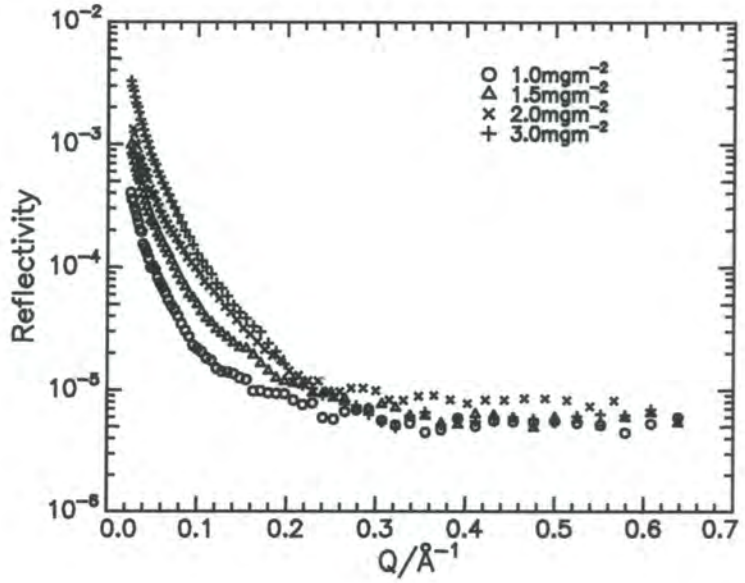

Figure 6.3.3. Reflectivity profiles for DPMMA-Q(D)P4VP on NRW

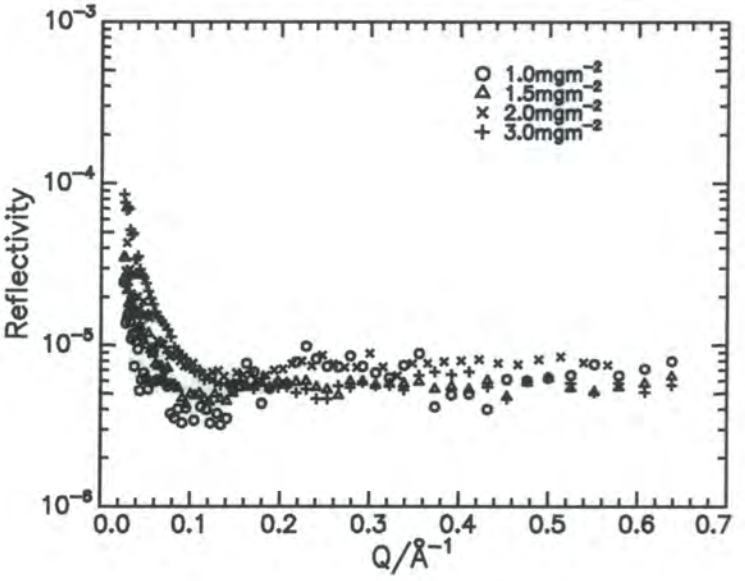

Figure 6.3.4. Reflectivity profiles for HPMMA-Q(D)P4VP on NRW

Two sets of reflectivity curves obtained on NRW are presented, DPMMA-Q(D)P4VP on NRW (figure 6.3.3) and HPMMA-Q(D)P4VP on NRW (figure 6.3.4). For both sets of data, the reflectivity increases with increasing surface concentration, consistent with the increased quantity of deuterated material present. This also explains the higher reflectivity recorded for the fully deuterated (in comparison to the partially deuterated) species. The deuterated Q(D)P4VP block contains an average of only 450 deuterium nuclei per polymer chain, compared to 3520 per DPMMA chain (and therefore 3970 for the fully deuterated system). Such data for HPMMA-Q(D)P4VP is therefore highly scattered with relatively large errors. A further feature of the reflectivity profiles (especially those of low surface concentration) is the occurrence of a minimum occurring at $Q \approx 0.1 Å^{-1}$. It has been suggested that this is due to inelastic scattering, although experiments to investigate this phenomenon further failed to yield any definite conclusion.[1]

To compare the reflectivity curves obtained by the differing polymers, data obtained at a surface concentration of 3.0mg m^{-2} is presented for all runs on D_2O (figure 6.3.5) and NRW (figure 6.3.6). The reflectivity curves on D_2O lie both above (D-H) and below (H-H and H-D) the curve recorded for clean D_2O. This is again indicative of the quantity of deuterated material present at the air-water interface. A film of the polymer containing a DPMMA block has a large scattering length density, which has the effect of increasing reflectivity at the interface. However, this result is surprising, as the calculated scattering length density of the polymer is less than that of D_2O. Conversely, the polymers with HPMMA blocks decrease reflectivity. For HPMMA-Q(D)P4VP, the behaviour of the HPMMA block of dominates that of the DP4VP block, resulting in the reduced reflectivity observed for this system. The observation that the H-H and H-D curves overlay almost perfectly is again an indication of the fact that the DP4VP block contributes very little to the overall reflectivity. This is also outlined by the curves on NRW (figure 6.3.6). Here, the reflectivity observed for D-H and D-D is substantially greater than that of H-D, the discrepancy being up to an order and a half of magnitude at the lowest Q explored.

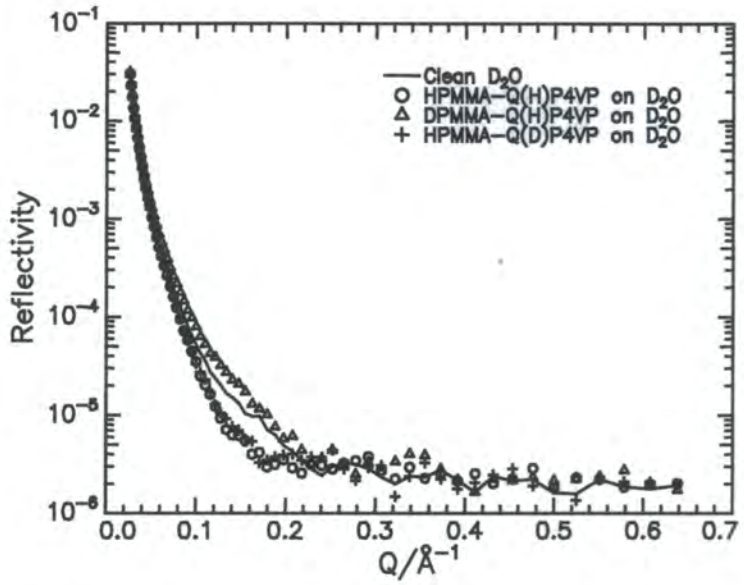

Figure 6.3.5. Reflectivity profiles for three contrasts on D_2O, Γ_s = 3.0mg m^{-2} (symbols) and clean D_2O (line)

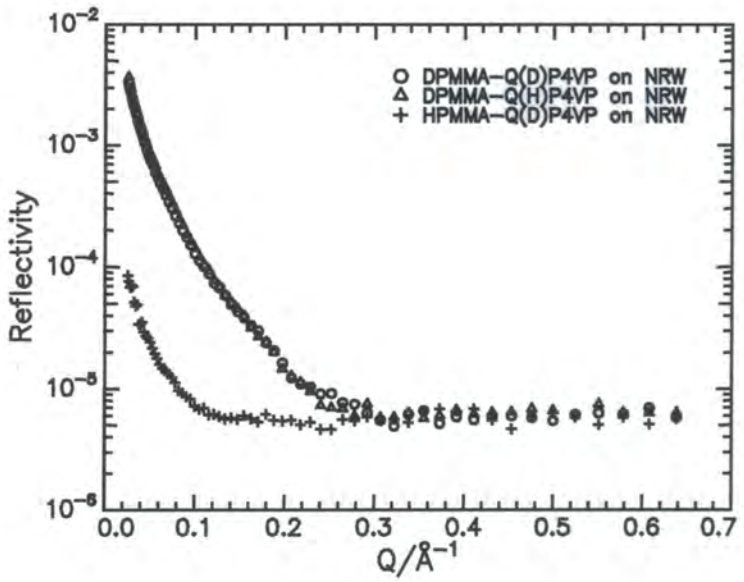

Figure 6.3.6. Reflectivity profiles for three contrasts on NRW, Γ_s = 3.0mg m^{-2}

6.3.2. Discussion

The experimental data presented in figure 6.3.1 show that the addition of a hydrogenous polymer layer to a D_2O subphase has the effect of depressing reflectivity. Such an effect results from both the reduction in scattering length density and the overall broadening of the interfacial region. However, the reflectivity does not decrease uniformly with decreasing scattering length density, the important parameter being the difference between the scattering length densities of the bare and the film-covered surfaces. The reflectivity can be expressed in the following terms:

$$R(Q) = \frac{16\pi^2}{Q^4}\left(\Delta\rho^2 - 4\rho_d(\Delta\rho - \rho_d)\sin^2(Qd/2)\right) \qquad \textbf{Equation 6.3.1}$$

Where $\Delta\rho$ is the difference in scattering length density of air and the subphase (6.35×10^{-6} Å^{-2} in the case of air - D_2O, approximately zero in the case of air – NRW). ρ_d and d are the scattering length density and thickness of the surface layer respectively. This equation can be simplified for the case when $Q = \pi/d$:

$$R(Q) = \frac{16\pi^2}{Q^4}(2\rho_d - \Delta\rho)^2 \qquad \textbf{Equation 6.3.2}$$

From equation 6.3.2, it is clear that the minimum reflectivity occurs when the term in parentheses is as small as possible. For a D_2O subphase, this occurs when ρ_d = 3.175×10^{-6} Å^{-2} (half the scattering length density of D_2O). Figure 6.3.7 shows a series of simulated reflectivity profiles (with no incoherent background) for films of thickness 20Å (approximately the thickness of a PMMA monolayer[2] at the surface concentration studied here) and varying scattering length densities spread on D_2O. It can clearly be seen that reflectivity decreases to a minimum when $\rho_d = 3.175 \times 10^{-6}$ Å^{-2}. Due to the symmetry inherent in the above expression, a further increase in ρ_d causes reflectivity to increase. A film of $\rho_d = 4.175 \times 10^{-6}$ Å^{-2} gives an identical simulated profile to one of $\rho_d = 2.175 \times 10^{-6}$ Å^{-2} and, likewise, a film of ρ_d = 5.175×10^{-6} Å^{-2} gives an identical profile to one of $\rho_d = 1.175 \times 10^{-6}$ Å^{-2}.

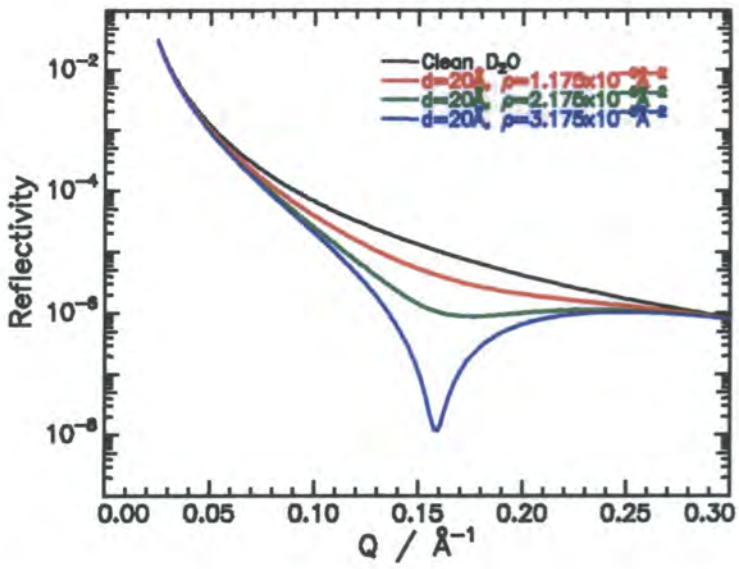

Figure 6.3.7. Simulated reflectivity profiles for clean D_2O (black line) and films of 20Å thickness and variable scattering length density on a D_2O subphase (coloured lines, see legend)

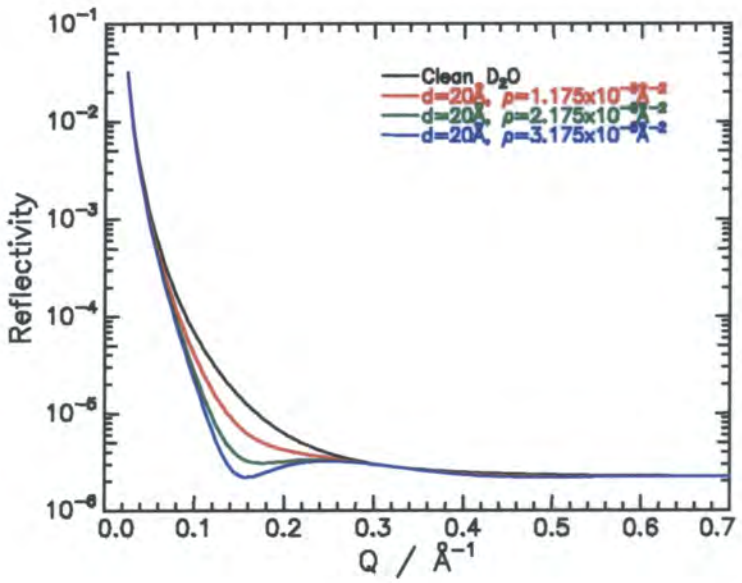

Figure 6.3.8. Simulated reflectivity profiles for clean D_2O (black line) and films of 20Å thickness and variable scattering length density on a D_2O subphase (coloured lines, see legend). Background reflectivity = 2.2×10^{-6}

It is observed that the reflectivity only passes through a minimum, rather than becoming zero, with a film of $\rho_d = 3.175x10^{-6}Å^{-2}$. This non-zero reflectivity is due to the kinematic approximation being (as the name suggests) only an approximation and not giving a precise description of the system. Using the expression $Q = \pi/d$, such a minimum is predicted to occur at $Q = 0.157Å^{-1}$ (when d = 20Å). This is confirmed by the simulated data.

The simulated reflectivity profiles obtained for the above films when a background reflectivity of $2.2x10^{-6}$ (typical in the reflectivity measurements performed) is included are shown in figure 6.3.8. A similar pattern is again observed, reflectivity being depressed with increased scattering length density up to a value of $\rho_d = 3.175x10^{-6}Å^{-2}$. A minimum in reflectivity is again observable at $Q = 0.157Å^{-1}$.

Simulations showing the effect of the incorporation of a layer with scattering length density greater than that of D_2O are given in figure 6.3.9. The reflectivity is shown to increase with scattering length, and, in every case, the reflectivity reported is greater than that of clean D_2O.

The effect of changing layer thickness is examined by the simulation shown in figure 6.3.10, profiles for films of a fixed scattering length density ($\rho_d = 4x10^{-6}Å^{-2}$) with thicknesses between 10 and 50Å being presented. An initial increase in film thickness is found to cause a reduction in the reflectivity, since $\rho_{air} < \rho_d < \rho_{D_2O}$. With thicker films, a minimum in reflectivity is observed and, for the film of 50Å thickness, two minima are observed in the Q range shown. Simulations of reflectivity profiles for the same interfacial conditions, with the addition of a background reflectivity of $2.2x10^{-6}$, are shown in figure 6.3.11. Again, a minimum is observed in the reflectivity profiles given by all but the thinnest films, such a minimum shifting to lower Q with increasing thickness. Multiple minima are again observed with the thickest films.

The above simulations can be used to explain the phenomena observed in the reflectivity profiles. For the H-H polymer on D_2O (figures 6.3.1 and 6.3.2), reflectivity decreases (albeit non-uniformly) with increasing surface concentration. Such a decrease must therefore be a result of the interfacial film becoming thicker, having higher scattering length density, or a combination of these factors. The most substantial change in the structure of the PMMA block occurs between 2.0 and $3.0mgm^{-2}$.

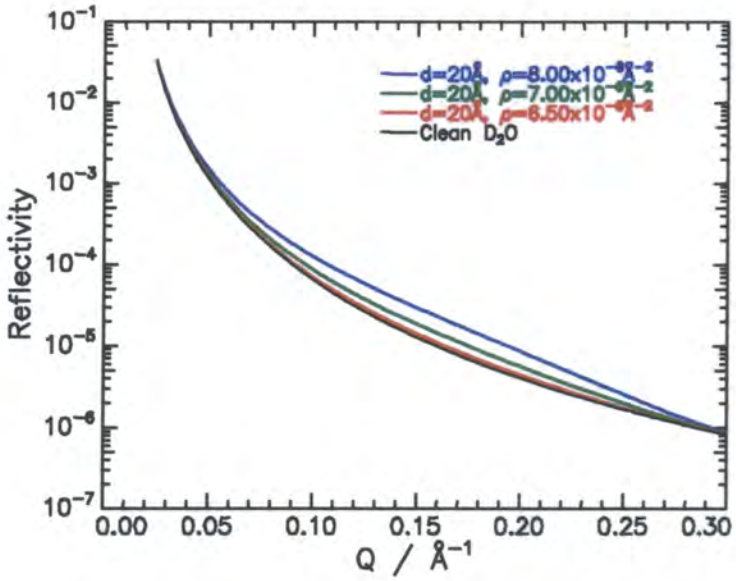

Figure 6.3.9. Simulated reflectivity profiles for clean D_2O (black line) and films of 20Å thickness and variable scattering length density (greater than that of D_2O) on a D_2O subphase (coloured lines, see legend)

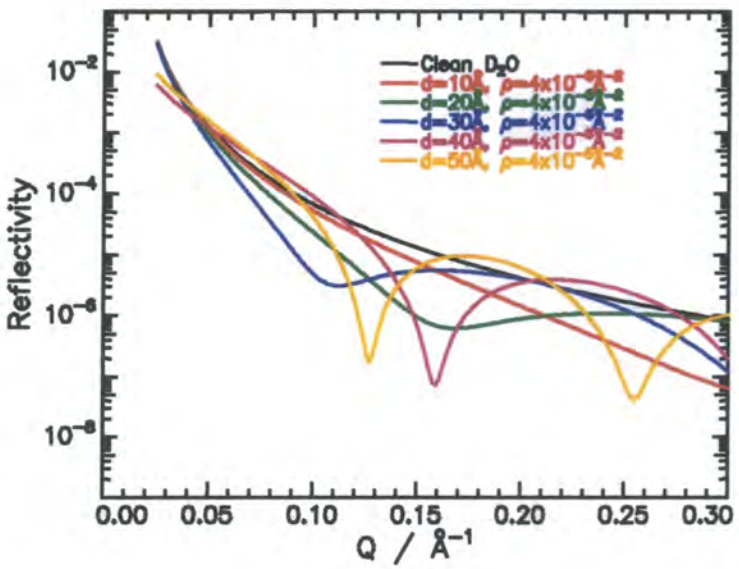

Figure 6.3.10. Simulated reflectivity profiles for clean D_2O (black line) and films with scattering length density of $4x10^{-6}Å^{-2}$ and variable thickness on a D_2O subphase (coloured lines, see legend)

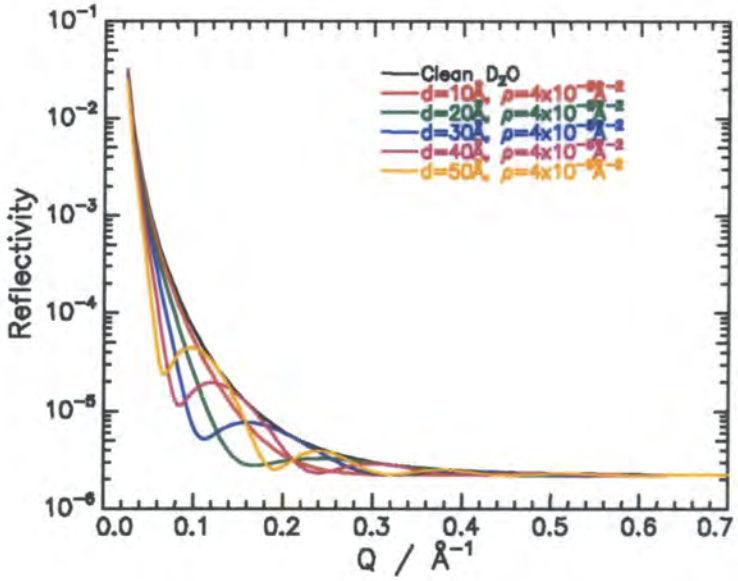

Figure 6.3.11. Simulated reflectivity profiles for clean D_2O (black line) and films with scattering length density of $4x10^{-6}Å^{-2}$ and variable thickness on a D_2O subphase (coloured lines, see legend). Background reflectivity = $2.2x10^{-6}$

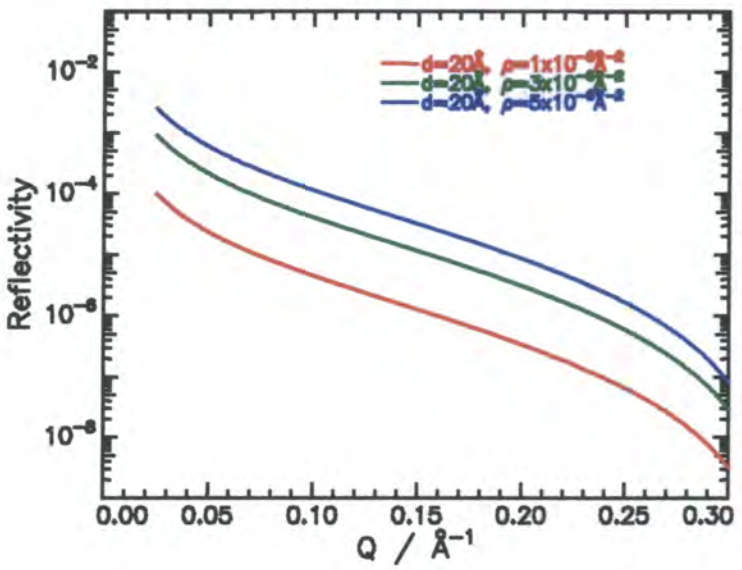

Figure 6.3.12. Simulated reflectivity profiles for films of 20Å thickness and variable scattering length density on a NRW subphase

The effect shown in figure 6.3.5, where a film of D-H exhibits an increased reflectivity from that of clean D_2O, is harder to explain. From figure 6.3.9, it intuitively seems that such a rise should be caused by an increase in scattering length density. However, both blocks of the copolymer have scattering length densities less than that of D_2O.

Films spread on NRW behave in a manner distinct from those on D_2O, due to the scattering length of air and the subphase both being zero. This renders the term $\Delta\rho$ in equations 6.3.1 and 6.3.2 also equal to zero, resulting in the reflectivity scaling more directly with scattering length density. This is shown by figure 6.3.12, where reflectivity simulations of films of thickness 20Å with varying scattering length densities are given. Unlike the simulations on D_2O, reflectivity increases with scattering length density and all three profiles are of identical shapes, offset from one another along the reflectivity axis. Reflectivity profiles for the same films incorporating a typical background reflectivity of $5.5x10^{-6}$ are presented in figure 6.3.13.

Figure 6.3.14 shows the trend observed with films of a fixed scattering length density ($4x10^{-6}Å^{-2}$) and variable thickness on NRW. At low Q, reflectivity increases with film thickness whereas at higher Q, a series of minima are again observed, the quantity of such minima increasing with film thickness. Again, the effect of incorporating a background reflectivity is shown (figure 6.3.15) and similar trends to those in figure 6.3.14 are observed.

Figure 6.3.3 compares the reflectivity profiles for four of the surface concentrations studied. All the profiles are of similar shapes and, comparing these to the simulations, it appears that the film thickness remains approximately constant, while the scattering length density increases.

This apparent constant film thickness over the region $1.0 < \Gamma_s < 2.0 mg\ m^{-2}$ seems to contradict results reported in chapter five. There, it was suggested that both surface pressure isotherm measurements and Brewster angle microscopy reveal an increasing film thickness in this region. However, the observation from the neutron reflectometry data only implies that there is little change in the thickness of the PMMA block. An increase in overall film thickness is more likely to be due to the

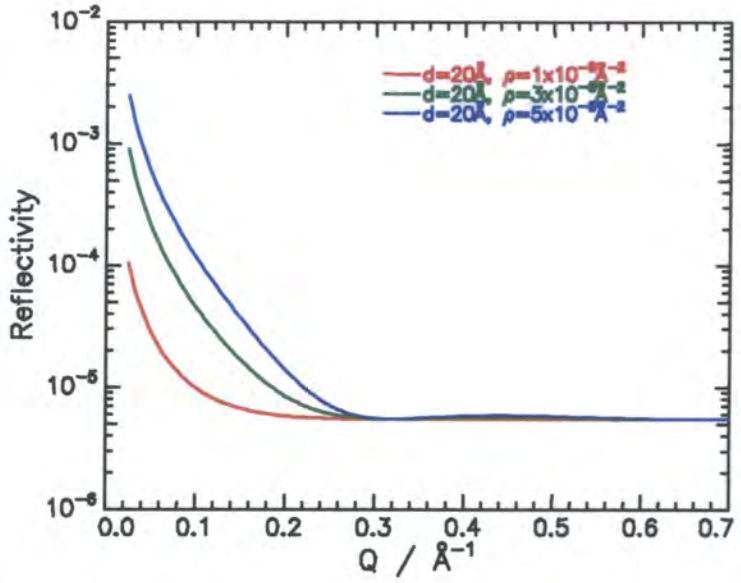

Figure 6.3.13. Simulated reflectivity profiles for films of 20Å thickness and variable scattering length density on a NRW subphase. Background reflectivity = 5.5×10^{-6}

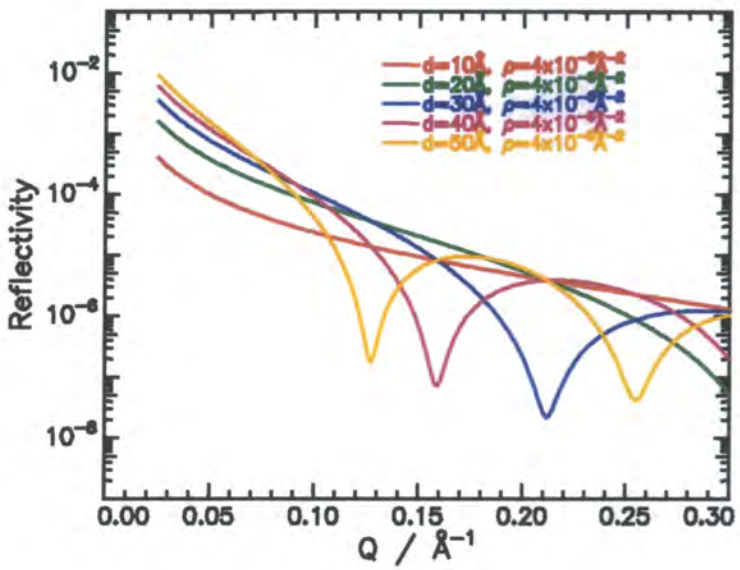

Figure 6.3.14. Simulated reflectivity profiles for films of scattering length density of 4×10^{-6}Å^{-2} and variable thickness on a NRW subphase

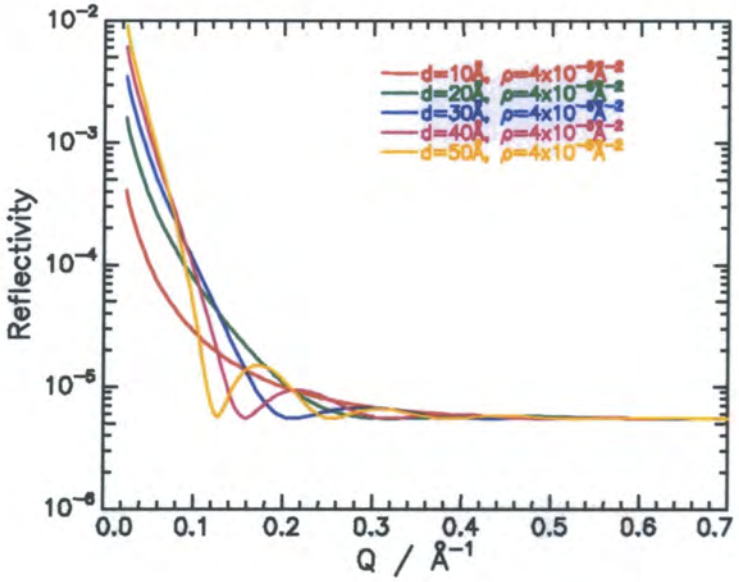

Figure 6.3.15. Simulated reflectivity profiles for films of scattering length density of $4x10^{-6}Å^{-2}$ and variable thickness on a NRW subphase. Background reflectivity = $5.5x10^{-6}$

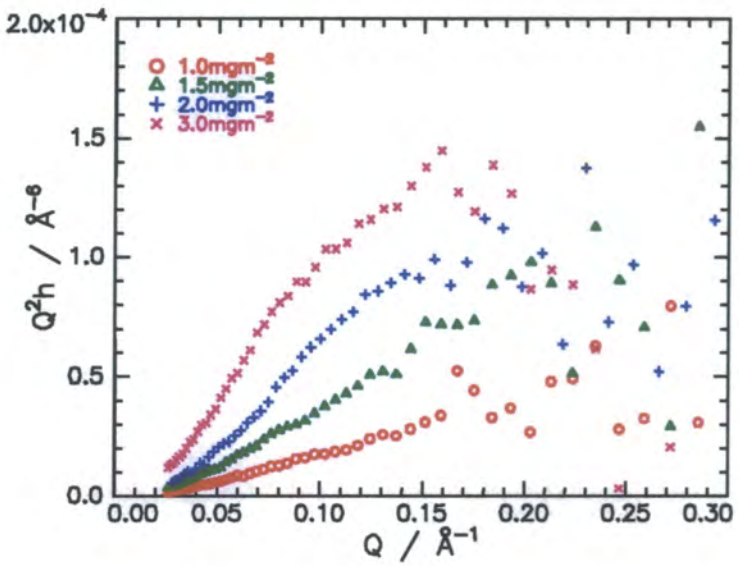

Figure 6.3.16. PMMA self partial structure factors

QP4VP chains extending into the liquid subphase. The reflectivity signal from these chains is dominated by that from the larger, surface-resident PMMA block. A better indication of the conformation of the QP4VP blocks may be obtained from the H-D on NRW contrast (figure 6.3.4). Here, the data, although very scattered, do seem to follow different shaped curves, implying a change in thickness of the QP4VP block and confirming the above hypothesis.

6.3.3. PARTIAL STRUCTURE FACTOR ANALYSIS: THE KINEMATIC APPROXIMATION

Analysis of neutron reflectometry data has taken place predominantly by use of the kinematic approximation[3] (section 2.2.4.2). In this section, the results obtained for the polymer surface concentrations of 1.0, 1.5, 2.0 and 3.0mg m^{-2} are presented. Each of the six partial structure factors is discussed in turn:

6.3.3.1. The PMMA Self Partial Structure Factor

The self partial structure factors obtained for the PMMA block of the copolymer are shown in figure 6.3.16. As expected, all the partial structure factors have values greater than zero, the property arising from the relationship between the partial structure factor and the number density of a species, n:

$$h_{ii}(Q) = |n_{ii}(Q)|^2 \qquad \textbf{Equation 6.3.3.}$$

All of the partial structure factors show an initial increase in Q^2h with increasing Q, the gradient of this rise increasing with surface concentration. The partial structure factors all reach a maximum in Q^2h, the value of Q at which the maximum occurs decreases with increasing surface concentration, from $Q \approx 0.24 Å^{-1}$ for Γ_s = 1.0mg m^{-2} to $Q \approx 0.16 Å^{-1}$ for Γ_s = 3.0mg m^{-2}. The values of Q^2h are subject to large errors at high Q and an investigation into the extent of such errors has been undertaken for some of the work on salt solutions (section 6.4.3.1).

A number of models have been utilised to fit the partial structure factors. Initially, only simple models such as the single uniform layer, single Gaussian layer, and single parabolic layer were used. A more complex model, a uniform layer with a parabolic decay ('uniform-parabolic') was later utilised. The expressions for a single uniform layer are given by equation 2.2.3 and those for a single Gaussian layers have been previously reported.[4] For the uniform-parabolic model, a typical profile is given in figure 6.3.17 and the density profile is given by:

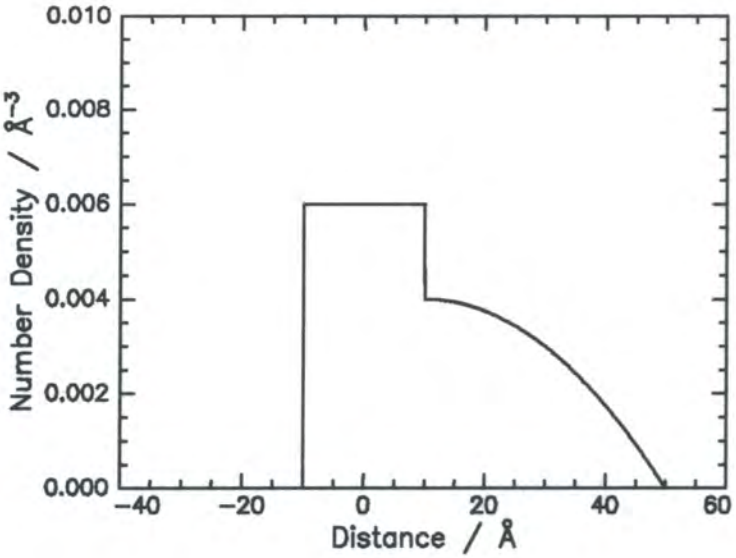

Figure 6.3.17. Number density profile for a uniform layer with a parabolic tail. Uniform layer thickness = 20Å, number density = 6 x 10^{-3} Å^{-3}. Parabolic layer thickness = 40Å, number density = 4 x 10^{-3} Å^{-3}

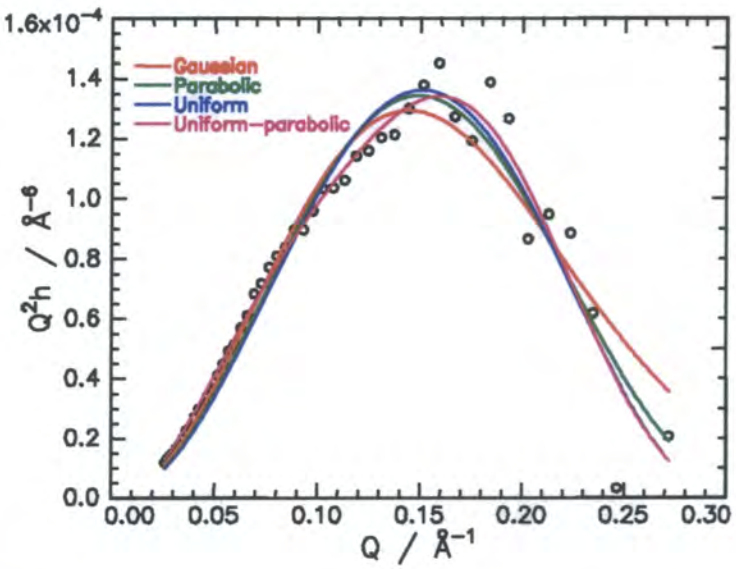

Figure 6.3.18. Comparison of fits (obtained using various models) to the PMMA self partial structure factor. Γ_s = 3.0mg m^{-2}

$$n_i(z) = 0 \qquad \text{for } z < -d_1 - d_2 \text{ and } z > 0$$

$$n_i(z) = n_1 \qquad \text{for } -d_1 < z < 0$$

$$n_i(z) = n_2\left[1 - \frac{(z-d_1)^2}{d_2}\right] \qquad \text{for } -d_1 - d_2 < z < -d_1 \qquad \textbf{Equation 6.3.4.}$$

The Fourier transform of $n_i(z)$ is:

$$n_i(Q) = \frac{in_1}{Q} - \frac{in_1}{Q}\exp(iQd_1) + \frac{in_2}{Q^3 d_2^2}\exp(iQd_1) - \frac{2in_2}{Q^3 d_2^2}\exp[iQ(d_1+d_2)] - \frac{2n_2}{Q^2 d_2}\exp[iQ(d_1+d_2)]$$

Equation 6.3.5.

Giving the partial structure factor expression:

$$Q^2 h_{ii}(Q) = 2n_1^2 + n_2^2 - 2n_1 n_2 + 2n_1\cos(Qd_1)(n_2 - n_1) + \frac{1}{Q^4 d_2^4}\left\{\begin{array}{l} 8n_2^2(1+Q^2 d_2^2) + [\cos(Qd_2) + Qd_2\sin(Qd_2)][4n_1 n_2 Q^2 d_2^2 - 4n_2^2 Q^2 d^2 - 8n_2^2] \\ + 4n_1 n_2 Q^2 d_2^2[\cos(Qd_1) - \cos(Q(d_1+d_2)) - Qd_2\sin(Q(d_1+d_2)) - 1] \end{array}\right\}$$

Equation 6.3.6.

In the above expressions, d_1 and d_2 are the layer thicknesses and n_1 and n_2 the number densities of the uniform and parabolic layers respectively. The partial structure factor expression for a single parabolic layer can be obtained by substituting $n_1 = 0$ into equations 6.3.4 to 6.3.6.

All four layer models appear to give adequate fits to the data. For comparison, examples of the fits obtained for the surface concentration of 3.0mg m^{-2} are given in figure 6.3.18 and the parameters extracted from such fits are given in table 6.3.1.

From figure 6.3.18, it can be seen that there is little to distinguish the fits obtained. In fact, all fits are seen to be of good quality when the errors on the data points are considered (see section 6.4.3.1). For low values of Q (< 0.07Å^{-1}), the data are best fitted by a single Gaussian layer model. In this region, the single uniform and single parabolic layer models give values of Q^2h which are slightly too low, whereas the uniform-parabolic model gives values which are too large. However, both the data

range $0.10 < Q / Å^{-1} < 0.15$ and the maximum in the partial structure factor at $Q \approx 0.16Å^{-1}$ are both best defined by a uniform-parabolic layer model. This is unsurprising considering the flexibility of the model, which has the ability to encompass the single layer models.

(a) Γ_s = 1.0mg m^{-2}

Model	d_1 / Å	n_1 / 10^{-3} Å^{-3}	d_2 / Å	n_2 / 10^{-3} Å^{-3}
Gaussian	14.5 ± 0.8	3.85 ± 0.19	-	-
Parabolic	10.8 ± 0.2	3.35 ± 0.04	-	-
Uniform	16.4 ± 0.8	2.93 ± 0.13	-	-
Unif – Para	14.4 ± 0.9	3.41 ± 0.15	46.5 ± 6.5	0.35 ± 0.15

(b) Γ_s = 1.5mg m^{-2}

Model	d_1 / Å	n_1 / 10^{-3} Å^{-3}	d_2 / Å	n_2 / 10^{-3} Å^{-3}
Gaussian	12.0 ± 0.4	6.31 ± 0.14	-	-
Parabolic	9.1 ± 0.2	5.50 ± 0.06	-	-
Uniform	13.9 ± 0.8	4.73 ± 0.10	-	-
Unif – Para	11.2 ± 1.9	5.70 ± 0.80	30.7 ± 4.7	0.47 ± 0.15

(c) Γ_s = 2.0mg m^{-2}

Model	d_1 / Å	n_1 / 10^{-3} Å^{-3}	d_2 / Å	n_2 / 10^{-3} Å^{-3}
Gaussian	15.9 ± 0.3	6.64 ± 0.04	-	-
Parabolic	12.0 ± 0.2	5.79 ± 0.04	-	-
Uniform	18.2 ± 0.3	5.01 ± 0.04	-	-
Unif – Para	17.1 ± 0.6	5.24 ± 0.10	14.0 ± 3.6	0.35 ± 0.12

(d) Γ_s = 3.0mg m^{-2}

Model	d_1 / Å	n_1 / 10^{-3} Å^{-3}	d_2 / Å	n_2 / 10^{-3} Å^{-3}
Gaussian	19.6 ± 0.2	7.48 ± 0.05	-	-
Parabolic	14.0 ± 0.2	6.64 ± 0.06	-	-
Uniform	20.9 ± 0.2	5.83 ± 0.05	-	-
Unif – Para	19.6 ± 0.5	6.25 ± 0.08	30.5 ± 2.9	0.72 ± 0.10

Table 6.3.1. Parameters of fits to the PMMA self partial structure factors

The profiles obtained from the fitted parameters are plotted in figures 6.3.19a-d. It is immediately clear than in all cases, the profiles obtained are highly similar. The obvious exception to this is the uniform-parabolic model, where the uniform layer is thicker and of lower density than that obtained by the single uniform layer model (with no parabolic tail). The parabolic 'tail' is of extremely small number density and extends substantially into the subphase.

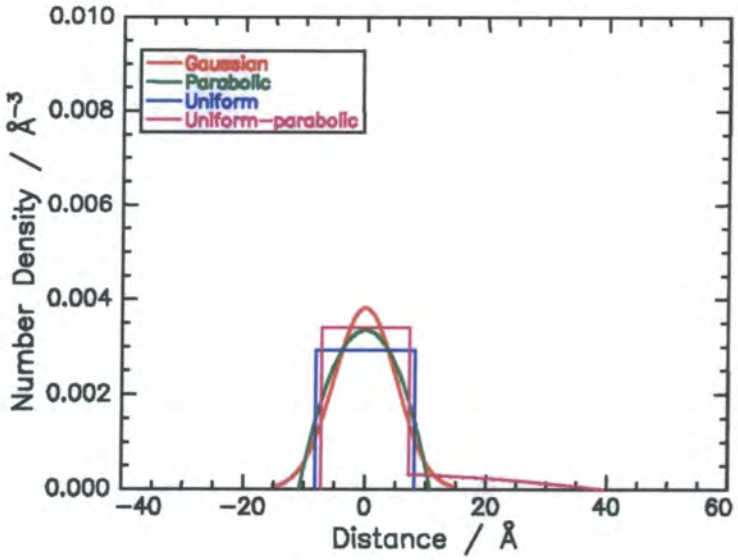

Figure 6.3.19a. Comparison between the number density profiles of PMMA obtained by various layer models (see legend). $\Gamma_s = 1.0\text{mg m}^{-2}$

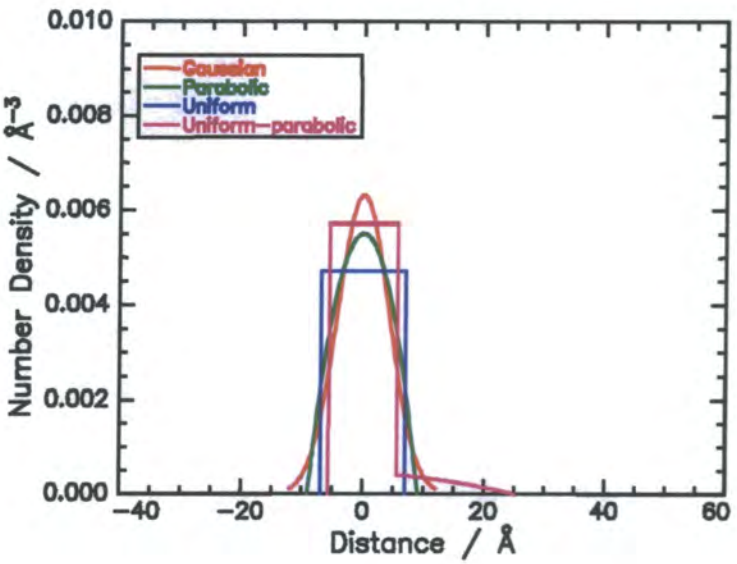

Figure 6.3.19b. Comparison between the number density profiles of PMMA obtained by various layer models (see legend). $\Gamma_s = 1.5\text{mg m}^{-2}$

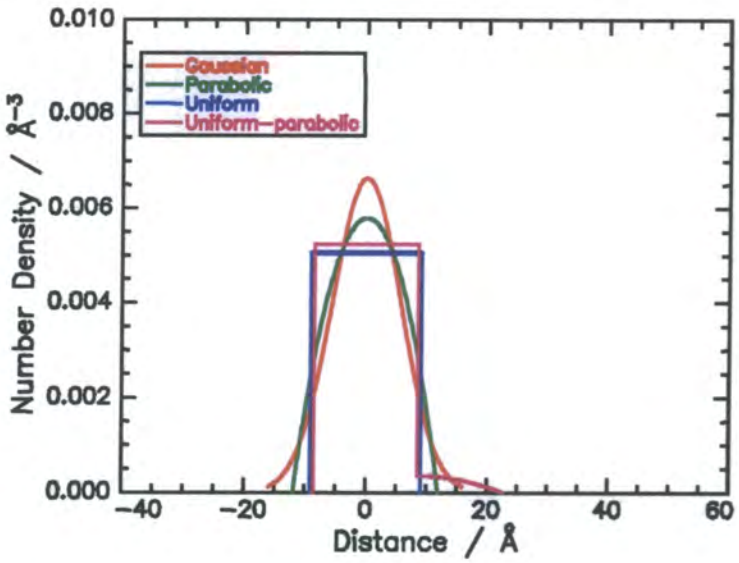

Figure 6.3.19c. Comparison between the number density profiles of PMMA obtained by various layer models (see legend). $\Gamma_s = 2.0$mg m^{-2}

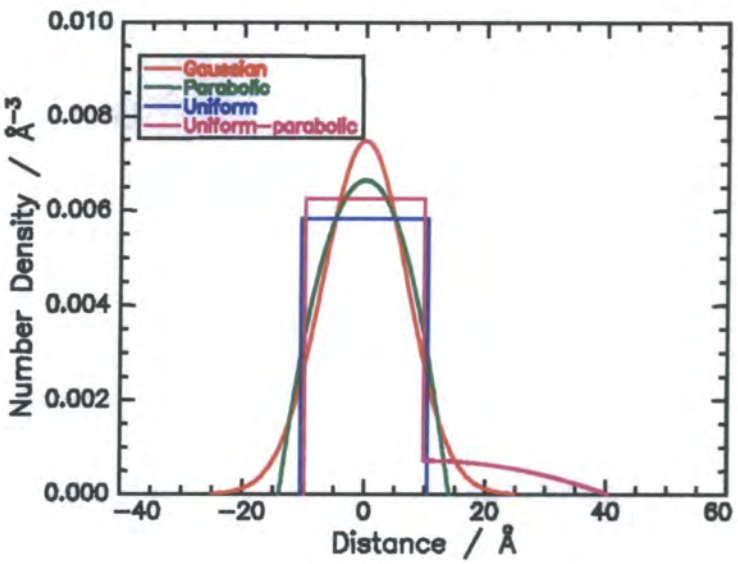

Figure 6.3.19d. Comparison between the number density profiles of PMMA obtained by various layer models (see legend). $\Gamma_s = 3.0$mg m^{-2}

Due to the similarity of the fits, it is very difficult to distinguish which describes the system most adequately. To assist in this, two methods are used. Firstly, the χ^2 ('goodness' of fit) parameters are compared. Secondly, the surface concentration of PMMA can be calculated from the parameters obtained from the fitting procedure.

Model	1.0mg m^{-2}	1.5mg m^{-2}	2.0mg m^{-2}	3.0mg m^{-2}
Gaussian	1.05×10^{-11}	7.78×10^{-12}	2.27×10^{-11}	3.36×10^{-11}
Parabolic	1.05×10^{-11}	8.79×10^{-12}	2.35×10^{-11}	4.37×10^{-11}
Uniform	1.05×10^{-11}	8.16×10^{-12}	2.88×10^{-11}	4.85×10^{-11}
Unif – Para	9.66×10^{-12}	4.48×10^{-12}	1.96×10^{-11}	1.64×10^{-11}

Table 6.3.2. Values of χ^2 for fits to PMMA self partial structure factors

Table 6.3.2 gives the values of χ^2 obtained for fits over such a range. The values obtained for the uniform-parabolic layer model are, in every case, lower than those for any of the single layer models. However, these values are not directly comparable with those from the other three models, due to the varying number of parameters being 'floated' during the course of a fit. For the three single layer models, only two parameters (thickness and number density) are fitted, whereas for the uniform-parabolic model, there are two thicknesses and densities, giving four parameters in total. This results in a closer (but not necessarily more realistic) fit of the data.

The Gaussian, parabolic and uniform layer models are now compared. At the lowest surface concentration, these models result in a fit of equal quality, the χ^2 values being identical to three significant figures. However, at higher surface concentrations the results are quite distinct, a Gaussian distribution clearly best describing the data.

As previously stated, a further check on the accuracy of any fit obtained can be given by calculating the surface concentration of PMMA from the parameters obtained by the fitting procedure.

The expressions used to calculate PMMA surface concentration, $\Gamma_{s,PMMA}$, for each of the layer models are:

Single uniform layer: $$\Gamma_{s,PMMA} = \frac{10^{23} Mn_1 d_1}{N_A}$$ **Equation 6.3.7.**

Single Gaussian layer: $$\Gamma_{s,PMMA} = \frac{10^{23} Mn_1 d_1 \sqrt{\pi}}{2N_A}$$ **Equation 6.3.8.**

Single parabolic layer: $$\Gamma_{s,PMMA} = \frac{4x10^{23} Mn_1 d_1}{3N_A}$$ **Equation 6.3.9.**

Uniform – parabolic layer: $$\Gamma_{s,PMMA} = \frac{10^{23} M}{N_A}\left(n_1 d_1 + \frac{2}{3} n_2 d_2\right)$$ **Equation 6.3.10.**

Where M is the molecular weight of a monomer unit and n and d are the number density and thickness of the layers.

The PMMA surface concentrations calculated from these expressions are given in table 6.3.3, along with the predicted values (calculated assuming a polymer composition of 80.9% PMMA, obtained from elemental analysis), and the discrepancy between these two values.

	Polymer surface concentration / mg m^{-2}			
	1.0	1.5	2.0	3.0
Model	**PMMA surface concentration / mg m^{-2}**			
Predicted	*0.81*	*1.21*	*1.62*	*2.43*
Gaussian	0.88 (8.8%)	1.21 (0.1%)	1.69 (4.6%)	2.35 (2.9%)
Parabolic	0.87 (8.0%)	1.20 (1.2%)	1.67 (3.2%)	2.24 (7.5%)
Uniform	0.87 (7.3%)	1.19 (2.4%)	1.66 (2.6%)	2.20 (9.3%)
Uniform-parabolic	1.08 (27.2%)	1.34 (10.1%)	1.68 (4.1%)	2.48 (2.2%)

Table 6.3.3. Calculated PMMA surface concentrations (with percentage errors from the theoretical values) for fits of the PMMA partial structure factor

At the two lowest surface concentrations, the closest correlation between the calculated and theoretical PMMA surface concentrations is given by the three single layer models, which report very similar values. The uniform-parabolic model significantly overestimates the quantity of polymer on the liquid surface and therefore the validity of such a fit is highly questionable. At 2.0mg m^{-2}, all four models yield approximately the same result and at the highest concentration, the Gaussian and uniform-parabolic models provide the closest value to the theoretical.

Of interest are the values of PMMA surface concentration which are greater than the theoretical value, the effect being greatest at the lowest surface concentration, where all three single layer models overestimate the PMMA surface concentration by approximately 8%. It has previously been reported[5] that polymer has been 'lost' when spread upon a liquid surface, but in this case the opposite effect is occurring, in fact, matter is effectively being gained!

At the highest surface concentration, the values obtained by the three single layer models indicate that some polymer is missing from the surface, although the discrepancy is not large and could be said to be within experimental error. Any real effect is suggested to be due to some of the PMMA being forced away from the liquid surface and coiling into either the air or the subphase. As PMMA is hydrophobic, it is highly unlikely that the chains penetrate or dissolve into the subphase to any significant extent.

From consideration of the above results, a single Gaussian layer appears to give the best fit to the PMMA partial structure factors. This, and other single layer models give fits of adequate quality and it is therefore not necessary to use more complex models. Although these multi-layer expressions do give slightly better fits to the data, this is simply because of over-parameterisation of the system. The uniform-parabolic layer described above has a parabolic tail of very low number density, implying that such fits are tending towards a single layer model. Furthermore, a number of the surface concentrations extracted from such fits are erroneous, indicating the model does not describe the polymer distribution accurately. Further models, for example double uniform, triple uniform and double Gaussian layers[6] have also been used in an attempt to fit the PMMA partial structure factor. Again, the improvement of fit obtained was insufficient to justify the incorporation of the extra layer or layers.

The data is therefore best described by a single layer model and, of the expressions used, the single Gaussian model gives the best fit to data. In addition, such a model is more physically realistic than, for example, the single uniform layer. A Gaussian distribution has been adopted to describe the organisation of the PMMA block.

6.3.3.2. The QP4VP Self Partial Structure Factor

The self partial structure factors obtained for the hydrophilic block of the copolymer, QP4VP, are given in figure 6.3.20. It is immediately obvious that the data are highly scattered, this being a direct result of the low reflectivity produced by the contrast of HPMMA-Q(D)P4VP on NRW (figure 6.3.6). For this reason, the data are only presented up to Q = 0.15Å^{-1}, as at higher Q, the reflectivity is inseparable from the background.

The data for the surface concentration of 3.0mg m^{-2} shows a definite trend, increasing to a maximum (albeit very small) value of Q^2h at Q ≈ 0.08Å^{-1}. The partial structure factors of the lowest three concentrations are highly scattered and it is difficult to discern any definite trend.

Because of this scatter, fitting the QP4VP self partial structure factors poses more problems than that of the PMMA terms discussed above. Initially, the single layer models discussed above were used to fit the data. Following this, more complex models were examined which again reduced the χ^2 values of the fits obtained, but did not necessarily result in better fits. Such data is liable to be fitted by any model with a large number of variables and therefore to avoid unnecessary complication, it was decided to limit these fits to the three single layer models used previously. An example of the fits obtainable is given in figure 6.3.21. Here, the QP4VP self partial structure factors for Γ_s = 3.0mg m^{-2} are given, overlayed with the fits obtained by single uniform, Gaussian and parabolic layers. The parameters extracted from such fits are given in table 6.3.4.

(a) Γ_s = 1.0mg m^{-2}

Model	d_1 / Å	n_1 / 10^{-4} Å^{-3}
Gaussian	23.5 ± 2.0	8.99 ± 0.24
Parabolic	17.4 ± 1.5	7.88 ± 0.33
Uniform	35.2 ± 1.9	6.07 ± 0.19

(b) Γ_s = 1.5mg m^{-2}

Model	d_1 / Å	n_1 / 10^{-4} Å^{-3}
Gaussian	28.6 ± 2.6	7.03 ± 0.36
Parabolic	19.0 ± 0.9	6.49 ± 0.17
Uniform	29.7 ± 2.7	5.65 ± 0.26

(c) Γ_s = 2.0mg m^{-2}

Model	d_1 / Å	n_1 / 10^{-4} Å^{-3}
Gaussian	27.4 ± 3.3	6.94 ± 0.43
Parabolic	30.7 ± 2.2	6.39 ± 0.37
Uniform	31.3 ± 3.2	5.28 ± 0.32

(d) Γ_s = 3.0mg m^{-2}

Model	d_1 / Å	n_1 / 10^{-4} Å^{-3}
Gaussian	23.5 ± 2.1	8.88 ± 0.23
Parabolic	27.7 ± 1.2	8.40 ± 0.23
Uniform	41.8 ± 1.6	7.37 ± 0.20

Table 6.3.4. Parameters of fits to the QP4VP self partial structure factors

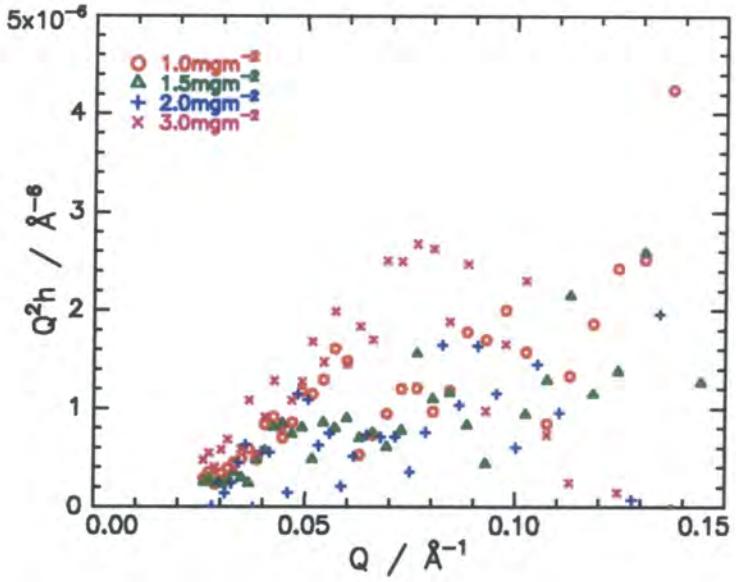

Figure 6.3.20. QP4VP self partial structure factors

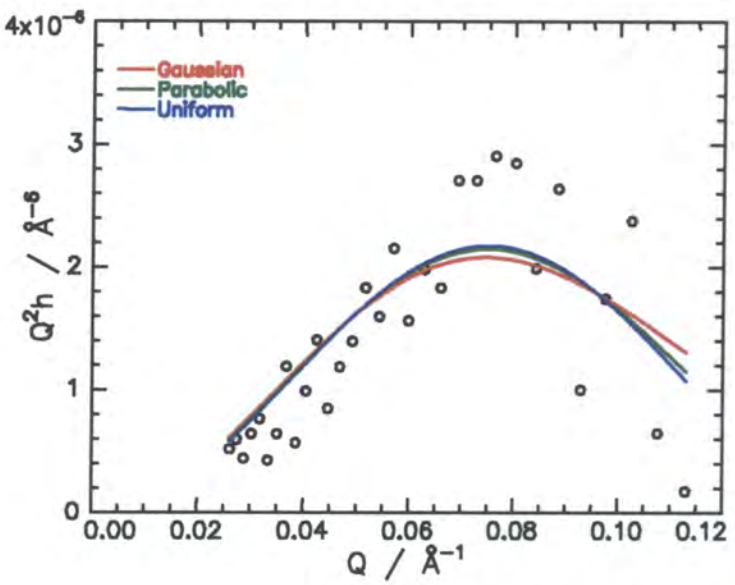

Figure 6.3.21. Comparison of fits (obtained using varying models) to the QP4VP self partial structure factor. $\Gamma_s = 3.0 mgm^{-2}$

As with the PMMA self partial structure factors, the fits are virtually indistinguishable by eye and other factors need to be considered to determine which model is the most appropriate. This can again be done by comparing the χ^2 values obtained from the fits (table 6.3.5). Although the χ^2 values obtained at any specific surface concentration are very similar, in every case it is the parabolic model which reports the lowest value of χ^2.

Model	1.0mg m^{-2}	1.5mg m^{-2}	2.0mg m^{-2}	3.0mg m^{-2}
Gaussian	1.500×10^{-13}	3.775×10^{-13}	1.751×10^{-13}	2.613×10^{-13}
Parabolic	1.499×10^{-13}	3.763×10^{-13}	1.309×10^{-13}	2.324×10^{-13}
Uniform	1.536×10^{-13}	3.864×10^{-13}	1.512×10^{-13}	2.402×10^{-13}

Table 6.3.5. Values of χ^2 for fits to QP4VP self partial structure factors

It is therefore this model which is adopted to describe the conformation of the QP4VP block. A further factor promoting the choice of the parabolic model is that it is such a model that is obtained from the scaling theories of Milner, Witten and Cates[7] for uncharged polymers and Misra[8] and others for polyelectrolyte brushes. The comparison of these results with such theories is presented in section 6.3.3.8.

Surface concentrations of QP4VP can be obtained from equation 6.3.9. However, due to the polyelectrolyte chains extending deep (up to 30Å) into the subphase, the results may be subject to considerable error. Nevertheless, the data obtained are presented in table 6.3.6.

	Polymer surface concentration / mg m^{-2}			
	1.0	1.5	2.0	3.0
	QP4VP surface concentration / mg m^{-2}			
Predicted	*0.19*	*0.29*	*0.38*	*0.57*
Calculated	0.42 (121%)	0.38 (34%)	0.60 (58%)	0.75 (32%)

Table 6.3.6. Calculated QP4VP surface concentrations (with percentage errors from the theoretical values) for fits of the QP4VP partial structure factor obtained using a single parabolic layer model

Clearly, the calculated surface concentrations compare very poorly indeed to the theoretical values obtained using knowledge of the polymer composition. The surface concentration calculated from reflectivity data does increase as the spread

surface concentration increases, but in all cases, the value from reflectivity is vastly overestimated. The most accurate value is that at the highest surface concentration. The errors are due (at least partly) to the weak reflectivity recorded for the QP4VP block and the errors inherent therein. As surface concentration increases, the noise on the data decreases, manifesting itself as a more accurate value of surface concentration.

Calculating the surface concentrations from the other layer models used shows the same phenomena of vastly overestimated surface concentration values, with the discrepancies being slightly greater than those for the parabolic model. This implies that the difference between the predicted and calculated values is due to an effect more fundamental than the use of an incorrect model.

From the quality of the fits to the data and the calculated surface concentrations, it is therefore concluded that the QP4VP data is best fitted with a single parabolic layer model. With increasing surface concentration, the QP4VP chain extends into the subphase, whereas the number density of the layer shows a slight, but unsystematic change.

6.3.3.3. The Water Self Partial Structure Factor

The self partial structure factors obtained for water are presented in figure 6.3.22, where it is clear that unusual behaviour is exhibited. As Q approaches zero, the water partial structure factor should tend towards a value of $Q^2h = 1.1x10^{-3}Å^{-6}$, the square root of the bulk density of water ($0.0332Å^{-3}$). Since Q is inversely related to penetration depth, Q = 0 should correspond to infinite depth, i.e. bulk water. The water partial structure factors obtained for the lowest two surface concentrations appear to approach this value at low Q. However, the remaining two sets of data show a significant deviation from this expected behaviour. The data for these concentrations (2.0 and 3.0mg m^{-2}) extrapolate to Q^2h values of *ca.* $0.7x10^{-3}$ and $1.7x10^{-3}Å^{-6}$ respectively at Q = 0. Clearly, this highly surprising result does not follow the expected behaviour.

A further unexpected observation is the downturn in two of the data sets which occurs at low Q. The effect is most noticeable in the 2.0mg m^{-2} data, but also arises, to a lesser extent, in the 1.0mg m^{-2} data set. Such an effect has been reported

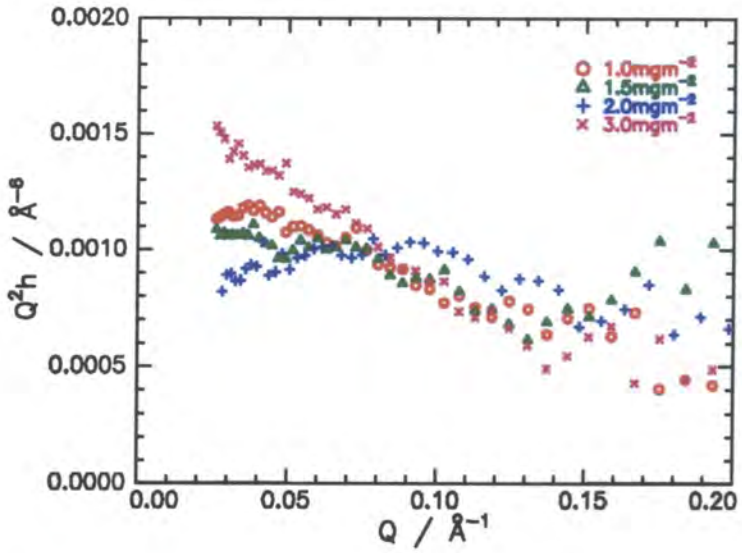

Figure 6.3.22. Water self partial structure factors

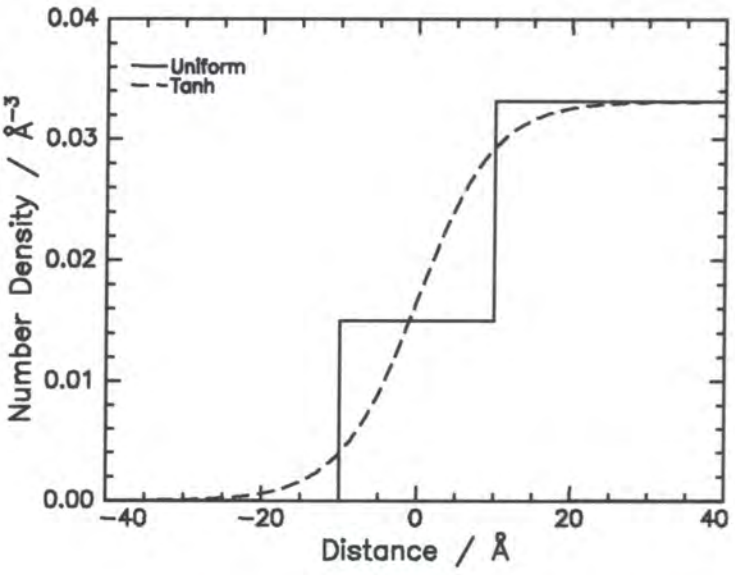

Figure 6.3.23. Number density profiles for a single uniform water layer (thickness = 20Å, number density = 0.015Å^{-3}, line) and a tanh layer (thickness = 10Å, dashes)

previously, predominately with systems containing PEO,[9,10,11] but also in monolayers of PMMA.[12,13] These sets of results were obtained using a wide range of polymer systems and therefore the effect does not seem to be system dependent. Furthermore, the introduction of a monolayer (especially one which is insoluble) upon a liquid surface should in no way affect the bulk properties of the liquid. One possibility is that the phenomenon is in some way due to small inaccuracies in the instrumental set-up when undertaking the experiments. If the detector were slightly misaligned, the value of Q measured would be either slightly greater or less than the actual value. This would not prevent data analysis taking place, but would result is the values extracted from such fitting procedures being unreliable.

Data fitting of the water self partial structure factors again takes place by the use of layer models, the two simplest models used are a single uniform water layer and a hyperbolic tangent (tanh) layer. The former of these is a step-wise function, whereas the latter gives a smoother transition of number density from air to bulk liquid. Examples of typical profiles obtained from each of the functions are given in figure 6.3.23. The number density of a uniform water layer is given by:

$$n_w(z) = 0 \qquad \text{for } z < -d_{w1}/2$$

$$n_w(z) = n_{w1} \qquad \text{for } -d_{w1}/2 < z < d_{w1}/2$$

$$n_w(z) = n_{w0} \qquad \text{for } z > d_{w1}/2 \qquad \textbf{Equation 6.3.11.}$$

Where d_{w1} is the thickness of the water layer and n_{w1} and n_{w0} are the number densities of the water layer and bulk water respectively. The partial structure factor is expressed as:

$$Q^2 h_w(Q) = n_{w0}^2 + 4n_{w1}(n_{w1} - n_{w0}) \sin^2\left(\frac{Qd_{w1}}{2}\right) \qquad \textbf{Equation 6.3.12.}$$

The number density profile of a tanh layer is given by:

$$n_w(z) = n_{w0}\left[0.5 + 0.5\tanh\left(\frac{z}{\sigma}\right)\right] \qquad \textbf{Equation 6.3.13.}$$

Where σ is the thickness of the layer. The partial structure factor is therefore:

$$Q^2 h_w(Q) = n_{w0}^2 \left(\frac{\sigma\pi Q}{2}\right)^2 \mathrm{cosech}^2\left(\frac{\sigma\pi Q}{2}\right) \qquad \textbf{Equation 6.3.14.}$$

As previously stated, the 1.0 and 1.5mg m^{-2} data exhibit classical behaviour at low Q and fits have been attempted with uniform and tanh layer models (figures 6.3.24 and 6.3.25), the values obtained being given in table 6.3.7.

	Tanh model		Uniform water layer model		
Γ_s / mg m^{-2}	σ / Å	χ^2	d_{w1} / Å	n_{w1} / 10^{-2} Å^{-3}	χ^2
1.0	5.4 ± 0.2	6.21×10^{-9}	9.2 ± 1.0	1.66 ± 0.04	5.99×10^{-9}
1.5	4.2 ± 0.23	1.41×10^{-8}	23.4 ± 1.0	3.06 ± 0.02	4.76×10^{-9}

Table 6.3.7. Parameters of fits obtained for the water self partial structure factor, Γ_s = 1.0 and 1.5mg m^{-2}.

The fits obtained from both models reproduce the data to a similar extent. However, the tanh model is the more physical realistic description of the surface water distribution as the uniform model includes an abrupt step in number density. Because the PMMA is described by a single Gaussian function, the number density of the water layer clearly does not change so abruptly. The water distribution is better represented by a model with a smoother transition of number density from that of air to that of bulk water. It is therefore a tanh model that is adopted here.

Next, it is attempted to resolve the dilemma of the unusual behaviour exhibited by the partial structure factors of the two highest surface concentrations. To confirm that the behaviour exhibited by the 3.0mg m^{-2} partial structure factor is indeed real, an alternative approach to calculating the partial structure factors is undertaken. Assuming that the reflectivity recorded for HPMMA-Q(H)P4VP on D_2O contrast is solely due to the D_2O, the water self partial structure factor can be approximated by:

$$Q^2 h \approx \frac{R(Q)Q^4}{16\pi^2 b^2} \qquad \textbf{Equation 6.3.15}$$

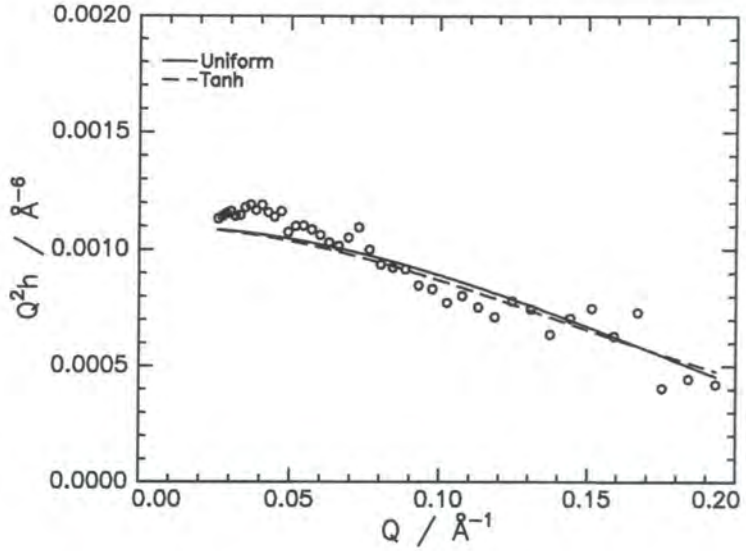

Figure 6.3.24. Water self partial structure factors (circles) for a polymer surface concentration of 1.0mg m^{-2} with uniform water (line) and tanh (dashes) model fits

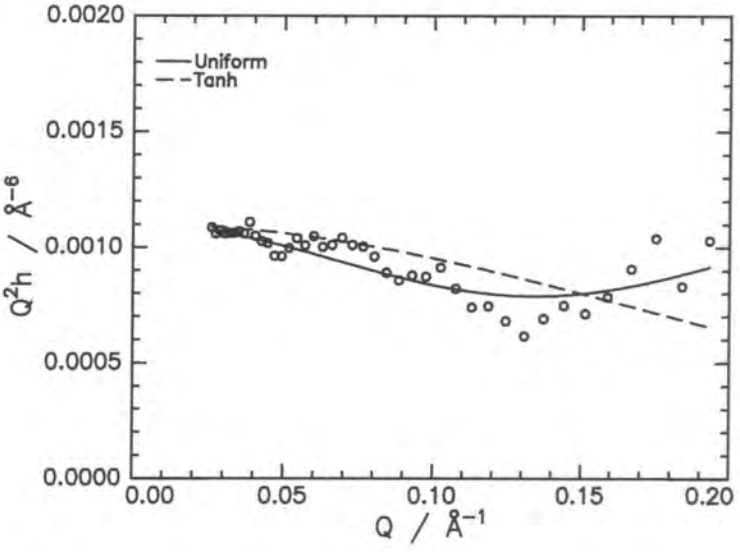

Figure 6.3.25. Water self partial structure factors (circles) for a polymer surface concentration of 1.5mg m^{-2} with uniform water (line) and tanh (dashes) model fits

Figure 6.3.26 compares the partial structure factor generated by equation 6.3.15 with that obtained by the standard method. The two sets of data follow similar trends, although the exact values differ somewhat, this being due to the approximation made regarding the contributing factors to the reflectivity. Both sets of data rise to values of Q^2h significantly greater than $1.1 \times 10^{-3} Å^{-6}$, implying that the partial structure factor does in fact represent the real behaviour of the system.

A variety of more complex models were used in an attempt to fit the two partial structure factors. One such model was a double uniform water layer, the number density of which is given by:

$$
\begin{aligned}
n_w(z) &= 0 && \text{for } z < -d_{w1}/2 \\
n_w(z) &= n_{w1} && \text{for } -d_{w1}/2 < z < d_{w1}/2 \\
n_w(z) &= n_{w2} && \text{for } d_{w1}/2 < z < d_{w2} + d_{w1}/2 \\
n_w(z) &= n_{w0} && \text{for } z > d_{w2} + d_{w1}/2
\end{aligned}
$$

Equation 6.3.16.

Which leads to a self partial structure factor of:

$$
\begin{aligned}
Q^2h_w = {} & n_{w1}^2 + (n_{w1} - n_{w2})^2 + (n_{w2} - n_{w0})^2 + 2n_{w1}(n_{w2} - n_{w1})\cos(Qd_{w1}) \\
& + 2(n_{w1} - n_{w2})(n_{w2} - n_{w0})\cos(Qd_{w2}) + 2n_{w1}(n_{w0} - n_{w2})\cos(Q(d_{w2} + d_{w1}))
\end{aligned}
$$

Equation 6.3.17.

The application of the above expression to the two data sets yields good quality fits, that for Γ_s = 2.0mg m^{-2} being shown in figure 6.3.27. The parameters yielded from such fits are given in table 6.3.8.

Γ_s / mg m^{-2}	d_{w1} / Å	n_{w1} / 10^{-2} $Å^{-3}$	d_{w2} / Å	n_{w2} / 10^{-2} $Å^{-3}$
2.0	14.8 ± 1.0	2.95 ± 0.05	60.1 ± 6.1	3.20 ± 0.05
3.0	14.4 ± 1.3	2.75 ± 0.04	42.0 ± 5.1	3.56 ± 0.04

Table 6.3.8. Parameters of fits obtained for the water self partial structure factors using a double uniform layer model

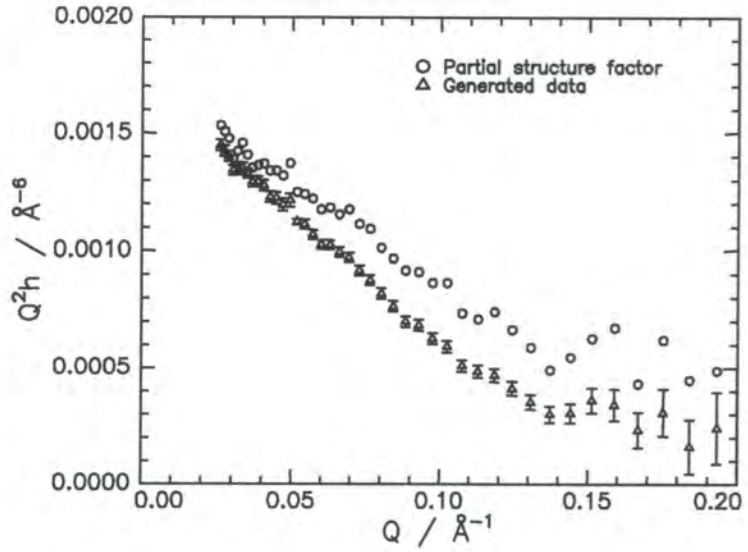

Figure 6.3.26. Comparison of the water self partial structure factor (circles) with data generated from equation 6.3.15 (triangles). Γ_s = 3.0mg m^{-2}

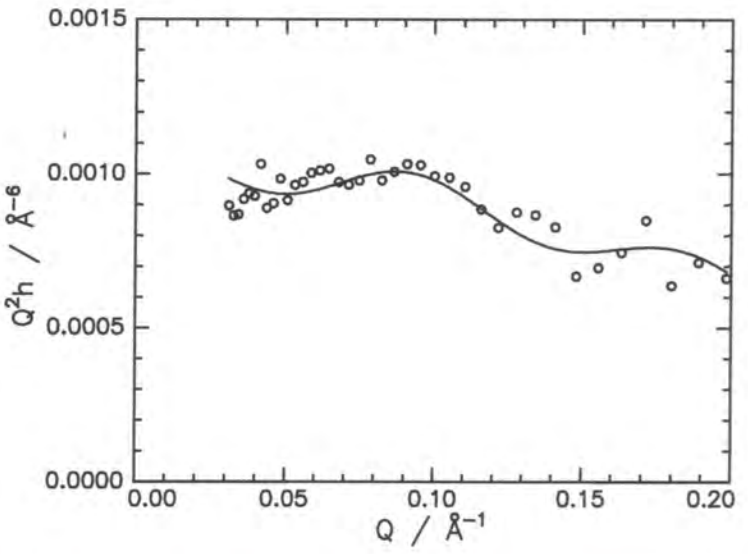

Figure 6.3.27. Water self partial structure (circles) and double uniform layer fit (line). Γ_s = 2.0mg m^{-2}

The number density profiles obtained from these data are presented in figure 6.3.28. The parameters for Γ_s = 2.0mg m^{-2} appear to be quite reasonable, layer one being of high number density, followed by a second, thicker layer with a number density slightly below that of bulk water. For the Γ_s = 3.0mg m^{-2} data however, an unusual phenomenon is exhibited. The first layer has a thickness and number density similar to the corresponding layer in the 2.0mg m^{-2} system. However, the number density of layer two is reported to be 0.0356$Å^{-3}$, slightly (7%) greater than that of bulk water, 0.0332$Å^{-3}$. Such a layer of water with increased number density is physically unrealistic. A similar layer has also been observed when attempting to fit the data set with other models, namely a triple uniform water layer and a uniform layer with an exponential tail. These both give good quality fits (see figure 6.3.29 for an example of the latter), except at the lowest values of Q. This phenomenon is probably an artefact of this specific data set, due to its unusual behaviour at low Q. Nevertheless, the fact that the value of number density is close to that of bulk water, along with a similar dense layer being reported by a number of layer models, implies that such a fit is realistic. The double uniform layer seems to be an appropriate description of the near surface water layers for these high surface concentrations of the spread copolymers.

A further attempt to fit the data was made following the method of Peace[5] who fitted the raw reflectivity data via the optical matrix approach and included very large values of interfacial roughness. The parameters returned from such a fit were then used to describe the organisation of the water layer at the liquid interface. However, when the method was attempted here, it was found that the data could best be fitted using values of interfacial roughness of 2-5Å, significantly smaller than the 60-70Å reported in the aforementioned work.

The water self partial structure factors, although exhibiting unusual behaviour, have therefore been fitted by application of one of two simple layer models. The two lowest surface concentrations have been described by a tanh distribution, whereas the two higher concentrations are best represented by a double uniform layer model.

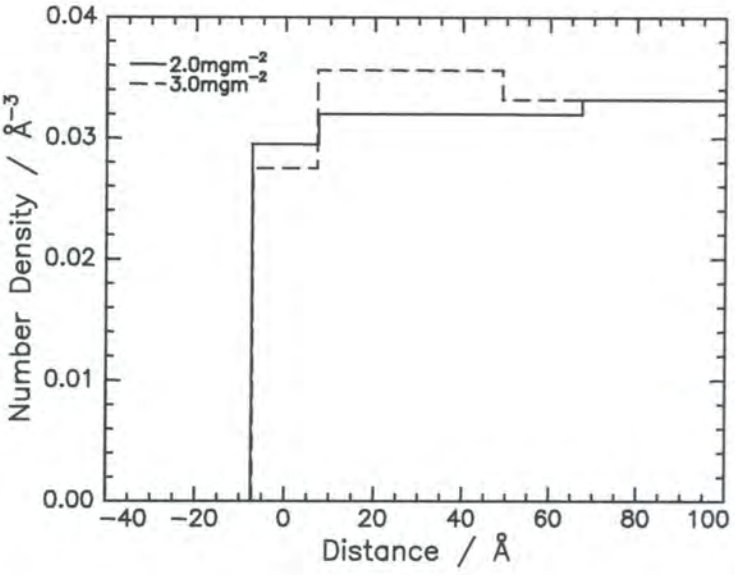

Figure 6.3.28. Number density profiles for double uniform layer model fits of the water self partial structure factors for surface concentrations of 2.0mg m^{-2} (line) and 3.0mg m^{-2} (dashes)

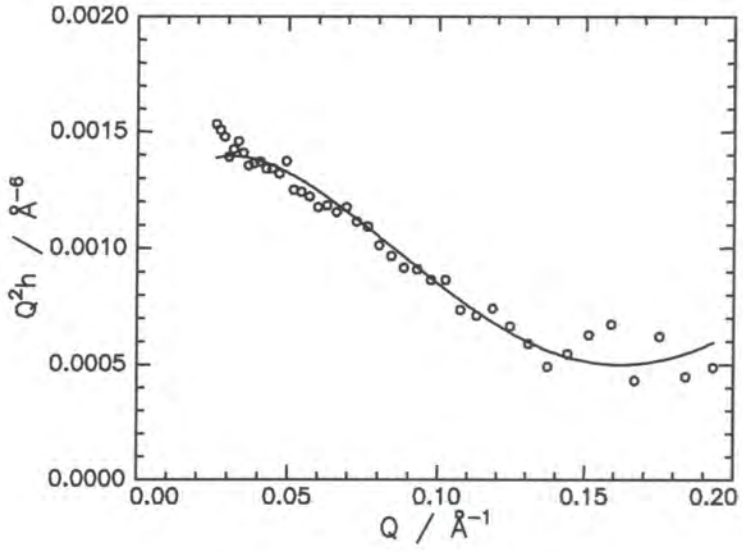

Figure 6.3.29. Water self partial structure (circles) and uniform-exponential layer fit (line). Γ_s = 3.0mg m^{-2}

To summarise the results obtained for the three self partial structure factors, the PMMA and QP4VP blocks of the polymer can be best be defined by the use of Gaussian and parabolic profiles respectively. Such layers, as expected, show changing characteristics with increasing polymer surface concentration, generally increasing in number density and thickness with increasing surface concentration.

Analysis of the self partial structure factors only gives details of the composition of each of the components in the system. To determine their relative positions, analysis of the cross partial structure factors is needed.

6.3.3.4. The PMMA – Water Cross Partial Structure Factor

Cross partial structure factors can be fitted to obtain the value of δ, the separation of the two components of the system. Such a fitting procedure can in some cases rely upon the parameters extracted from the fits of the self partial structure factors and this therefore requires these fits to be of adequate quality.

For the simplest systems, the cross partial structure factor is given by a simple trigonometric expression. For two perfectly even systems (e.g. single parabolic, single uniform or single Gaussian layers), the expression is:

$$h_{ij}(Q) = \pm\left(h_{ii}h_{jj}\right)^{1/2}\cos(Q\delta) \qquad \textbf{Equation 6.3.18.}$$

Whereas for one perfectly even and one perfectly odd (e.g. tanh) distribution, the expression becomes:

$$h_{ij}(Q) = \pm\left(h_{ii}h_{jj}\right)^{1/2}\sin(Q\delta) \qquad \textbf{Equation 6.3.19.}$$

For more complex models, such as the double uniform water layer utilised in the previous section, more complex expressions have to be derived. Each of the three cross partial structure factors is now discussed in turn, beginning with that between PMMA and water.

The PMMA-water cross partial structure factors are shown in figure 6.3.30. Each partial structure factor consists of negative values of Q^2h. Attempts to reproduce the partial structure factors were initially made for the 1.0 and 1.5mg m^{-2} data using equation 6.3.19, relating an even and odd distribution. Such an expression is appropriate in this case where we have a Gaussian polymer layer and a tanh water layer. The two appropriate experimental self partial structure factors were used in the process and good representations were obtained in both cases, resulting in layer separation of δ = 3 and 5Å respectively. An example of such a function, for Γ_s = 1.5mg m^{-2}, is given in figure 6.3.31.

For the two higher surface concentrations, where the water self partial structure factors has been fitted using a double uniform layer model, an alternative approach was initially taken. The following expression for the cross term between a Gaussian polymer layer and a double uniform water layer was generated:

$$Q^2h_{ij} = \frac{Q}{2}\left\{ n_1 d_1 \sqrt{\pi} \exp\left(-\frac{Q^2 d_1^2}{16}\right)\left[\begin{array}{l} n_{w1}\sin\left(\frac{1}{2}(d_{w1}-2\delta)Q\right)+(n_{w1}-n_{w2})\sin\left(\frac{1}{2}(d_{w1}-2\delta)Q\right)+ \\ (-n_{w0}+n_{w2})\sin\left(\frac{1}{2}(d_{w1}+2(d_{w2}+\delta))Q\right) \end{array}\right]\right\}$$

Equation 6.3.20.

Where the subscripts 1, w1, w2 and w0 represent polymer, water layer 1, water layer 2 and bulk water respectively.

Attempts to fit the above expression were made using the values of n and d obtained from the self partial structure fits and varying only the layer separation, δ. However, only poor quality fits were obtainable using this method, with large values of δ = 13 and 25Å being returned for Γ_s = 2.0 and 3.0mg m^{-2} respectively (see figure 6.3.32 for an example).

As this approach was clearly unsuccessful, it was then attempted to use the method outlined above, using equation 6.3.19 and effectively assuming the double uniform water layer to be an odd function. Although this is not completely rigorous, the partial structure factors generated by the use of this expression give very good representations of the data, resulting in values of δ of 6 and 7Å for Γ_s = 2.0 and

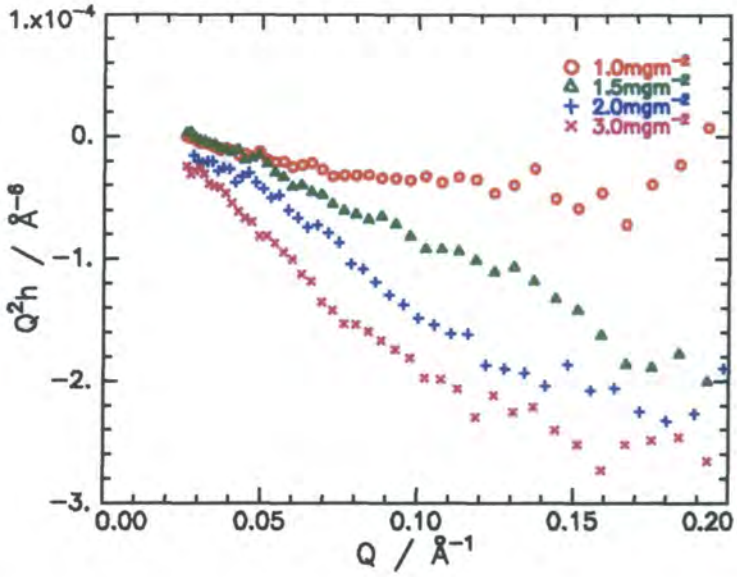

Figure 6.3.30. PMMA – water cross partial structure factors

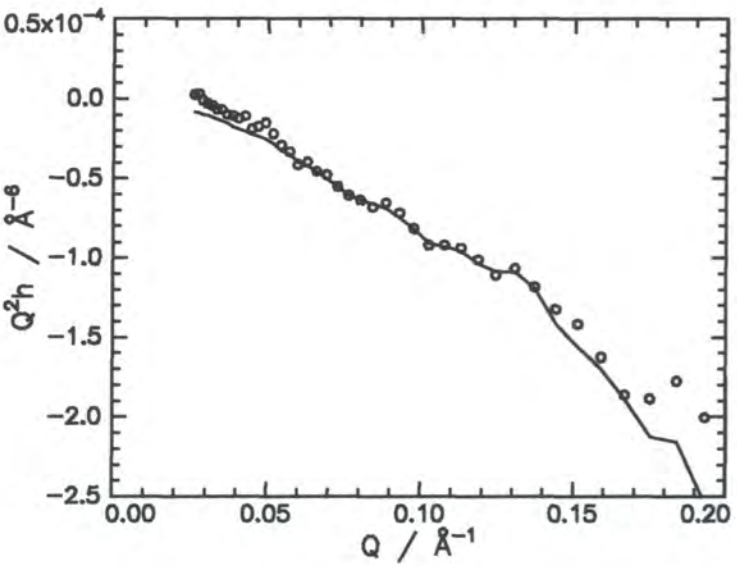

Figure 6.3.31. Experimental PMMA – water cross partial structure factor, Γ_s = 1.5mg m^{-2} (circles) overlayed with generated partial structure factor obtained with δ = 5Å (line)

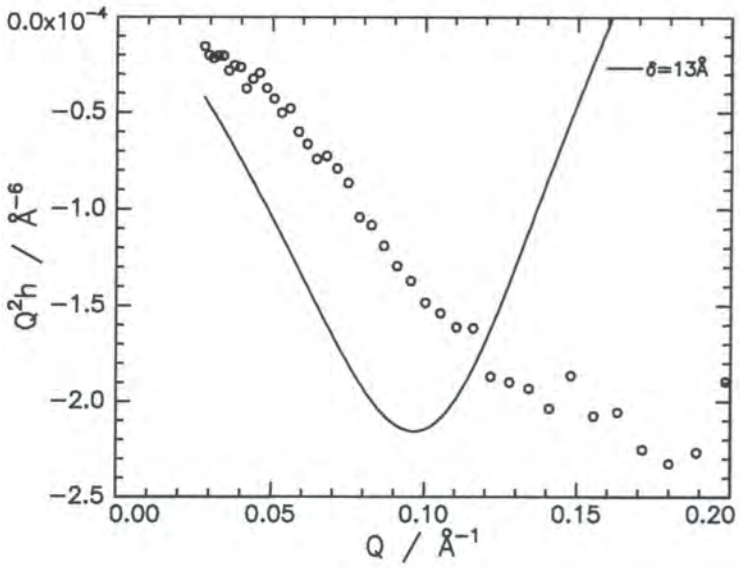

Figure 6.3.32. Experimental PMMA – water cross partial structure factor, Γ_s = 2.0mg m^{-2} (circles) overlayed with attempted fit using equation 6.3.20 (line)

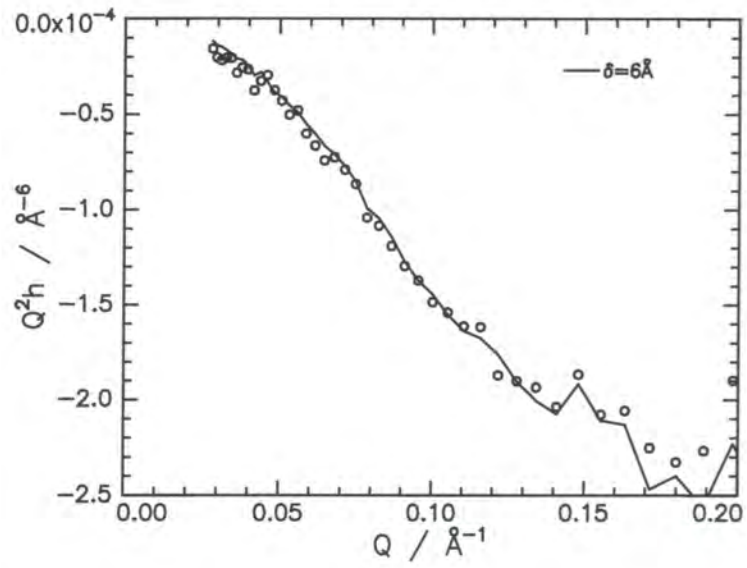

Figure 6.3.33. Experimental PMMA – water cross partial structure factor, Γ_s = 2.0mg m^{-2} (circles) overlayed with generated partial structure factor obtained with δ = 6Å (line)

3.0mg m^{-2} respectively (see figure 6.3.33 for an example). Although the first method used should, in theory, give the more accurate description for the partial structure factor, it is clear that a better representation is obtained with the simpler expression. In both of these higher surface concentrations, the double uniform water layer has a second layer with a number density extremely close to that of bulk water. Such a dilute layer is not determinable by equation 6.3.20, resulting in the water distribution effectively being described by a single uniform water layer, which in turn is approximated to an odd function. Consequently, the PMMA - water self partial structure can be best fitted by the use of equation 6.3.19 and the outputted parameters are given in table 6.3.9.

Γ_s / mg m^{-2}	$\delta_{PMMA\text{-}Water}$ / Å
1.0	3 ± 1
1.5	5 ± 1
2.0	6 ± 1
3.0	7 ± 1

Table 6.3.9. Separations obtained for the PMMA - water cross partial structure factors

6.3.3.5. The PMMA – QP4VP Cross Partial Structure Factor

The cross partial structure factors obtained for the two polymer blocks are given in figure 6.3.34. As both of the polymers blocks can be described by even functions, the data are simulated using equation 6.3.18. Due to large uncertainties inherent in the data, these simulations overlay the experimental data less well than those in the previous section. Figure 6.3.35 shows the 1.0mg m^{-2} experimental data, with partial structure factors generated with δ = 7Å and 15Å overlayed. The 15Å data overlays the low Q region well, but is highly inaccurate at representing the layer at higher Q.

Γ_s / mg m^{-2}	$\delta_{PMMA\text{-}QP4VP}$ / Å
1.0	7 ± 1
1.5	8 ± 1
2.0	9 ± 1
3.0	14 ± 2

Table 6.3.10. Separations obtained for the PMMA – QP4VP cross partial structure factors

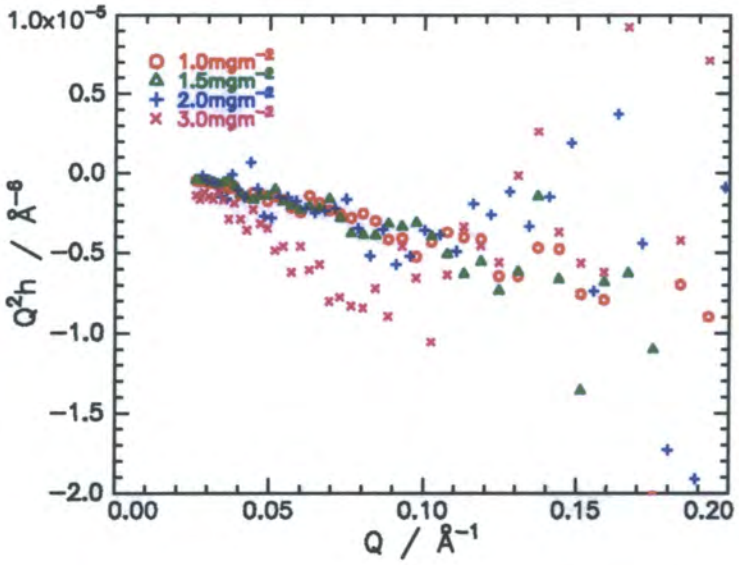

Figure 6.3.34. PMMA – QP4VP cross partial structure factors

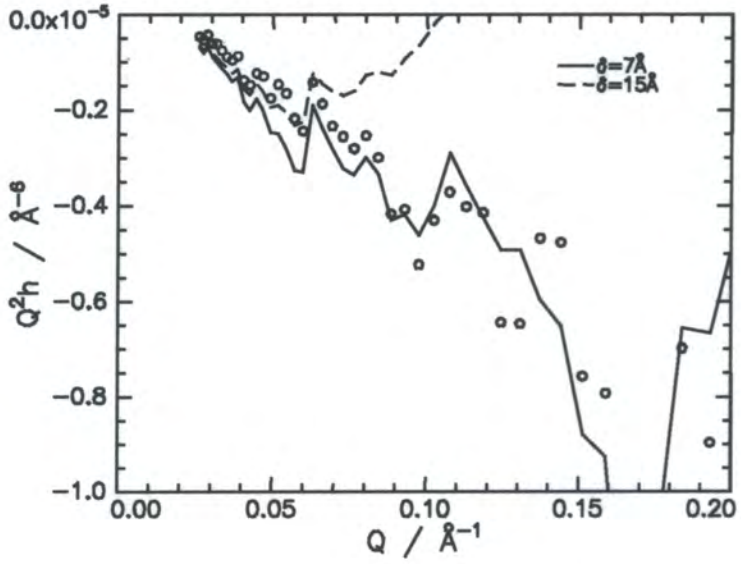

Figure 6.3.35. Experimental PMMA – QP4VP cross partial structure factor, Γ_s = 1.0mg m^{-2} (circles) overlayed with generated partial structure factors obtained with δ = 7Å (line) and δ = 15Å (dashes)

The data with $\delta = 7$Å gives a better representation of the partial structure factor over the whole Q range. The results obtained for the remaining three surface concentrations are given in table 6.3.10.

6.3.3.6. The QP4VP - Water Cross Partial Structure Factor

The QP4VP – water cross partial structure factors are shown in figure 6.3.36. As the two highest surface concentrations have used a double uniform water layer to fit the self partial structure factor, the same approach as in section 6.3.3.4 is taken. Equation 6.3.19 is used to fit the data, rather than the expression generated from the two self partial structure factors.

The results obtained are severely affected by the quality of the data. For a surface concentration of 1.0mg m^{-2} (figure 6.3.37), the data lies approximately horizontally around $Q^2h = 0$. The best representation of the data is shown in the figure, with a separation of $\delta = 1$Å. Although such a plot does not overlay the data, the overall trend exhibited is followed well, much more so than for any higher value of δ. A similar occurrence is found for the highest surface concentration, where a value of $\delta = 7$Å is returned. The data for surface concentrations of 1.5 and 2.0mg m^{-2} are best described by $\delta = 2$ and 3Å respectively and in both cases, the data is reproduced quite accurately. A summary of these data is given in table 6.3.11.

Γ_s / mg m^{-2}	$\delta_{QP4VP\text{-}Water}$ / Å
1.0	1 ± 1
1.5	2 ± 1
2.0	3 ± 1
3.0	7 ± 1

Table 6.3.11. Separations obtained for the QP4VP - water cross partial structure factors

6.3.3.7. Summary & Discussion

A complete partial structure analysis has been undertaken for four surface concentrations of PMMA-QP4VP on water. The data obtained from the self and cross partial structure factors are presented in tables 6.3.12 and 6.3.13 respectively.

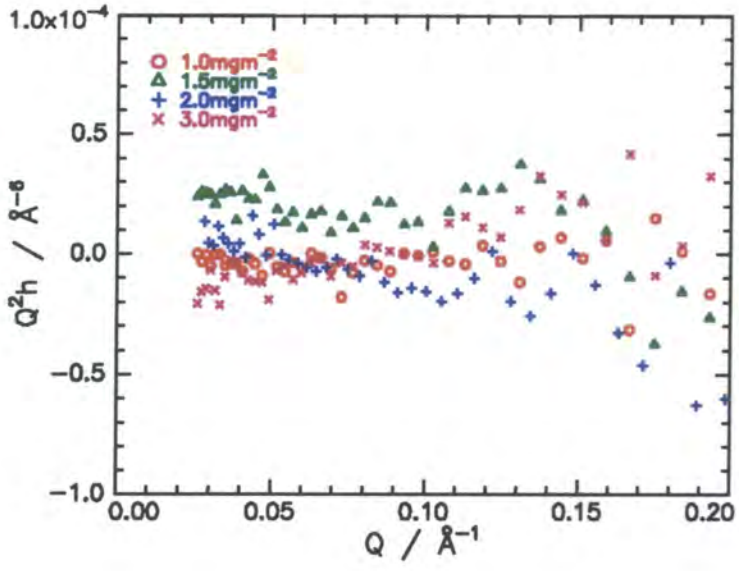

Figure 6.3.36. QP4VP - water cross partial structure factors

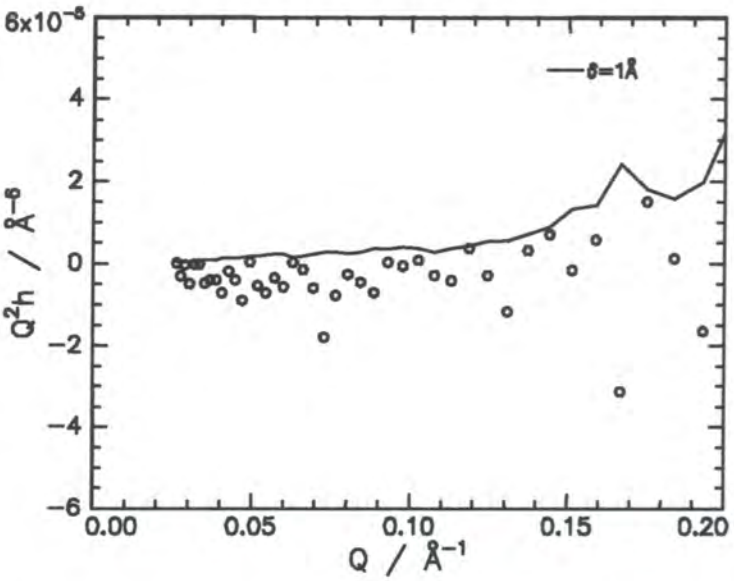

Figure 6.3.37. Experimental QP4VP - water cross partial structure factor, Γ_s = 1.0mg m^{-2} (circles) overlayed with generated partial structure factor obtained with δ = 1Å (line)

Due to the nature of the fitting procedure, the separations presented above yield no information regarding the position of the blocks in real space. To construct a number density profile, it is therefore necessary to make certain assumptions. Firstly, an arbitrary zero has to be defined, which is usually taken to be the centre of the water distribution. Secondly, the relative positions of each of the polymer blocks with respect to the water layer have to be determined. As the PMMA block is hydrophobic in nature, it is assumed that centre of its distribution lies above the water layer. Conversely, the hydrophobic QP4VP block is assumed to exist below the water.

	PMMA self PSF (Single Gaussian layer)		QP4VP self PSF (Single parabolic layer)	
Γ_s / mg m^{-2}	d_1 / Å	n_1 / 10^{-3} Å^{-3}	d_1 / Å	n_1 / 10^{-4} Å^{-3}
1.0	14.5 ± 0.8	3.85 ± 0.19	17.4 ± 1.5	7.88 ± 0.33
1.5	12.0 ± 0.4	6.31 ± 0.14	19.0 ± 0.9	6.49 ± 0.17
2.0	15.9 ± 0.3	6.64 ± 0.04	30.7 ± 2.2	6.39 ± 0.37
3.0	19.6 ± 0.2	7.48 ± 0.05	27.7 ± 1.2	8.40 ± 0.23

Table 6.3.12a. Summary of the polymer self partial structure factors for films of PMMA-QP4VP spread on water

	Tanh Layer	Double uniform water layer			
Γ_s / mg m^{-2}	σ / Å	d_1 / Å	n_1 / 10^{-2} Å^{-3}	d_2 / Å	n_2 / 10^{-2} Å^{-3}
1.0	5.4 ± 0.2	-	-	-	-
1.5	4.2 ± 0.3	-	-	-	-
2.0	-	14.8 ± 1.0	2.95 ± 0.05	60.1 ± 6.1	3.20 ± 0.05
3.0	-	14.4 ± 1.3	2.75 ± 0.04	42.0 ± 5.1	3.56 ± 0.04

Table 6.3.12b. Summary of the water self partial structure factors for films of PMMA-QP4VP spread on water

Γ_s / mg m^{-2}	$\delta_{PMMA\text{-}Water}$ / Å	$\delta_{PMMA\text{-}QP4VP}$ / Å	$\delta_{QP4VP\text{-}Water}$ / Å
1.0	3 ± 1	7 ± 1	1 ± 1
1.5	5 ± 1	8 ± 1	2 ± 1
2.0	6 ± 1	9 ± 1	3 ± 1
3.0	7 ± 1	14 ± 2	7 ± 1

Table 6.3.13. Summary of the cross partial structure factors for films of PMMA-QP4VP spread on water

These assumptions are supported by the data in table 6.3.13, where it can be seen that $\delta_{PMMA\text{-}QP4VP} \approx \delta_{PMMA\text{-}Water} + \delta_{QP4VP\text{-}Water}$, implying that the three components do

indeed exist in the order PMMA, water, QP4VP (from air to liquid). In the cases where the above equation is an approximation as opposed to an equality, the two separations used are $\delta_{PMMA\text{-}Water}$ and $\delta_{PMMA\text{-}QP4VP}$, due to the smaller errors associated the data. With the above information, it is possible to compile number density profiles, which are shown in figures 6.3.38a-d. In all four cases, the number densities of the two polymer blocks have been multiplied by a factor of four, solely to increase the clarity of the plot.

Evidently, the PMMA block exhibits increasing number density and the QP4VP block becomes increasingly stretched into the subphase as surface concentration increases. Furthermore, a portion of the polyelectrolyte block appears to be in the air phase at the highest surface concentrations. By integrating the areas underneath the curves in figures 6.3.38, it is found that 8.6%, 25.7% and 14.9% of the QP4VP block exists in the air at Γ_s = 1.5, 2.0 and 3.0mg m^{-2} respectively. At the lowest surface connection (1.0mg m^{-2}), the QP4VP is submerged completely. This existence of QP4VP in the air phase is suggested to be due to the over-packing of the liquid surface. As some of the PMMA chains are forced out of the surface region and into the air, at least some of the QP4VP block of the copolymer will also be forced upwards, resulting in the effect observed above.

A further interesting observation is that the two polymer blocks overlap to a large extent at all surface concentrations, although the extent of such mixing does seem to decrease slightly with increasing concentration. This implies that there is a area around the middle of the interfacial region where all three components of the system are present. The polymer does therefore not exist as a truly hydrophobic - hydrophilic system with the PMMA entirely on the subphase and the polyelectrolyte block wholly submerged.

At low surface concentrations, the water layer is best described by a tanh function, providing a smooth transition between air and bulk water density. At higher concentrations, a double step function is used, which results in a layer of higher number density for the 3.0mg m^{-2} system.

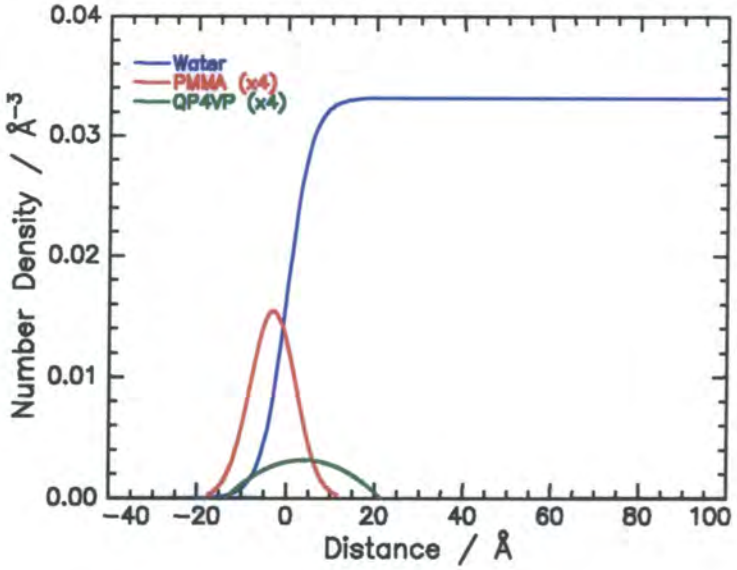

Figure 6.3.38a. Number density profile for $\Gamma_s = 1.0$mg m^{-2}

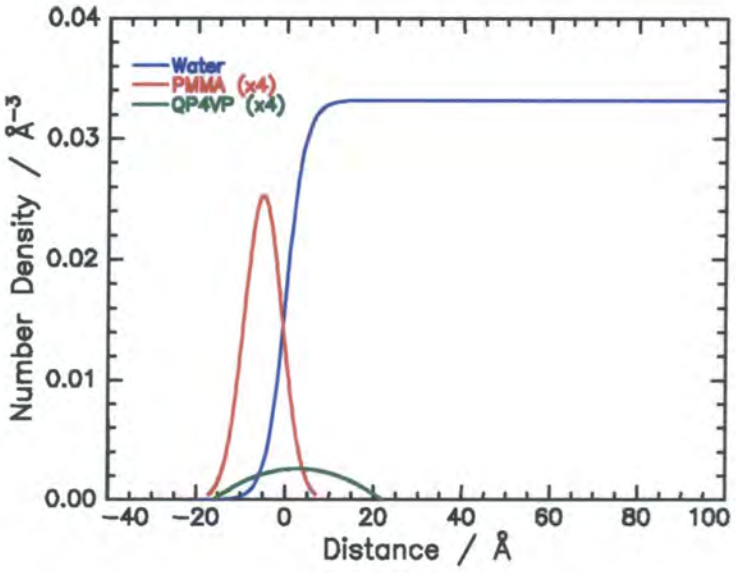

Figure 6.3.38b. Number density profile for $\Gamma_s = 1.5$mg m^{-2}

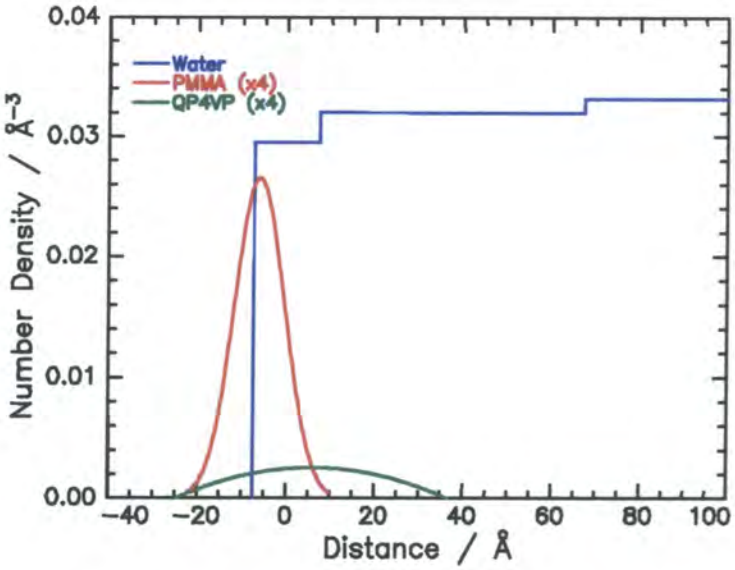

Figure 6.3.38c. Number density profile for $\Gamma_s = 2.0$mg m^{-2}

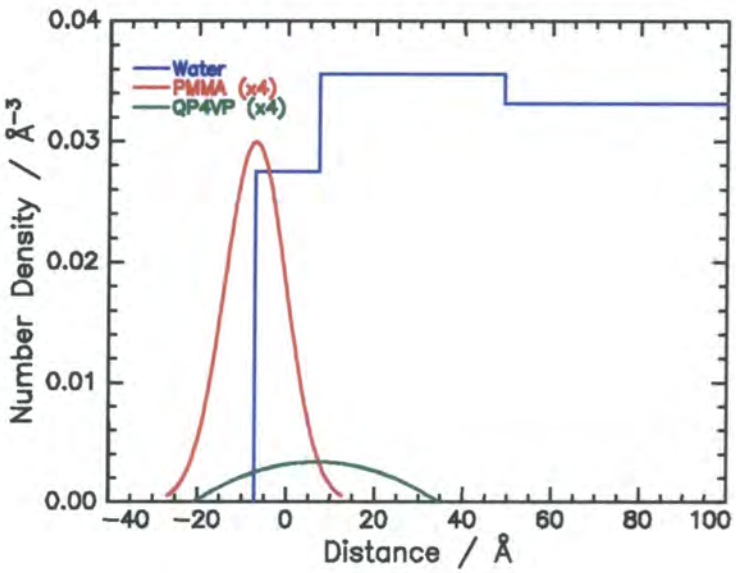

Figure 6.3.38d. Number density profile for $\Gamma_s = 3.0$mg m^{-2}

6.3.3.8. Comparison to Brush Theory

The scaling theory discussed in section 2.1.4 states that a polymer brush should stretch with increasing grafting density, minimising the free energy of the system. For the polymer system used here, the QP4VP chains can be assumed to be pseudo brush-like in nature, with the grafting surface being the air-liquid interface. The grafting density is in this case directly related to the surface concentration of polymer.

Alexander[14] and de Gennes[15] have developed a scaling expression where the height of a polymer brush, H, is related to the grafting density, σ:

$$H = Na\sigma^{z} \qquad \textbf{Equation 6.3.21.}$$

Where N is the number of monomer units in a chain, a the statistical step length and z the scaling exponent, reported to have the value 1/3. An attempt to reproduce this result was made by rearranging the above expression to obtain:

$$\log(H/N) = \log a + z \log \sigma \qquad \textbf{Equation 6.3.22.}$$

A plot of log (H/N) against log σ will therefore yield z as the gradient of the slope. Before this can be done however, the grafting density has to be calculated from the QP4VP component of surface concentration, $\Gamma_{s,QP4VP}$, by use of the expression:

$$\sigma = \frac{10^{-23}\Gamma_{s,QP4VP}N_A}{M} \qquad \textbf{Equation 6.3.23.}$$

Where M is the mass (in amu) of a monomer unit and σ the number of polymer chains per $Å^2$. The values of σ calculated from this expression are given in table 6.3.14, along with the obtained polymer brush heights.

Using an average value of N = 90 monomer units per polymer chain, the data are plotted in figure 6.3.39. When taking into account the uncertainties of the values of brush height obtained, especially in the case of Γ_s = 2.0mg m^{-2}, a reasonable least

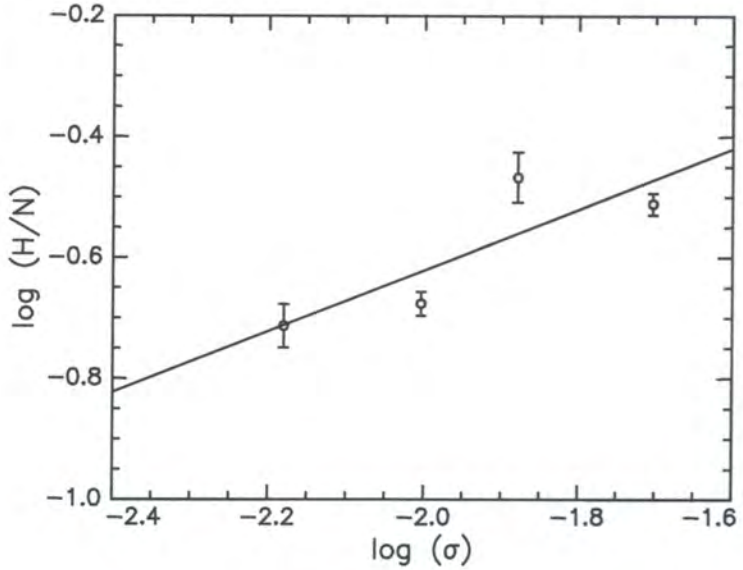

Figure 6.3.39. Plot of log (H/N) against log (σ) overlayed with a least squares fit (line) to calculate the scaling factor z in equation 6.3.21.

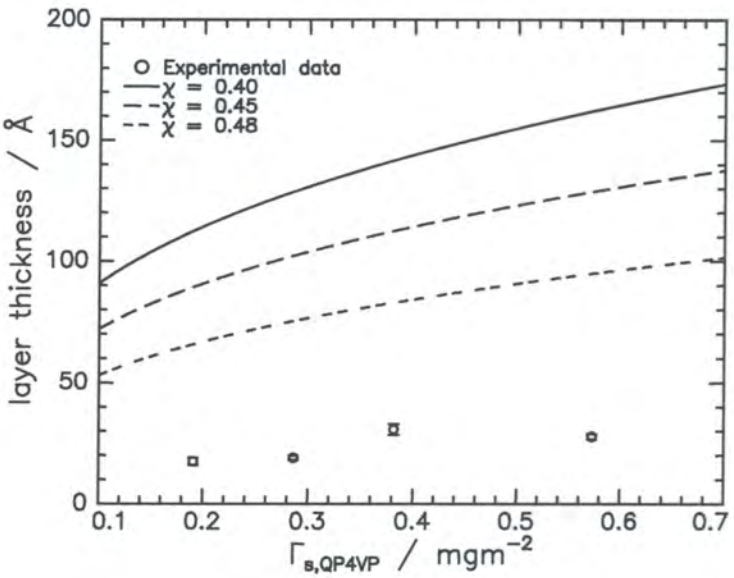

Figure 6.3.38. Layer thicknesses of QP4VP (circles) overlayed with data generated using equation 6.3.24 using different values of χ (lines, see legend)

squares fit is achieved. The slope of the gradient extracted form such a plot is z = 0.503 and the intercept of the plot occurs at y = 0.385, giving a very small statistical step length of a = 2.4Å.

Γ_s / mg m^{-2}	σ / chains Å^{-2}	H / Å
1.0	6.61×10^{-3}	17 ± 2
1.5	9.91×10^{-3}	19 ± 1
2.0	1.32×10^{-2}	31 ± 2
3.0	1.98×10^{-2}	27 ± 1

Table 6.3.14. Values of grafting density and brush height

The value of z is significantly greater than that of 1/3 found in the scaling expressions of Alexander and de Gennes. The polyelectrolyte scaling theory of Misra[8] found that the values of the scaling parameter deviated from this if the polymer brush was charged. However, in this case, the value for z was found to decrease.

Clearly, a discrepancy exists between the calculated value of z and those predicted by theoretical studies. The main reason for such a discrepancy may be that the Alexander - de Gennes theory assumes that all of the brush ends are the same distance form the surface. This is clearly not the case here, as a parabolic distribution has been used to fit the QP4VP block. In addition, the length of the polyelectrolyte chains, which are small (20-30Å) compared to those used in theoretical studies. This effect has been found in a recent experimental study,[16] where the scaling law has been followed for polyelectrolyte brushes with a length of *ca.* 100Å. For shorter brushes, there is a significant deviation form theory. Another contributory factor could be the bulky pyridinium rings on the polyelectrolyte chains meaning that brushes do not exhibit the ideal behaviour assumed by theory.

In a further comparison with theory, the layer thicknesses can be compared to the following expression generated by Milner, Witten and Cates:[7]

$$H = \left(\frac{12}{\pi^2}\right)(0.5-\chi)^{1/3} N\sigma^{1/3} a^{5/3} \qquad \textbf{Equation 6.3.24.}$$

This theory results in a parabolic profile being obtained for the polymer brush, an identical outcome to that of the partial structure analysis discussed previously. In equation 6.3.24, χ is an interaction parameter between the polymer and the solvent. a is again the statistical step length which for the purposes of this study is allotted the value obtained from the plot in figure 6.3.39, namely a = 2.4Å.

Figure 6.3.40 shows a plot of QP4VP surface concentration against layer thickness. The lines are data generated from equation 6.3.24 using values of χ = 0.40, 0.45 and 0.48. It can clearly be seen that none of these values reproduce quantitatively the experimental data to any extent; in fact the only way in which this can be achieved is to use very high values of the interaction parameter, namely $\chi > 0.499$.

Neither of the above theoretical models therefore give an exact description of the behaviour of the polymer at the air-liquid interface. However, the polyelectrolyte brush clearly does stretch with increasing grafting density, it is only the quantification of such an expression which the theory fails to establish.

6.3.4. Optical Matrix Analysis

Attempts to fit the entire set of reflectivity curves (six for each surface concentration studied) using the optical matrix approach proved to be unsuccessful, predominantly due to the low reflectivity and large errors encountered for the Q(D)P4VP data. However, useful data could be obtained for other copolymer – subphase combinations. The results obtained are presented in this section and compared with those obtained from the kinematic approximation.

6.3.4.1. DPMMA-Q(H)P4VP on NRW

The reflectivity of DPMMA-Q(H)P4VP on NRW was analysed to obtain information on the structure of the PMMA block of the polymer. Initially, a single layer fit was attempted. This gave an adequate fit to the data, indeed it was found that the introduction of further layer into the system in no way improved the quality of the fit. A typical fit (for Γ_s = 1.0mg m^{-2}) is given in figure 6.3.41 and the data obtained is presented in table 6.3.15.

Γ_s / mg m^{-2}	d_1 / Å	ρ_1 / 10^{-6} $Å^{-2}$
1.0	15.6 ± 1.0	2.96 ± 0.09
1.5	15.5 ± 1.3	4.34 ± 0.24
2.0	15.9 ± 1.2	5.45 ± 0.25
3.0	19.3 ± 0.8	6.47 ± 0.36

Table 6.3.15. Parameters obtained from single layer fits of DPMMA-Q(H)P4VP on NRW

Initially, there is little change of layer thickness, d, with increasing surface concentration, although an increase in layer thickness is observed at the highest surface concentration. The scattering length density of the layer, ρ, increases, with an unusual result observed the highest concentration where the value obtained is greater than that of bulk PMMA. This is discussed below.

If we assume that PMMA is the sole contributor to the reflectivity of the system, the surface concentration of polymer (in mg m^{-2}) can be calculated, using the expressions below:

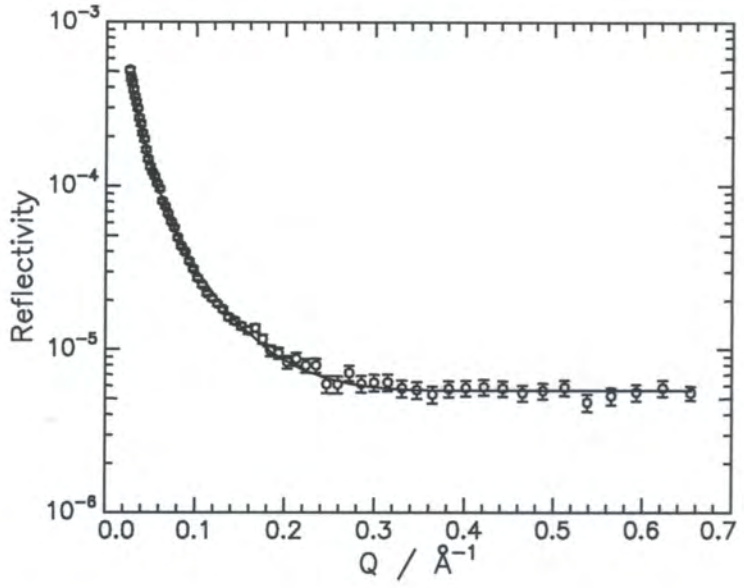

Figure 6.3.41. Single layer fit (line) to reflectivity curve of DPMMA-Q(H)PMMA on NRW. Γ_s = 1.0mg m^{-2}

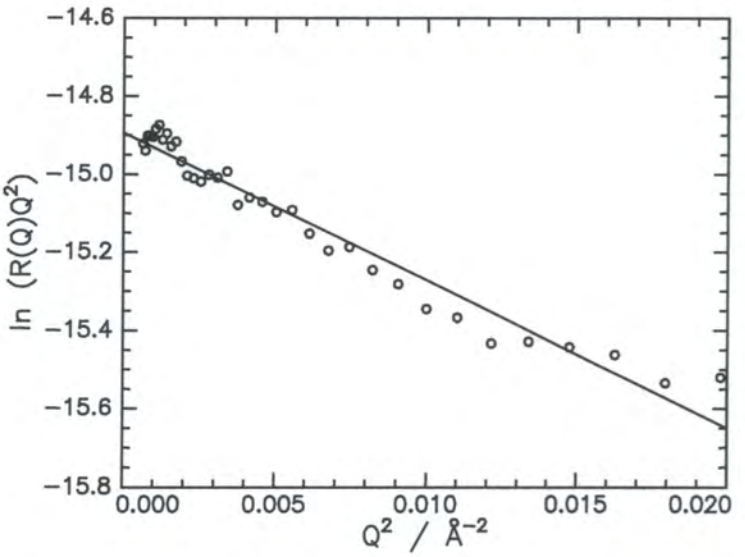

Figure 6.3.42. Guinier plot for the low Q region of DPMMA-Q(H)PMMA on NRW. Γ_s = 1.0mg m^{-2}

$$\phi_i \rho_i = b_i n_i \qquad \text{and} \qquad \textbf{Equation 6.3.25.}$$

$$\Gamma_s = \frac{10^{20} n_i M_i d}{N_A} \qquad \textbf{Equation 6.3.26.}$$

Where ϕ_i is the volume fraction, n_i the number density and M_i the weight of a monomer unit of a component of the system. The values of ϕ_i and $\Gamma_{s,PMMA}$ are given in table 6.3.16:

Γ_s / mg m^{-2}	ϕ_i	$\Gamma_{s,PMMA}$		Error
		Calculated	***Predicted***	
1.0	0.49	0.85	*0.81*	4.7%
1.5	0.72	1.24	*1.21*	2.4%
2.0	0.90	1.60	*1.62*	1.4%
3.0	1.07	2.31	*2.43*	5.1%

Table 6.3.16. Volume fractions and surface concentrations of PMMA obtained from optical matrix analysis

Similar trends in the calculated surface concentration are observed as those obtained by the kinematic approximation analysis. The calculated value of $\Gamma_{s,PMMA}$ is initially greater than that of the theoretical value before dropping below the theoretical values at higher surface concentration. One point of note is the unrealistically high value of $\phi_i > 1$ obtained for $\Gamma_s = 3.0$mg m^{-2}, this being a corollary of the high value of scattering length density obtained. Such an outcome is similar to the phenomenon observed for the 3.0mg m^{-2} data set using the kinematic approximation. In that case, the water is represented by a layer with a large number density, the equivalent effect to that reported here.

Further analysis of the data uses a Guinier plot,[2] originally developed for small-angle scattering.[17] When the media on either side of the interface are of identical scattering length (as is the case here with air and NRW), the following approximation is valid:

$$R(Q)Q^2 = 16\pi^2 m^2 \exp\left(-Q^2\sigma^2\right) \qquad \textbf{Equation 6.3.27.}$$

Where R(Q) is the background subtracted reflectivity, m the scattering mass per unit area of the thin film and σ the standard deviation of rate of change of scattering length density. A plot of $\ln(R(Q)Q^2)$ against Q^2 (figure 6.4.42) therefore yields a straight line with a gradient of $-\sigma^2$ and intercept $\ln(16\pi^2m^2)$, enabling the values of σ and m to be calculated (table 6.3.17).

Γ_s / mgm^{-2}	Slope	Intercept	σ / chains Å^{-2}	m / 10^{-6}Å^{-1}
1.0	-37.8	-14.9	6.15	46.5
1.5	-32.3	-14.2	5.68	66.6
2.0	-23.3	-13.7	4.83	83.9
3.0	-54.4	-12.9	7.38	123.8

Table 6.3.17. Slope and intercept of Guinier plots, along with the extracted values of σ and m

The values of m obtained can be compared with the product of the scattering length density and film thickness obtained from the single layer optical matrix fits (see table 6.3.18). Clearly, the two data analysis techniques yield highly similar results for all surface concentrations studied, giving reassurance of the validity of the fits obtained.

Γ_s / mgm^{-2}	m / 10^{-6}Å^{-1}	ρd / 10^{-6}Å^{-1}
1.0	46.5	46.1
1.5	66.6	67.2
2.0	83.9	86.6
3.0	123.8	125.3

Table 6.3.18. Comparison of values of m obtained from a Guinier plot with ρd from the optical matrix approach

6.3.4.2. HPMMA-Q(H)P4VP on D_2O

If it is assumed that all the reflectivity for the HPMMA-Q(H)P4VP on D_2O contrast arises from the subphase, the fitting of such a profile allows an idea of the conformation of the near-surface water layer to be obtained. Again, a single layer fit was found to be adequate, the example shown (figure 6.3.43) being for Γ_s = 1.0 mg m^{-2}. The parameters extracted from such fits are given in table 6.3.19:

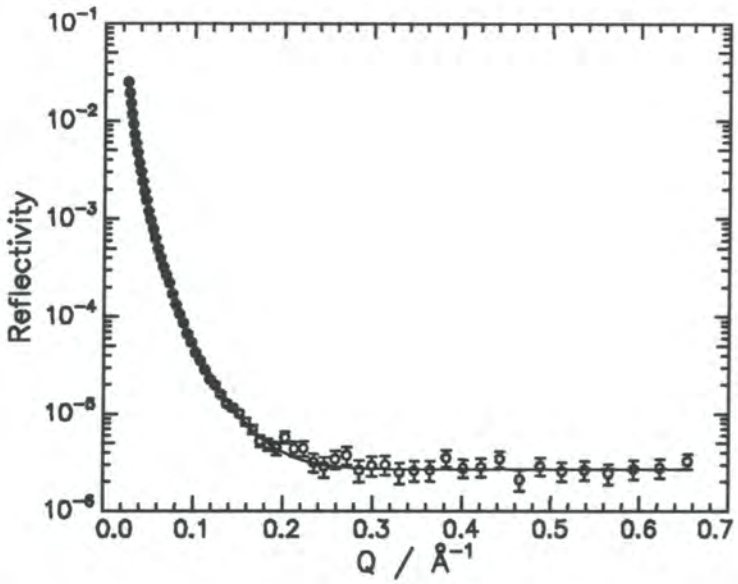

Figure 6.3.43. Single layer fit (line) to reflectivity curve of HPMMA-Q(H)PMMA on D_2O. $\Gamma_s = 1.0 mg\ m^{-2}$

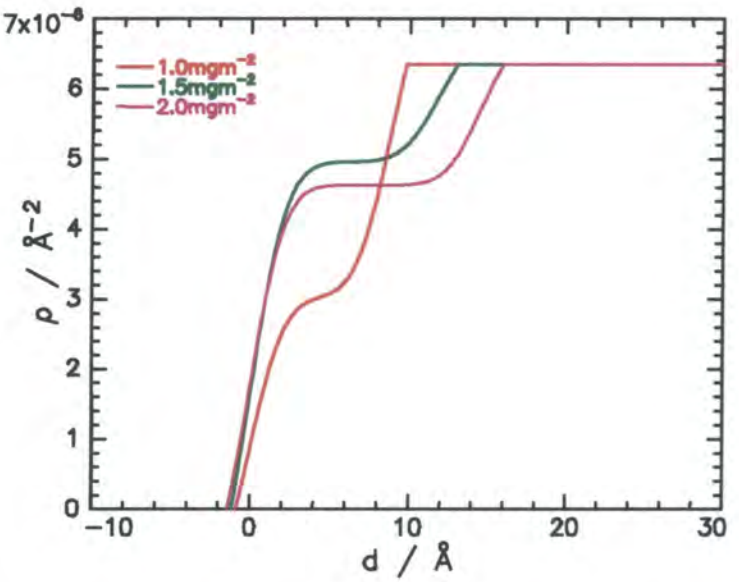

Figure 6.3.44. Scattering length density of surface water layer derived from single layer fits of reflectivity profiles for HPMMA-Q(H)PMMA on D_2O

Γ_s / mg m^{-2}	d_1 / Å	ρ_1 / 10^{-6} Å^{-2}
1.0	8.9 ± 0.8	2.96 ± 0.05
1.5	11.8 ± 0.9	4.99 ± 0.21
2.0	14.5 ± 1.3	4.66 ± 0.26

Table 6.3.19. Parameters obtained from single layer fits of DPMMA-Q(H)P4VP on D_2O

No adequate fit to the 3.0mg m^{-2} data was achievable, even with the addition of a second and third layer to the system. This observation follows the findings of the kinematic approximation, where the 3.0mg m^{-2} water self partial structure factor could not be fitted without the inclusion of a layer of number density greater than that of water itself.

The above data is plotted in figure 6.3.44 as scattering length density against depth. Here, it is notable that the thickness of the near surface water layer increases with surface concentration. The scattering length density of such a layer generally increases from half that of bulk water for 1.0mg m^{-2} to larger values at higher polymer surface concentrations. Such results are comparable to those obtained by the kinematic approximation, where the two lowest concentrations are represented by a smooth tanh function and the 2.0mg m^{-2} data represented by a step function.

Attempts to fit other data by the optical matrix approach proved to be unsuccessful, especially the contrast HPMMA-Q(D)P4VP on NRW, which was unable to be fitted due to the minimum in the reflectivity curve. In an attempt to compensate for this and to gain information on the conformation of the QP4VP block of the system, it was then attempted to fit the HPMMA-Q(D)P4VP on D_2O contrast. The data could apparently be fitted highly accurately with either two or three layer model fits. However, it was found that the layer furthest away from the interface consistently reported a value of $\rho > 6.35 \times 10^{-6}$ Å^{-2}, higher than that of bulk D_2O and physically unrealistic.

6.3.5. Model Independent Fitting

The third technique used to analyse neutron reflectometry data is the model independent fitting technique. As outlined in section 3.2.5.3, the technique relies upon the selection of an appropriate value of the Lagrangian multiplier, λ, to fit the data. The effects of varying such a parameter are shown in figures 6.3.45 to 6.3.47, the example presented being for the contrast DPMMA-Q(H)P4VP on NRW at a polymer surface concentration of 3.0mg m^{-2}.

Figure 6.3.45 shows the raw reflectivity curve and the fits obtained by varying λ. As the value of λ is decreased, a better fit to the data is achieved, the fits for $\lambda = 1x10^{-7}$ and $\lambda = 1x10^{-8}$ being almost identical. The fits to the data in the form of $R(Q)Q^4$ against Q are also compared (figure 6.3.46). Again, the same phenomenon is observed, the quality of the fit improving with decreasing λ. The scattering length density profiles obtained by each of the above fits are shown in figure 6.3.47. These profiles give an indication of the structure of the PMMA block, which is the dominant contributor to the reflectivity in the contrast shown here.

In the example given above, the best representations of the data are clearly given by $\lambda = 1x10^{-7}$ and $\lambda = 1x10^{-8}$, and is the former of these which is chosen as the 'best' fit in this case. This is primarily because the use of $\lambda = 1x10^{-8}$ appears to fit the data overly accurately. This is best exemplified in figure 6.3.46 when the fit for this value of λ passes through the centre of almost every data point. At higher values of Q, the data is subject to large errors (hence the size of the error bars on the points) and it is therefore unrealistic to expect a fit of such high quality to be reasonably obtained.

The process of selecting the most appropriate value of λ is repeated for each contrast used and for each surface concentration studied. This results in a series of data sets of scattering length density distribution as a function of distance from surface and, from these, volume fraction profiles may be obtained. As an example, the profile for the lowest surface concentration, 1.0mg m^{-2}, is shown in figure 6.3.48. An important point to note is that no layer separations are included in this data, the profiles of each of the three components all being positioned at the same origin.

To obtain a more complete profile of the interfacial region of the system, a series of layer separations are added. This is achieved by fixing one of the components of the

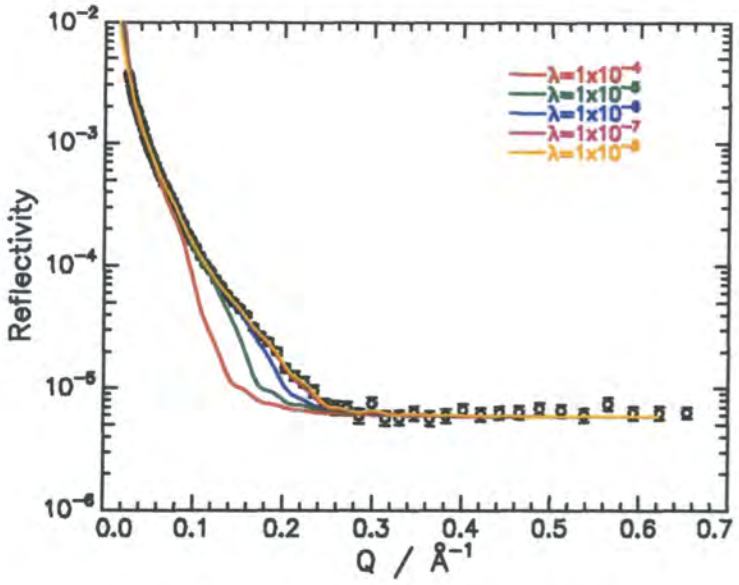

Figure 6.3.45. Model independent fits using various values of λ (lines, see legend) to the reflectivity curve of DPMMA-Q(H)P4VP on NRW, $\Gamma_s = 3.0 mgm^{-2}$ (circles)

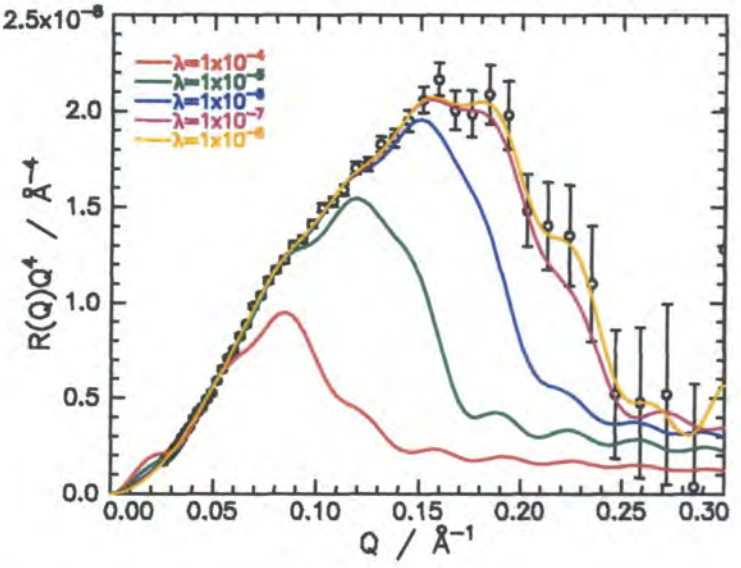

Figure 6.3.46. Model independent fits using various values of λ (lines, see legend) to R(Q)Q^4 data from DPMMA-Q(H)P4VP on NRW, $\Gamma_s = 3.0 mgm^{-2}$ (circles)

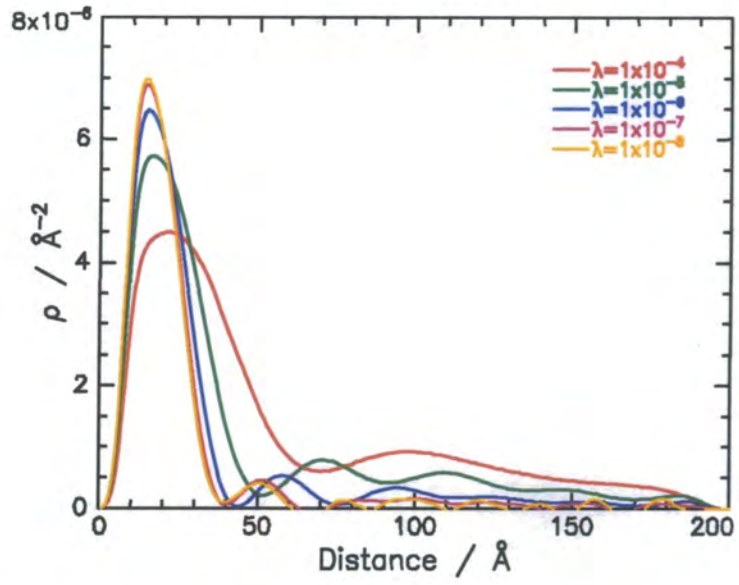

Figure 6.3.47. Plots of scattering length density against distance from an arbitrary origin obtained from fits in figure 6.3.43

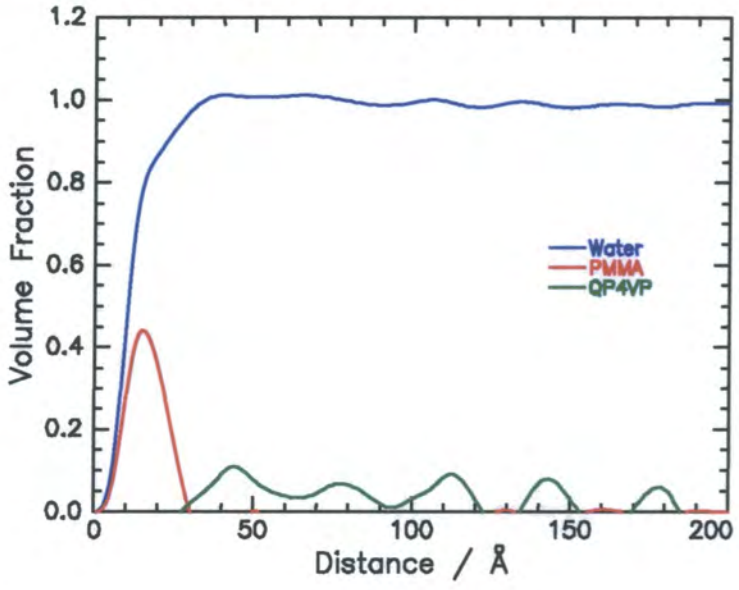

Figure 6.3.48. Volume fraction of the three components against distance, Γ_s = 1.0mg m^{-2}

system and varying the separations of the other two from this until the most realistic profile is obtained. A good indication of such an occurrence is given when the total volume fraction of the three components is equal to unity over the whole interfacial region. The outcome of this procedure is shown in figures 6.3.49a-d, which give the final volume fraction profiles obtained for each of the surface concentrations studied.

In all cases, the basic shapes of the profiles are highly similar. The PMMA block is represented by a single layer of gradually increasing volume fraction and thickness. The water layer is described by a tanh-like function, which gradually rises from a volume fraction of zero to that of unity, corresponding to bulk water. The results for the QP4VP block are once again problematic due to the low reflectivity recorded. For all surface concentrations studied, it can clearly be seen that no real information on the block is obtainable. An oscillatory volume fraction profile is observed, indicating that the signal cannot be extracted from the noise in the system. There is some evidence that one layer of QP4VP exists in the same region as the end of the PMMA layer, although this is highly debatable.

Notwithstanding this lack of information on the QP4VP block of the system, the results generally confirm those attained by the kinematic approximation and optical matrix approaches. The profiles for the PMMA and water components of the system bear great similarities to those obtained previously. The anomalous result of an 'overdense' water layer is again recorded for the 3.0mg m^{-2} system, the volume fraction of the water layer at one stage being greater than unity. All three fitting techniques therefore yield similarly unexpected results. This implies that either some unusual behaviour occurs at this highest surface concentration, or that the data set is in some way erroneous.

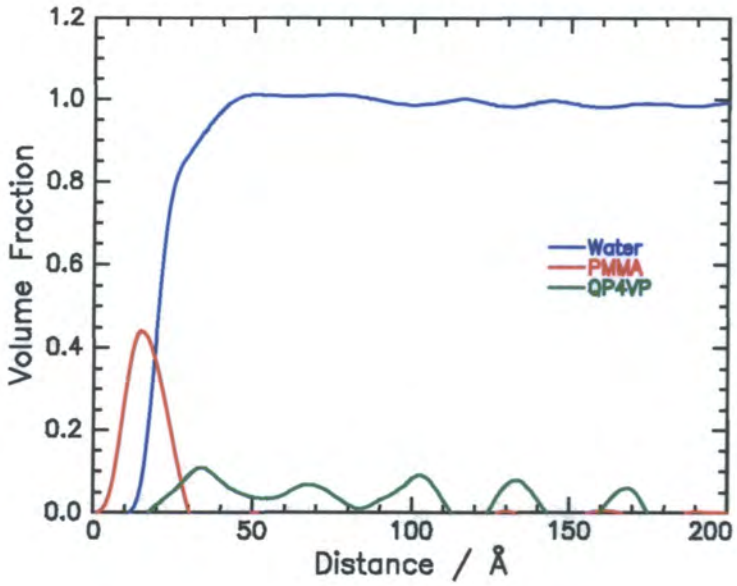

Figure 6.3.49a. Volume fraction profile for Γ_s = 1.0mg m^{-2} obtained from model independent fitting. Layer separations included

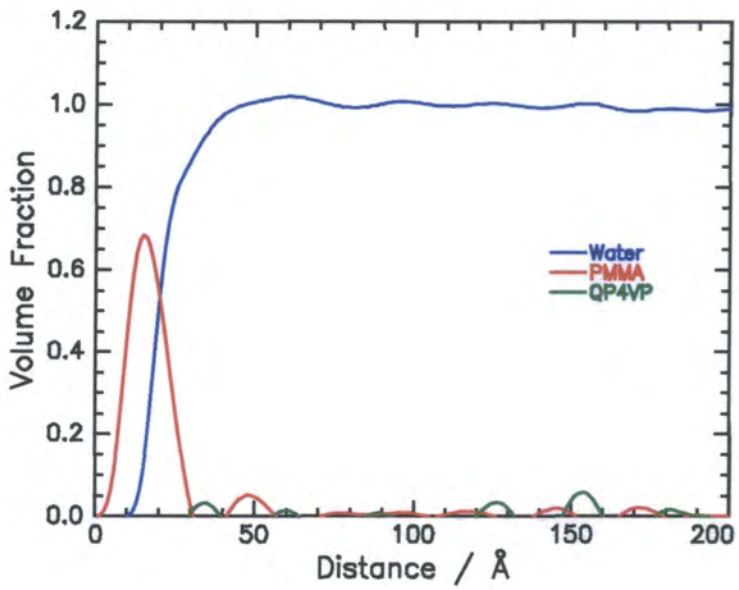

Figure 6.3.49b. Volume fraction profile for Γ_s = 1.5mg m^{-2} obtained from model independent fitting. Layer separations included

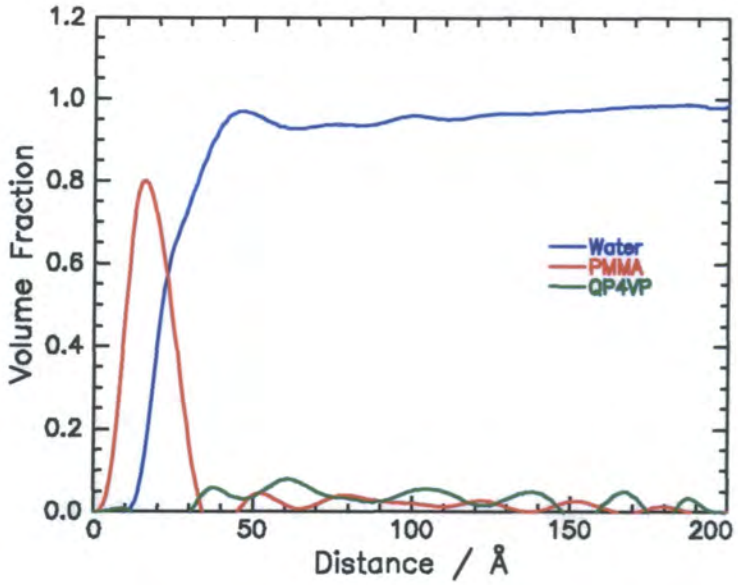

Figure 6.3.49c. Volume fraction profile for Γ_s = 2.0mg m^{-2} obtained from model independent fitting. Layer separations included

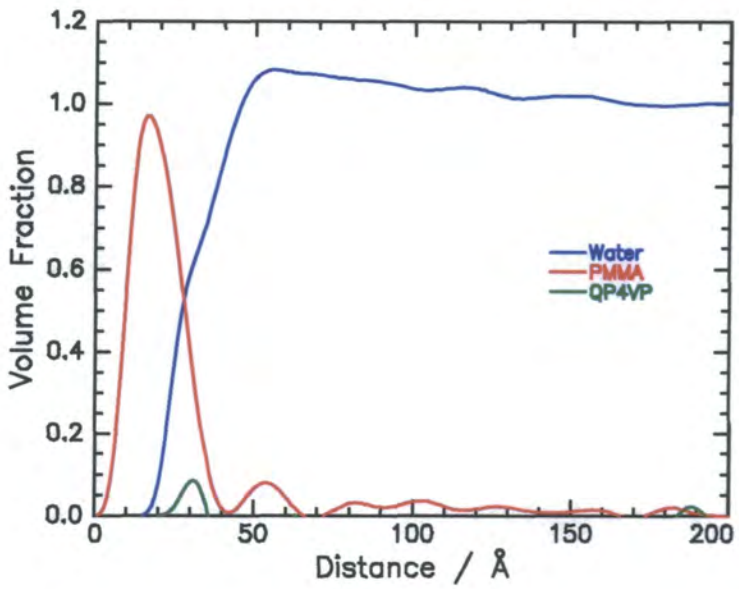

Figure 6.3.49d. Volume fraction profile for Γ_s = 3.0mg m^{-2} obtained from model independent fitting. Layer separations included

6.3.6. FURTHER DATA

In addition to the four polymer surface concentrations on water whose results are presented and analysed above, an additional series of experiments were also undertaken. These studied surface concentrations of 2.2 and 2.5mg m^{-2}, along with a repeat of the 1.5mg m^{-2} data.

For reasons eventually assigned to problems with instrumental set-up and alignment, the data obtained from these experiments is unreliable. This is best outlined by the low Q region of the reflectivity data for the DPMMA-Q(H)P4VP on NRW contrast, and the PMMA partial structure factor resulting from this (figures 6.3.50 and 6.3.51 respectively). The discrepancies between the two sets of data can clearly be seen, most noticeably in the non-overlap of the two sets of data at 1.5mg m^{-2}. Furthermore, the reflectivity data for Γ_s = 2.2mg m^{-2} overlaps somewhat the original data for Γ_s = 2.0mg m^{-2}. For each of the sets of data discussed here, the recorded reflectivity is lower than expected. To rectify this situation, it was attempted to 'correct' all the raw reflectivity data by the introduction of a scaling factor calculated from the difference in reflectivity of the two sets of 1.5mg m^{-2} data. Assuming that the original data were correct and the repeated data subject to instrumental artefacts, the following scaling factors were calculated and used to correct the more recent sets of data:

Contrast	Scaling Factor
H-H on D_2O	1.147
D-H on D_2O	1.144
H-D on D_2O	1.175
D-D on NRW	1.510
D-H on NRW	1.568
H-D on NRW	1.519

Table 6.3.20. Parameters obtained from single layer fits of DPMMA-Q(H)P4VP on D_2O

The effects that this process had on the reflectivity data are shown in the corrected reflectivity and partial structure factor data (figures 6.3.52 and 6.3.53 respectively).

By eye, the data now appears to follow the trends expected, there being good agreement between the two sets of 1.5mg m^{-2} data. Furthermore, the 2.2 and 2.5mg m^{-2} data sets lie between those of 2.0 and 3.0mg m^{-2}. However, attempts to fit this

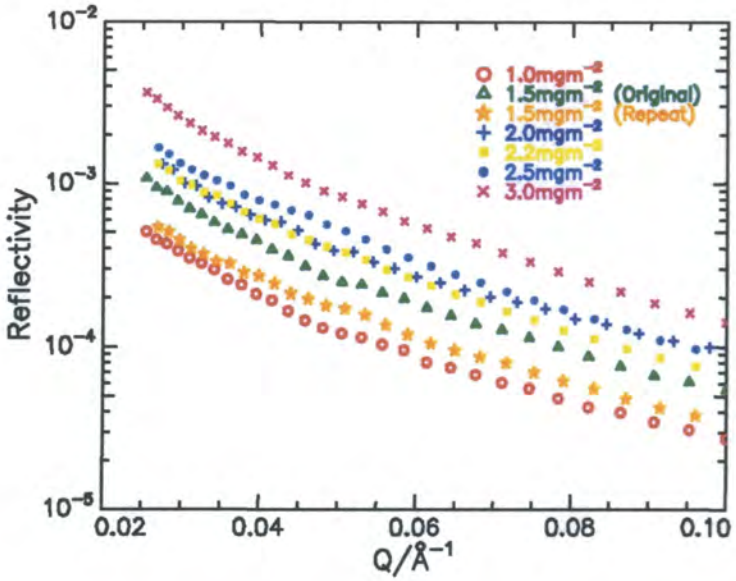

Figure 6.3.50. Low Q region of the reflectivity profiles of DPMMA-Q(H)P4VP on NRW for the full range of surface concentrations explored

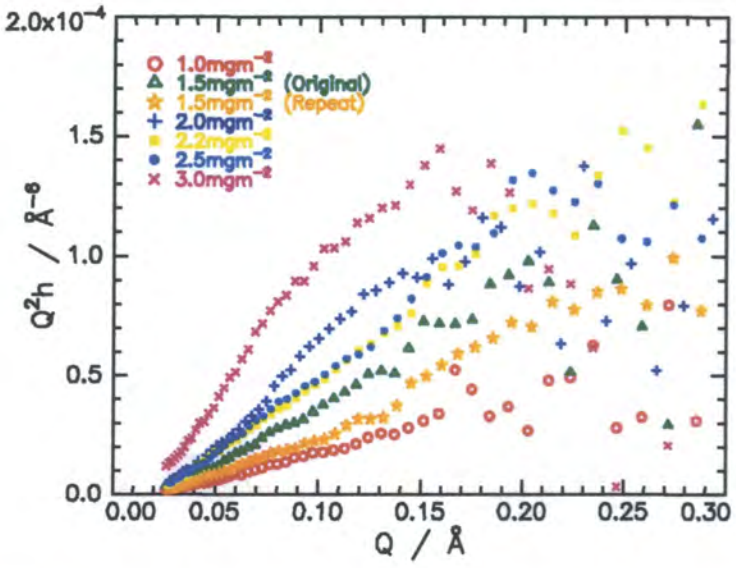

Figure 6.3.51. PMMA self partial structure factors for the full range of surface concentrations explored

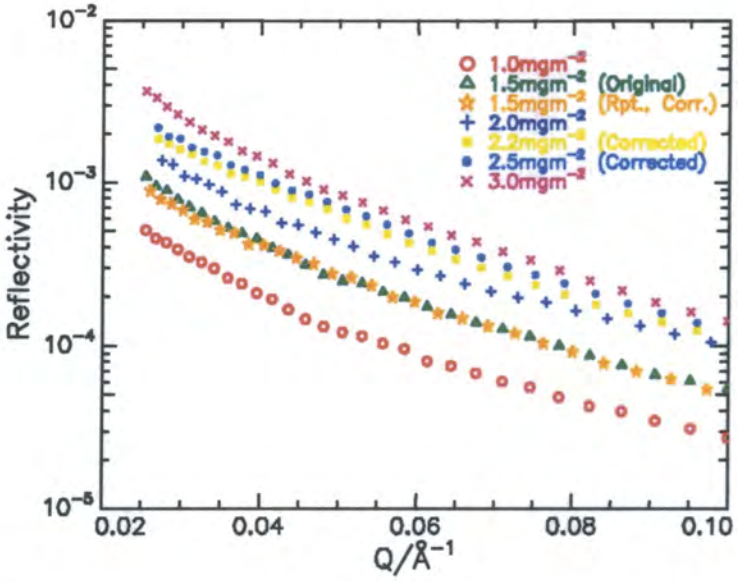

Figure 6.3.52. Low Q region of the reflectivity profiles of DPMMA-Q(H)P4VP on NRW for the full range of surface concentrations explored. The data for 1.5, 2.2 and 2.5mg m^{-2} has been 'corrected' by the use of a scaling factor

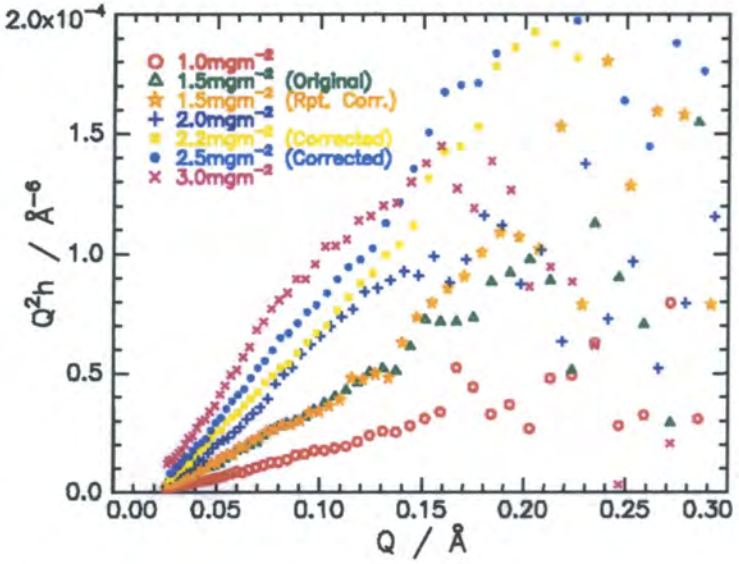

Figure 6.3.53. PMMA self partial structure factors for the full range of surface concentrations explored. The data for 1.5, 2.2 and 2.5mg m^{-2} has been 'corrected' by the use of a scaling factor

modified data by any of the three techniques used above was either to prove unsuccessful or to yield unrealistic results. This was especially true for the component of the system most sensitive to small changes in reflectivity, the QP4VP block.

Further attempts to salvage some information from the data were carried out by changing either the scaling factors or the values of background reflectivity to be subtracted from the data sets. Although this did result in some improvements, there was no real justification for either of the methods used.

It was therefore concluded that without the use of an excessive number of unjustifiable assumptions or by changing specific parameters in a non-systematic fashion, no reliable information could be extracted form these data sets, and further analysis was abandoned.

6.3.7. SUMMARY

The results obtained from the application of neutron reflectometry to study the organisation of PMMA-QP4VP at the air-water interface are summarised briefly below:

1. The kinematic approximation best described the PMMA and QP4VP blocks as single Gaussian and single parabolic layers respectively.
2. The water self partial structure factors exhibited unusual behaviour at higher surface concentrations and such a distribution was best defined as either a tanh or a double uniform layer function. However, one of the latter models included a layer of unusually high number density.
3. By obtaining the separations between these layers from analysis of the cross partial structure factors, a series of number density profiles were generated.
4. From these, the most significant changes observed with increasing polymer surface concentration are the increase in number density of the PMMA block and the increase in thickness of the QP4VP block.
5. Model independent fitting gave highly similar results to those obtained by the kinematic approximation, the distribution of the PMMA and water layers showing the highest correlation with those obtained from the kinematic approximation. Unfortunately, the uncertainties inherent in the experimental data prevented information regarding the distribution of the QP4VP being obtained. The incorporation of arbitrary layer separations to these results allowed the production of volume fraction profiles.
6. The only data analysis method to prove unsuccessful was the optical matrix approach, where problems encountered in fitting a number of the reflectivity curves rendered it impossible to obtain a complete description of the copolymer at the interface.

6.4 POTASSIUM CHLORIDE SOLUTION SUBPHASES

Neutron reflectometry was also used to study films of the PMMA-QP4VP polymer on subphases of 10^{-3}M, 0.1M and 1M potassium chloride solutions. The surface concentration of such films was, in all cases, 3.0mg m^{-2}. Each data analysis technique was described in full in section 6.3 and this section therefore concentrates predominately on the results obtained from such analysis methods.

6.4.1. REFLECTIVITY DATA

As for the experiments on water, a full set of six contrasts were recorded for each salt solution. As an example of the data obtained, a comparison of the reflectivity profiles for HPMMA-Q(H)P4VP on salt solutions of D_2O and DPMMA-Q(D)P4VP on salt solutions of NRW are given. Generally, the characteristics of the reflectivity profiles are highly similar to those obtained for films of the same polymer concentration spread on a water subphase (section 6.3.1).

Figure 6.4.1 shows the data obtained for HPMMA-Q(H)P4VP on D_2O. A region of the curve at intermediate Q range ($0.10 < Q / Å^{-1} < 0.20$) is enlarged in figure 6.4.2. At low Q, the introduction of salt into the subphase seems to somewhat depress the measured reflectivity. A different behaviour is exhibited at higher Q, where the film spread on a subphase of 0.1M KCl yields the highest reflectivity. However, such an effect occurs near the onset of background and therefore may not be due to reflectivity alone. The remaining three subphases report similar values of reflectivity, although reflectivity is depressed to the greatest extent by the lowest salt concentration subphase (10^{-3}M KCl).

Similar behaviour is exhibited by a film of DPMMA-Q(D)P4VP spread upon NRW (figures 6.4.3 and 6.4.4). Again, the data for the 0.1M KCl solution shows the highest reflectivity. In this case however, the lowest reflectivity is recorded by 1M KCl. The two remaining sets of data, on subphases of water and 0.1M KCl are highly similar.

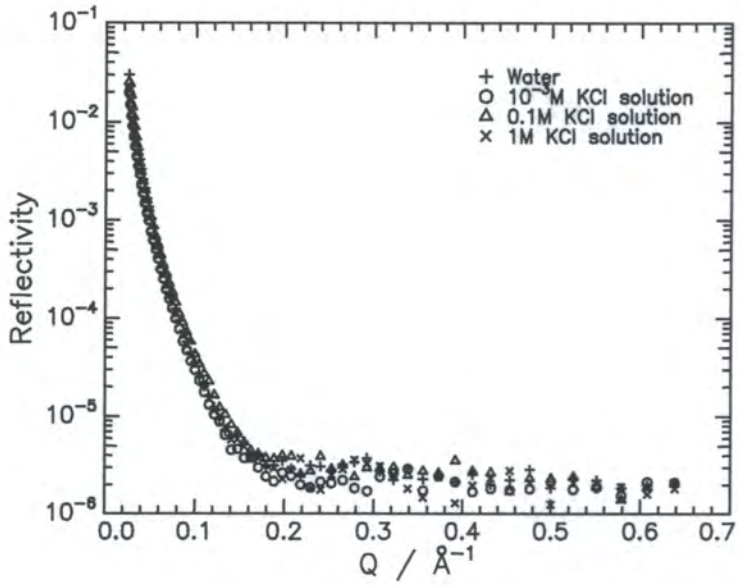

Figure 6.4.1. Reflectivity profiles for HPMMA-Q(H)P4VP on D_2O salt solution and water subphases (see legend). Γ_s = 3.0mg m^{-2}

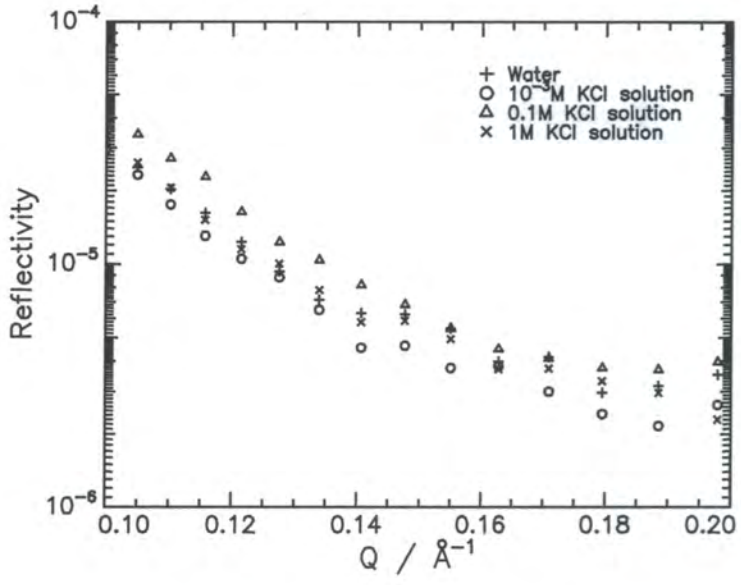

Figure 6.4.2. Expansion of the Q range 0.10 < Q/Å^{-1} < 0.20 in figure 6.4.1

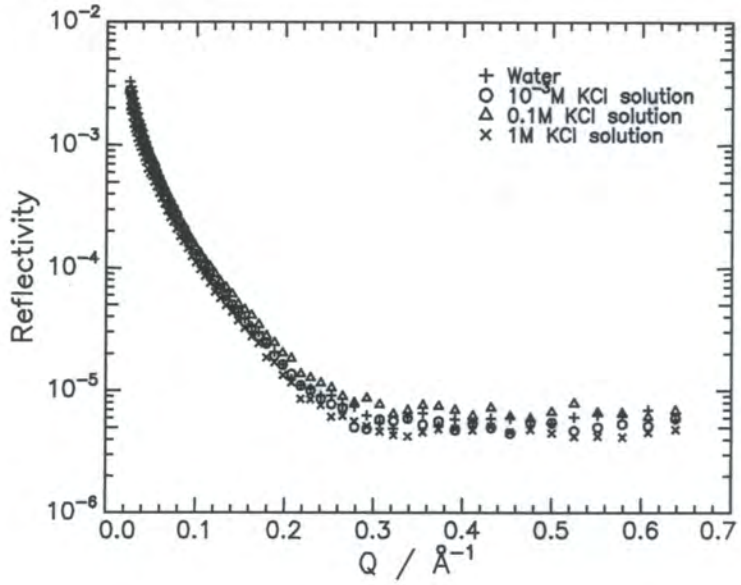

Figure 6.4.3. Reflectivity profiles for DPMMA-Q(D)P4VP on NRW salt solutions. Γ_s = 3.0mg m^{-2}

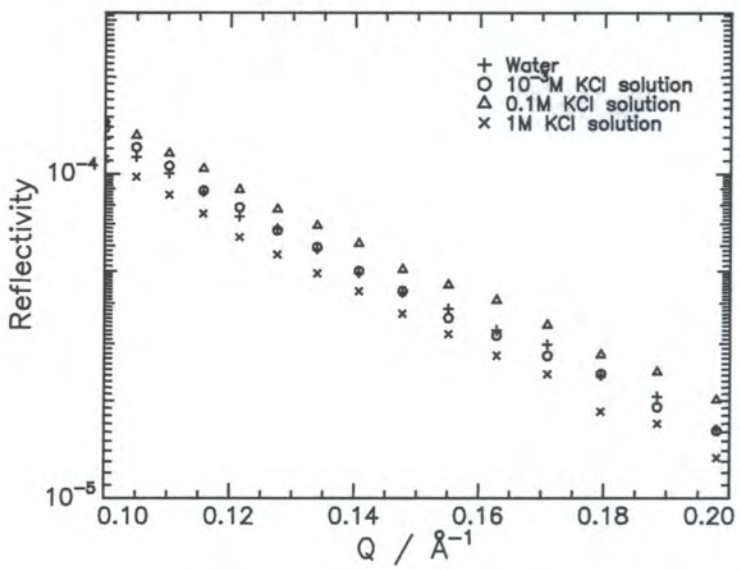

Figure 6.4.4. Expansion of the Q range 0.10 < Q/Å^{-1} < 0.20 in figure 6.4.3

6.4.2. Discussion

The difference in reflectivities between the data obtained on water and that on salt solutions is shown in figure 6.4.2. Such a difference corresponds to a change in the properties of both the polymer film and the water layer. The effect is minimal for the 1M subphase, but more significant for the lower salt concentrations. By comparing the experimental data to the simulations in figures 6.3.8 and 6.3.11, an idea of the nature of such a change can be obtained. It appears when spread upon a solution of 0.1M KCl solution, the interfacial film is thinner and of a higher scattering length density than when spread on water. The opposite effect is observed on the lowest salt concentration. Again, as the PMMA block is by far the dominant contributor to the reflectometry, such information does not necessarily imply that the QP4VP block of the polymer will behave in a similar manner.

Figure 6.4.4 shows that there is insignificant change in the polymer organisation when spread on 10^{-3}M KCl solution compared to on water. This behaviour is intuitively expected with the introduction of such a small quantity of salt. By comparing the data with figure 6.3.13, it appears that the scattering length density of the film is greatest when spread upon 1M KCl and least when on 10^{-3}M KCl. The shapes of the reflectivity profiles show little change, indicating that the film thickness (or rather the thickness of the PMMA block) remains approximately constant.

6.4.3. Partial Structure Factor Analysis

As for the water subphase, the data for the six contrasts permitted application of the kinematic approximation to determine the organisation of the polymer at the interface. Data fitting was identical with that in section 6.3.3.

6.4.3.1. Error Quantification

To give an indication of the reliability of the partial structure factor data, an knowledge of the errors on each of the data points was required. As the program used to generate the partial structure factors did not return uncertainties, the errors

were calculated manually. One salt concentration, 0.1M, was selected for study and the errors on three data points were calculated for each of the six partial structure factors. The points selected, at Q = 0.0261, 0.0802 and 0.167Å^{-1}, were chosen to give an indication of the errors at low, intermediate and high values of Q. The results obtained are given numerically (as the percentage error of the value of Q^2h) in table 6.4.1 and represented as graphically as error bars on the partial structure factors in figure 6.4.5.

Partial Structure Factor	Q = 0.0261Å^{-1}	Q = 0.0802Å^{-1}	Q = 0.167Å^{-1}
PMMA self	2.6%	2.6%	11.6%
QP4VP self	14.3%	19.9%	134.4%
water self	3.1%	5.3%	61.5%
PMMA – water cross	16.6%	4.8%	17.9%
PMMA – QP4VP cross	11.5%	13.5%	254.5%
QP4VP – water cross	85.5%	72.4%	161.0%

Table 6.4.1. Partial structure factor errors

A number of conclusions may be drawn form the above data. Firstly, as expected, the data at the lowest two Q values contain substantially smaller errors than those at Q = 0.167Å. These larger errors are a result of the lower reflectivity recorded in this near-background region. A similar rationalisation is given for the observation that the largest errors are reported for those structure factors incorporating QP4VP. Finally, the self partial structure factor data are, in the majority of cases, more reliable that than of the cross terms, because the latter result from combining two data sets each incorporating their own errors.

At low Q, the majority of the partial structure factors contain only small errors. At higher Q, these errors become more substantial, especially for those partial structure factors including QP4VP. In these cases, the errors can exceed the data values even at intermediate Q. These inaccuracies in the data have to be taken into account when fitting procedures attempted.

6.4.3.2. Self Partial Structure Factors

The polymer self partial structure factors were fitted with a variety of layer models. As for the experiments on water, the PMMA self partial structure factor was again

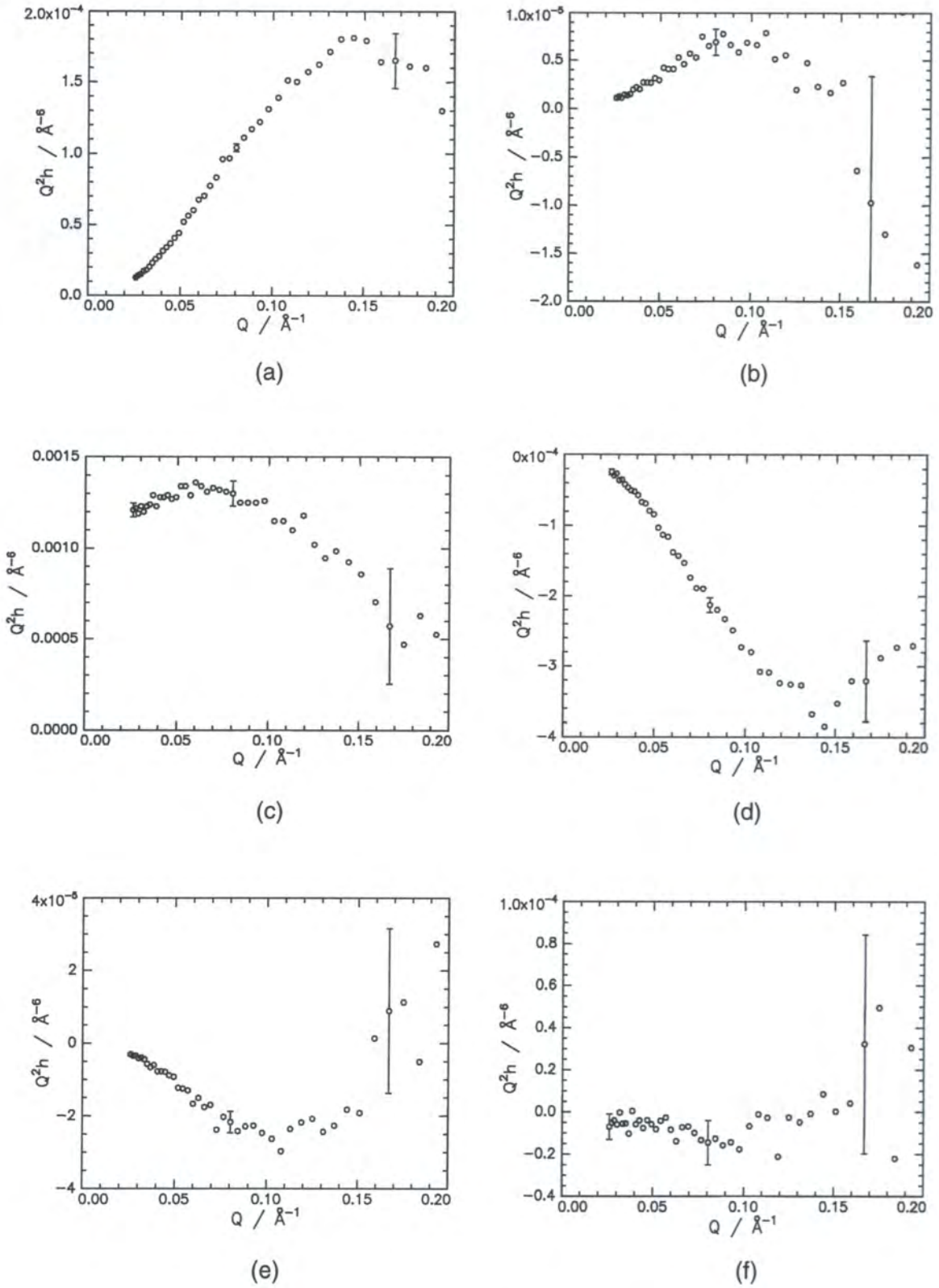

Figure 6.4.5. Partial structure factors obtained on 0.1M KCl solution with the errors on the points indicated at Q = 0.0261, 0.0802 and 0.167Å^{-1}. (a) PMMA self term (b) QP4VP self term (c) water self term (d) PMMA – water cross term (e) PMMA – QP4VP cross term (f) QP4VP – water cross term

best described by a single Gaussian layer model. The data for the QP4VP self term were again highly scattered, but adequate fits were attainable by use of a single parabolic model. Examples of such fits are given in figure 6.4.6 and 6.4.7 and the outputted parameters are presented in table 6.4.2.

	PMMA self PSF (Single Gaussian layer)		QP4VP self PSF (Single parabolic layer)	
Subphase	**d_1 / Å**	**n_1 / 10^{-3} Å^{-3}**	**d_1 / Å**	**n_1 / 10^{-3} Å^{-3}**
10^{-3}M KCl	19.7 ± 0.3	7.43 ± 0.07	32.3 ± 1.4	0.68 ± 0.02
0.1M KCl	19.1 ± 0.2	8.66 ± 0.06	23.4 ± 0.5	1.46 ± 0.02
1M KCl	18.9 ± 0.3	7 88 ± 0.09	22.6 ± 0.3	1.56 ± 0.02

Table 6.4.2. Summary of the polymer self partial structure factors for films of PMMA-QP4VP spread on KCl solution subphases.

Clearly, the PMMA self partial structure factor exhibits an unusually high number density on 0.1M KCl solution (with regard to that of water). Little difference is observed between the layer thickness on the three subphases. The QP4VP block shows a decrease in thickness with increasing salt concentration, whereas the number density of such layers increase. The polymer surface concentrations calculated from such fits are given in table 6.4.3:

	Subphase KCl concentration		
	10^{-3}M	0.1M	1.0M
Model	**PMMA surface concentration / mg m^{-2}**		
Predicted	*2.43*	*2.43*	*2.43*
Gaussian	2.34 (3.3%)	2.65 (9.1%)	2.39 (1.7%)
	QP4VP surface concentration / mg m^{-2}		
Predicted	*0.57*	*0.57*	*0.57*
Parabolic	0.65 (13%)	1.02 (77%)	1.04 (82%)

Table 6.4.3. Calculated polymer surface concentration values (with percentage errors form the theoretical values) from partial structure factor fits

The calculated values of $\Gamma_{s,PMMA}$ show quite good correlation with the those predicted. The greatest discrepancy is found for the 0.1M subphase, which is the only salt concentration to yield a surface concentration higher than the predicted value. As for the runs on water, the calculated values of $\Gamma_{s,QP4VP}$ are substantially greater than the theoretical values, presumably due to errors caused by the QP4VP chains being submerged in the subphase and the poor quality of the data.

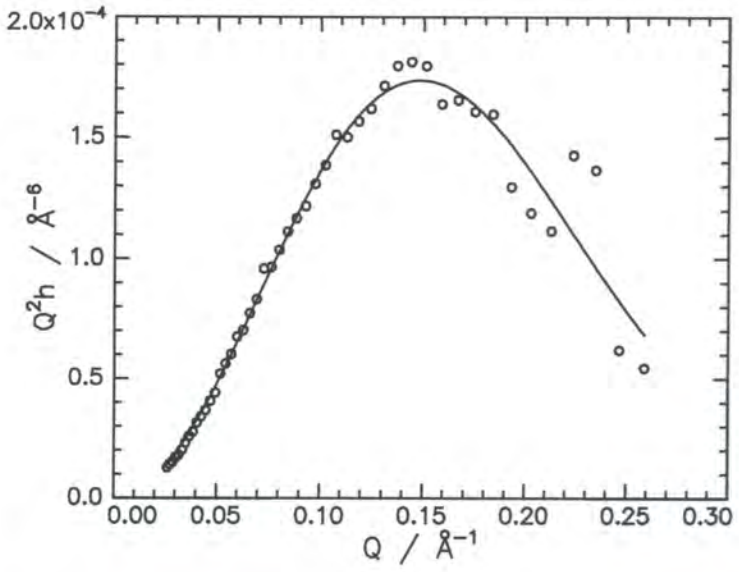

Figure 6.4.6. PMMA self partial structure factor (circles) with single Gaussian layer fit (line). 0.1M KCl solution subphase, Γ_s = 3.0mg m^{-2}

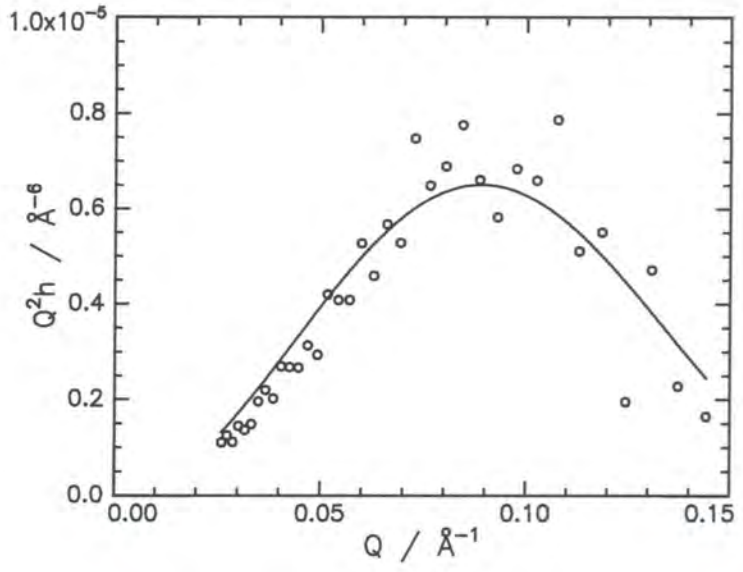

Figure 6.4.7. QP4VP self partial structure factor (circles) with single parabolic layer fit (line). 0.1M KCl solution subphase, Γ_s = 3.0mg m^{-2}

The water partial structure factors again exhibit unusual behaviour and are shown in figure 6.4.8, along with attempted fits of the data using a tanh model. The partial structure factors for 10^{-3}M and 1M KCl solution subphases are represented to an adequate extent by such a layer model and these fits are adopted here. This is clearly not the case for the data recorded on 0.1M KCl. Further layer models were then attempted and, as was the case with the water subphases, a double uniform layer model was found to give a very good representation of the data. This fit is shown in figure 6.4.9 and although a second water layer with a number density greater than that of bulk water was again found, the fit was adopted here. A summary of the fits obtained is given in table 6.4.4.

	Tanh Layer	**Double uniform water layer**			
Subphase	**σ / Å**	**d_1 / Å**	**n_1 / 10^{-2} Å^{-3}**	**d_2 / Å**	**n_2 / 10^{-2} Å^{-3}**
10^{-3}M KCl	7.8 ± 0.3	-	-	-	-
0.1M KCl	-	17.7 ± 1.6	0.59 ± 0.49	28.9 ± 9.8	3.74 ± 0.29
1M KCl	5.2 ± 0.1	-	-	-	-

Table 6.4.4. Summary of the separations obtained from the water self partial structure factors for films of PMMA-QP4VP spread on KCl solution subphases.

6.4.3.3. Cross Partial Structure Factors

Fitting of cross partial structure factors was accomplished using the same procedures described in section 6.3.3. The polymer-polymer cross terms were simulated using equation 6.3.18 and the water-polymer cross terms by using equation 6.3.19. Again, these expressions provided better quality fits than the expressions generated from the self term formulae, even in the case of the double uniform water layer model, which is approximated to an odd function. A summary of the cross partial structure factors is given in table 6.4.5.

Subphase	**$\delta_{PMMA\text{-}Water}$ / Å**	**$\delta_{PMMA\text{-}QP4VP}$ / Å**	**$\delta_{QP4VP\text{-}Water}$ / Å**
10^{-3}M KCl	9 ± 1	15 ± 2	10 ± 2
0.1M KCl	8 ± 1	6 ± 1	2 ± 1
1M KCl	7 ± 1	4 ± 1	3 ± 1

Table 6.4.5. Summary of the separations obtained from the cross partial structure factors for films of PMMA-QP4VP spread on KCl solution subphases.

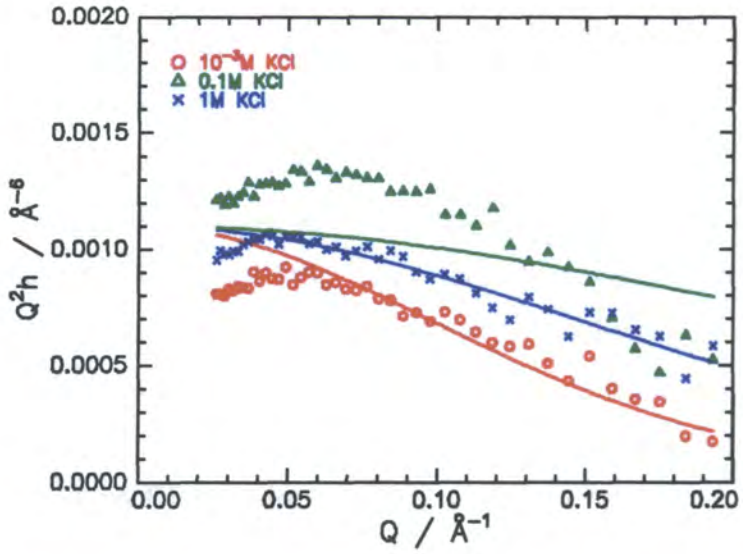

Figure 6.4.8. Water self partial structure factors (symbols) with tanh layer fits (line). KCl solution subphases (see legend), Γ_s = 3.0mg m^{-2}

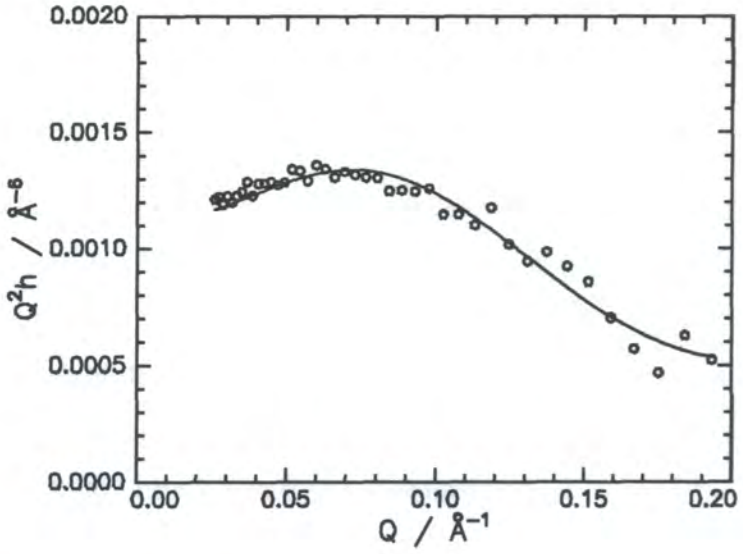

Figure 6.4.9. Water self partial structure factor (circles) with double uniform water layer fit (line). 0.1M KCl solution subphase, Γ_s = 3.0mg m^{-2}

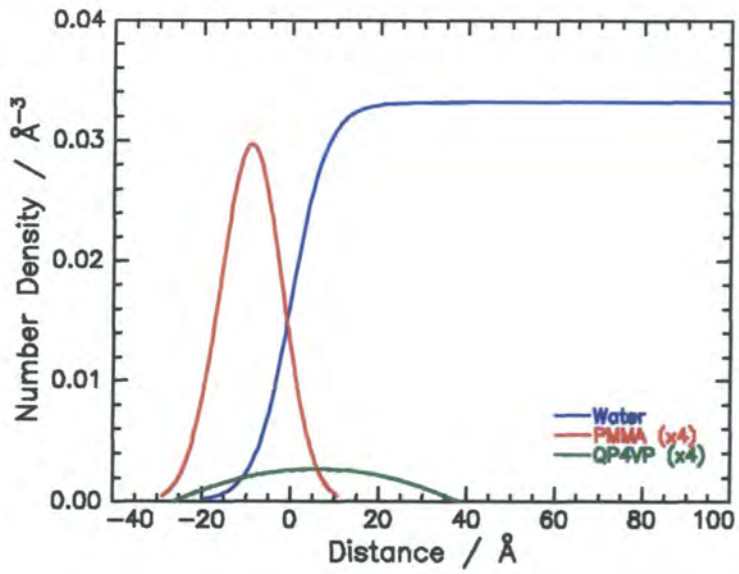

Figure 6.4.10a. Number density profile. 10^{-3}M KCl solution, Γ_s = 3.0mg m^{-2}

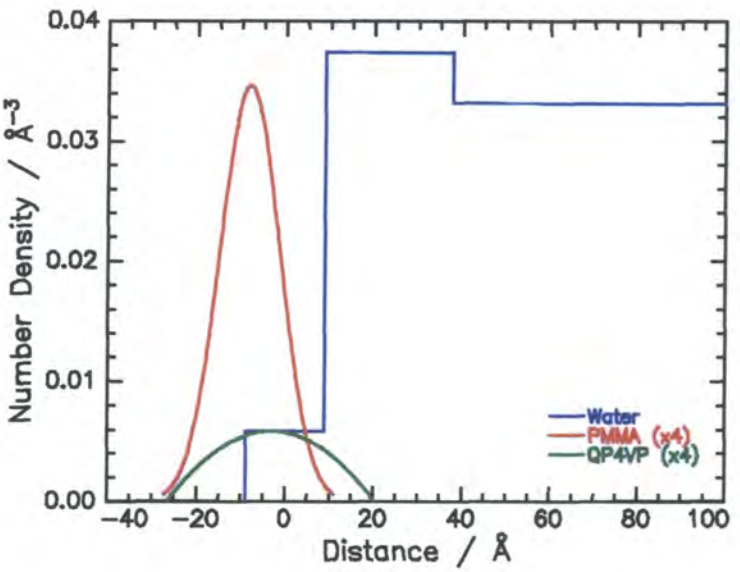

Figure 6.4.10b. Number density profile. 0.1M KCl solution, Γ_s = 3.0mg m^{-2}

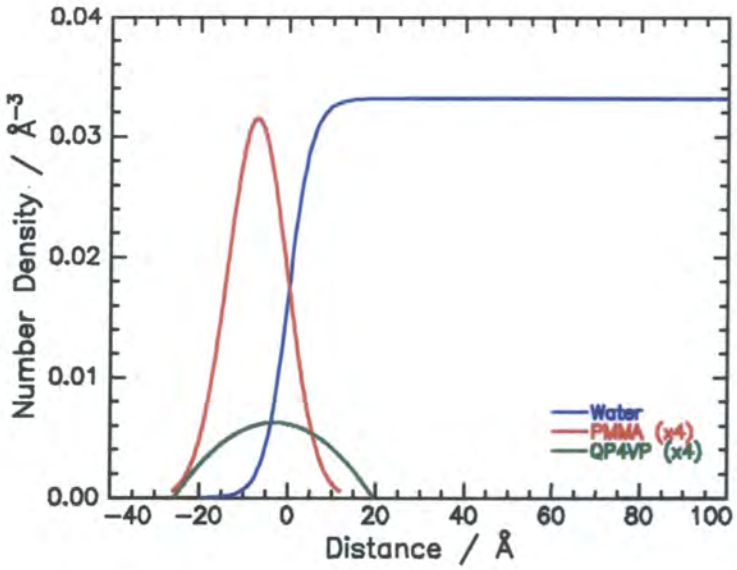

Figure 6.4.10c. Number density profile. 1M KCl solution, $\Gamma_s = 3.0$mg m^{-2}

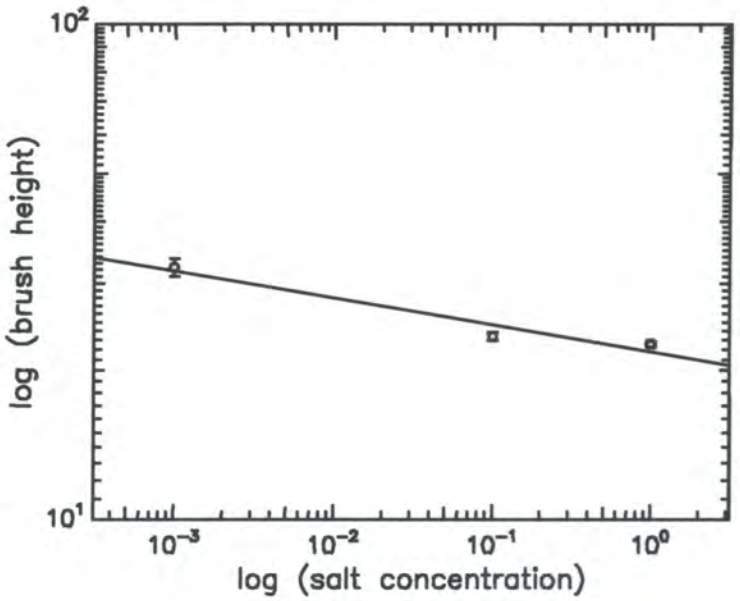

Figure 6.4.11. Plot of log (brush height) against log (salt concentration) overlayed with a least squares fit (line) to calculate the scaling factor in equation 6.3.21.

KCl conc. / mol l^{-1}	Brush height / Å
10^{-3}	32.3 ± 1.4
0.1	23.4 ± 0.5
1.0	22.6 ± 0.3

Table 6.4.6. Polyelectrolyte brush heights

Although only three data points are available (table 6.4.6), a straight line plot is obtained, a linear least squares fits of which gives a gradient of –0.055 and an intercept of 1.34, i.e. $h \sim c_s^{-0.055}$. Although the sign of this scaling factor is correct, there is clearly a large discrepancy between the experimentally obtained and theoretical values. The reasons for such a discrepancy are difficult to determine, although as discussed in section 6.3.3.8, the discrepancy could arise from the polyelectrolyte brush length being too small to follow the predicted behaviour. A further possible cause is the existence of a surface depletion layer which may render the salt concentration of the region of the polymer chains different to that of the bulk solution, thus affecting the above calculation. This is explored by comparison with data in the literature[18] (table 6.4.7).

KCl concentration / mol l^{-1}	Surface deficiency / μmol m^{-2}	Debye length / Å	Brush height / Å
0.1	-0.035	9.8	23.4
1.0	-0.380	3.0	22.6

Table 6.4.7. Values of surface deficiency and Debye length for KCl solutions

Two points from this table are of importance. Firstly, the values of surface deficiency for these KCl concentrations are quite small. Any surface depletion layer will therefore also be small and have a negligible effect upon any calculations. Secondly, the Debye lengths of the solutions are less than the QP4VP brush lengths, signifying that the polymer brush extends well into the bulk solution.

Counterion condensation theory[19] developed by Manning[20] could also be a contributory factor. A fraction of the counterions may be located in the same region as the polyelectrolyte chains, having the effect of reducing the effect charge on the brushes. This will have the effect of complicating the system, which can no longer be reduced to a simple Debye-Hückel screening.

In an attempt to recalculate the scaling factor, the brush height was redefined as the distance from the 'end' of the PMMA layer (at half height of the Gaussian distribution) to the end of the parabolic QP4VP distribution. This could be calculated simply by the summation of d_{QP4VP} and $\delta_{PMMA\text{-}QP4VP}$. Such a calculation gives 'brush heights' of 47.3, 29.4 and 26.6Å for 10^{-3}M, 0.1M and 1M subphases respectively, resulting in a scaling factor of –0.09. Although this value is closer to theory than that above, there remains a large discrepancy.

6.4.4. Optical Matrix Analysis

The increased reflectivity recorded due to the high polymer surface concentration (3.0mg m^{-2}), meant that it was possible to obtain fits for the all of the six contrasts, including HPMMA-Q(D)P4VP on NRW. By fitting three of these, one corresponding to each component of the system, it was attempted to obtain a complete description of the polymer at the interface. Each of these three contrasts are discussed in turn:

6.4.4.1. DPMMA-Q(H)P4VP on NRW

The reflectivity curves for DPMMA-Q(H)P4VP on NRW could be fitted to a sufficient extent by the use of a single layer. However, much better fits could be obtained by the introduction of a second layer, albeit with an extremely small scattering length density. An example of such a fit is given in figure 6.4.12, with the resulting parameters presented in table 6.4.8.

Subphase	d_1 / Å	ρ_1 / 10^{-6} Å^{-2}	d_2 / Å	ρ_2 / 10^{-8} Å^{-2}
10^{-3}M KCl	19.3 ± 1.4	6.15 ± 0.36	15.0 ± 1.2	9.91 ± 2.09
0.1M KCl	18.9 ± 1.3	6.89 ± 0.35	10.5 ± 0.7	5.40 ± 1.20
1M KCl	19.5 ± 1.3	6.13 ± 0.40	24.3 ± 1.5	8.12 ± 1.13

Table 6.4.8. Parameters obtained from double layer fits of DPMMA-Q(H)P4VP on NRW. Γ_s = 3.0mg m^{-2}

The fits obtained to data on 10^{-3}M and 1M KCl solutions are highly similar. The most unusual result is again obtained with 0.1M KCl, where the first polymer layer

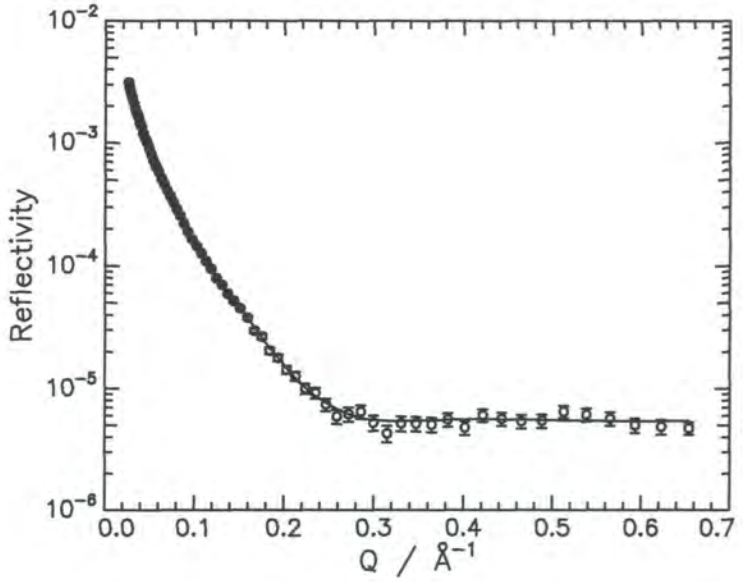

Figure 6.4.12. Double layer fit (line) to reflectivity curve of DPMMA-Q(H)P4VP on NRW. Subphase = 10^{-3}M KCl solution, Γ_s = 3.0mg m^{-2}

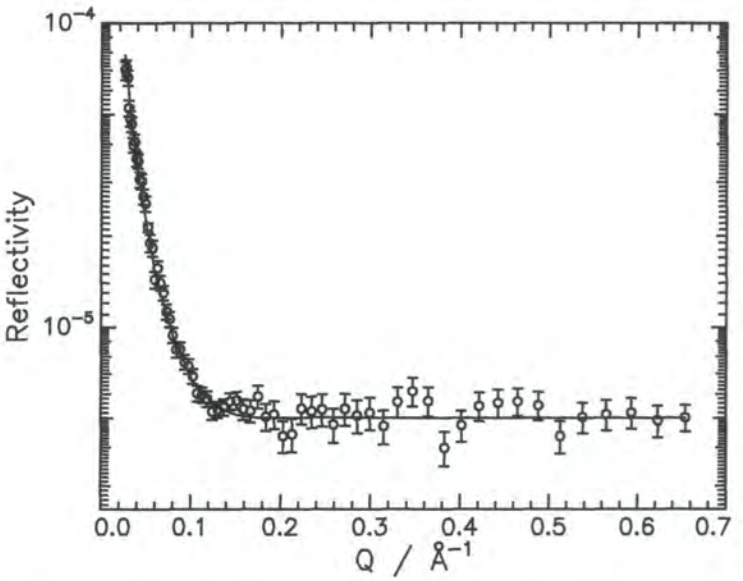

Figure 6.4.13. Single layer fit (line) to reflectivity curve of HPMMA-Q(D)P4VP on NRW. Subphase = 10^{-3}M KCl solution, Γ_s = 3.0mg m^{-2}

as found to have a high scattering length density, greater than that of D_2O or PMMA.

Again, assuming that the PMMA block is the sole contributor to the measured reflectivity, the use of equations 6.3.25 and 6.3.26 allows the volume fraction and surface concentration of PMMA to be calculated. In such calculations, the scattering length density of the second layer is assumed to be negligible. The results obtained are given in table 6.4.9.

Subphase	ϕ_i	$\Gamma_{s,PMMA}$		Error
		Calculated	***Predicted***	
10^{-3}M KCl	1.02	2.19	*2.43*	9.9%
0.1M KCl	1.15	2.40	*2.43*	1.2%
1.0M KCl	1.02	2.20	*2.43*	9.5%

Table 6.4.9. Volume fractions and surface concentrations of PMMA obtained from optical matrix analysis

As for the results from partial structure factor analysis, the calculated value of $\Gamma_{s,PMMA}$ is greatest for a subphase of 0.1M KCl solution, although here the result is slightly less than the theoretical value. The remaining results report lower values of surface concentration, which has previously been explained by the polymer being partially disrobed from the liquid surface. Here, a second, dilute layer of PMMA is observed to stretch into the subphase. Due to the extension of the QP4VP chains into the salt solution subphases, it is suggested that a small quantity of the PMMA is being 'pulled' into the liquid, thus creating this second layer of very low scattering length density.

6.4.4.2. HPMMA-Q(D)P4VP on NRW

The reflectivity curves for HPMMA-Q(D)P4VP on NRW were fitted in an attempt to obtain a description of the form of the QP4VP block. All of the profiles could be adequately fitted by a single layer model, an example being given in figure 6.4.13. The incorporation of further layers did not improve the quality of the fits. The parameters extracted are given in table 6.4.10.

Subphase	d_1 / Å	ρ_1 / 10^{-7} Å^{-2}
10^{-3}M KCl	32.8 ± 1.6	5.62 ± 0.65
0.1M KCl	33.6 ± 1.7	5.53 ± 0.72
1M KCl	32.3 ± 1.6	4.80 ± 0.69

Table 6.4.10. Parameters obtained from double layer fits of HPMMA-Q(D)P4VP on NRW. Γ_s = 3.0mg m^{-2}

This fitting technique returns similar layer thickness on all three salt subphases, a different result to that obtained using the kinematic approximation, where the QP4VP block decreases in length with increasing salt concentration. This is discussed below.

6.4.4.3. HPMMA-Q(H)P4VP on D_2O

The contrasts of HPMMA-Q(H)P4VP on D_2O were best represented by double layer models. An example of such a fit is given in figure 6.4.14 and the parameters given in table 6.4.11.

Subphase	d_1 / Å	ρ_1 / 10^{-6} Å^{-2}	d_2 / Å	ρ_2 / 10^{-6} Å^{-2}
10^{-3}M KCl	12.6 ± 1.1	3.04 ± 0.20	21.2 ± 1.6	5.56 ± 0.20
0.1M KCl	18.8 ± 1.2	2.97 ± 0.21	19.9 ± 2.0	7.64 ± 0.31
1M KCl	10.3 ± 0.7	3.30 ± 0.18	20.7 ± 1.5	5.82 ± 0.27

Table 6.4.11. Parameters obtained from double layer fits of HPMMA-Q(H)P4VP on D_2O. Γ_s = 3.0mg m^{-2}

The data for the lowest and highest salt concentrations are very similar. An initial layer of intermediate scattering length density is followed by a second, with a scattering length density slightly less that than of D_2O. The 0.1M data again returns the anomalous result that the second layer has a very high scattering length density. This is a similar result to that returned by the kinematic approximation, where the data can only be fitted by the inclusion of a model that includes a number density greater than that of bulk water.

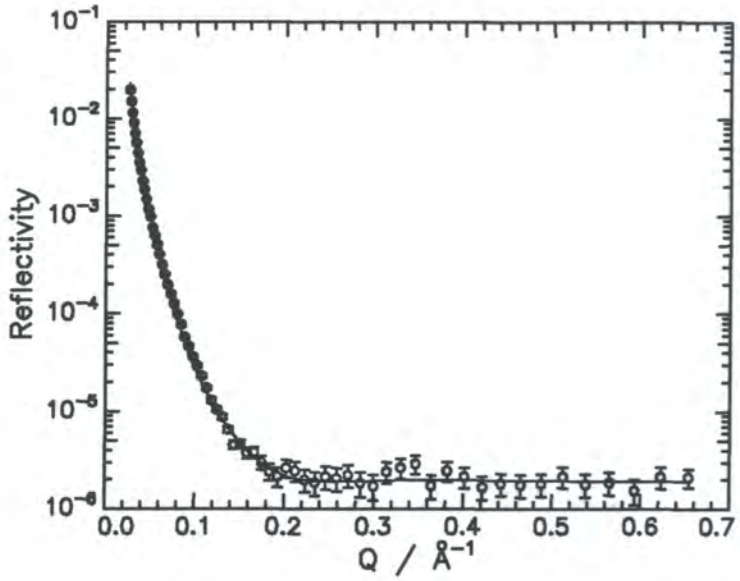

Figure 6.4.14. Double layer fit (line) to reflectivity curve of HPMMA-Q(H)P4VP on D_2O. Subphase = 10^{-3}M KCl solution, Γ_s = 3.0mg m^{-2}

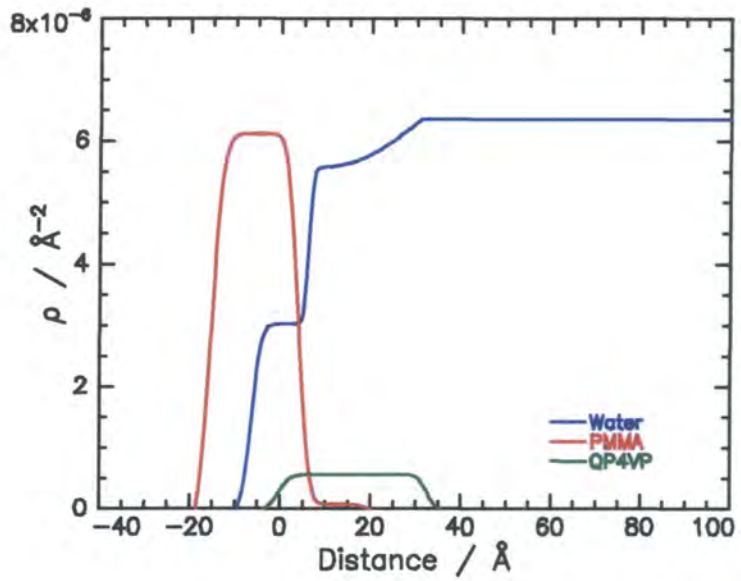

Figure 6.4.15a. Scattering length density profile of each component of the system obtained from optical matrix analysis. Subphase = 10^{-3}M KCl solution, Γ_s = 3.0mg m^{-2}

6.4.4.4. Discussion

The high values of scattering length density recorded for the fits of both DPMMA-Q(H)P4VP and HPMMA-Q(D)P4VP on NRW mean that it is impossible to produce a volume fraction block profile from the parameters outputted here. Any attempts at such a procedure result in volume fractions greater than unity being recorded. An alternative way to represent the organisation of the system at the interface is to take a similar approach to that in the model independent fitting technique (section 6.3.5) and plot the scattering length density profiles with arbitrary separations. To do this, it has to be assumed that the only factor contributing to the reflectivity of each of the contrasts is from the deuterated component. If this is indeed the case, the contrasts D-H/NRW, H-D/NRW and H-H/D_2O are used to represent the PMMA, QP4VP and water layers respectively.

The results obtained in this manner are presented in figures 6.4.15a-c. The layer separations used in the production of these plots are those obtained from the kinematic approximation analysis (table 6.3.13), the centre of the first water layer being defined as zero depth.

The profiles obtained from the kinematic approximation and this approach (figures 6.4.10 and 6.4.15 respectively) show great similarities. The PMMA blocks show similar characteristics, although those from the optical matrix analysis incorporate a second layer of very small scattering length. The water layers are also highly comparable. The lowest and highest salt concentration subphases show relatively smooth water profiles (similar to the tanh profiles returned by the kinematic approximation), while the 0.1M concentration again exhibits a layer of high scattering length density at around 20Å depth.

The structure of the QP4VP block initially seems to differ between the two sets of analyses, the optical matrix approach appearing to give a block with thickness independent of salt concentration. However, closer examination of the data reveals that there does appear to be a decrease in the length of the polyelectrolyte chain with increasing subphase salt concentration. The extension of the chains beyond the first layer of the PMMA block is calculated to give an indication of the length of the P4VP chain where no other polymer is present. The values obtained are approximately 27Å, 20Å and 19Å for subphases of 10^{-3}M, 0.1M and 1M KCl respectively. The length of the QP4VP block calculated in this manner does

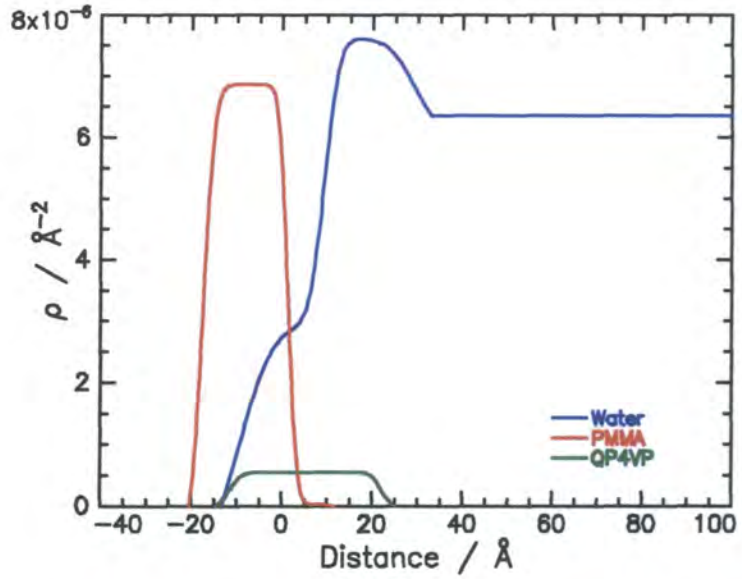

Figure 6.4.15b. Scattering length density profile of each component of the system obtained from optical matrix analysis. Subphase = 0.1M KCl solution, Γ_s = 3.0mg m^{-2}

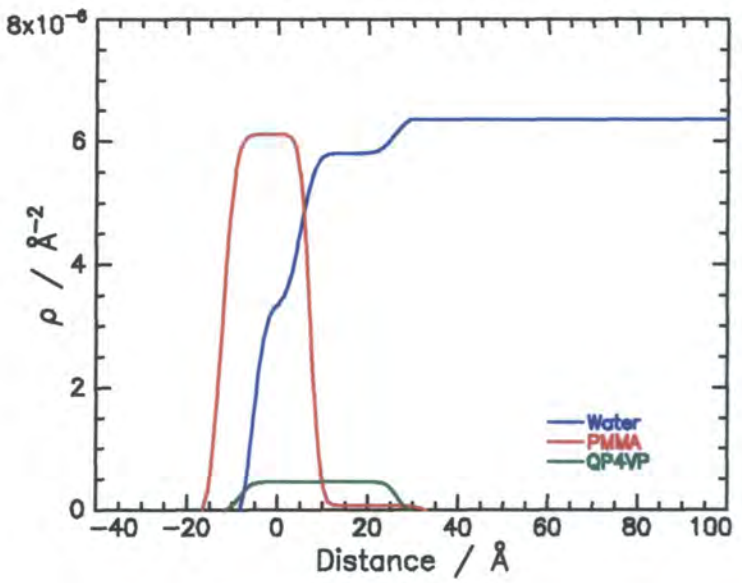

Figure 6.4.15c. Scattering length density profile of each component of the system obtained from optical matrix analysis. Subphase = 1M KCl solution, Γ_s = 3.0mg m^{-2}

therefore clearly decrease with increasing salt concentration, although again, the decrease is not of the extent predicted by scaling theory.

6.4.5. Model Independent Fitting

Model independent fitting analysis was performed in an identical manner as outlined in section 6.3.5. Plots of volume fraction against distance were produced for each salt subphase studied and these are presented in figures 6.4.16a-c. As in figures 6.3.47, zero depth has arbitrarily been defined as the upper boundary of the PMMA block and the layer separations have been determined on a 'trial-and-error' basis.
Again, the model independent fitting technique fails to give a feasible description of the organisation of the QP4VP block, an oscillatory volume fraction profile being obtained. However, in all cases there does appear to be a small and poorly defined single layer of QP4VP present as a 'tail' at the end of the PMMA block. This gives a similar picture to that obtained by the other two analysis methods.
The portrayals of the water and PMMA components also concur well with those obtained by alternative methods. The plots for the lowest and highest salt concentrations are again highly similar, whereas the polymer on 0.1M KCl solution reports unusually high volume fractions for both the water and PMMA.

6.4.6 Summary

Neutron reflectometry data obtained for films of PMMA-QP4VP spread upon potassium chloride solutions has been analysed by the kinematic approximation, optical matrix and model independent fitting techniques. From each of these, it was possible to produce a profile displaying the distributions of the three components of the system and their relative positions to one another. All three profiles obtained were found to show great similarities.
In all cases, the PMMA block shows little change with subphase concentration, although such a layer appears denser on 0.1M KCl solution. The QP4VP block was found to decrease in length as subphase salt concentration increases. This, along with the fact that the PMMA-QPVP layer separation decreases, indicates that the QP4VP chains become more 'coiled' on salt solutions of higher concentrations. The water distribution on 10^{-3}M and 1M KCl subphases can best be described by a

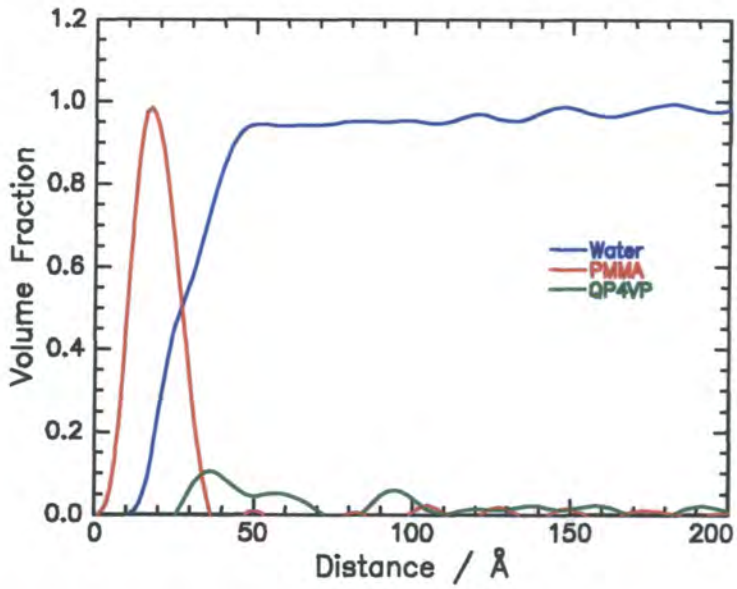

Figure 6.4.16a. Volume fraction profile obtained from model independent fitting. Subphase = 10^{-3}M KCl solution, Γ_s = 3.0mg m^{-2}

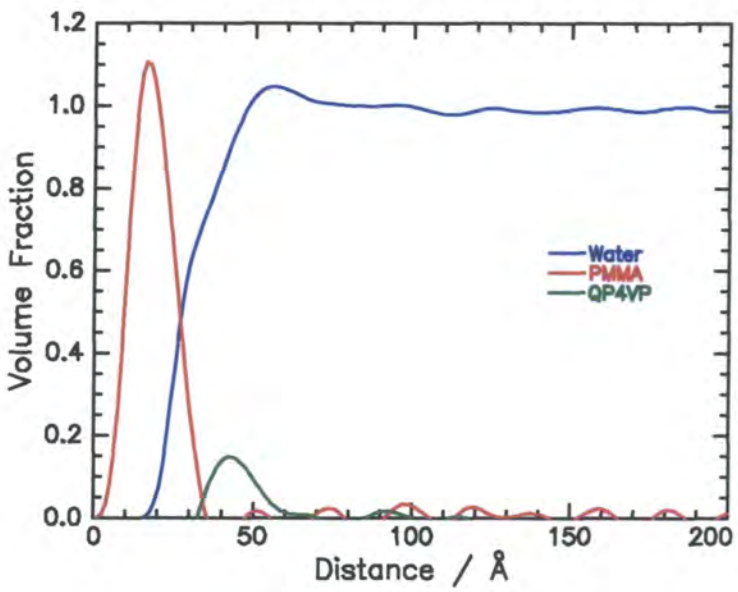

Figure 6.4.16b. Volume fraction profile obtained from model independent fitting. Subphase = 0.1M KCl solution, Γ_s = 3.0mg m^{-2}

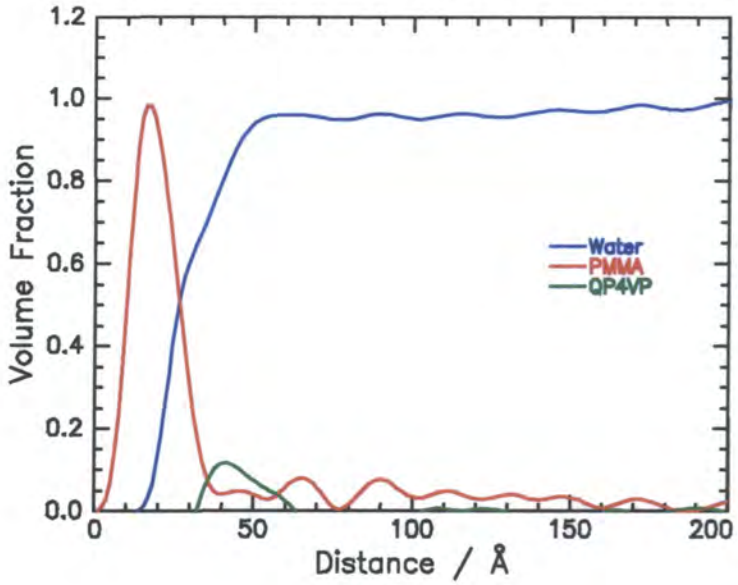

Figure 6.4.16c. Volume fraction profile obtained from model independent fitting. Subphase = 1M KCl solution, Γ_s = 3.0mg m^{-2}

smooth function (such as a tanh layer in the kinematic approximation), whereas that on 0.1M KCl shows unusual characteristics. All of the data analysis techniques reveal that a small layer of water with a density greater than that of bulk water exists at a region approximately 20Å deeper into the subphase than the end of the PMMA block. No plausible explanation can be given for such a physically unrealistic observation unless it is assumed that this, and the unusually high PMMA density obtained on the same subphase, is due to errors in the data caused by instrumental misalignment.

6.5. CONCLUSIONS

Neutron reflectometry has been used to provide details on the conformation of the copolymer at the air-liquid interface. The results obtained on subphases of water and potassium chloride solutions are summarised briefly in sections 6.3.7 and 6.4.6 respectively.

In general, it was found that the results obtained were comparable to the appropriate scaling theory. Although these models could not be reproduced quantitatively, the data produced exhibited the correct overall trends. Specific features of the results obtained can be explained by comparison with surface pressure data (chapter five), as is discussed below.

The observation that a quantity of PMMA is 'lost' at higher surface concentrations has been assigned to the coiling and looping of the chains away from the interface. These results can be compared with the surface pressure isotherm of PMMA (figure 5.2.1), where the surface pressure is constant for $\Gamma_{s,PMMA} > 2.4mg\ m^{-2}$. This corresponds to a copolymer surface concentration of $\Gamma_s \approx 3.0mg\ m^{-2}$, the concentration where substantial 'loss' of PMMA is recorded. This implies that at this point, the liquid surface is fully packed, and the introduction of any further PMMA can only be incorporated into either the air or liquid phases.

As previously stated, the PMMA block exhibits little change in conformation when spread on subphases of varying salt concentration. This result is unsurprising when compared to the surface pressure isotherms of PMMA on salt solutions (figure 5.3.2), which are also independent of subphase.

The changes in conformation of the QP4VP block can also be explained. Neutron reflectometry results show that increasing polymer surface concentration causes the vinyl pyridine chains to extend into the subphase. The same conclusion was drawn from surface pressure data in section 5.2.3.1.

Results from the kinematic approximation analysis of neutron reflectometry data reveal that the QP4VP chains extend further into the subphase when spread on 10^{-3}M KCl solution than when spread on water. A further increase in subphase salt concentration causes the chain length to decrease. These results can be at least partially explained by comparison with figure 5.3.4. Here, from the 'take-off'

concentrations of the isotherms, it was deduced that the above phenomenon was indeed occurring as the extension of the chains into the subphase removes material from the surface region. The only difference between the two sets of results is that neutron reflectometry reveals the most significant coiling of the chains to occur between 10^{-3}M and 0.1M KCl, whereas surface pressure isotherms show this to be between 0.1M and 0.3M. However, despite this minor discrepancy, it is clear that there is a strong correlation between the results obtained by neutron reflectometry and those by the measurement of surface pressure.

6.6. REFERENCES

1 J. R. P. Webster, *Personal Communication*, 1998.

2 J. A. Henderson, *Ph.D. Thesis*, University of Durham, 1992.

3 E. M. Lee and J. E. Milnes, *J. Appl. Cryst.*, 1995, **28**, 518.

4 J. D. Hines, P. R. Garrett, G. K. Rennie, R. K. Thomas and J. Penfold, *J. Chem. Phys. B*, 1997, **101**, 7121.

5 S. K. Peace, *Ph.D. Thesis*, University of Durham, 1996.

6 P. F. Dewhurst, M. R. Lovell, J. L. Jones, R. W. Richards and J. R. P. Webster, *Macromolecules*, 1998, **31**, 7851.

7 S. T. Milner, T. A. Witten and M. E. Cates, *Macromolecules*, 1988, **21**, 2610.

8 S. Misra, S. Varansi and P. P. Varansi, *Macromolecules*, 1989, **22**, 4173.

9 J. A. Henderson, R. W. Richards, J. Penfold, J. R. Lu and R. K. Thomas, *Macromolecules*, 1993, **26**, 4591.

10 R. W. Richards, B. R. Rochford and J. R. P. Webster, *Faraday Discuss.*, 1994, **98**, 263.

11 A. F. Miller, *Work in progress*, 1999.

12 S. K. Peace, R. W. Richards, F. T. Kiff, J. R. P. Webster and N. Williams, *Polymer*, 1999, **40**, 207.

13 J. A. Henderson, R. W. Richards, J. Penfold, and R. K. Thomas, *Acta Polymer*, 1993, **44**, 184.

14 S. V. Alexander, *J. Phys. (Paris)*, 1977, **28**, 983.

15 P.-G. de Gennes, *Macromolecules*, 1980, **13**, 1069.

16 H. Ahrens, S. Förster and C. A. Helm, *Phys. Rev. Lett.*, 1998, **81**, 4172.

17 J. S. Higgins and H. C. Benôit, *Polymers and Neutron Scattering*, Oxford Science, Oxford, UK, 1994.

18 P. K. Weissenborn and R. J. Pugh, *J. Colloid Interface Sci.*, 1996, **184**, 550.

19 H. Dautzenberg, W. Jaeger, J. Kötz, B. Philipp, Ch. Seidel and D. Stscherbina, *Polyelectrolytes: Formation, Characterisation and Application*, Hanser, Munich, Germany, 1994.

20 G. S. Manning, *J. Chem. Phys.*, 1969, **51**, 924.

CHAPTER SEVEN

SURFACE QUASI-ELASTIC LIGHT SCATTERING

7.1. INTRODUCTION

The use of surface quasi-elastic light-scattering (SQELS) to determine the viscoelastic behaviour of spread films of PMMA-QP4VP at the air-liquid interface is discussed in this chapter.

The chapter begins with a brief discussion of the spectral fitting procedure used to extract the viscoelastic parameters.[1] Following this, the results obtained will be presented and discussed, beginning with those for films spread on water subphases. Three series of experiments have been undertaken, namely surface concentration variation, frequency and time dependence studies and these are presented and discussed in turn. For varying surface concentration and frequency studies, the data has been analysed by the use of both damped cosine[2] and spectral fits. For the study of the temporal evolution of capillary waves, data analysis involved the use of the damped cosine fit, extracting only parameters of capillary wave frequency and damping. For clarity, the experimental results for each study are presented in full, before their discussion takes place. A similar procedure is followed in section 7.4, where data obtained for film spread on solutions of potassium chloride are presented and discussed. The results for the two sets of subphases are then compared.

7.2. DATA FITTING

The use of the spectral fitting technique (section 2.3.4.2) for SQELS data has been the source of much discussion in the literature.

In a number of studies, Yu[3,4,5,6] analysed surface light scattering data assuming that $\gamma' = 0$, and that the dynamic value of surface tension was equal to the static value (as measured using a Wilhelmy plate). The justification given for these assumptions was that this method led to the reporting of consistent values of ε_0 and ε'.

The development of a direct spectral analysis method by Earnshaw[1] allowed the extraction of all four surface properties directly from light scattering data, without any *a priori* assumptions. This technique superseded that developed by Yu and has been used in the analysis of SQELS data in the majority of literature published throughout the last decade. A more recent development in the theory of polymers at fluid-fluid interfaces was the work of Buzza,[7] which reported the addition of two new parameters to the dispersion equation, namely a bending modulus, κ, and a coupling constant, λ. However, due to the small polymer brush height of the polymer and the high surface tension at a typical air-liquid interface, these two terms can be neglected. A more important consequence for data fitting is the assertion that $\gamma' \equiv 0$, implying that only three viscoelastic moduli are now needed to describe the behaviour of the liquid surface. Published work of experimental data analysed by this technique has recently started to appear.[8] The observation that $\gamma' = 0$ was also found experimentally for a mixed surfactant-oil monolayer[9] before the publication of the above theoretical work.

To determine whether or not the value of γ' should be constrained to zero, a series of experiments were undertaken for a spread film of PMMA-QP4VP on subphases of water and 0.1M and 1M KCl solutions. The data used in the example given here being that on 1M KCl solution.

In these experiments, a specific polymer surface concentration (in this case 0.7mg m^{-2}) was selected and a series of experiments undertaken at different values of q. The data was fitted using the damped cosine analysis, yielding two sets of results, capillary wave frequency and damping against q. One of the q values (in this example q = 266cm^{-1}) was selected and the viscoelastic parameters extracted via the

spectral fitting technique. Two methods were use to do this: (a) fitting all four parameters and (b) constraining $\gamma' = 0$ and fitting the remaining three parameters. In both cases no further constraints (e.g. forcing values to be positive) were employed. The viscoelastic parameters extracted in each case are given in table 7.2.1:

Parameter	Method (a)	Method (b)
γ_0 / mN m^{-1}	75.68	73.73
γ' / mN s m^{-1}	-4.073x10^{-4}	0
ε_0 / mN m^{-1}	6.15	1.96
ε' / mN s m^{-1}	1.282x10^{-4}	4.739x10^{-5}

Table 7.2.1. Viscoelastic parameters for PMMA-QP4VP on 1M KCl solution, Γ_s = 0.7mg m^{-2}, q = 266cm^{-1}. Values obtained by fitting (a) four parameters (b) three parameters

These values were then inserted into the dispersion equation to generate a theoretical plot of both capillary wave frequency and damping against q. These are shown, along with the experimental data, in figures 7.2.1 and 7.2.2. In both cases, it is immediately clear that the experimentally obtained values of capillary wave frequency and damping are best reproduced by the line corresponding to the data fitting procedure where only three parameters are floated (i.e. where transverse shear viscosity is constrained to zero). One factor that does have to be taken into account is that the viscoelastic moduli are frequency dependent. The result of this can be best seen in figure 7.2.1, where the experimental data slightly diverge from the theoretically generated data at higher wavenumbers. Nevertheless, it is clear (especially from figure 7.2.2) that the experimental data are best reproduced when $\gamma' = 0$.

This result, along with the overall quality of the fits obtained using this method gave a clear indication that this method of data analysis was the most appropriate in this case. An identical result was found for subphases of water and 0.1M KCl solution and a process of constraining $\gamma' = 0$ was therefore adopted for all data analysis.

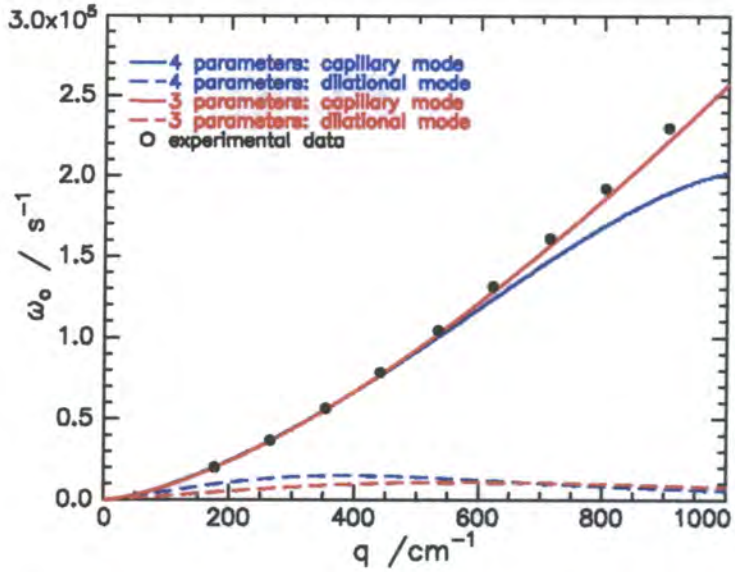

Figure 7.2.1. Comparison of theoretical lines (see legend) and experimental (circles) frequency data for PMMA-QP4VP on 1M KCl solution, $\Gamma_s = 0.7$mg m^{-2}

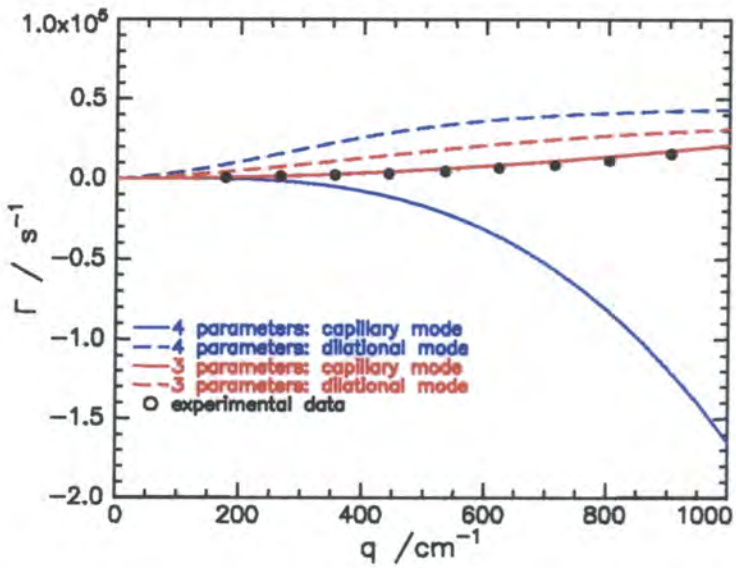

Figure 7.2.2. Comparison of theoretical lines (see legend) and experimental (circles) damping data for PMMA-QP4VP on 1M KCl solution, $\Gamma_s = 0.7$mg m^{-2}

7.3 WATER SUBPHASE

The results obtained from SQELS experiments for spread films of PMMA-QP4VP on water subphases are presented in this section. Three series of experiments were undertaken. Initially, a wavenumber of q = 270cm^{-1} was selected and the behaviour of the surface waves studied as a function of polymer surface concentration. The values of capillary wave frequency and damping obtained from damped cosine fitting of the data are presented, along with the viscoelastic parameters extracted from direct spectral analysis and the discussion of these results.

The surface concentration scan is followed by a frequency dependence study of the wave properties. In these experiments, one fixed polymer surface concentration is selected and q varied. The results of both direct spectral analysis techniques are again presented and discussed.

Finally, in an attempt to determine whether the polymer monolayer exists as a uniform film or as a series of 'islands' on the liquid surface, time dependence studies have been undertaken. Correlation functions were recorded over a period of time for the same film and phenomenologically analysed. This yields values of capillary wave frequency and damping, from which it is possible to obtain information regarding both the homogeneity and the stability of the film.

7.3.1. CONCENTRATION DEPENDENCE STUDIES

7.3.1.1. Results: Capillary Wave Frequency & Damping

The variation of capillary wave frequency with polymer surface concentration is shown in figure 7.3.1. The data presented is a combination of two sets of experiments carried out over a year apart, using two different correlator and photomultiplier tube systems (see section 3.3.2). The data follow highly similar trends, which gives a good indication of the reproducibility of the experiments and implies that the results obtained are independent of instrumentation.

The capillary wave frequency maintains a value equivalent to that of pure water (*ca.* $3.7x10^4 cm^{-1}$ at this wavenumber) up to $\Gamma_s \approx 0.7mg\ m^{-2}$. At surface concentrations above this, the frequency decreases approximately monotonically, this decrease continuing until the highest surface concentration explored. This decrease in frequency can be analysed mathematically by the application of a least squares fit to the concentration range $0.7 < \Gamma_s$ / mg $m^{-2} < 3.5$. This yields a value of $d\omega_o/d\Gamma_s = -4184 m^2\ mg^{-1}\ s^{-1}$, which will be compared with the values obtained on potassium chloride solutions in section 7.4.1.

The capillary wave damping (figure 7.3.2) displays a more characteristic variation with surface concentration. From a value equivalent to that of pure water, damping increases slowly up to $\Gamma_s = 0.5mg\ m^{-2}$ and then much more rapidly, attaining a maximum at a surface concentration of $0.8mg\ m^{-2}$. The value of damping at this concentration is approximately twice that of pure water. At higher surface concentrations, damping decreases, although there is some evidence of a second, much smaller maximum at $\Gamma_s = 1.5mg\ m^{-2}$.

7.3.1.2. Results: Viscoelastic Parameters

As demonstrated in section 7.2, the data from these experiments can be best fitted using three viscoelastic parameters, surface tension, γ_o; dilational modulus, ε_o and

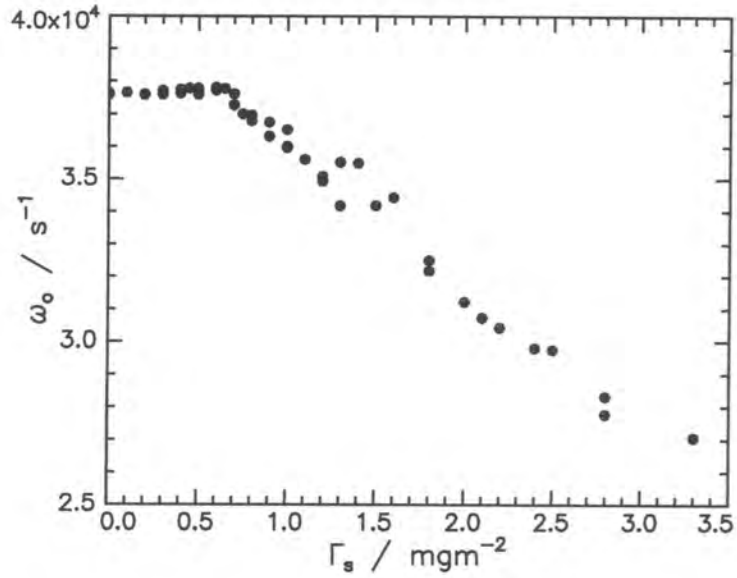

Figure 7.3.1. Frequency of capillary waves against Γ_s. q = 270cm^{-1} (error bars within points)

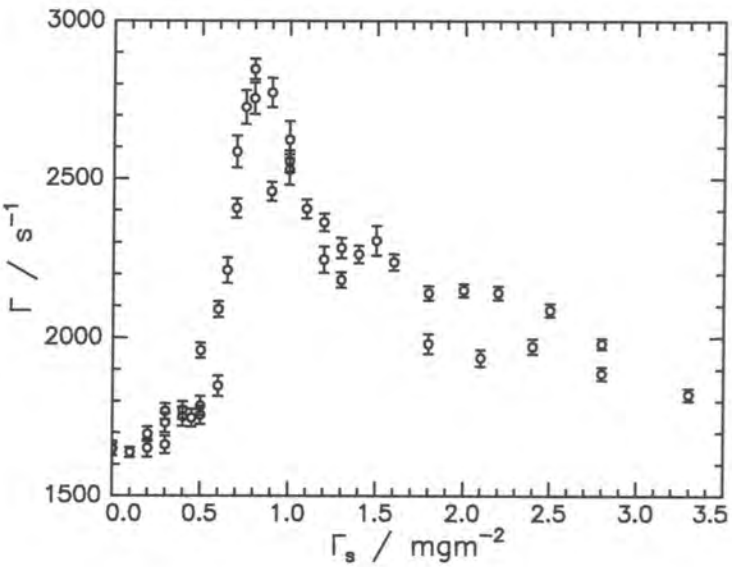

Figure 7.3.2. Damping of capillary waves against Γ_s. q = 270cm^{-1}

dilational viscosity, ε'. The dependence on each of these with surface concentration is outlined in turn:

Surface Tension

The variation of dynamic surface tension with polymer surface concentration is shown by the circles in figure 7.3.3. A highly similar dependence to that in figure 7.3.1 is exhibited, surface tension remaining constant at its original value until $\Gamma_s \approx 0.7\text{mg m}^{-2}$. This similarity arises from equation 2.3.7, which shows that damping is directly related to surface tension.

The data is also compared with the static surface tension obtained from surface pressure data measured using a Wilhelmy plate, $\gamma_{o,static}$ (shown by the line on figure 7.3.3). Different behaviour is clearly exhibited. In the range $0.8 < \Gamma_s / \text{mg m}^{-2} < 1.3$, $\gamma_{o,dynamic} < \gamma_{o,static}$. At higher surface concentrations, the two sets of data cross and $\gamma_{o,dynamic}$ becomes greater that $\gamma_{o,static}$ at the highest surface concentrations studied. Unlike the plot of static surface pressure, there appears to be no plateau present in the dynamic surface tension data. Similar effects, where $\gamma_{o,dynamic} \neq \gamma_{o,static}$ have been observed with a graft copolymer of PMMA-PEO.[10]

Dilational Modulus

A plot of dynamic dilational modulus against surface concentration is shown by the circles in figure 7.3.4. At the lowest polymer surface concentration studied, the value of ε_o (3mN m^{-1}) is distinct from that of pure water (zero). ε_o then rises steadily with increasing surface concentration until a maximum value of $\varepsilon_o \approx 13\text{mN m}^{-1}$ is attained at $\Gamma_s = 1.0\text{mg m}^{-2}$. Around this region of the plot, the error bars are noticeably larger, indicating greater deviation within the ten individual values of ε_o from which the mean value is obtained. Beyond the maximum value, the plot of dilational modulus then follows a similar form to that of capillary wave damping, initially decreasing before levelling out slightly and decreasing again at the highest concentrations. There is some evidence of a second maximum of smaller magnitude at $\Gamma_s = 1.3\text{mg m}^{-2}$, a similar concentration to where there is also an increase in capillary wave damping.

The static Gibbs elasticities are calculated from equation 5.2.2 and plotted as the line in figure 7.3.4. It is clear that the behaviour is totally unlike that of the dynamic

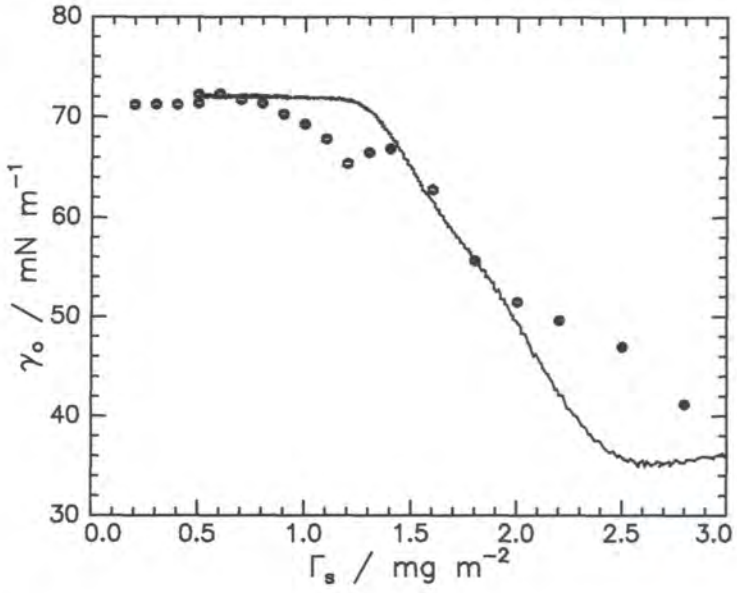

Figure 7.3.3. Surface concentration dependence of the dynamic (circles) and static (line) surface tension values obtained from SQELS and surface pressure isotherms respectively

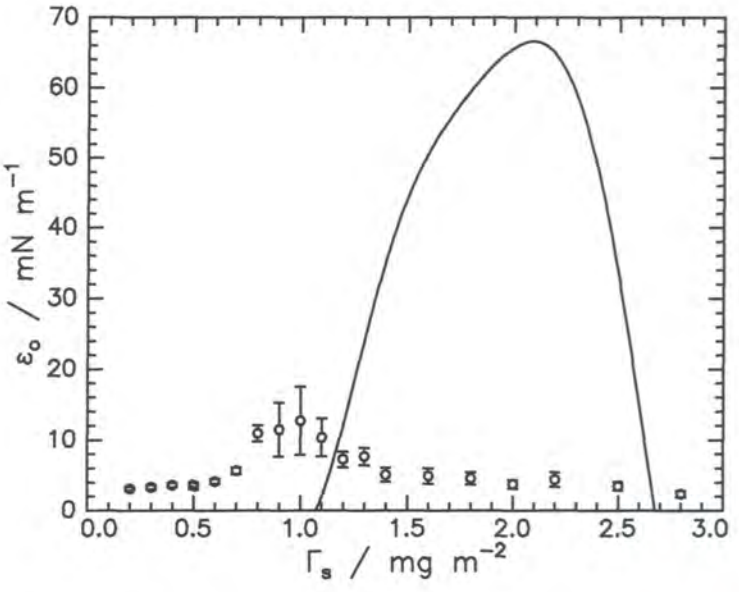

Figure 7.3.4. Surface concentration dependence of the dynamic (circles) and static (line) dilational modulus values obtained from SQELS and surface pressure isotherms respectively

dilational moduli. Similar differences in values of dilational moduli have been observed in other systems,[11] although other work has shown a good agreement between the two values.[12] No rise in $\varepsilon_{o,static}$ is observed until $\Gamma_s \approx 1.1$mg m^{-2} and the maximum obtained by these static values occurs at twice the surface concentration and over five times the value of dilational modulus as the static values.

Dilational Viscosity

All values of dilational viscosity reported (figure 7.3.5) are found to be positive, a significantly different observation from that in a number of recent studies,[13,14] where negative values have been observed. ε' increases slowly from a surface concentration of 0.5mg m^{-2}. A small maximum is observed at $\Gamma_s \approx 1.4$mg m^{-2} and at higher surface concentrations, a plateau is seen at $\varepsilon' \approx 2.2\text{x}10^{-4}$ mN s m^{-1}.

7.3.1.3. Discussion: Capillary Wave Frequency & Damping

The predominant feature in the plot of capillary wave damping against polymer surface concentration is the occurrence of a maximum at $\Gamma_s = 0.8$ mg m^{-2}. Typically, a maximum in a plot of either capillary wave frequency or damping is due to resonance[15] occurring between the transverse and longitudinal modes of the system. This phenomenon is observed when the frequencies of the two modes, given to first approximations below, are equal.

$$\omega_C \approx \left(\frac{\gamma q^3}{\rho}\right)^{1/2} \qquad \textbf{Equation 7.3.1.}$$

$$\omega_D \approx \frac{\sqrt{3}}{2}\left(\frac{\varepsilon^2 q^4}{\eta\rho}\right)^{1/3} \qquad \textbf{Equation 7.3.2.}$$

Where ω_C and ω_D are the frequencies of the capillary and dilational modes respectively. At low q (as used here), classical resonance is observed where the ratio $\varepsilon_o/\gamma_o \approx 0.16$. To determine if this is indeed the cause of the maximum in the plot of capillary wave damping, the values of ε_o/γ_o were calculated (figure 7.3.6). At Γ_s =

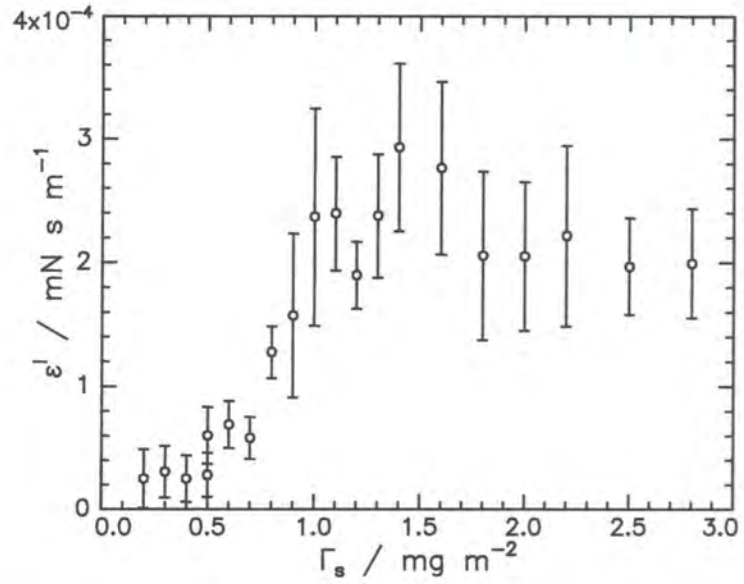

Figure 7.3.5. The variation in dilational viscosity with surface concentration

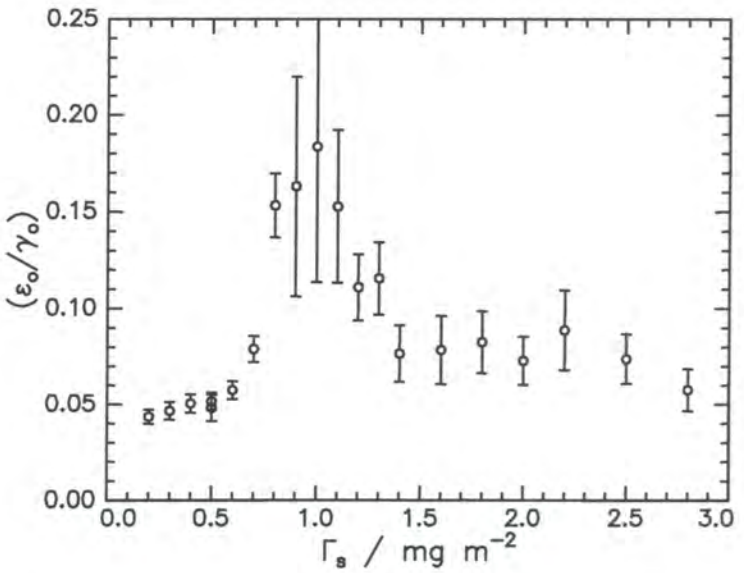

Figure 7.3.6. The ratio of ε_o/γ_o against surface concentration. A value of $\varepsilon_o/\gamma_o \approx 0.16$ can indicate resonance between the capillary and dilational modes

0.8mg m^{-2}, ε_o/γ_o = 0.153 ± 0.016, implying that at this surface concentration, classical resonance does indeed appear to be occurring.

Attention is now turned to the small maximum in the capillary wave damping at $\Gamma_s \approx$ 1.5mg m^{-2}. Although small, a maximum is observed consistently in this region for more than one set of experimental data, implying that the effect is indeed real. Figure 7.3.6 shows that at this surface concentration, $\varepsilon_o/\gamma_o \approx 0.07$, a value substantially smaller than the 0.16 indicative of classical resonance. An alternative explanation for the occurrence of this maximum is that at this surface concentration, the capillary waves may be resonating with another surface mode (not the dilational waves). This observation has been reported previously[13] and the existence of these 'extra' surface modes has been reported by Kramer.[16]

The resonance of two sets of surface waves can be compared to the coupling of two oscillators[17] with frequencies Ω_1 and Ω_2. In such a system, neither 'lossy oscillator' can move independently, but the uncoupled oscillation frequencies, ω_1 and ω_2 are related to the coupled frequencies by the expression:

$$(\Omega - \omega_1)(\Omega - \omega_2) = \kappa^2 \qquad \textbf{Equation 7.3.3.}$$

Where κ is the coupling constant. When $\kappa = 0$ (indicating that there is no coupling between the two modes), $\Omega_1 = \omega_1$ and/or $\Omega_2 = \omega_2$. For $\kappa > 0$, the frequencies diverge, ω_1 becoming greater than Ω_1 and ω_2 less than Ω_2. This implies that if the coupling was to reach a maximum value, ω_1 (in this case the capillary wave frequency) will also reach a maximum while ω_2 (the dilational wave frequency) will record a minimum. This is tested by calculating the frequency of the dilational waves at each surface concentration studied (dilational wave frequency and damping are inaccessible by experimental techniques other than at resonance). To do this, the viscoelastic parameters obtained from the spectral fit (section 7.3.1.2) were inputted into the dispersion equation. Solving the equation results in two sets of frequency and damping roots being obtained, one related to the capillary waves, the other to the dilational waves. The frequencies of the dilational waves are plotted in figure 7.3.7.

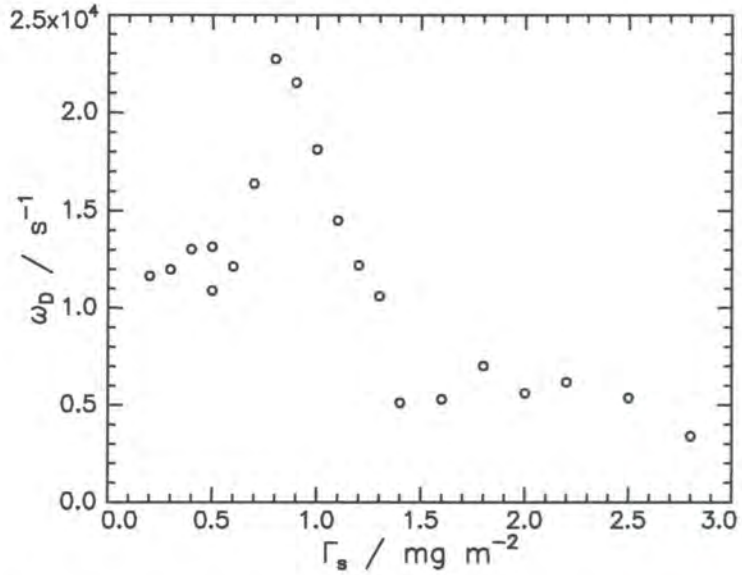

Figure 7.3.7. Variation of calculated dilational wave frequency, ω_D, with surface concentration

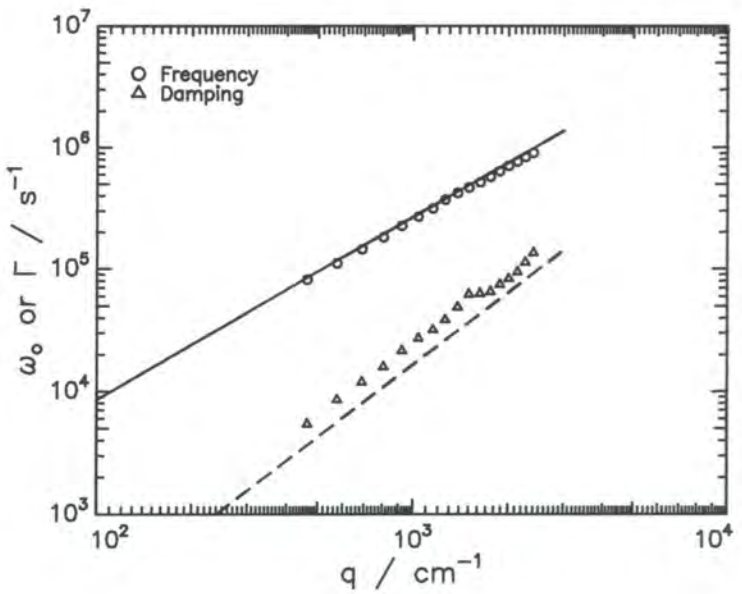

Figure 7.3.8. Wavenumber dependence of frequency and damping for a film of Γ_s= 0.8mg m^{-2} (symbols, see legend) and values calculated for a clean water surface (line)

From these results, it can be seen that there is a small minimum in the dilational wave frequency occurring at $1.4 < \Gamma_s$ / mg $m^{-2} < 1.6$. In fact, it is within this surface concentration range where the difference between the frequencies of the capillary and dilational waves is maximum ($\omega_C - \omega_D \approx 3.0x10^4 cm^{-1}$). This divergence of the frequencies of the two modes implies that it is at this surface concentration where κ is a maximum, indicating that coupling between the two modes is occurring. However, the amplitudes of the maximum in frequency and minimum in damping are both very small, implying that the coupling is very weak, substantially less than the coupling inherent in classical resonance occurring at $\Gamma_s = 0.8$mg m^{-2}.

7.3.1.4. Discussion: Viscoelastic Parameters

The plot of surface tension against surface concentration is shown in figure 7.3.3. Theoretically,[7] surface pressure is predicted to scale with polymer grafting density as:

$$\Pi \approx \sigma_o^{11/6} b^{5/3} N_A k_B T \qquad \textbf{Equation 7.3.4.}$$

As grafting density is directly proportional to surface concentration, the above scaling relationship is still valid if Γ_s is substituted for σ_o. The experimental data obtained from SQELS scales as $\Pi \sim \Gamma_s^{3.5}$, a significant departure from the value predicted above.

A further observation is the significant difference between the values measured by static and dynamic techniques. At low surface concentrations, the static values of surface tension are greater than the dynamic values. A 'crossover' of the two data sets occurs at $\Gamma_s \approx 1.5$mg m^{-2}, the surface concentration where it has been determined that coupling of modes takes place. For higher surface concentrations, the values of surface tension obtained from SQELS are larger than the static values, indicating that the spread film relaxes when perturbed by a capillary oscillation.

Neglecting γ, κ and λ, the remaining two viscoelastic parameters, dilational modulus and dilational viscosity are expected to scale as:

$$\varepsilon_o \sim \sigma_o^{11/6} b^{5/3} N_A k_B T \qquad \textbf{Equation 7.3.5.}$$

$$\varepsilon' \sim \sigma_o^2 b^5 \eta_l N_A^3 \qquad \textbf{Equation 7.3.6.}$$

The experimental data shows some agreement with these scaling expressions. For surface concentrations of $0.5 < \varepsilon_o < 1.0$mg m^{-2}, ε_o scales as $\varepsilon_o \sim \Gamma^{2.2}$, close to the predicted value of $\varepsilon_o \sim \Gamma^{11/6}$. Dilational viscosity scales as $\varepsilon' \sim \Gamma^2$ for concentrations up to 1.0mg m^{-2}, exactly as predicted by theory.

Clearly, the dynamic dilational modulus and the static Gibbs elasticity show significantly different behaviour, most noticeably at surface concentrations greater than 1.2mg m^{-2}. The explanation for this substantial difference between the two sets of data is thought to be the difference between the experimental time and length scales. Light scattering experiments involve microscopic displacement of the film on a short time scale of $\sim 1/\omega_o$. Classical (static) values of dilational modulus on the other hand involve large-scale compression of the film and much larger times. During this period, film rearrangement may take place and the conformation of the film may differ from that sampled by light scattering.

An abrupt change is observed in the values of ε_o and ε' (figures 7.3.4 and 7.3.5 respectively) over the concentration range $1.0 < \Gamma_s$ / mg m^{-2} < 1.5. Dilational viscosity shows a slight maximum at the higher end of this range, although the above scaling theory predicts that it should increase continuously with grafting density (and therefore surface concentration). This behaviour suggests that there is a change in the arrangement of the polyelectrolytic QP4VP chains. However, results for neutron reflectometry work presented in chapter six appear to preclude this as a possibility.

The neutron reflectometry studies reveal that the length of the polyelectrolyte 'brush' increases uniformly with surface concentration, rather than in the small concentration range suggested by the SQELS results. The fact that the brush is a polyelectrolyte also has a bearing on its behaviour. The high degree of dissociation of the chain results in strong polyelectrolyte behaviour, causing the brush to stretch, minimising the Coulombic interaction between monomer units. Further factors, such as the reduction of the apparent charge of the polyelectrolyte by counterion condensation,[18] may limit the brush extension relative to that of a completely dissociated QP4VP unit.

7.3.2. Frequency Dependence Studies

The frequency dependence of the surface properties of a film of PMMA-QP4VP have also been studied. In these experiments, one surface concentration was chosen, in this case that where classical resonance was observed to occur, 0.8mg m^{-2}. By using a 400mW laser, the q range was greatly extended, up to a wavenumber of 2407cm^{-1} (corresponding to frequencies of $9.88x10^5s^{-1}$ for the clean water surface and $9.06x10^5s^{-1}$ with a spread monolayer). The results obtained are presented and discussed in a manner similar to that in section 7.3.1.

7.3.2.1. Results: Capillary Wave Frequency & Damping

A plot of capillary wave frequency and damping against wavenumber is shown in figure 7.3.8. The symbols represent the experimental data, whereas the lines are the theoretical values calculated for a pure water surface, using literature values of surface tension, density and viscosity. As expected, the introduction of a monolayer to the liquid surface depresses the value of frequency and increases the value of damping from that of pure water. Linear least squares fits of these data show the frequency and damping to scale as $\omega_o \sim q^{1.47}$ and $\Gamma \sim q^{1.88}$, giving reasonable agreement with the expected scaling factors of 1.5 and 2 respectively.

Unusual behaviour is exhibited in the plot of capillary wave damping at both intermediate ($q \approx 1500cm^{-1}$) and high ($q \approx 2400cm^{-1}$) values of wavenumber. In both of these regions, the values of damping recorded for a monolayer covered surface diverge from those for pure water. Similar divergences in damping have been observed in the study of surfactant systems, where the values of damping have been found to rise away from[14] or fall towards[19] that predicted for pure water. This effect is discussed in section 7.3.2.3.

7.3.2.2. Results: Viscoelastic Parameters

Surface Tension

The behaviour of surface tension with capillary wave frequency is presented in figure 7.3.9. The data is highly scattered, values of γ_o between 67 and 76mN m^{-1} are

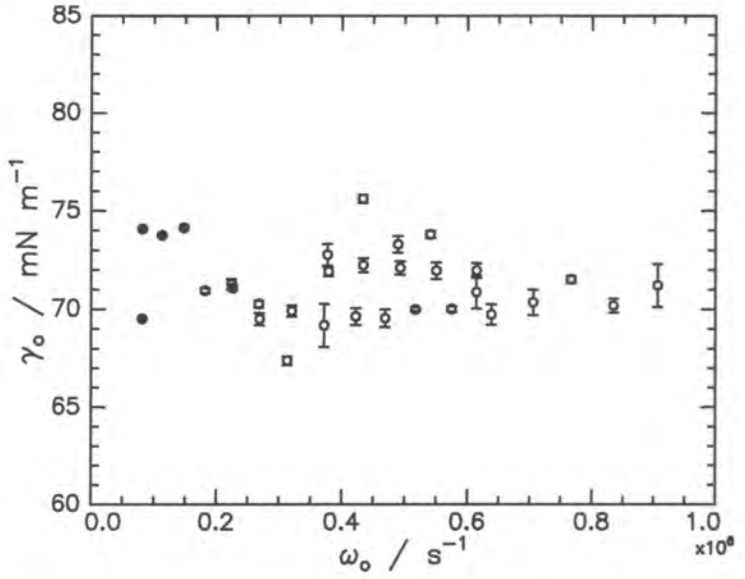

Figure 7.3.9. Frequency variation of γ_o for a film of $\Gamma_s = 0.8$mg m^{-2}

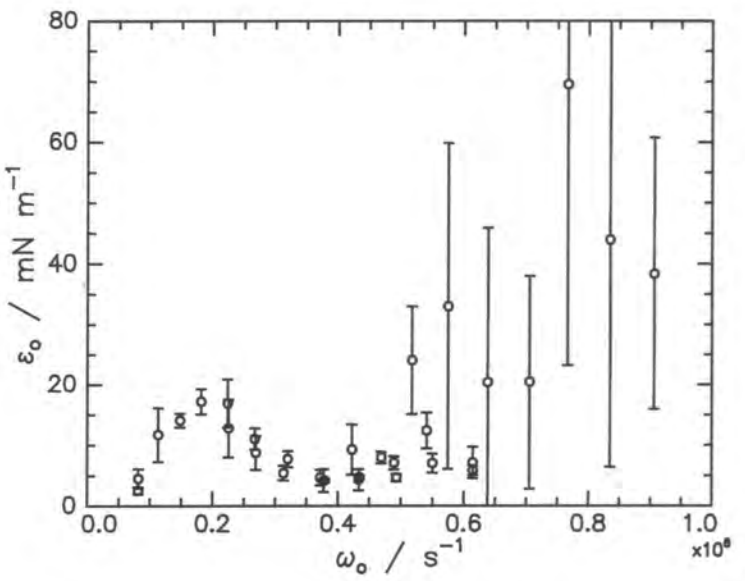

Figure 7.3.10. Frequency variation of ε_o for a film of $\Gamma_s = 0.8$mg m^{-2}

found and no trend is discernible.

Dilational Modulus

A plot of dilational modulus against frequency (figure 7.3.10) reveals a much more interesting trend. From a low value at the lowest surface concentration, dilational modulus increases to a maximum of *ca.* 17mN m^{-1} at $\omega_0 \approx 2.0x10^5 s^{-1}$ before decreasing to a minimum of *ca.* 5mN m^{-1} at $\omega_0 \approx 3.7x10^5 s^{-1}$. The data in the low frequency regime show very good reproducibility. At higher frequencies, dilational modulus appears to rise to larger values, although the data in this region has very large uncertainties due to the range of values of ε_0 returned by the fitting of each correlation function.

Dilational Viscosity

The variation of dilational viscosity with frequency (figure 7.3.11) is also found to exhibit a discernible trend. The maximum value of ε' ($1.0x10^{-4}$mN s m^{-1}) is observed at the lowest frequency studied. From there, the data decreases steadily until a broad minimum is reached at $\omega_0 \approx 5.0x10^5 s^{-1}$. Even in this region, all values of ε' remain positive. At higher frequencies, ε' again rises, although the rise is shallower and less well defined than the initial drop.

7.3.2.3. Discussion: Capillary Wave Frequency & Damping

The most unusual observation from the plot of capillary wave frequency and damping against q (figure 7.3.8) is the discontinuity observed in the values of damping. It has previously been suggested[20] that this deviation at high q is due to the coupling of the dilational waves. However, here it is suggested that instrumental effects may play a significant part in this phenomenon. This is now discussed.

It was observed that there are two regions (at q ≈ 1500 and 2400cm^{-1}) where the damping of a monolayer covered surface increases significantly compared to that of pure water. Due to the inflexible channel width architecture of the correlator, it is at these values of wavenumber that changes in experimental set-up took place. Generally, the following experimental conditions were used:

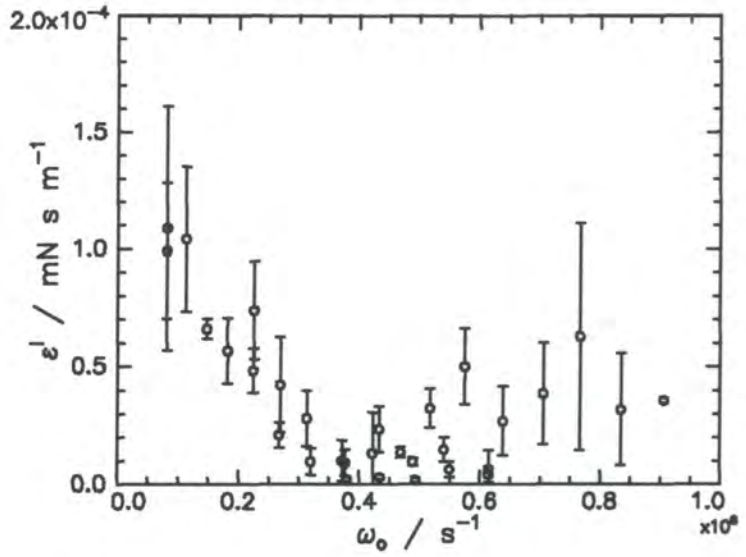

Figure 7.3.11. Frequency variation of ε' for a film of $\Gamma_s = 0.8\text{mg m}^{-2}$

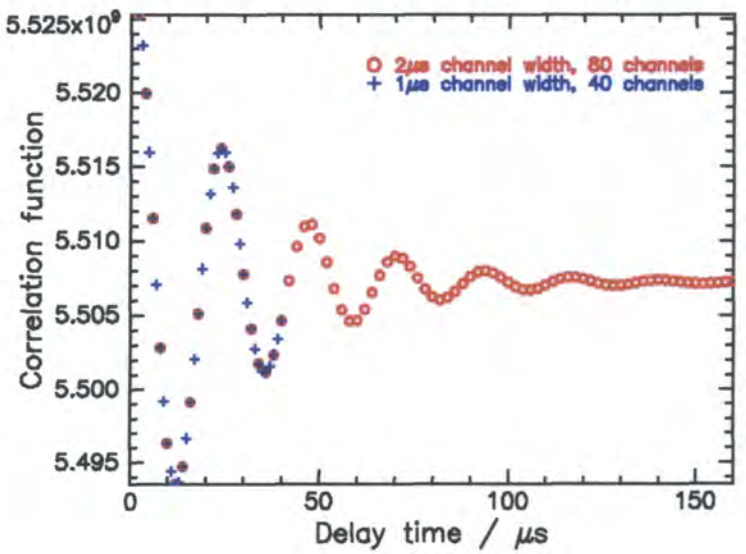

Figure 7.3.12. Simulated correlation functions with channel widths of 1μs (blue) and 2μs (red)

Wavenumber / cm^{-1}	Channel width / μs	Number of channels
400-600	5	192 + 8 delay
700-1500	2	72 + 8 delay
1600-2500	1	32 + 8 delay

Table 7.3.1. Typical conditions for the running of SQELS experiments

The data in the third column in the above table details the number of data points collected. The first figure is the number of data channels forming the actual correlation function. These are evenly spaced by the channel width. The eight delay channels are recorded at much longer delay times, to measure the 'background' count, where the correlation function has decayed to zero.

The most significant 'step' recorded in the capillary wave damping occurs as the experimental set-up changes from a channel width of 2μs to one of 1μs. To determine whether the effect was real, or simply an artefact of this change, a simulated correlation function was generated from an arbitrary set of viscoelastic parameters ($q = 1730cm^{-1}$, $\gamma_o = 70mN\ m^{-1}$, $\gamma' = 0$, $\varepsilon_o = 24mN\ m^{-1}$ and $\varepsilon' = 3.2x10^5 mN\ s\ m^{-1}$). From this single set of data, specific points were selected to give two new correlation functions. The first of these had 80 data points with a 2μs channel width an the second 40 data points with a 1μs channel width. Both are shown in figure 7.3.12.

These two correlation functions were then fitted to obtain values of capillary wave frequency and damping. The fits obtained are shown in figures 7.3.13 and 7.3.14 and the data obtained presented in table 7.3.2.

Channel width / μs	Frequency / s^{-1}	Damping / s^{-1}
2	270334 ± 78	35466 ± 215
1	270439 ± 68	34488 ± 223

Table 7.3.2. Values of capillary wave frequency and damping extracted from simulated correlation functions with 2μs and 1μs channel widths

The two values of capillary wave frequency are very similar and are within the estimated error. On the other hand, the values of damping are not so alike, the correlation function with the longer channel width resulting in the higher value of damping. The difference between the two values is approximately 3% and greater

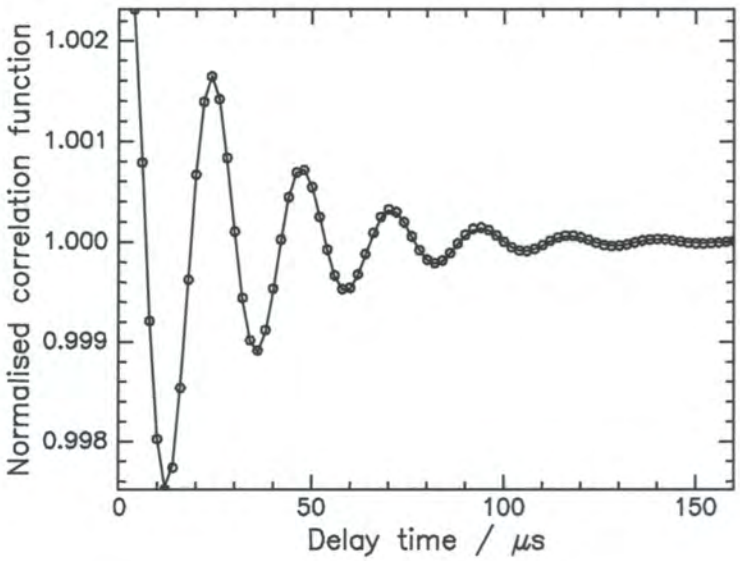

Figure 7.3.13. Simulated correlation function (circles) with fit (line). 80 data points, channel width = 2μs

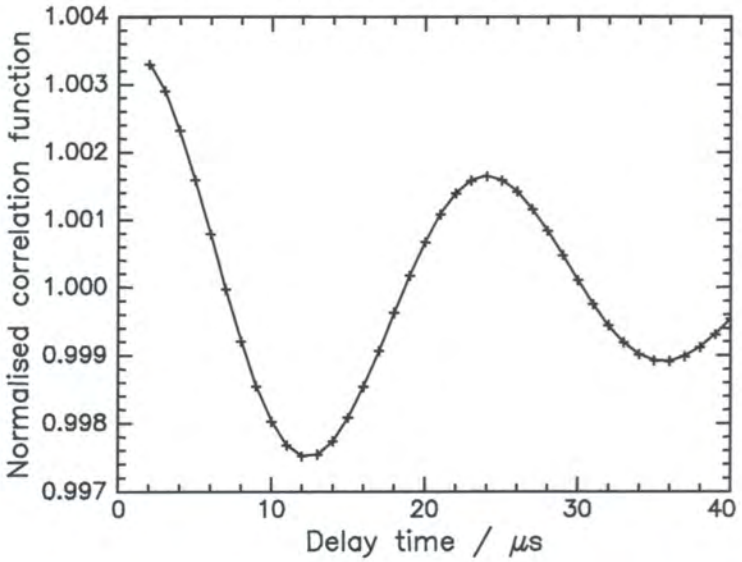

Figure 7.3.14. Simulated correlation function (crosses) with fit (line). 40 data points, channel width = 1μs

than the errors estimated on each. As the two correlation functions were produced from an identical set of data, this disagreement is due to the differences between the actual data selected for fitting. The reasons for this are as follows. Firstly, the correlation function with a 2μs channel width has more widely spaced data points, meaning that the maxima and minima of the correlation function are poorly defined. Generally, only a single data point describes any minimum or maximum. This results in the fit in this region being 'pointed' (figure 7.3.13) compared to the much 'smoother' fit of the data with a shorter channel width (figure 7.3.14). It is the maxima and minima of a correlation function that have to be fitted accurately in order to obtain true values of damping; the truncating of these points implying a more damped correlation function than is actually the case. Secondly, the correlation function with a 1μs channel width is truncated and does not decay to background, giving only three maxima or minima from which to calculate both the frequency and the damping.

A second simulation was carried out for correlation functions with longer channel widths. Correlation functions with channel widths of 5μs and 10μs, each with 200 data points, were produced from one set of parameters ($q = 1645cm^{-1}$, $\gamma_o = 70mN\ m^{-1}$, $\gamma' = 0$, $\varepsilon_o = 24mN\ m^{-1}\gamma_o = 3.2x10^5 mN\ s\ m^{-1}$). The values of capillary wave frequency and damping obtained are presented below:

Channel width / μs	Frequency / s^{-1}	Damping / s^{-1}
10	16208 ± 5	1867 ± 12
5	16213 ± 5	1775 ± 13

Table 7.3.3. Values of capillary wave frequency and damping extracted from simulated correlation functions with 10μs and 5μs channel widths

A similar result to above is found, the values of frequency vary by only 0.03% and are within their errors, whereas the values of damping differ by around 5%.

Clearly, in both cases, the longer channel width gives the higher value of capillary wave damping. This is therefore the reason (or at least a significant part of the reason) for the rise in damping relative to that of pure water. At $q \approx 1550cm^{-1}$, the wavenumber where the experimental channel width is reduced from 2μs to 1μs, the

value of damping relative to that of water decreases. Therefore, if two sets of data were to be collected, each with a different channel width, at points around this transition, two distinct results would be expected. Such an experiment has been undertaken for a film of $\Gamma_s = 0.8 mg\ m^{-2}$ spread on water and the results are presented in table 7.3.4:

Wavenumber / cm^{-1}	Damping / s^{-1}	
	Channel width = 2μs	Channel width = 1μs
1264	34578 ± 416	27205 ± 1070
1384	44194 ± 759	32548 ± 1189
1506	52578 ± 1120	51016 ± 866
1630	68050 ± 2010	65648 ± 1160
1752	69454 ± 1160	64783 ± 1232

Table 7.3.4. Comparison of capillary wave damping values obtained using channel widths of 2 and 1μs

From the above table, it is clear that at high wavenumbers the selection of two different experimental channel widths does indeed yield different results. In all cases, capillary wave damping is reported to be higher for the longer channel width, explaining the 'rise' observed in figure 7.3.8.

7.3.2.4. Discussion: Viscoelastic Parameters

A common method used in an attempt to gain more information on the viscoelastic behaviour of the system is the application of viscoelastic models[21] to describe the relaxation processes occurring. In previous work,[22] models have been used to describe the behaviour of films of (amongst other systems) a PMMA homopolymer. A similar approach is adopted here, in an attempt to obtain similar information for the diblock copolymer.

The two simplest (and most commonly used) of these models[11] are the Maxwell fluid and the Voigt solid. These can be represented in terms of elements comprised of mechanical components of springs and dashpots, connected either in series or in parallel. The resulting Maxwell and Voigt elements are shown schematically in figure 7.3.15.

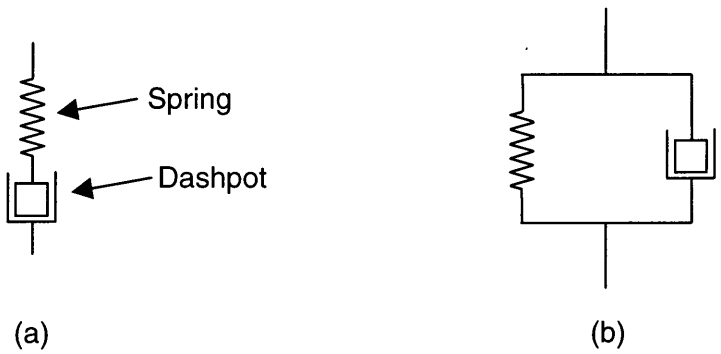

Figure 7.3.15. Schematic representations of (a) Maxwell and (b) Voigt viscoelastic models.

The capillary waves of the liquid surface impart an oscillatory stress and strain on the spread film. These two properties are connected *via* the complex modulus, $G^*(\omega)$:

$$G^*(\omega) = G'(\omega) + iG''(\omega) \qquad \textbf{Equation 7.3.7.}$$

Where $G'(\omega)$ and $G''(\omega)$ are the storage and loss moduli respectively, which in SQELS experiments are usually equal to γ_o and $\omega_o\gamma'$. However, in this work, $\gamma' = 0$ and therefore the equivalent dilational expressions are used, namely $G'(\omega) = \varepsilon_o$ and $G''(\omega) = \omega_o\varepsilon'$. These expressions are only valid at the resonance point, where the frequencies of the capillary and dilational modes are equal.

The expressions for $G'(\omega)$ and $G''(\omega)$ for a Maxwell model are:

$$G'(\omega) = G_e + \frac{G_i\omega_o^2\tau^2}{1+\omega_o^2\tau^2} \qquad \textbf{Equation 7.3.8.}$$

$$G''(\omega) = \frac{G_i\omega_o\tau}{1+\omega_o^2\tau^2} \qquad \textbf{Equation 7.3.9.}$$

Whereas, for the Voigt model:

$$G'(\omega) = G_i \qquad \textbf{Equation 7.3.10.}$$

$$G''(\omega) = G_i\omega_o\tau \qquad \textbf{Equation 7.3.11.}$$

Where G_i is the strength of the relaxation process (with relaxation time τ) and G_e the zero-frequency (or equilibrium) modulus.

For the Voigt model, the surface tension and dilational modulus are clearly frequency independent and, from equations 7.3.8 and 7.3.9, the following expression for relaxation time is obtained:

$$\tau = \frac{\varepsilon'}{\varepsilon_o} \qquad \textbf{Equation 7.3.12.}$$

This expression describes the dilational mode of the system. As the frequencies of the dilational mode are experimentally inaccessible, we have to use the capillary wave frequencies. As outlined above, this is an acceptable procedure at the resonance position. Although the relaxation times calculated at surface concentrations other than where resonance prevails are therefore only 'apparent' values, the results obtained are still valid in ascertaining the nature of the spread film

A similar expression for the dilational mode can be generated for the Maxwell model, where the frequency is in this case dependent upon dilational modulus:

$$\tau = \frac{\varepsilon_{o,dynamic} - \varepsilon_{o,static}}{\omega_o^2 \varepsilon'_{dynamic}} \qquad \textbf{Equation 7.3.13.}$$

Figure 7.3.9 shows that the surface tension of the PMMA-QP4VP diblock copolymer is essentially independent of capillary wave frequency, the same result observed for a film of PMMA homopolymer.[22] A straight line of γ_o = 71.38mN m^{-1} is fitted to these data in figure 7.3.16, suggesting that the spread film of the copolymer behaves as a Voigt fluid.

To obtain the relaxation time for the system, a plot of loss modulus (the product of capillary wave frequency and dilational viscosity) is shown in figure 7.3.17. When attempting to fit this data, it was found that a large number of equally 'good' fits could be obtained. To counter this, G_i was fixed to the value of 71.28mN m^{-1}

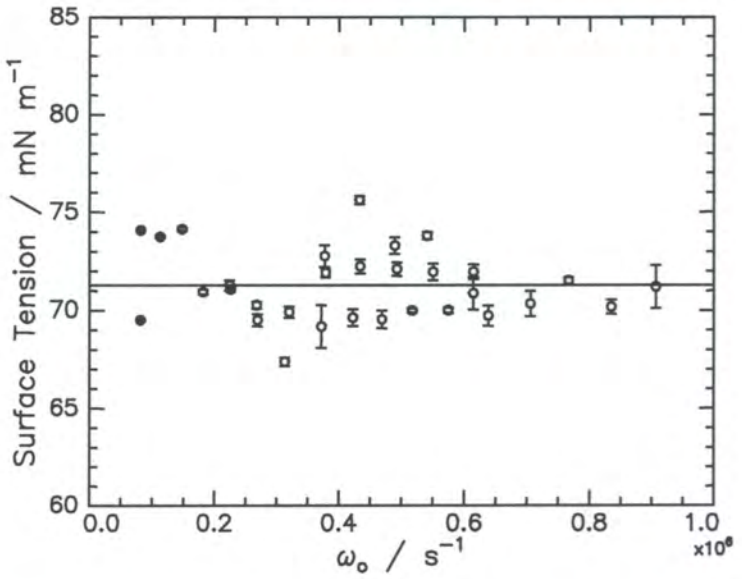

Figure 7.3.16. Straight line fit (line) to plot of surface tension against frequency (points)

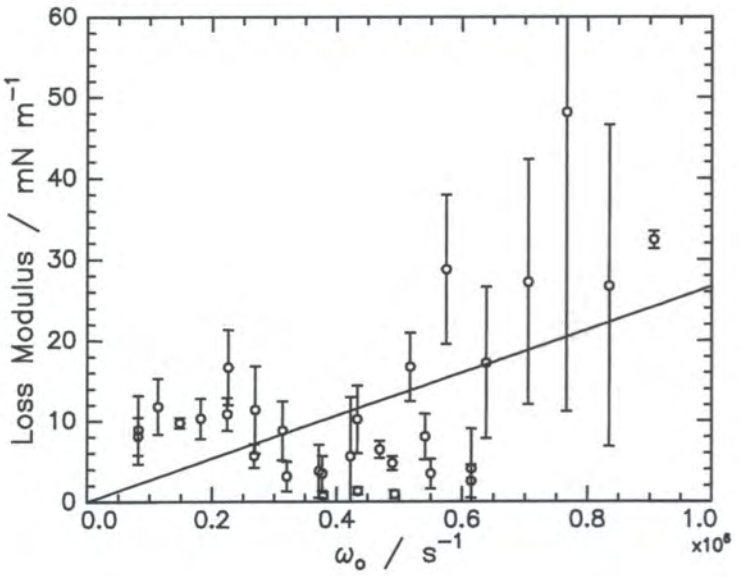

Figure 7.3.17. Voigt model fit (line) to plot of loss modulus against frequency (points)

obtained above. As can be seen, the resulting fit to the data is poor, the trends in the plot not being followed to any real extent. The value of relaxation time obtained from this process is $\tau = 3.73 \times 10^{-6} \pm 4.87 \times 10^{-8}$s, approximately an order of magnitude greater than the value of τ obtained for a PMMA homopolymer[22] and an order of magnitude less than that for a PMMA-PEO linear diblock copolymer.[23]

Assuming a Voigt model, the relaxation times for each surface concentration were calculated by the use of equation 7.3.12. The resulting data are shown in figure 7.3.18. At low surface concentrations, the relaxation time is approximately constant ($\tau \approx 10\mu$s) before increasing in the concentration range $0.8 < \Gamma_s$ / mg m^{-2} < 1.4 and reaching at plateau of $\tau \approx 60\mu$s at this higher concentration. This increase in τ with surface concentration is the result expected from the increase in the concentration of QP4VP units. The shorter relaxation times imply that the polymer exists in a coiled conformation, whereas the longer times imply a rigid-rod (stretched) conformation. Such an increase in τ begins at $\Gamma_s \approx 1.0$mg m^{-2}. Surface pressure isotherm studies (chapter five) reveal this to be approximately the concentration where the polymer chains on the surface begin to interact and the QP4VP is 'pushed' into the liquid subphase. This is confirmed by neutron reflectometry experiments (chapter six), which show an increase in polyelectrolyte chain lengths with surface concentration.

Figure 7.3.17 clearly shows that the loss modulus cannot be represented by a Voigt model. As an alternative, despite the lack of an obvious surface tension dependence on frequency, it was attempted to apply a Maxwell model to the system. Fitting the plot of surface tension against capillary wave frequency in this manner simply resulted in a fit very similar to that shown in figure 7.3.16, with an unphysical negative value of relaxation time.

It therefore appears that the interfacial rheology of the system is described by neither a Voigt nor a Maxwell model. Another indication of this is shown by the production of a Cole-Cole plot.[24] If a single relaxation time is present, a plot of $\omega_o\varepsilon'$ against ε_o should describe a semi-circle of radius $G_i/2$ and origin $G_e + G_i/2$. As illustrated in figure 7.3.19, for the present data this is clearly not the case.

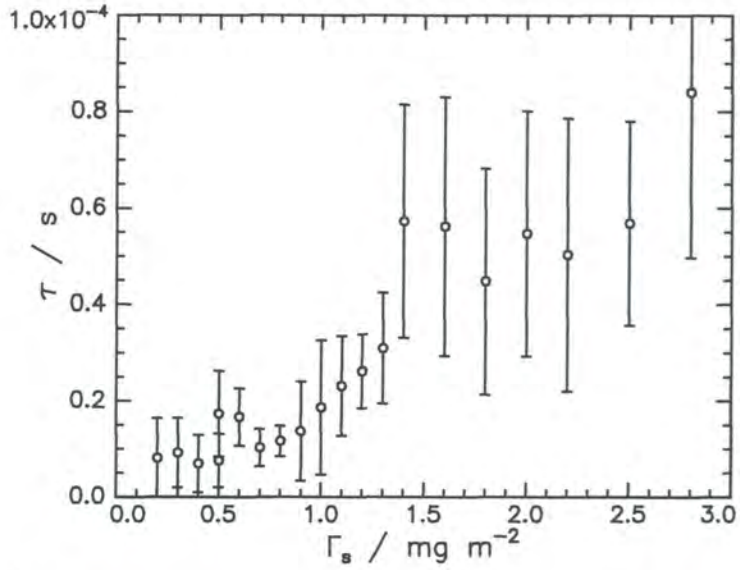

Figure 7.3.18. Apparent relaxation time (calculated using a Voigt model) against surface concentration

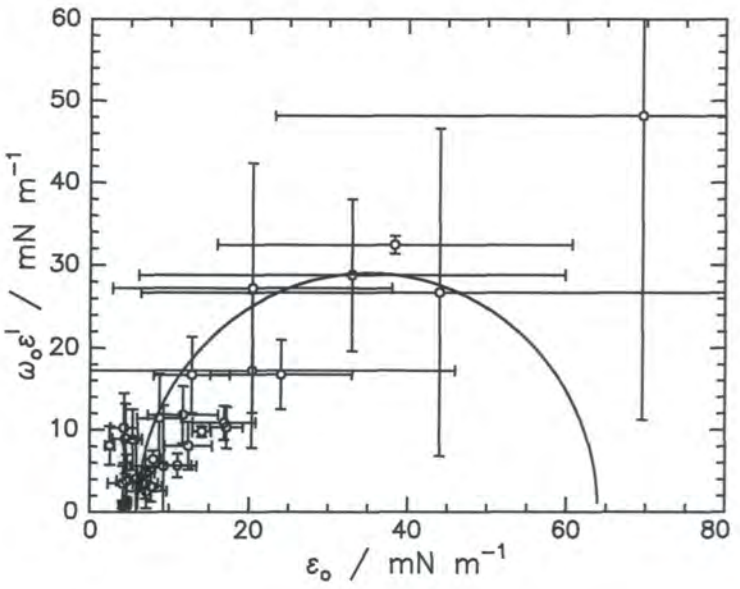

Figure 7.3.19. Cole-Cole plot of loss modulus ($\omega_o\varepsilon'$) against dilational modulus (points) overlayed with an empirically generated example of model behaviour (line)

Neither the Maxwell nor the Voigt models adequately describe the experimental data obtained here. The Voigt model comes the closer of the two to representing the data, but fails to model the loss modulus curve and a Cole-Cole plot is unsatisfactory. The viscoelastic behaviour of the system is therefore more complex than either of these two models and successful portrayal would require a model consisting of a more intricate arrangement of springs and dashpots.

In section 7.3.1.3, the theory of coupled oscillators was discussed briefly. With knowledge of the viscoelastic parameters, this can now be used to extract further information on the system. One phenomenon that can be investigated in this manner is that of mode mixing.

Equation 7.3.3 gives an expression for the coupling of two classical oscillators. For surface waves, however, the conditions are not ideal and, as in any real system, energy losses occur. The system is therefore best described by analogy to coupled lossy oscillators. Allowing the frequencies to be complex, the square of the coupling constant, κ^2, can take positive and negative values. The coupling can be defined as reactive (when $\kappa^2 > 0$) or resistive (when $\kappa^2 < 0$) and it is the former of these which is of relevance here.
In a system where the frequencies of the two oscillations are constant but the coupling changes, an increase in coupling can lead to the imaginary components of the normal modes converging. A further increase in κ^2 causes the values to become equivalent, before the normal modes separate. At this point and thereafter, the two normal modes exhibit mixed characteristics, giving rise to mode mixing.

This theory can be applied to results obtained from SQELS experiments, to determine if mode mixing is occurring. When there is resonance between the capillary and dilational modes (as is the case here when $\Gamma_s = 0.8\text{mg m}^{-2}$), it is clear that mode mixing may occur if the dampings of the two modes converge. To investigate this, a series of simulations have been undertaken.

Firstly, the effects of transverse shear viscosity on capillary and dilational wave damping have been examined in the absence of a dilational viscosity. Using a

wavenumber of q = 270cm^{-1} and the parameters γ_o = 72.6mN m^{-1} and ε_o = 11mN m^{-1}, the value of γ' has been varied between 0 and 6x10^{-4}mN s m^{-1}. The results are plotted in figure 7.3.20. It can been seen that the values of capillary and dilational wave damping converge as γ' increases.

As the experimental data in this work has been fitted constraining the value of transverse shear viscosity to zero, a more pertinent simulation is presented in figure 7.3.21. The same values of γ_o, ε_o and q as above are used, γ' set to zero and ε' varied. For positive values of ε', the damping of the dilational mode is significantly greater than that of the capillary mode. The two damping values begin to converge at higher values of ε'. For negative values of dilational viscosity, the dilational wave damping is reduced significantly and the two plots cross at $\varepsilon' \approx -1.6\text{x}10^{-4}$ mN s m^{-1}. It is in this region where mode mixing may occur.

Scrutiny of dispersion plots (of normalised frequency against normalised damping) can determine whether mode mixing is possible. Normalised frequency and damping are calculated by:

$$\omega_{o,norm} = \frac{\omega_o}{\sqrt{(\gamma_o q^3/\rho)}} \qquad \textbf{Equation 7.3.14.}$$

$$\Gamma_{norm} = \frac{\Gamma}{(2\eta q^3/\rho)} \qquad \textbf{Equation 7.3.15.}$$

Figure 7.3.22 shows a theoretical dispersion plot generated with a typical value of γ_o, γ' = 0 and $\varepsilon' < 0$ (of approximately the same value as the crossover of the two modes in figure 7.3.22). A variety of dilational moduli were used and q was varied to produce such a profile. At high values of ε_o, the dilational mode appears on the right-hand side of the plot, normalised damping decreasing as q increases. The capillary mode takes the form of a semi-circular arc, dropping down from a point with co-ordinates (1,5). When mode mixing occurs (at ε_o = 8mN m^{-1}), a significant change in behaviour is observed. The mode that appears to be the dilational mode at high values of normalised damping curls at high q and follows the path of a capillary mode. The opposite effect is show by the mode originating at (1,5). Initially showing

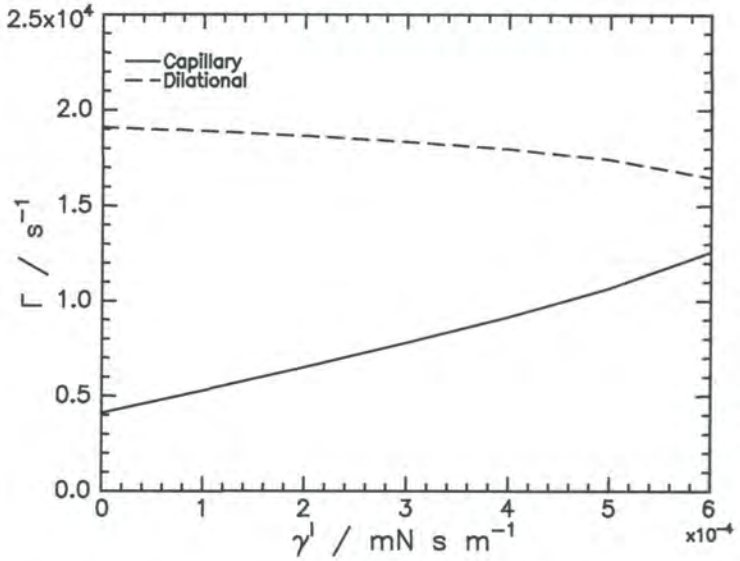

Figure 7.3.20. Capillary and dilational wave damping dependence upon transverse shear viscosity. Data generated using γ_o = 72.6mN m^{-1}, ε_o = 11mN m^{-1}, ε' = 0 and q=270cm^{-1}

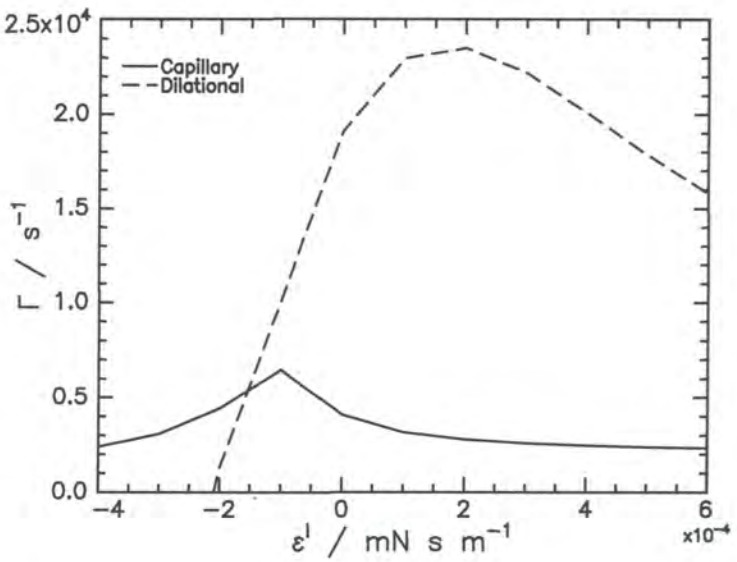

Figure 7.3.21. Capillary and dilational wave damping dependence upon dilational viscosity. Data generated using γ_o = 72.6mN m^{-1}, γ' = 0 ε_o = 11mN m^{-1} and q=270cm^{-1}

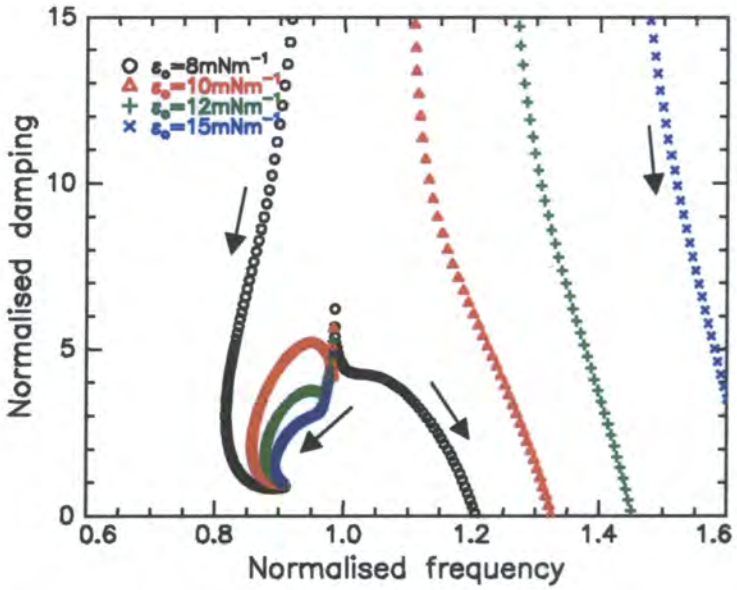

Figure 7.3.22. Theoretical surface wave dispersion plot for a negative dilational viscosity. Data generated using γ_o = 72.6mN m^{-1}, γ' = 0, ε' = -1.6x10^{-4}mN s m^{-1} and varying ε_o (see legend). Arrows indicate the direction of increasing q

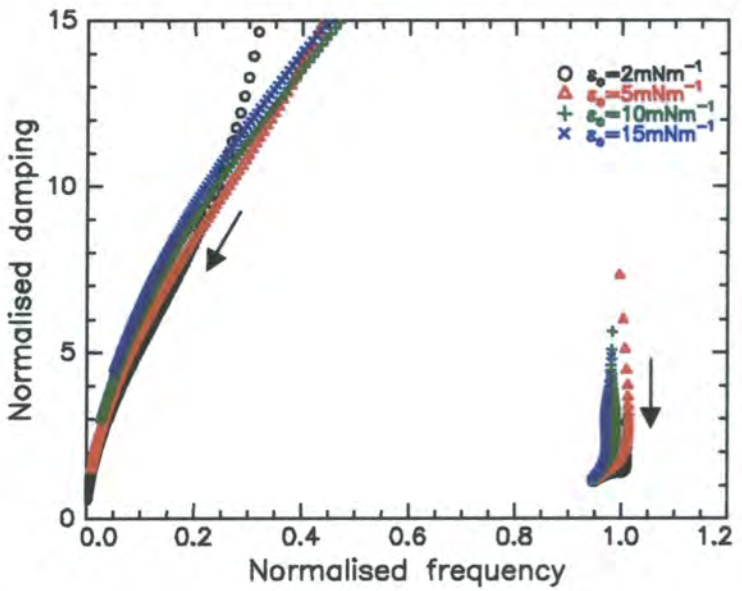

Figure 7.3.23. Theoretical surface wave dispersion plot for a positive dilational viscosity. Data generated using γ_o = 72.6mN m^{-1}, γ' = 0, ε' = 1.6x10^{-4}mN s m^{-1} and varying ε_o (see legend). Arrows indicate the direction of increasing q

capillary behaviour, this mode adopts the path of a dilational mode as normalised damping decreases.

A similar calculation (figure 7.3.23) shows that for a positive value of dilational viscosity, $\varepsilon' = 1.6 \times 10^{-4}$mN s m^{-1}, the two modes clearly retain their own characteristics and mode mixing does not occur. This simulation (where ε_o = 10mN m^{-1}) represents a film of the diblock copolymer at the resonance concentration and therefore indicates that mode mixing does not occur in this example.

As confirmation of this, figure 7.3.24 shows an experimental plot of wavenumber against normalised damping, produced from the data obtained from a film of Γ_s = 0.8mg m^{-2}. Clearly, the data is highly scattered, but there appears to be a decrease in normalised damping with increasing q. These results are compared with figure 7.3.25, using the same viscoelastic parameters as in figure 7.3.22, where mode mixing was observed to occur. Here, the normalised damping of the capillary wave initially decreases slightly with increasing q, before becoming overdamped and dropping further. The dilational mode initially drops rapidly before levelling off at higher q. As mode mixing is occurring, these two modes do not cross, rather the dilational mode assumes pseudo capillary mode behaviour at high q and *vice versa.* A similar transformation from one mode to another is not observed in the experimental data which, as previously stated, is almost continuous in behaviour. This is therefore another indication that mode mixing is not occurring in this instance.

A dispersion plot of normalised damping against normalised frequency is shown in figure 7.3.26. Although the data appears to fall in the shape of a chevron, there is no discernible trend with increasing wavenumber. If mode mixing was occurring in the system, the data would follow a 'hook'-like path, which is clearly not observed in this case. For clarity, a set of data from a single experimental run is presented in figure 7.3.27. Alongside each point is the wavenumber (in cm^{-1}) at which the data was obtained. This plot makes it easier to see that the data is in fact scattered with no real trend observable as wavenumber increases. The line on figure 7.3.27 is a theoretical plot calculated for the average values of the viscoelastic parameters over the q range explored, namely γ_o = 70.24mN m^{-1}, γ' = 0, ε_o = 27.68mN m^{-1} and ε' =

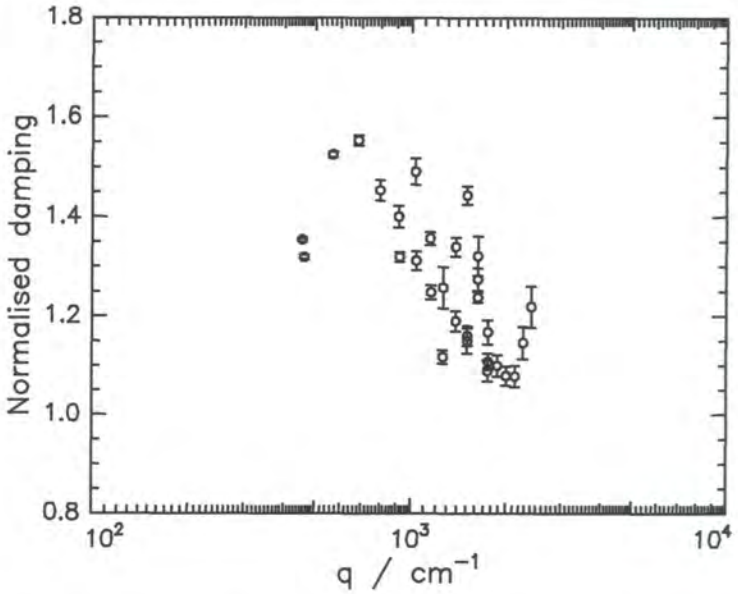

Figure 7.3.24. Experimentally obtained normalised capillary wave damping against wavenumber

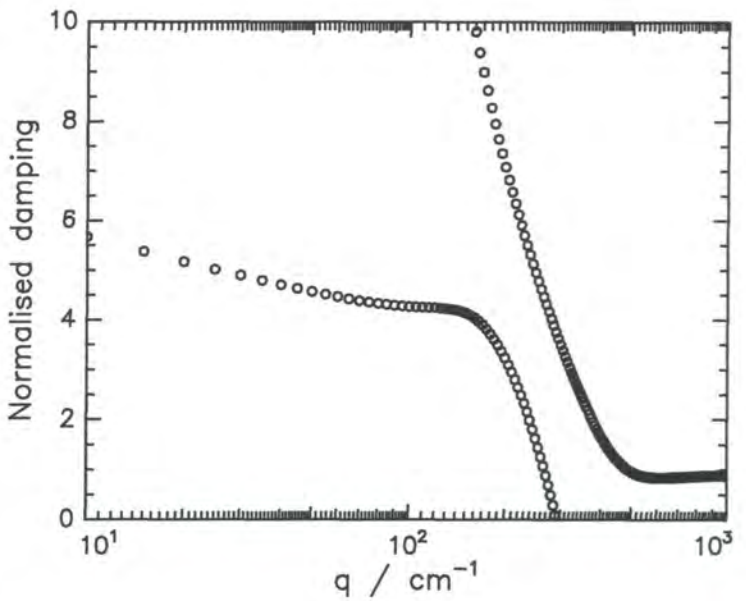

Figure 7.3.25. Theoretical normalised wave damping against wavenumber showing typical characteristics of mode mixing. Data generated using the parameters γ_o = 72.6mN m^{-1}, $\gamma' = 0$, ε_o = 8mN m^{-1} and ε' = -1.6x10^{-4}mN s m^{-1}

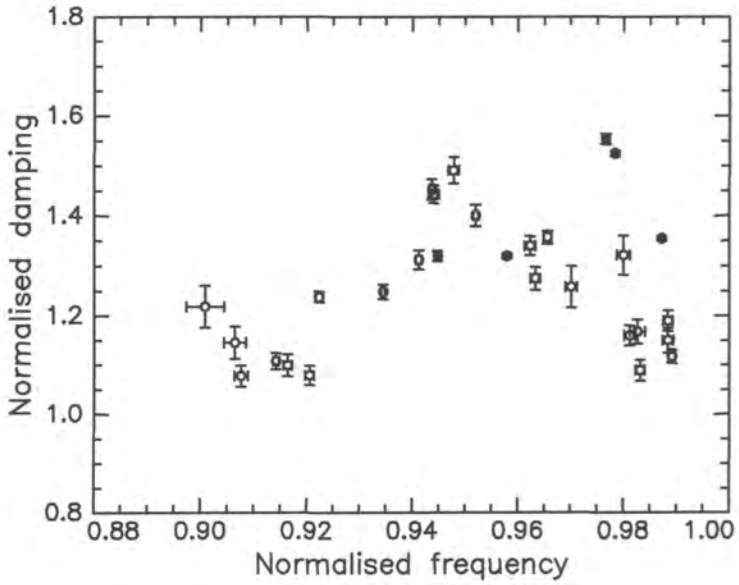

Figure 7.3.26. Dispersion plot of normalised frequency against normalised damping. $\Gamma_s = 0.8$mg m^{-2}

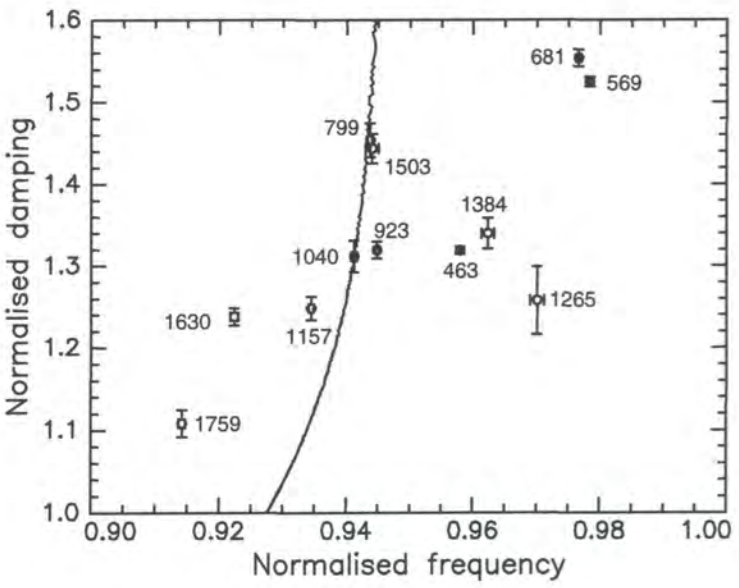

Figure 7.3.27. Selected data from figure 7.3.26 (circles, the adjacent numbers represent the value of wavenumber, in cm^{-1}, at which each data point was recorded). Solid line is a theoretical plot generated from the parameters γ_o = 70.24mN m^{-1}, $\gamma' = 0$, $\varepsilon_o = 27.68$mN m^{-1} and $\varepsilon' = 6.357\text{x}10^{-4}$mN s m^{-1}

$6.537x10^{-4}$mN m s^{-1}. This theoretical plot shows similar characteristics to the experimental data and any discrepancies can be assigned to the use of only average values of the viscoelastic parameters to generate such a plot.

A further indication of the influence of the value of ε' on the system is shown in figure 7.3.28, plots of frequency and damping against the ratio ε_o/γ_o. Each of the three plots has been calculated using γ_o = 72.6mN m^{-1}, γ' = 0, q = 270cm^{-1} and varying ε_o. Figure (a) shows the results obtained when both viscosities are constrained to zero. Here, the frequencies of the capillary and dilational waves coincide at $\varepsilon_o/\gamma_o \approx 0.16$, indicating classical resonance. When a positive value of ε' = $1.6x10^{-4}$mN s m^{-1} is introduced (figure (b)), the plot of the dilational frequency significantly changes shape and resonance now occurs at $\varepsilon_o/\gamma_o \approx 0.28$. With a negative value of $\varepsilon' = -1.6x10^{-4}$ mN s m^{-1}, the frequency of the capillary wave takes on new characteristics, increasing with ε_o/γ_o. This rapid increase has the effect that the two modes do not cross, although cross-over in the behaviour of the capillary and dilational modes does occur and is indicated by the dotted lines. The dilational mode attains capillary mode character and *vice versa*, the crossover predicted to take place at $\varepsilon_o/\gamma_o \approx 0.08$, indicating that mode mixing can occur at positions other than the classical resonance point of $\varepsilon_o/\gamma_o \approx 0.16$.

To summarise, mode mixing does not appear to be occurring at the resonance point in this system (Γ_s = 0.8mg m^{-2}). Simulations carried out with the viscoelastic parameters extracted at this concentration show none of the properties associated with this phenomenon. However, mode mixing is seen to occur with negative values of dilational viscosity, which are not observed in this study.

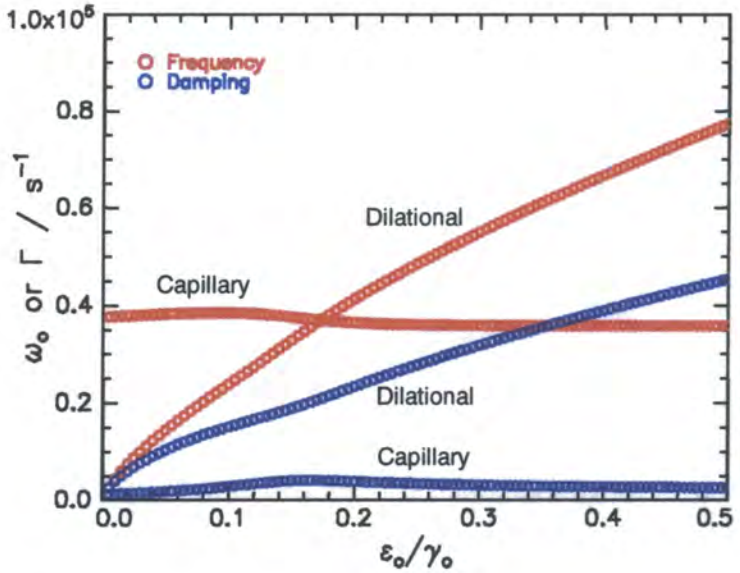

Figure 7.3.28a. Frequency (red) and damping (blue) of the capillary and dilational modes (marked on plot) as a function of ε_o/γ_o for a system with zero dilational viscosity. Data generated from the parameters γ_o = 72.6mN m^{-1}, γ' = 0, ε' = 0 and q = 270cm^{-1}

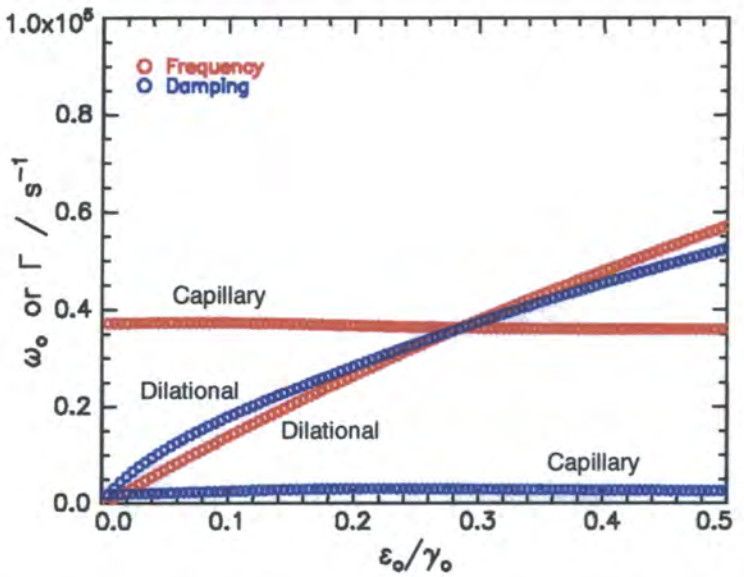

Figure 7.3.28b. Frequency (red) and damping (blue) of the capillary and dilational modes (marked on plot) as a function of ε_o/γ_o for a system with a positive dilational viscosity. Data generated from the parameters γ_o = 72.6mN m^{-1}, γ' = 0, ε' = 1.6x10^{-4}mN m s^{-1} and q = 270cm^{-1}

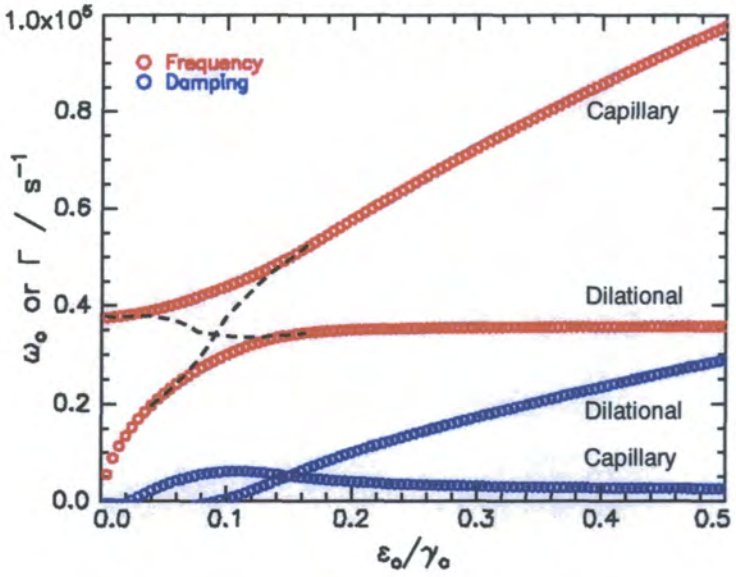

Figure 7.3.28c. Frequency (red) and damping (blue) of the capillary and dilational modes (marked on plot) as a function of ε_o/γ_o for a system with a negative dilational viscosity. Data generated from the parameters γ_o = 72.6mN m^{-1}, γ' = 0, ε' = -1.6x10^{-4}mN m s^{-1} and q = 270cm^{-1}. The dashed lines represent the crossover between the behaviour of the capillary and dilational waves

7.3.3. TIME DEPENDENCE STUDIES

Time dependence runs were used to assess the inhomogeniety and stability of the polymer films on the liquid surface. In these experiments, one correlation function was recorded per minute and each function was analysed individually to obtain values of capillary wave frequency and damping.

If the polymer film exists as a series of 'islands' on the liquid surface, it was expected that fluctuations in these parameters would be observed. As the islands 'float' across the liquid surface, the incident beam samples either water or polymer film and therefore the values of ω_0 and Γ are therefore expected to fluctuate between high and low values.

If film relaxation occurs over a long time scale, this will also be observed in these experiments as a gradual change in capillary wave frequency and damping with time.

7.3.3.1. Results

Plots of damping against time for the three surface concentrations studied in this fashion (0.2, 0.5 and 2.0mg m^{-2}) are shown in figures 7.3.29 to 7.3.31.

For a film of 0.2mg m^{-2} (figure 7.3.29), the value of capillary wave damping does not vary significantly from that of pure water ($1329s^{-1}$) indicated by a line on the plot. Any increase in damping is due to statistical and experimental effects. In these experiments, each data point corresponds to one correlation function, rather than an average of ten functions, causing a spread of values.

Notably different behaviour is observed at higher surface concentrations. For a film of 0.5mg m^{-2} (figure 7.3.30), a marked variation in capillary wave frequency with time is observed. This is discussed below. At 2.0mg m^{-2} (figure 7.3.31), there is again little change in capillary wave damping with time, although in this instance all these values are greater than Γ_{water}.

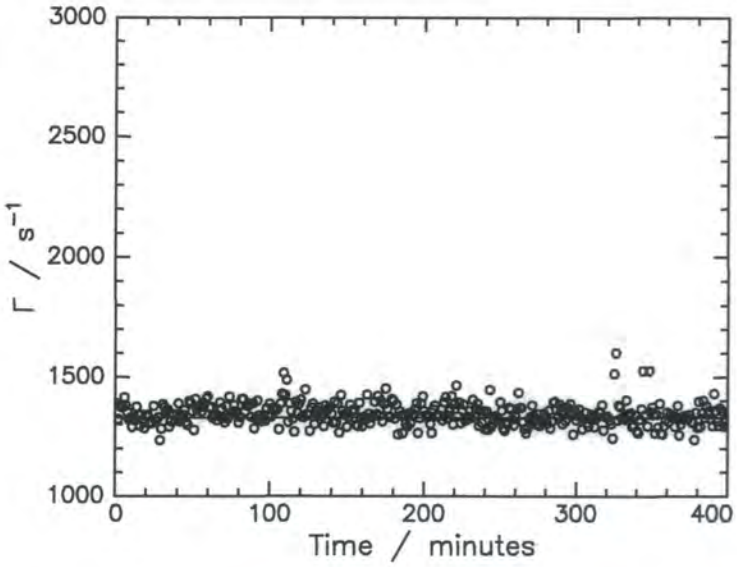

Figure 7.3.29. Capillary wave damping against time for PMMA-QP4VP on water (circles). Γ_s = 0.2mg m^{-2}, q = 259.6cm^{-1}. Data overlayed with Γ_{water} = 1329s^{-1} (line)

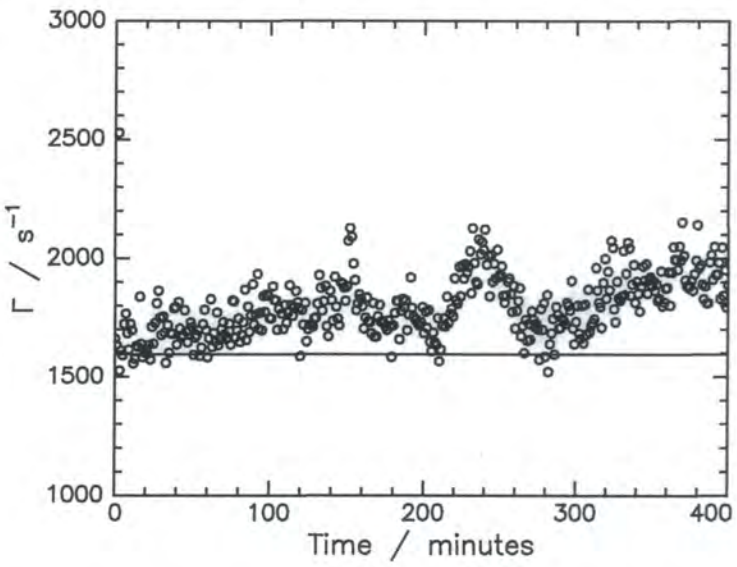

Figure 7.3.30. Capillary wave damping against time for PMMA-QP4VP on water (circles). Γ_s = 0.5mg m^{-2}, q = 269.9cm^{-1}. Data overlayed with Γ_{water} = 1596s^{-1} (line)

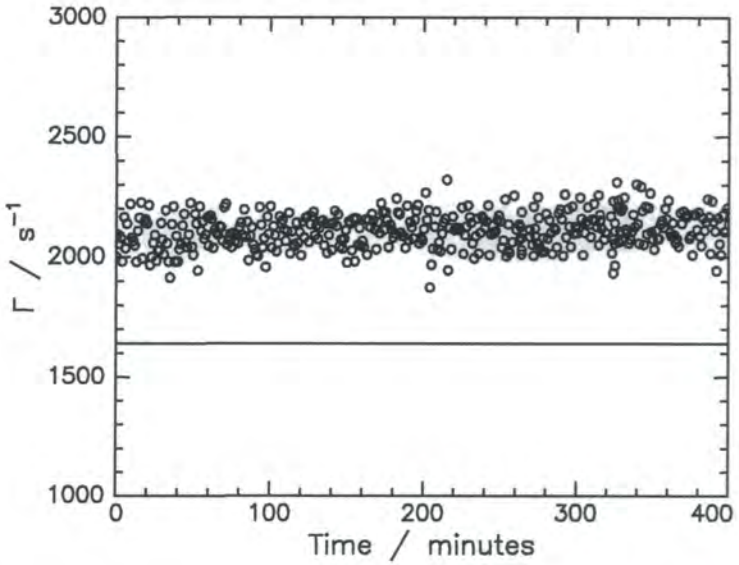

Figure 7.3.31. Capillary wave damping against time for PMMA-QP4VP on water (circles). Γ_s = 2.0mg m^{-2}, q = 265.6cm^{-1}, Data overlayed with Γ_{water} = 1640s^{-1} (line)

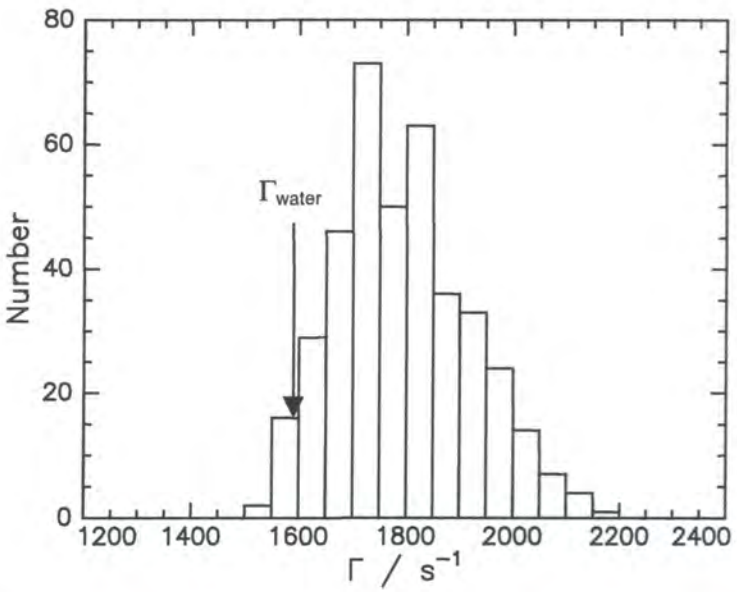

Figure 7.3.32. Histogram plot of capillary wave damping for PMMA-QP4VP on water. Γ_s = 0.5mg m^{-2}, q = 269.9cm^{-1}. Value of Γ_{water} = 1596s^{-1} indicated by the arrow

7.3.3.2. Discussion

The results obtained for a polymer surface concentration of 0.2mg m^{-2} show a value of capillary wave damping consistently around that of pure water. From this, it is difficult to ascertain whether or not the film completely covers the liquid surface at this low concentration. It could be deduced that as $\Gamma \approx \Gamma_{water}$, the small quantity of polymer exists as a single island which, over the course of the seven hours of the experiment, never once enters the part of the surface illuminated by the laser beam. More likely is that at this low surface concentration, the film does not increase the value of damping recorded from that of pure water. If this is this case, it is impossible to determine at whether or not the polymer does exist as a uniform film.

At 2.0mg m^{-2}, it is clear that polymer does exist as a uniform film. The vast majority of values of capillary wave damping fall in the range $2000 < \Gamma / s^{-1} < 2200$, substantially greater than the value of $\Gamma = 1640 s^{-1}$ obtained for a pure water surface. The overall consistency of the values indicates that, at long time periods, the film does not undergo relaxation. Surface pressure studies (section 5.2.3.3) find that film relaxation takes place in the first ten minutes following compression, after which time the film becomes stable. This is not observed by SQELS experiments as after compression of the film, the experimental equipment has to be aligned and sufficient time then given for the apparatus to 'settle'. This takes approximately ten minutes and these relaxation effects are therefore not observed by SQELS experiments.

It is the data obtained from a film of Γ_s = 0.5mg m^{-2} which exhibit the most interesting phenomena. Except for a short period at the start of the experiment, all the values of capillary wave damping are greater those that of pure water. However, the values of damping recorded are not consistent throughout the experiment. The data is presented in an alternative fashion in the histogram in figure 7.3.32. Here the data are binned into $50 s^{-1}$ damping ranges and plotted against the number of these values recorded. This latter plot emphasises that a wide range of damping values are recorded, the most prevalent being in the range $1650 < \Gamma / s^{-1} < 1850$. The fact that the values are greater than that of pure water implies that at all stages of the experiment, some quantity of polymer is present in the region of the surface

illuminated by the laser beam. However, the varying values of damping indicate that there are differences between each individual run. It is suggested that this is a result of the liquid surface consisting of islands that are small and/or moving rapidly. If this were indeed the case, a typical 30 second correlation function would consist of data collected when polymer is in the beam, and that collected when the beam is illuminating only pure water. The total correlation function would therefore be a combination of these two extremes.

7.3.4. SUMMARY

A SQELS study of a film of PMMA-QP4VP spread on water has been undertaken. At low surface concentrations, the polymer appears to exist as islands on the liquid surface before forming a uniform film at higher concentrations.

Surface concentration studies have revealed that a resonance between the capillary and dilational waves is observed at $\Gamma_s = 0.8\text{mg m}^{-2}$. A further peak in the capillary wave damping is seen at $\Gamma_s = 1.5\text{mg m}^{-2}$. A minimum in dilational wave damping is also found at this surface concentration and this observation is therefore assigned to an unidentified form of mode coupling. The viscoelastic parameters (extracted by constraining transverse shear viscosity to zero) show different characteristics to those shown by the static ($\omega_o = 0$) equivalents. The data has been compared to polymer scaling theory with varying degrees of success.

A frequency dependence study at the resonance concentration shows an interesting variation of capillary wave damping with frequency. This has partially been explained by an examination of the fitting procedure used. Attempts to fit the viscoelastic parameters using the Maxwell fluid and Voigt solid model ultimately proved unsuccessful, implying that the application of more complex model is required. The absence of a simple relaxation process in confirmed by the production of a Cole-Cole plot. An investigation into mode mixing shows that the phenomenon requires a negative value of dilational modulus. Mode mixing is therefore found not to occur in this instance.

7.4. Potassium Chloride Solution Subphases

As an extension to the studies at the air-water interface reported in section 7.3, SQELS experiments have also been carried out on potassium chloride solution subphases. The work is again presented in three sections. The first of these studies the polymer surface concentration dependence of the capillary wave frequency and damping and the viscoelastic parameters. These experiments have been carried out on subphases of the same salt concentrations used in neutron reflectometry experiments, namely 10^{-3}M, 0.1M and 1M KCl solutions.

The frequency dependence of the capillary wave properties are then examined. For both 0.1M and 1M KCl solution subphases, one polymer surface concentration (where the maximum is capillary wave damping is observed) has been selected. The behaviour of the viscoelastic parameters with capillary wave frequency is used to give an insight into the viscoelastic properties of the system.

Finally, an investigation into the surface structure of the polymer monolayer has been undertaken by studying any change in the capillary wave damping with time.

7.4.1. CONCENTRATION DEPENDENCE STUDIES

7.4.1.1. Results: Capillary Wave Frequency & Damping

The variation of capillary wave frequency with surface concentration is shown in figure 7.4.1, where the results for the three salt concentration solutions are presented and compared to those on water. Importantly, due to slight differences in experimental set-up, the wavenumber at which each set of data was obtained differed slightly. The values of wavenumber used are given in table 7.4.1 and the effect of this discrepancy on the results obtained is discussed in section 7.4.1.3.

Subphase	q /cm^{-1}
Water	269 – 270
10^{-3}M KCl solution	277 – 278
0.1M KCl solution	275 – 276
1M KCl solution	267 – 268

Table 7.4.1. Wavenumber range used in SQELS experiments

All four plots show the similar characteristic of a decrease in frequency at the higher surface concentrations, although the details of each plot differ somewhat. A film spread on the lowest salt concentration subphase records a constant value of capillary wave frequency (equal to that of water) for surface concentrations up to 0.9mg m^{-2}. Frequency then decreases rapidly up to $\Gamma_s \approx$ 1.2mg m^{-2}. After this, the rate of decrease falls, before increasing again at higher surface concentrations. Similar results are recorded on 0.1M KCl solution, although in this case the data in the low surface concentration region are quite scattered. Experiments on the highest concentration salt solution, 1.0M, also show a steady decrease for surface concentrations greater than 1.5mg m^{-2}. At low surface concentrations, the capillary wave frequency is generally lower than that recorded for the equivalent surface concentration on water.

The capillary wave damping (figure 7.4.2) shows a more characteristic dependence upon polymer surface concentration, increasing rapidly to a maximum before decreasing more slowly. As the salt concentration of the subphase increases, the

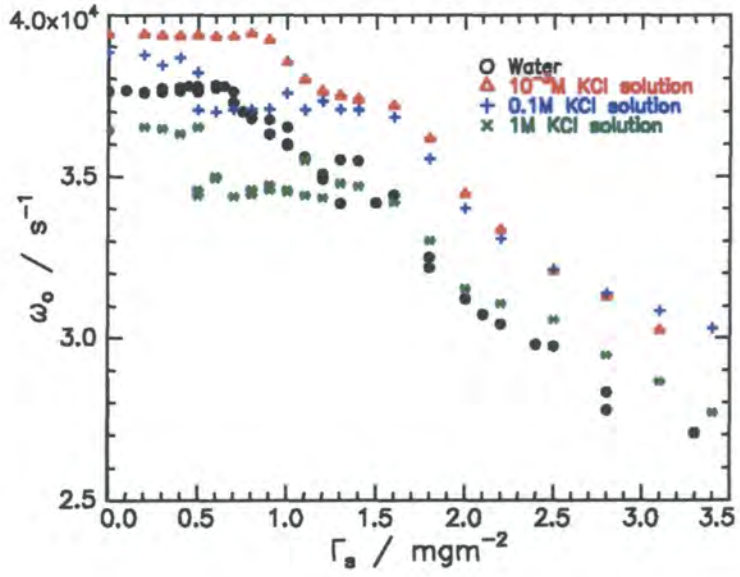

Figure 7.4.1. Capillary wave frequency against surface concentration for PMMA-QP4VP spread on salt solutions (see legend). Results compared with those obtained for a film on pure water

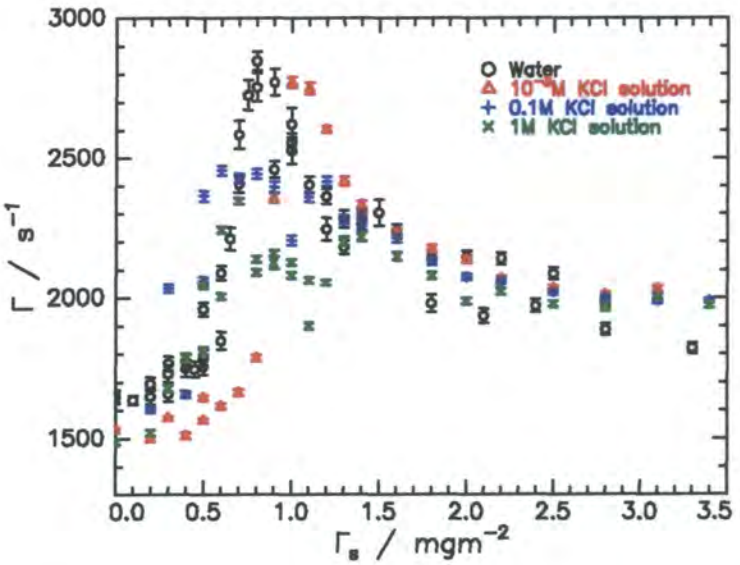

Figure 7.4.2. Capillary wave damping against surface concentration for PMMA-QP4VP spread on salt solutions (see legend). Results compared with those obtained for a film on pure water

maximum value of damping decreases. From a value of $2850s^{-1}$ on water, this drops to $2780s^{-1}$ on 10^{-3}M KCl solution, $2450s^{-1}$ on 0.1M KCl and $2320cm^{-1}$ on 1M KCl. The surface concentration at which these maxima arise also differs between subphases. On 10^{-3}M KCl solution, this maximum in damping occurs at 1.0mg m^{-2}, a shift from the values 0.8mg m^{-2} for a film spread on water. For higher salt concentration subphases, the maxima are both broad and much less well defined. In both cases (for 0.1M and 1M KCl solutions), a surface concentration of 0.7mg m^{-2} is taken to relate to the maximum in capillary wave damping.

At higher surface concentrations (above 1.3mg m^{-2}), the values of capillary wave damping are very similar and appear to be almost independent of subphase.

7.4.1.2. Results: Viscoelastic Parameters

Again, data fitting was carried out constraining transverse shear viscosity to zero. The surface concentration dependencies of the remaining three viscoelastic parameters are outlined below:

Surface Tension

The surface tension dependence on surface concentration is shown in figure 7.4.3, where the three data sets obtained on potassium chloride solutions show similar characteristics. In all cases, surface tension is approximately constant until a surface concentration of 1.4mg m^{-2} is reached. Thereafter, surface tension decreases with polymer surface concentration. These results differ from those recorded on water, where surface tension begins to decrease at a lower surface concentration. The results obtained on salt solutions are reproduced in figure 7.4.4, where they are compared with the static surface tension values obtained *via* a Wilhelmy plate. For clarity, the data for 0.1M and 1M solutions are shifted from their absolute values by 15mN m^{-1} and 30mN m^{-1} respectively. The two sets of results for each subphase show a strong correlation, much greater than the data for the polymer spread on water shown in figure 7.3.3. For the salt solution subphases discussed here, the correlation between the two sets of data holds until the highest surface concentration recorded, 3.0mg m^{-2}. Here, the surface pressure isotherm begins to reach a plateau, resulting in constant values of $\gamma_{o,static}$ whilst $\gamma_{o,dynamic}$ continues to decrease.

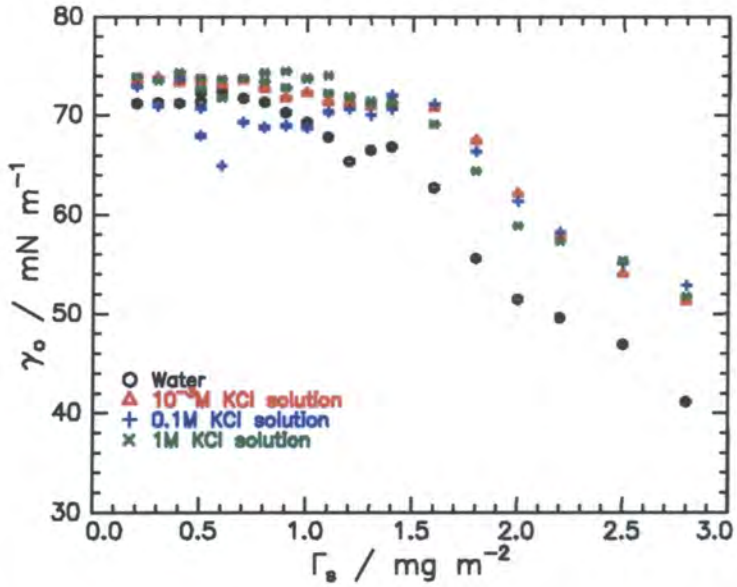

Figure 7.4.3. Surface tension against surface concentration for PMMA-QP4VP spread on salt solutions (see legend). Results compared to those on water

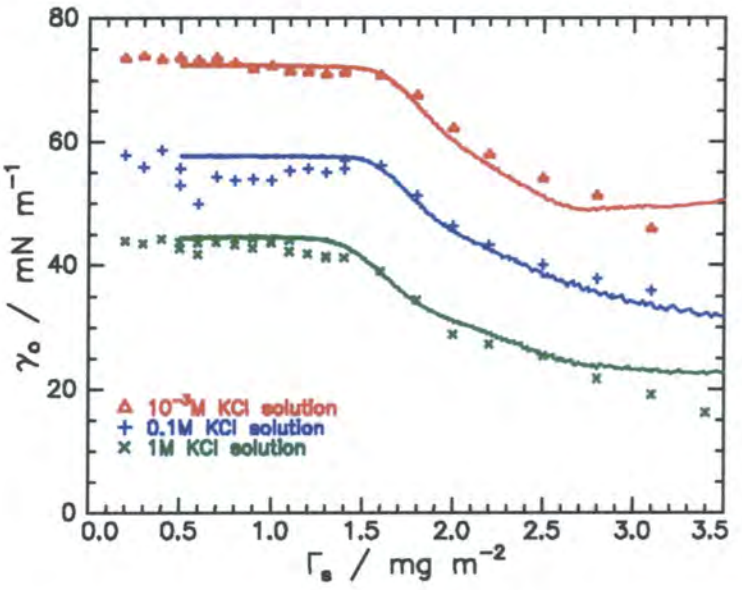

Figure 7.4.4. Comparison between dynamic (symbols) and static (lines) surface pressure for PMMA-QP4VP spread on salt solutions. Data obtained from SQELS and surface pressure isotherms respectively, that for 0.1M and 1M KCl shifted by 15mN m^{-1} and 30mN m^{-1} respectively to increase clarity

Dilational Modulus

The plots of dilational modulus against surface concentration are shown in figure 7.4.5. Generally, the data follow similar paths at low surface concentrations, ε_o increasing with Γ_s. At higher concentrations the characteristics of the plots differ remarkably.

The values of ε_o recorded on 10^{-3}M KCl solution remain around zero until Γ_s = 0.7mg m^{-2}, before increasing steadily until a concentration of 1.6mg m^{-2} is reached. After this, large values of ε_o with large uncertainties are measured and it is difficult to ascertain any firm trend in the data. When spread upon 0.1M KCl solution, the dilational modulus rises to $\varepsilon_o \approx$ 8mN m^{-1} at Γ_s = 0.7mg m^{-2}, remains approximately constant at this value until Γ_s = 1.4mg m^{-2} and rises to higher values at high surface concentrations. The dilational moduli recorded on 1.0M KCl increase more rapidly. A large discontinuity in the data appears at Γ_s = 0.7mg m^{-2}, where the value of ε_o rises from 5mN m^{-1} to 50mN m^{-1}. At higher surface concentrations, dilational modulus remains at *ca.* 50mN m^{-1}, although two values of very low ε_o are recorded. These data sets contrast with the values of dilational modulus recorded on water, where the values go through a maximum at Γ_s = 1.0mg m^{-2}, rather than continuing to increase at higher concentrations.

Figure 7.4.6 compares these dynamic values of dilational modulus with those calculated from equation 5.2.2 using the surface pressure data reported in chapter five. The data on 10^{-3}M and 0.1M KCl solution are shifted by 50mN m^{-1} and 100mN m^{-1} respectively, to increase clarity. For all three sets of data, the correlation between the dynamic and static values is much greater than that on water. Although the exact values are not reproduced, some definite trends in the data are followed. For a film on 10^{-3}M KCl solution, the two plots rise at approximately the same gradient to a maximum at Γ_s = 2.0mg m^{-2}. On 0.1M KCl solution, the two sets of data are highly similar until Γ_s = 2.0mg m^{-2}, after which $\varepsilon_{o,dynamic} > \varepsilon_{o,static}$. For 1M KCl, the overall trend shown by static dilational modulus mimics that of the dynamic dilational modulus, although for all surface concentrations, $\varepsilon_{o,dynamic} > \varepsilon_{o,static}$. The discrepancy at the highest surface concentrations is *ca.* 40mNm^{-1}. The only concentration range where the two sets of data do not follow similar trends is

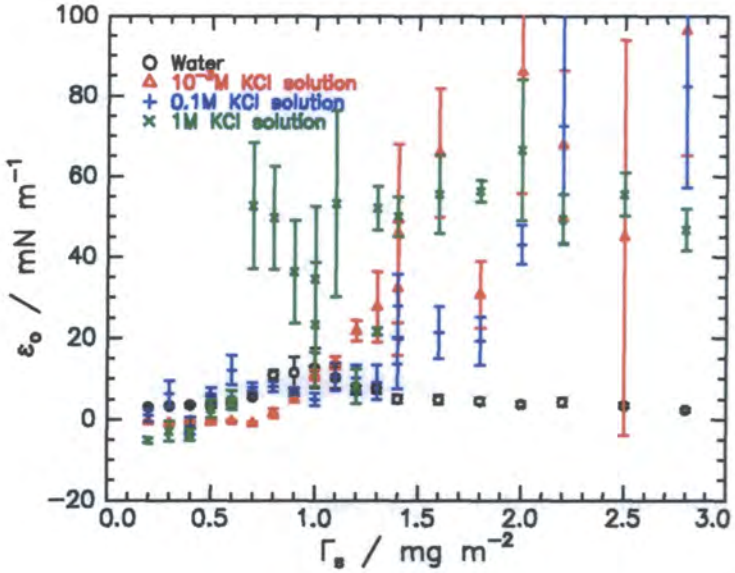

Figure 7.4.5. Dilational modulus against surface concentration for PMMA-QP4VP spread on salt solutions (see legend). Results compared to those on water

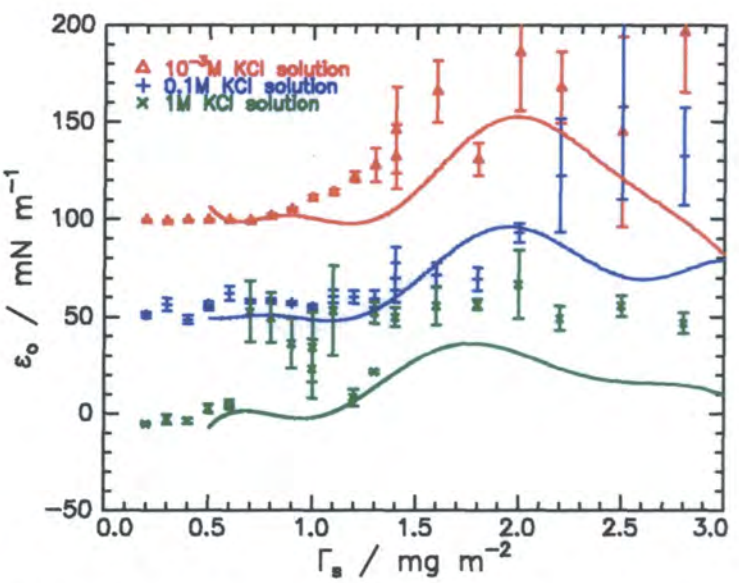

Figure 7.4.6. Comparison between dynamic (symbols) and static (lines) dilational modulus for PMMA-QP4VP spread on salt solutions. Data obtained from SQELS and surface pressure isotherms respectively, that for 0.1M and 1M KCl shifted upwards by 50mN m^{-1} and 100mN m^{-1} respectively to increase clarity

$0.7 < \Gamma_s$ / mg $m^{-2} < 0.9$, where exceptionally high values of dynamic dilational modulus are recorded.

Dilational Viscosity

The plots of dilational viscosity against surface concentration are shown in figure 7.4.7. The data obtained on 10^{-3}M and 0.1M KCl solutions bear similarities to the dilational moduli plots (figure 7.4.6). For films spread on these subphases, ε' is initially small, before increasing to a maximum at $\Gamma_s = 2.0$mg m^{-2}. The data recorded on 1M KCl is unique. Here, the values of dilational modulus rise to a maximum at $\Gamma_s \approx 1.1$mg m^{-2}, before decreasing to negative values of *ca.* $-3x10^{-4}$mN s m^{-1} for surface concentrations greater than 1.3mg m^{-2}. This result, being the only occurrence of negative dilational viscosities in this work, is significant and is discussed in section 7.4.1.4.

7.4.1.3. Discussion: Capillary Wave Frequency & Damping

As outlined in table 7.4.1, experimental effects resulted in each set of experiments being carried out at a slightly different wavenumber. This has no effect of the relative value of either capillary wave damping or frequency in each individual data set. However, as both of these parameters are directly related to q, the discrepancy (although the difference between the highest and lowest values is only 4%) makes it difficult to compare the values between experiments. To counteract this, the data has been 'scaled' to q = 270cm^{-1}, the value of q used for a film of polymer on a water subphase. From equation 7.3.1, frequency is approximately related to q by $\omega_o \sim q^{3/2}$. Capillary wave damping is given to a first approximation[25] by equation 7.4.1, where its relationship with q is seen to be $\Gamma \sim q^2$.

$$\Gamma = \frac{2\eta q^2}{\rho} \qquad \textbf{Equation 7.4.1.}$$

These two relationships have been used to produce figures 7.4.8 and 7.4.9, where the data has been 'scaled' to a wavenumber of 270cm^{-1} to allow their direct comparison. The capillary wave frequency dependence on surface concentration (figure 7.4.8)

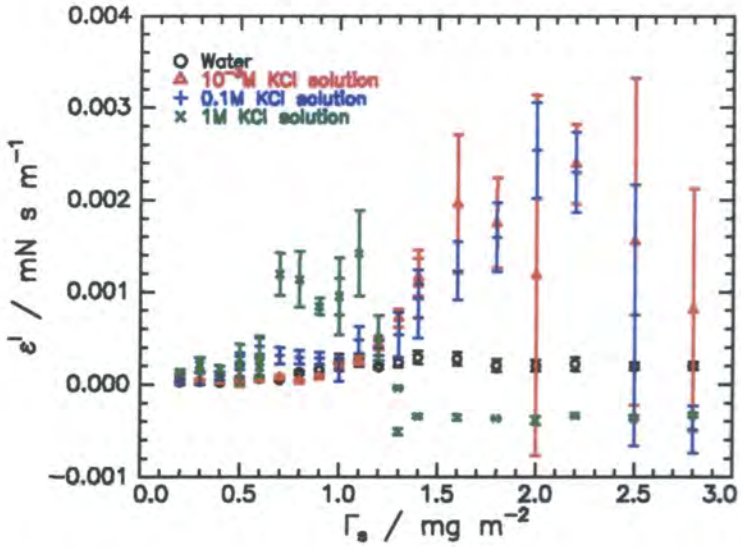

Figure 7.4.7. Dilational viscosity against surface concentration for PMMA-QP4VP spread on salt solutions (see legend). Results compared to those on water

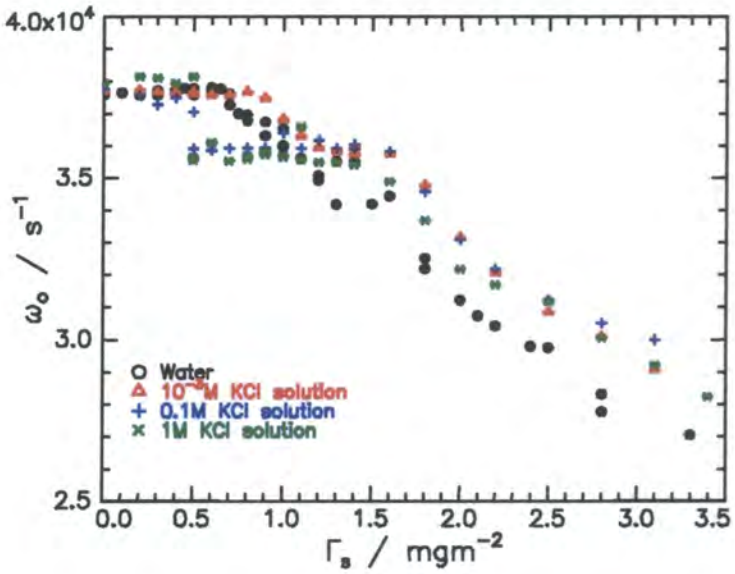

Figure 7.4.8. 'Scaled' capillary wave frequency against surface concentration for PMMA-QP4VP spread on salt solutions and water (see legend). Data has been adjusted to q =270cm^{-1}, the wavenumber used for the experiments on water

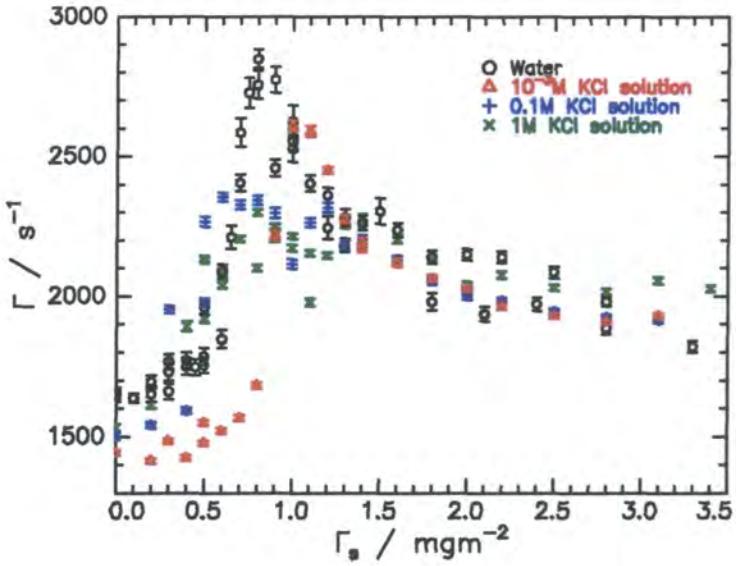

Figure 7.4.9. 'Scaled' capillary wave damping against surface concentration for PMMA-QP4VP spread on salt solutions and water (see legend). Data has been adjusted to q =270cm^{-1}, the wavenumber used for the experiments on water

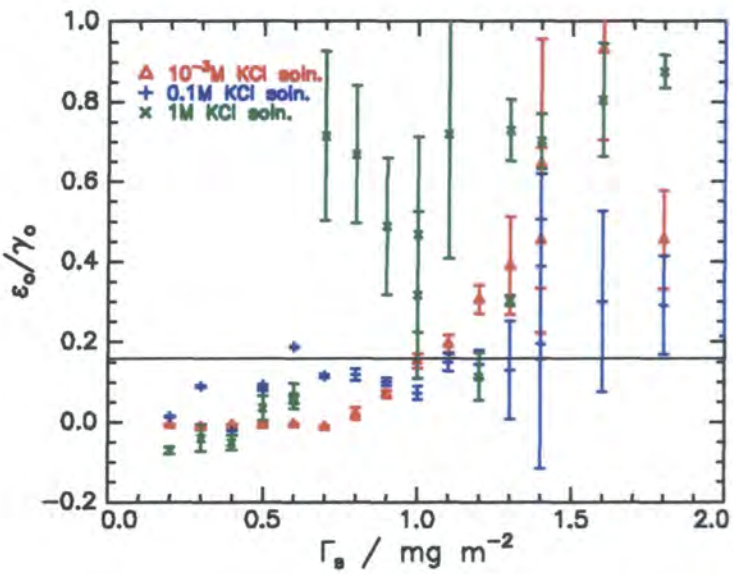

Figure 7.4.10. The ratio of ε_o/γ_o for PMMA-QP4VP spread on salt solutions. The horizontal line at $\varepsilon_o/\gamma_o \approx 0.16$ signifies the possible occurrence of classical resonance

now shows highly similar characteristics to the surface pressure isotherms (figure 5.3.4). From the data at low surface concentrations, it is difficult to determine any real trends, although the value of frequency begins to decrease at a lower concentration for the film spread on water compared to that spread on salt solutions. At a specific surface concentration in the range $1.5 < \Gamma_s$ / mg $m^{-2} < 2.2$, the capillary wave frequencies on each of the subphases vary as 10^{-3}M $\approx$ 0.1M > 1M > water. This is clearly consistent with the static surface pressures measured at these concentrations, which varies as 10^{-3}M $\approx$ 0.1M < 1M < water. Trends are more difficult to discern from the scaled capillary wave damping (figure 7.4.9), although it still appears that the maximum value of damping decreases as salt concentration increases. At higher surface concentrations, damping remains relatively independent of subphase salt concentration.

Attention is now turned to the monotonic decrease in capillary wave frequency recorded after the initial plateau. Despite the difficulty of pinpointing exactly the concentration range of this decrease, a least squares fit can be applied to this region to extract the gradient of the slope, $d\omega_o/d\Gamma_s$. The values obtained are given in table 7.4.2:

Subphase	$(d\omega_o/d\Gamma_s)$ / m^2 mg^{-1} s^{-1}
Water	-4184
10^{-3}M KCl solution	-4051
0.1M KCl solution	-3052
1M KCl solution	-2760

Table 7.4.2. Values of $d\omega_o/d\Gamma_s$ extracted form the linear decrease in capillary wave frequency

Clearly, the gradient of the slope becomes more positive as subphase salt concentration increases. The values of $d\omega_o/d\Gamma_s$ for films spread on water and 10^{-3}M KCl solution are approximately equivalent and are more negative than the values obtained on 0.1M and 1M salt solutions. The above data implies that the behaviour of the polymer film at high surface concentrations is in some way dependent upon the subphase. These results can be compared with those from neutron reflectometry experiments (chapter six). At low salt concentrations, the polyelectrolyte chains have been found to extend deep into the liquid surface, whereas increasing the salt

content causes the chains to contract and become resident nearer the liquid surface. This greater quantity of material in the near surface region correlates with a more positive value of $d\omega_o/d\Gamma_s$, indicating that the reduction in capillary wave damping with surface concentration is hindered by this extra material.

Finally, the significance of the maxima in the capillary wave damping plots (figure 7.4.2) is discussed. To investigate the possibility of classical resonance between the dilational and capillary modes, a plot of ε_o/γ_o has been generated (figure 7.4.10). The maximum in damping for a film on a subphase of 10^{-3}M KCl occurs at 1.0mg m^{-2} and at this concentration $\varepsilon_o/\gamma_o = 0.153 \pm 0.017$, indicating that classical resonance does indeed occur at this surface concentration. For 0.1M and 1M KCl solutions, the maxima in capillary wave damping are much less well defined, but appear to occur at *ca.* 0.7mg m^{-2}. At this concentration, the values of ε_o/γ_o are 0.115 ± 0.015 and 0.715 ± 0.213 respectively. For 0.1M KCl, classical resonance could possibly be occurring in this region, even though the value of ε_o/γ_o obtained is slightly lower than theoretical value of 0.16. For the next two surface concentrations examined, 0.8mg m^{-2} and 0.9mg m^{-2}, the values of ε_o/γ_o oscillate around 0.16, indicating that resonance is indeed likely to be occurring somewhere in this region. Values close to $\varepsilon_o/\gamma_o \approx 0.16$ are also reported for Γ_s = 1.2mg m^{-2}, where a second smaller maximum is observed in the capillary wave damping. The data obtained on 1M KCl solution are much more bizarre. Clearly the value of ε_o/γ_o at Γ_s = 0.7mg m^{-2} does not indicate classical resonance, although this may simply be an artefact of the very high dilational modulus recorded at this concentration. It appears that resonance occurs at no other surface concentration.

7.4.1.4. Discussion: Viscoelastic Parameters

The viscoelastic parameters extracted from SQELS experiments have been compared to polymer scaling theory. For the surface pressure data (calculated from figure 7.4.3), the scaling factors for the concentration range $1.5 < \Gamma_s$ / mg $m^{-2} < 3.0$ are given in table 7.4.3.

Subphase	Scaling factor
10^{-3}M KCl solution	3.5
0.1M KCl solution	3.3
1M KCl solution	2.2

Table 7.4.3. Scaling factors extracted from the surface tension data in figure 7.4.3 for the concentration range $1.5 < \Gamma_s$ / mg m^{-2} < 3.0

Only the film on 1M KCl solution reports a value near the theoretical scaling relationship of $\Pi \sim \Gamma_s^{11/6}$ (equation 7.3.4). The scaling factors obtained on the lowest two salt concentration subphases are similar to the value found for a film on water. As discussed previously, figure 7.4.4 shows that the static and dilational values of surface tension are very similar. At the highest surface concentrations, the two sets of data diverge somewhat due to the static values of surface tension reaching a plateau. This is ascribed to be due to false surface pressure readings caused by the displacement of the Wilhelmy plate from the vertical. These effects do not occur in SQELS experiments and surface tension therefore continues to decrease with surface concentration.

Scaling factors are more difficult to extract from the plot of dilational modulus (figure 7.4.5), due to the uncertainties on the data. The initial increase in dilational modulus scales with surface concentration as 3.8, 0.9 and 1.5 for 10^{-3}M, 0.1M and 1M salt solutions respectively. However, these results are not directly comparable with each other as a different range of surface concentrations is selected for fitting in each case. None of the values compare well with the theoretical scaling relationship of $\varepsilon_o \sim \Gamma_s^{11/6}$ (equation 7.3.5). The static and dynamic values of dilational moduli (figure 7.4.6) show similar characteristics to each other, although the values obtained from SQELS experiments are generally larger.
The dilational viscosity values again show linear regions in different surface concentration ranges. The scaling factors extracted, 0.6, 1.3 and 2.3 on 10^{-3}M, 0.1M and 1M KCl solutions respectively, show little resemblance to the theoretical relationship of $\varepsilon' \sim \Gamma_s^2$.

Attention is now turned to the negative values of dilational viscosity observed for high surface concentrations of the film spread upon 1M KCl solution. The phenomenon of negative dilational moduli was first reported by Earnshaw for a

solution of primary alcohols[26] and has since been observed for a variety of systems. Examples of these include foam forming,[27] surfactant[14] and polymer[28] solutions and surfactant[9] and polymer monolayers.[10,13,22,29]

The occurrence of negative dilational viscosities implies that mechanical energy is in some way being gained from an external source. This has been suggested to be due to diffusive exchange[30] and adsorption barriers between surface excess layers and the bulk solution.[31] In these processes, energy is transferred to the dilational modes. A further possible cause of negative dilational viscosities is the Marangoni effect,[32] the conversion of local variations of surface tension into mechanical energy. However, in a system such as this, the effect is too small to account for the occurrence of negative dilational moduli. A final suggestion is that negative dilational viscosities are in fact 'effective' parameters[19] due to the inadequacies of the dispersion equation. Despite recent theoretical developments,[7] it may be that case that the equation used still does not give a thorough description of the viscoelastic properties of a spread film at the air-liquid interface.

Dilational viscosity is directly related to the damping of the dilational waves and a negative ε' results in a decrease in this damping. This is shown in figures 7.4.11 and 7.4.12, where the viscoelastic parameters obtained at each surface concentration have been used in the dispersion equation. This process results in the extraction of frequency (fig 7.4.11) and damping (figure 7.4.12) of the capillary and dilational waves.

At the surface concentration where negative dilational viscosities are first recorded (1.3mg m^{-2}), a clear change in the values of both frequency and damping of the dilational mode are observed. The frequency of the dilational waves increases significantly, to values substantially greater than the damping of the capillary waves. The expected shift in the dilational wave damping does occur, Γ_D decreasing significantly where negative values of ε' are recorded.

The reasons why negative dilational viscosities are only observed at these high concentrations on 1M KCl solution are unclear. Γ_s = 1.3mg m^{-2} is approximately the surface concentration where there is an increase in surface pressure in the isotherm

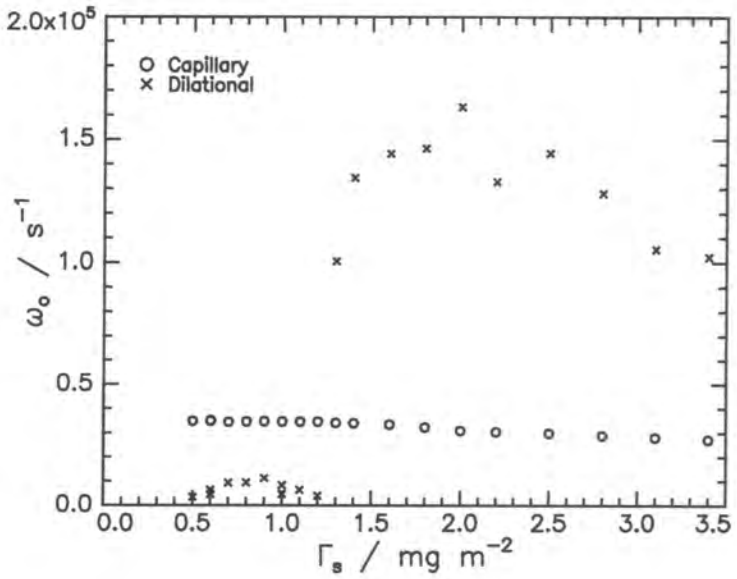

Figure 7.4.11. Comparison of capillary and dilational mode frequencies for a film of PMMA-QP4VP on 0.1M KCl solution

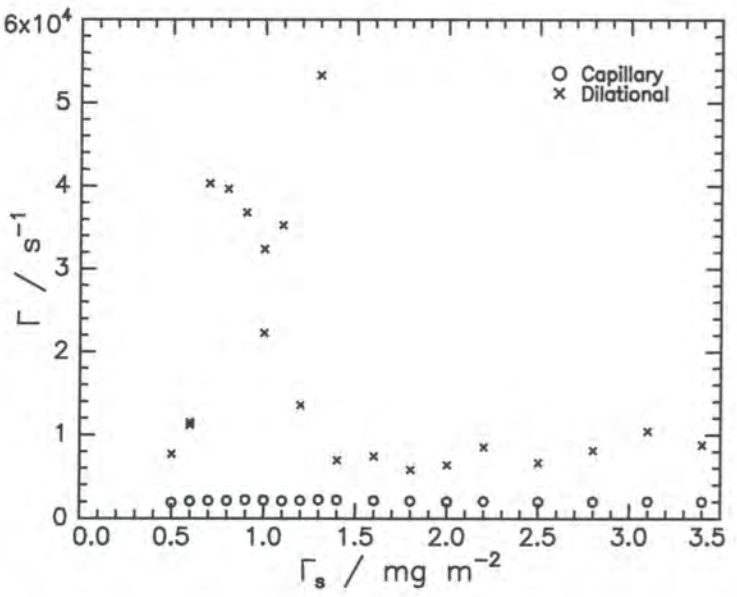

Figure 7.4.12. Comparison of capillary and dilational mode dampings for a film of PMMA-QP4VP on 0.1M KCl solution

due to the penetration of the QP4VP chains into the subphase. Why this phenomenon should not be observed for the film spread on 10^{-3}M KCl and 0.1M KCl, which show similar shaped isotherms (albeit with a 'take-off' surface concentration of 1.5mg m^{-2}) is difficult to determine.

7.4.2. Frequency Dependence Studies

Frequency dependence studies were carried out in a similar manner to those in section 7.3.2. Two salt subphases were studied, 0.1M KCl and 1M KCl. For each of these, one polymer surface concentration, 0.7mg m^{-2}, was examined, selected to correspond to the surface concentration at which at which the maximum in capillary wave damping was thought to occur. For both sets of experiments, a maximum wavenumber of approximately 2000cm^{-1} (corresponding to $\omega_o \approx 7.4x10^5 s^{-1}$ for the monolayer covered surface) was accessible.

7.4.2.1. Results: Capillary Wave Frequency and Damping

Double logarithmic plots of capillary wave frequency and damping against wavenumber for monolayers of Γ_s = 0.7mg m^{-2} are shown in figures 7.4.13 and 7.4.14 respectively. Linear least squares fits of the data reveal that the frequency and damping scale as $\omega_o \sim q^{1.48}$ and $\Gamma \sim q^{1.96}$ on both 0.1M and 1M KCl salt solutions. These results, which bear good agreement with the predicted scaling factors of 1.5 and 2 respectively, indicate that the scaling of ω_o and Γ with wavenumber appears to be independent of subphase salt concentration.

An effect most noticeable in the monolayer damping data is that the data values, especially those recorded on a 1M KCl solution, do not lie in an entirely straight line, but are in fact somewhat scattered. This is discussed in section 7.4.2.3.

7.4.2.2. Results: Viscoelastic Parameters

The viscoelastic parameters obtained are shown in figures 7.4.15 to 7.4.17, where, for comparative purposes, the results are overlayed with those obtained on a water subphase. The results obtained are outlined below:

Surface Tension

Surface tension (figure 7.4.15) again appears to be independent of frequency, there being no definite trend being observable for either of the films spread on salt solution.

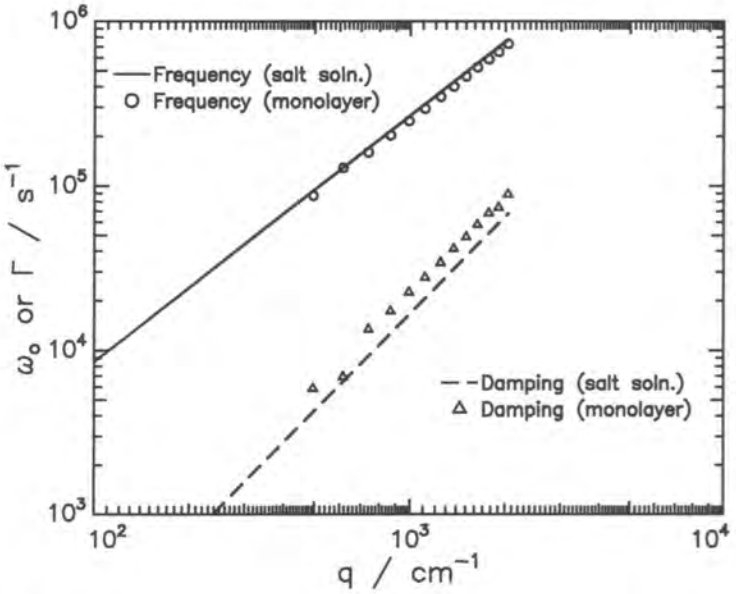

Figure 7.4.13. Wavenumber dependence of capillary wave frequency and damping for a PMMA-QP4VP film of Γ_s = 0.7mg m^{-2} on 0.1M KCl solutions (symbols, see legend). Data compared to that calculated for a clean salt solution surface (lines)

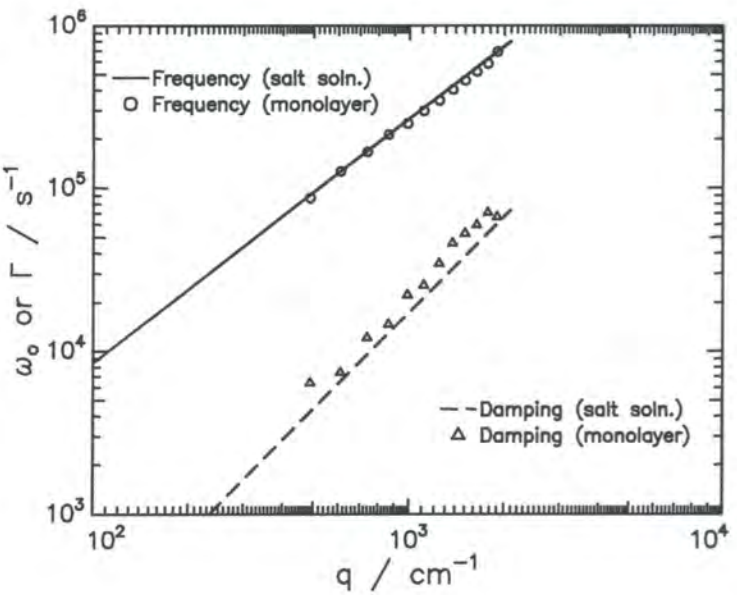

Figure 7.4.14. Wavenumber dependence of capillary wave frequency and damping for a PMMA-QP4VP film of Γ_s = 0.7mg m^{-2} on 1M KCl solutions (symbols, see legend). Data compared to that calculated for a clean salt solution surface (lines)

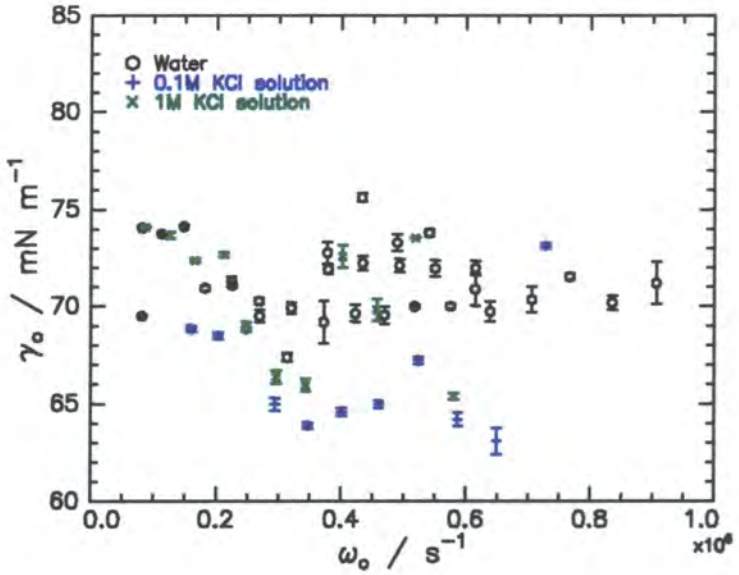

Figure 7.4.15. Frequency variation of γ_o for films of PMMA-QP4VP spread on 0.1M and 1M KCl solutions. Results compared with those on a water subphase

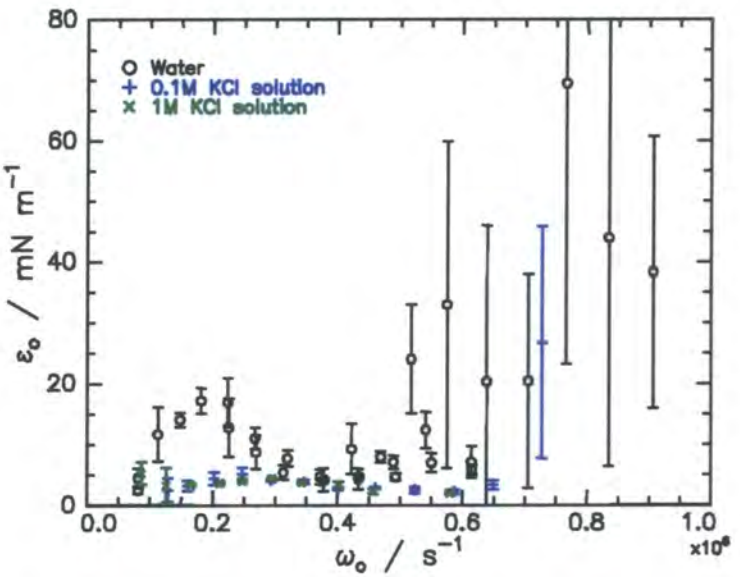

Figure 7.4.16. Frequency variation of ε_o for films of PMMA-QP4VP spread on 0.1M and 1M KCl solutions. Results compared with those on a water subphase

Dilational Modulus

For films on both salt solutions, small values of dilational modulus (figure 7.4.16) are recorded compared to those on water. In both cases, ε_o initially rises, reaching a maximum of 5.1mN m^{-1} at $\omega_o = 2.5x10^5 s^{-1}$ for the film on 0.1M KCl and 4.4mN m^{-1} at $\omega_o = 3.0x10^5 s^{-1}$ for that on 1M KCl. The well-defined maximum observed at low surface concentrations for a water subphase is not seen for either of the two salt solutions.

Dilational Viscosity

The plots of dilational viscosity against wavenumber (figure 7.4.17) are highly similar, irrespective of subphase. In all cases, the largest value of dilational modulus is recorded at low frequency before descending to a minimum of approximately zero at $\omega_o \approx 3.5x10^{-5} s^{-1}$. At higher frequencies, dilational viscosity again appears to rise, although this region of the plot is poorly defined. All values of ε' are positive.

7.4.2.3. Discussion: Capillary Wave Frequency and Damping

Attention is now refocused on figures 7.4.13 and 7.4.14. In general, the frequency of the capillary waves with a spread monolayer is less than that of the clean salt solution. The opposite effect is found for the capillary wave damping, which increases upon the spreading of a monolayer. The major exception to this is the second data point (relating to $q \approx 615cm^{-1}$), where for both salt subphases the frequency and damping appears to be similar to that of the clean salt solution. This is thought to be due to no polymer being in the region illuminated by the laser beam for the duration of the experiment. Results to be discussed in section 7.4.3 reveal that at this low surface concentration (0.7mg m^{-2}), the film on both subphases is not in fact uniform, but is 'patchy' in character. This non-uniformity of the film is also thought to account for the scattered values of damping observed for the film on 1M KCl.

Figure 7.4.13 shows a decrease in capillary wave damping between the third last and penultimate data points, the same effect being observed in figure 7.4.14 between the final two data points. A similar result was observed in section 7.3.2.3, where the

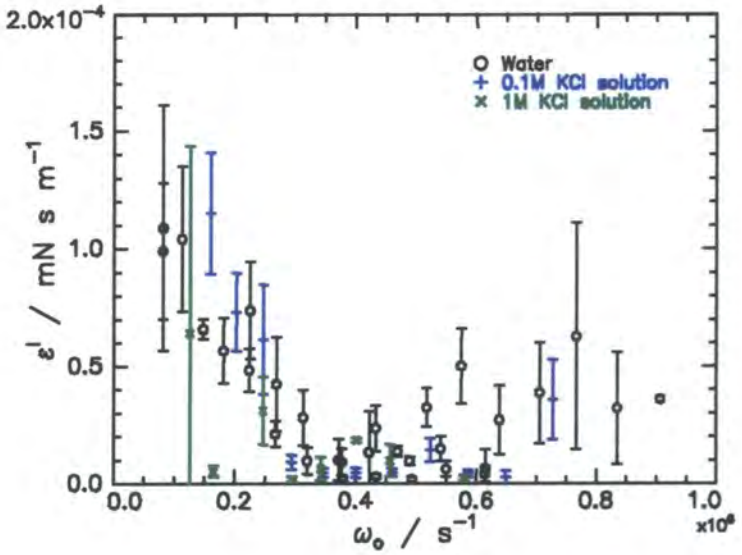

Figure 7.4.17. Frequency variation of ε' for films of PMMA-QP4VP spread on 0.1M and 1M KCl solutions. Results compared with those on a water subphase

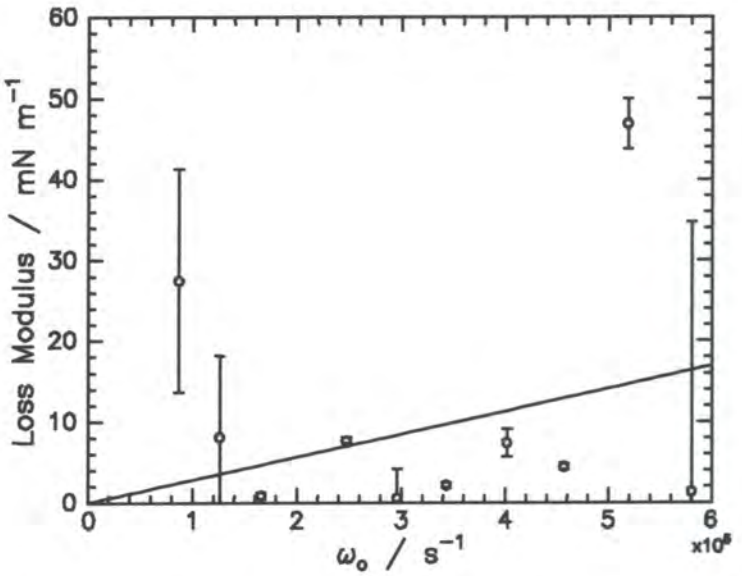

Figure 7.4.18. Attempted Voigt model fit (line) to plot of loss modulus against frequency (points) for a film of PMMA-QP4VP, Γ_s = 0.7mg m^{-2} on 1M KCl solution

phenomenon was assigned to a change in the experimental channel width. For a film on both of the salt solutions, the decrease in damping occurs where the experimental channel width is reduced from 2μs to 1μs, confirming this conclusion.

7.4.2.4. Discussion: Viscoelastic Parameters

Attempted fits of viscoelastic models to the frequency dependence data, using the Maxwell fluid and Voigt solid models discussed in section 7.3.2.4. Again, as with the data obtained on a water subphase, problems were found to occur. The Maxwell model could not be applied successfully due to there being no clear dependence of surface tension on frequency. In response to this, the Voigt model was applied. An example of an attempted 'fit' is shown in figure 7.4.18, a plot of loss modulus against frequency, where it is clear that the data is not fitted by the application of such a model. It was therefore concluded that, as for the frequency dependence study on water, a film of Γ_s = 0.7mg m^{-2} spread on 0.1M and 1M KCl solutions cannot be described by these simple arrangements of viscoelastic elements. As conformation of this, Cole-Cole plots of $\omega_o\varepsilon'$ against ε_o were plotted from the data obtained on both salt solutions (figures 7.4.19 and 7.4.20). The plots clearly do not show the semi-circular behaviour expected if a single relaxation time is present in the system, providing further evidence that the viscoelastic behaviour of the system is complex.

An investigation into whether mode mixing occurs in any of the systems here is explored by generating simulations from the viscoelastic parameters obtained experimentally. Figure 7.4.21 shows dispersion plots produced from the parameters obtained for the surface concentration where the maxima in capillary wave damping occur (1.0mg m^{-2} on 10^{-3}M KCl solution and 0.7mg m^{-2} on both 0.1M and 1M solutions). In all of these cases, transverse shear viscosity is set equal to zero and a positive value of dilational viscosity is recorded. Under these conditions, mode mixing is not expected to occur and this is confirmed by the plot generated, where the capillary and dilational modes clearly retain their own characteristics.

As discussed previously, high surface concentration films on a solution of 1M KCl exhibit negative dilational viscosities. Figure 7.4.22 shows a theoretical dispersion

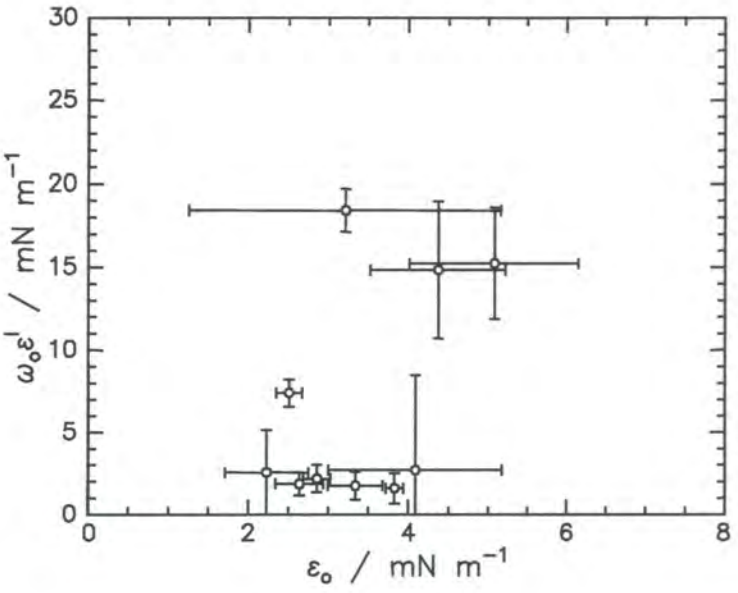

Figure 7.4.19. Cole-Cole plot of loss modulus ($\omega_o\varepsilon'$) against dilational modulus for a film of PMMA-QP4VP, Γ_s = 0.7mg m^{-2} on 0.1M KCl solution

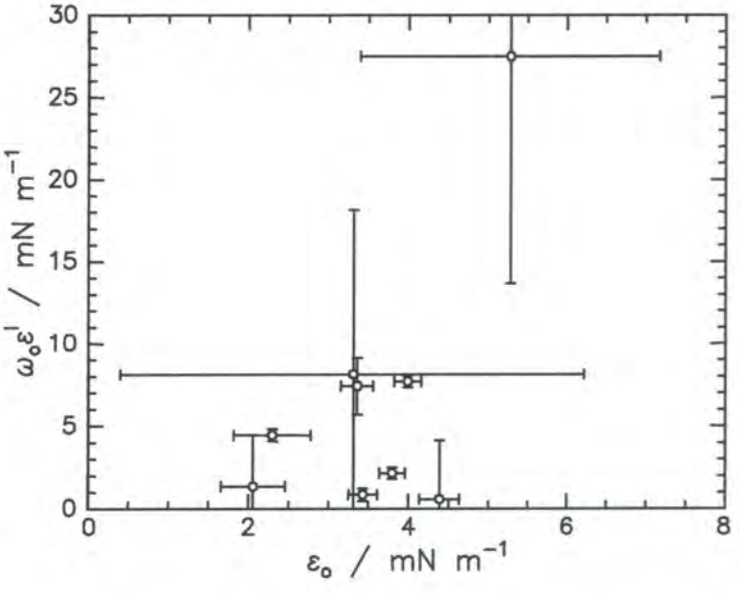

Figure 7.4.20. Cole-Cole plot of loss modulus ($\omega_o\varepsilon'$) against dilational modulus for a film of PMMA-QP4VP, Γ_s = 0.7mg m^{-2} on 1M KCl solution

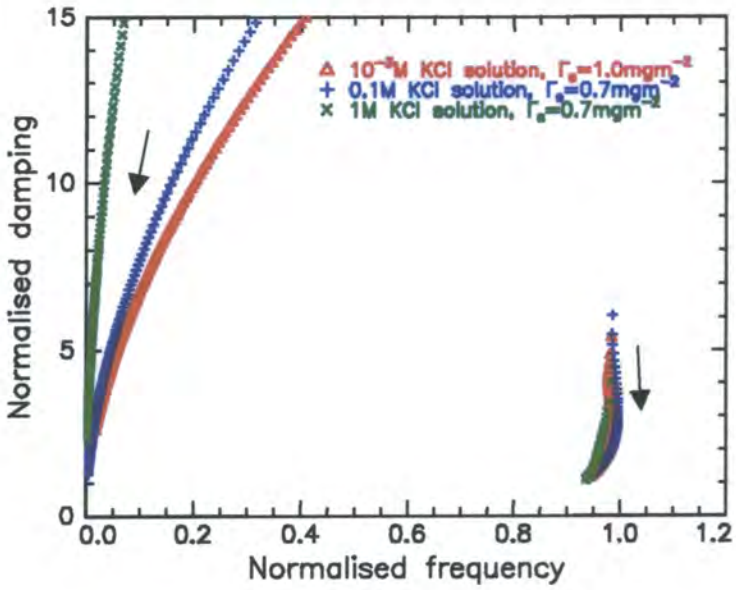

Figure 7.4.21. Theoretical surface wave dispersion plots generated from the viscoelastic parameters obtained at the surface concentrations where the maximum in capillary wave damping occurs (see legend). Arrows indicate the direction of increasing q

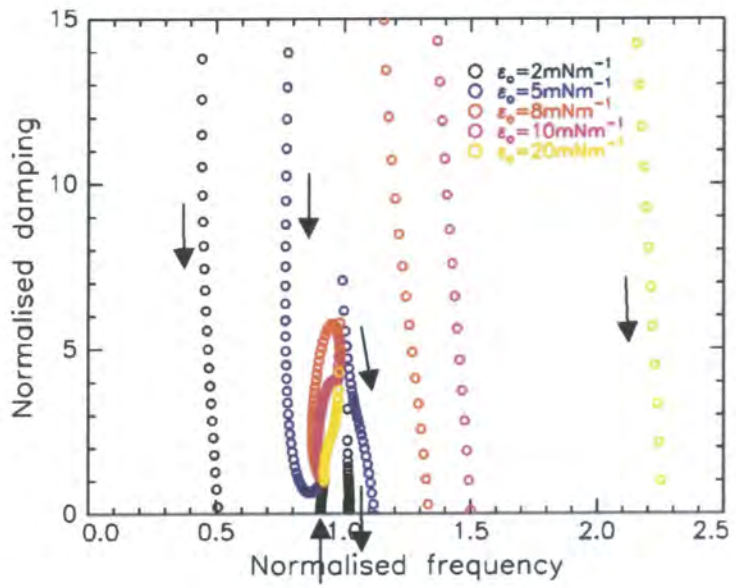

Figure 7.4.22. Theoretical surface wave dispersion plots generated from viscoelastic parameters for a film of PMMA-QPVP on 1M KCl solution, Γ_s = 1.8mg m^{-2} on 1M KCl solution. Parameters used are γ_o = 64.4mN m^{-1}, γ' = 0, ε' = -3.6x10^{-4}mN s m^{-1} and varying ε_o (see legend), arrows indicate the direction of increasing q

plot generated from the viscoelastic parameters obtained at the surface concentration where this phenomenon occurs, 1.8mg m^{-2}. Surface tension and dilational viscosity are set to the values extracted (64.4mN m^{-1} and -3.6×10^{-4}mN s m^{-1} respectively), transverse shear viscosity is constrained to zero and four values of dilational modulus are explored. For large values of ε_o, no mode mixing is observed, as the capillary and dilational modes of the system are clearly independent. As the experimentally measured value of dilational modulus was ε_o = 56.4mN m^{-1}, it is clear that mode mixing does not occur for a spread film of PMMA-QP4VP under these conditions. In fact, this value is quite distinct from ε_o = 5mN m^{-1}, the condition where mode mixing is found to occur. Here, the capillary mode, with its origin at (1,7), adopts dilational mode character at higher q. The opposite effect occurs with the initially dilational mode, which descends with increasing q before passing through a minimum at (0.87,0.64) and thereafter attaining capillary behaviour. A similar result is found with the lowest value of ε_o studied, 2mN m^{-1}. In this case, the mode originating at (1,5) immediately shows dilational behaviour. The dilational mode initially appears to regain dilational behaviour throughout the range of q explored. However, the data in fact passes through a minimum at negative values of normalised damping and reappears at (0.9,0). Thereafter, capillary behaviour is observed, confirming that mode mixing does indeed occur for such a low value of dilational modulus.

Figures 7.4.23 and 7.4.24 show plots of normalised capillary wave damping against wavenumber generated from the experimental data for films of Γ_s = 0.7mg m^{-2} spread on solutions on 0.1M KCl and 1M KCl respectively. In figure 7.4.23, normalised damping is seen to decrease almost approximately linearly with wavenumber (plotted on a logarithmic scale). Figure 7.4.24 shows no real relationship is observed, the data being highly scattered. In neither of these instances does the data follow the behaviour exhibited by the theoretical plot of figure 7.3.25, giving another indication that mode mixing does not occur.

Dispersion plots of normalised damping against normalised frequency are shown in figures 7.4.25 and 7.4.26 for films spread on 0.1M and 1M KCl solutions respectively. The number adjacent to each data point represents the wavenumber at

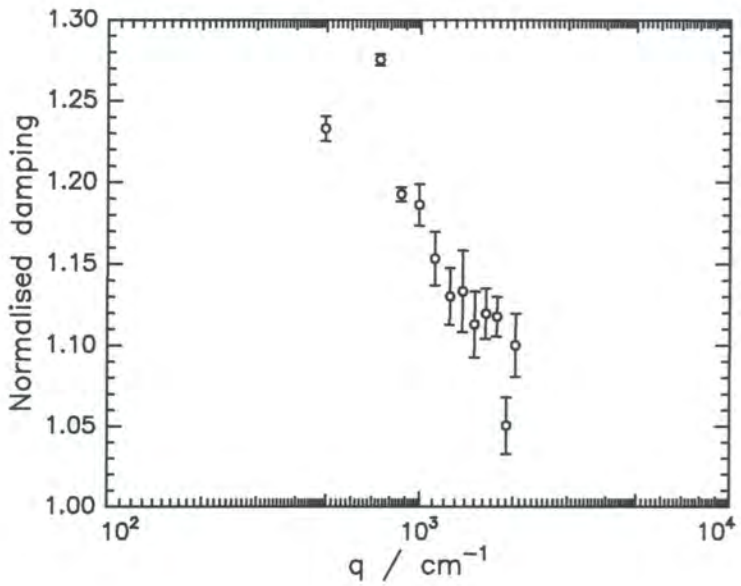

Figure 7.4.23. Normalised capillary wave damping against wavenumber for a film of PMMA-QP4VP, Γ_s = 0.7mg m^{-2}, on 0.1M KCl solution

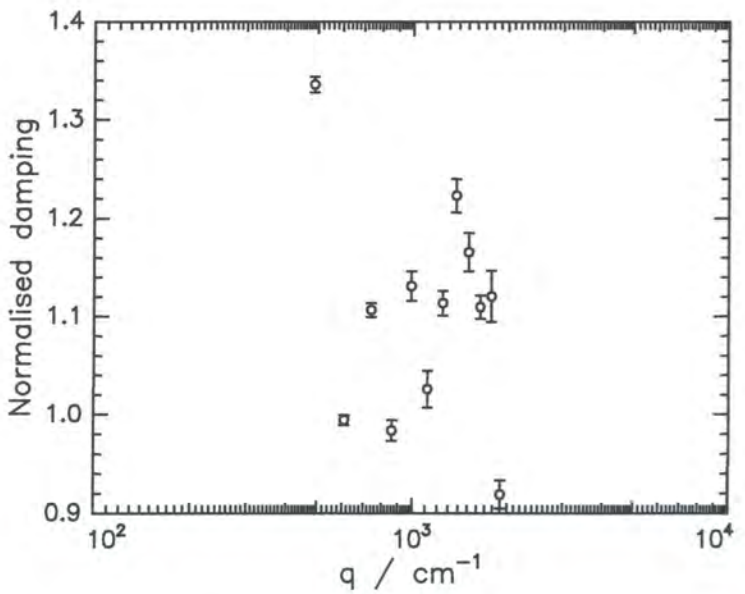

Figure 7.4.24. Normalised capillary wave damping against wavenumber for a film of PMMA-QP4VP, Γ_s = 0.7mg m^{-2}, on 1M KCl solution

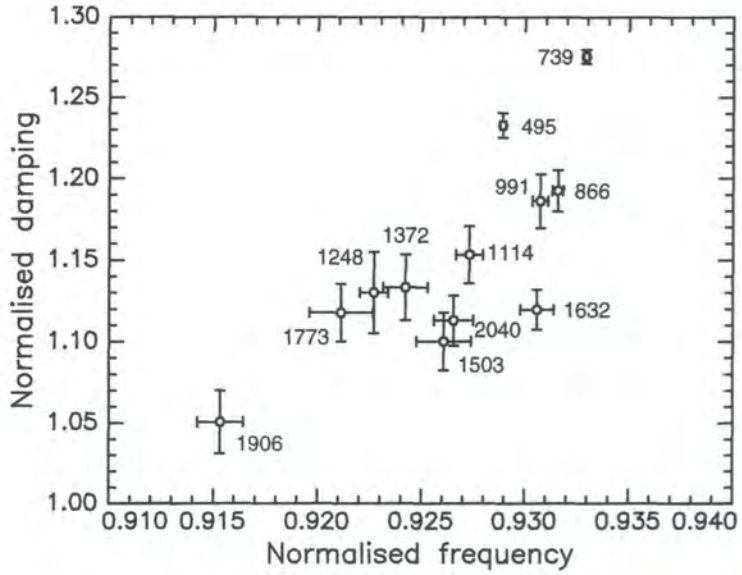

Figure 7.4.25. Dispersion plot of normalised frequency against normalised damping for a film of PMMA-QP4VP, Γ_s = 0.7mg m^{-2}, on 0.1M KCl solution. The number adjacent to each point represents the wavenumber (in cm^{-1}) at which the data point was recorded

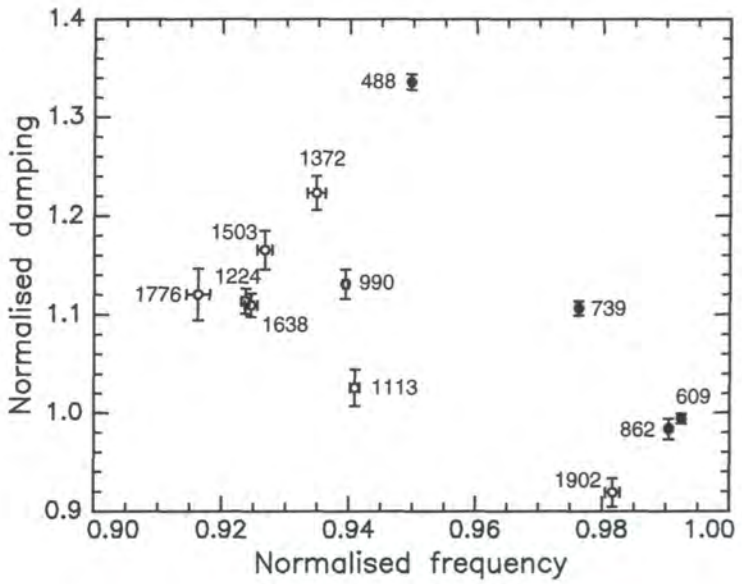

Figure 7.4.26. Dispersion plot of normalised frequency against normalised damping for a film of PMMA-QP4VP, Γ_s = 0.7mg m^{-2}, on 1M KCl solution. The number adjacent to each point represents the wavenumber (in cm^{-1}) at which the data point was recorded

which the data was obtained. A result similar to that for a film spread on water is obtained. The data do not follow a 'hook'-like path that would indicate the occurrence of mode mixing, in fact no real trend is observed with increasing wavenumber.

Figures 7.4.27 to 7.4.30 show an assortment of plots of frequency and damping against the ratio ε_o/γ_o. The first three of these are constructed from the viscoelastic parameters extracted at the maximum in capillary wave damping for polymer films spread on subphases of 10^{-3}M, 0.1M and 1M KCl solutions respectively. These plots are similar in form, although the frequencies of the capillary and dilational modes coincide at different points, at values of $\varepsilon_o/\gamma_o \approx 0.33$, 0.46 and 1.92 respectively. Mode mixing (as exhibited in figure 7.3.28c) is not found to occur in this case. The final plot, figure 7.4.30 is generated from the parameters found for a system where negative dilational viscosities are observed, a film of $\Gamma_s = 1.8$mg m^{-2} spread on 1M KCl. Here, unusual behaviour is exhibited as the capillary and dilational wave frequencies are seen to cross at a low value of $\varepsilon_o/\gamma_o \approx 0.07$. Furthermore, both the dilational frequency and damping take non-positive values, $\omega_D = 0$ for $\varepsilon_o/\gamma_o < 0.046$ and $\Gamma_D < 0$ for $\varepsilon_o/\gamma_o < 0.73$. Despite this behaviour, mode mixing does not occur, as the dilational and capillary waves retain their own characteristics throughout the range of ε_o/γ_o studied.

The above evidence points to the fact that, as on water, a film of PMMA-QP4VP spread on KCl solutions does not exhibit mode mixing at any of the surface concentrations where a maximum in capillary wave damping is observed. At higher surface concentrations on 0.1M KCl solution, negative dilational viscosities are reported. However, even for these systems, mode mixing is found not to occur.

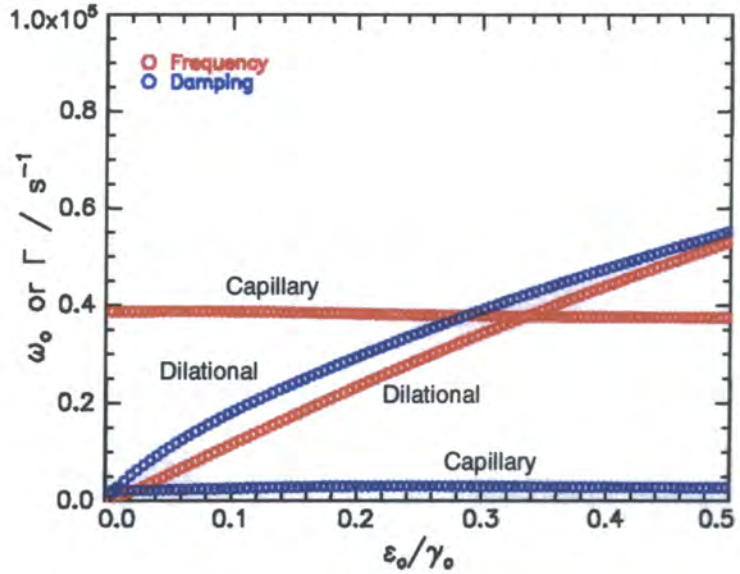

Figure 7.4.27. Frequency (red) and damping (blue) of the capillary and dilational modes (marked on plot) as a function of ε_o/γ_o. Data generated from the parameters for a film of PMMA-QP4VP, $\Gamma_s = 1.0$mg m^{-2} on 10^{-3}M KCl solution: $\gamma_o = 72.3$mN m^{-1}, $\gamma' = 0$, $\varepsilon' = 2.02\text{x}10^{-3}$mN s m^{-1} and q = 278cm^{-1}

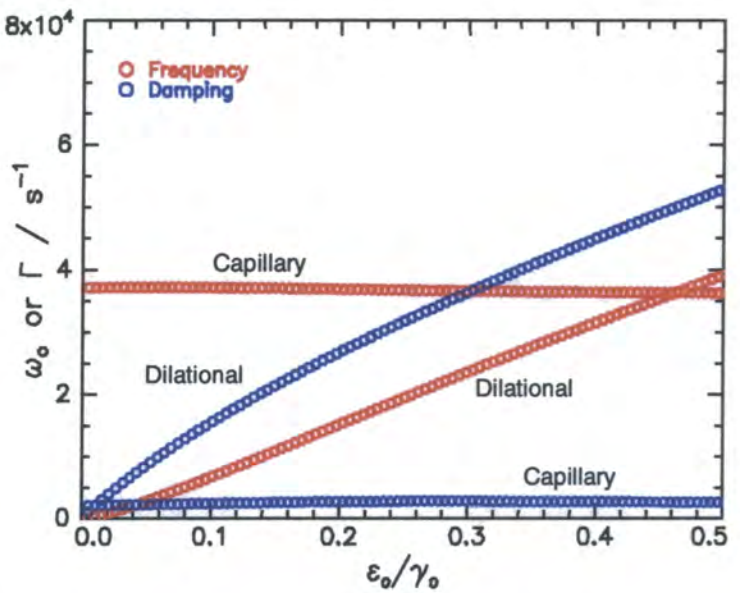

Figure 7.4.28. Frequency (red) and damping (blue) of the capillary and dilational modes (marked on plot) as a function of ε_o/γ_o. Data generated from the parameters for a film of PMMA-QP4VP, $\Gamma_s = 0.7$mg m^{-2} on 0.1M KCl solution: $\gamma_o = 69.3$mN m^{-1}, $\gamma' = 0$, $\varepsilon' = 3.12\text{x}10^{-3}$mN s m^{-1} and q = 276cm^{-1}

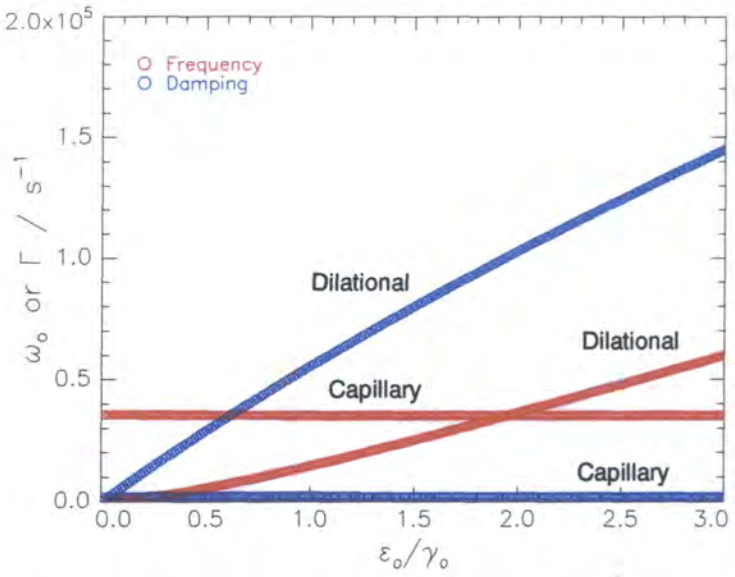

Figure 7.4.29. Frequency (red) and damping (blue) of the capillary and dilational modes (marked on plot) as a function of ε_o/γ_o. Data generated from the parameters for a film of PMMA-QP4VP, Γ_s = 0.7mg m^{-2} on 1M KCl solution: γ_o = 73.8mN m^{-1}, γ' = 0, ε' = 1.19x10^{-3}mN s m^{-1} and q = 268cm^{-1}

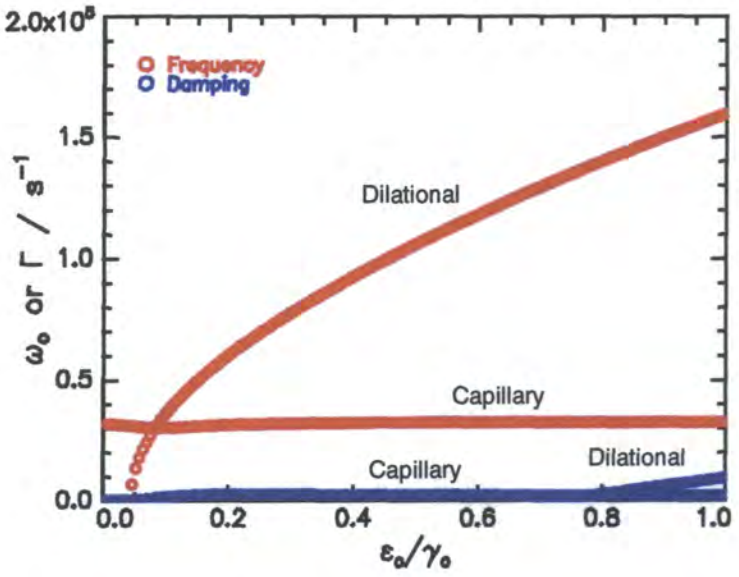

Figure 7.4.30. Frequency (red) and damping (blue) of the capillary and dilational modes (marked on plot) as a function of ε_o/γ_o. Data generated from the parameters for a film of PMMA-QP4VP, Γ_s = 1.8mg m^{-2} on 1M KCl solution: γ_o = 64.5mN m^{-1}, γ' = 0, ε' = -3.65x10^{-3}mN s m^{-1} and q = 268cm^{-1}.

7.4.3. TIME DEPENDENCE STUDIES

Time dependence studies were undertaken to determine the homogeneity and stability of the polymer films on subphases of 0.1M and 1M KCl solutions. On the former of these, polymer films of surface concentrations of 0.5mg m^{-2}, 1.0mg m^{-2} and 2.0mg m^{-2} were studied, whereas for a 1M KCl solution subphase, only the first two of these surface concentrations were explored. The results from these experiments are presented and discussed below.

7.4.3.1. Results

The experimental results are plotted in the form of capillary wave damping against time in figures 7.4.31 to 7.4.36. For a film of Γ_s = 0.5mg m^{-2} on 0.1M KCl solution (figure 7.4.31), the capillary wave damping fluctuates rapidly between two values, 1550s^{-1} (the damping recorded for pure water) and 2550s^{-1}. At the higher surface concentration (1.0mg m^{-2}, figure 7.4.32) the majority of values are $\Gamma \approx$ 2200s^{-1}, although on two occasions, the value of damping falls briefly to that of pure water (in this instance 1265s^{-1}). The 2.0mg m^{-2} film (figure 7.4.33) exhibits the most unusual characteristics. All values of capillary wave damping are high and greater than those of pure water, but the values are not constant throughout the course of the experiment, instead appearing to vary slightly around $\Gamma \approx$ 2200s^{-1}.

For a 1.0M KCl solution, a 0.5mg m^{-2} film (figure 7.4.35) reveals values of capillary wave damping which are initially highly scattered, before rising to a constant 2300s^{-1}. This value is retained for approximately three hours, before dropping to that of pure water over a period of 10 minutes. For a 1.0mg m^{-2} film (figure 7.4.36), damping initially oscillates between a high and low value before finally stabilising at the higher value.

7.4.3.2. Discussion

A film of Γ_s = 0.5mg m^{-2} on 0.1M KCl solution exhibits values of damping which change rapidly between that of pure water and a higher value corresponding to a

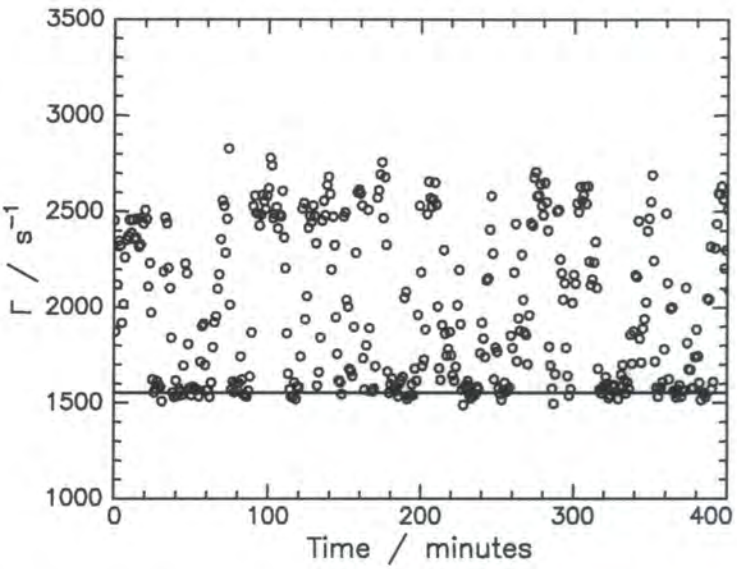

Figure 7.4.31. Capillary wave damping against time for PMMA-QP4VP on 0.1M KCl solution (circles). Γ_s = 0.5mg m^{-2}, q = 266.9cm^{-1}. Data overlayed with Γ_{water} = 1552s^{-1} (line)

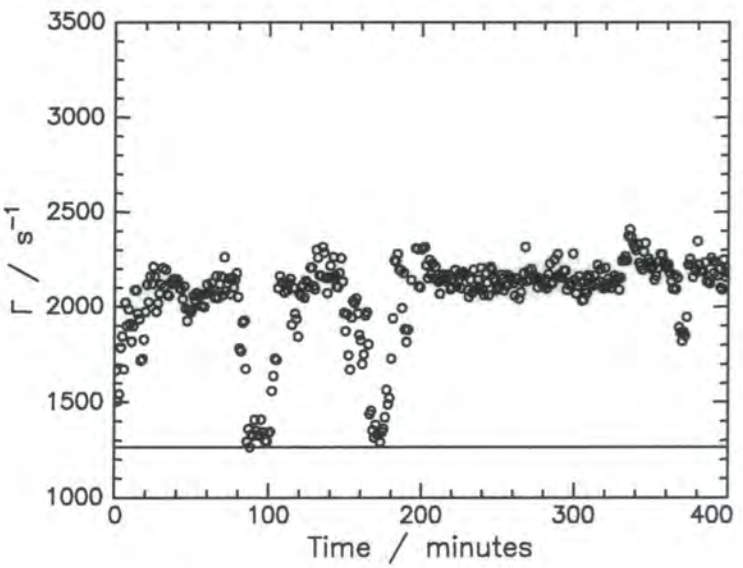

Figure 7.4.32. Capillary wave damping against time for PMMA-QP4VP on 0.1M KCl solution (circles). Γ_s = 1.0mg m^{-2}, q = 261.4cm^{-1}. Data overlayed with Γ_{water} = 1265s^{-1} (line)

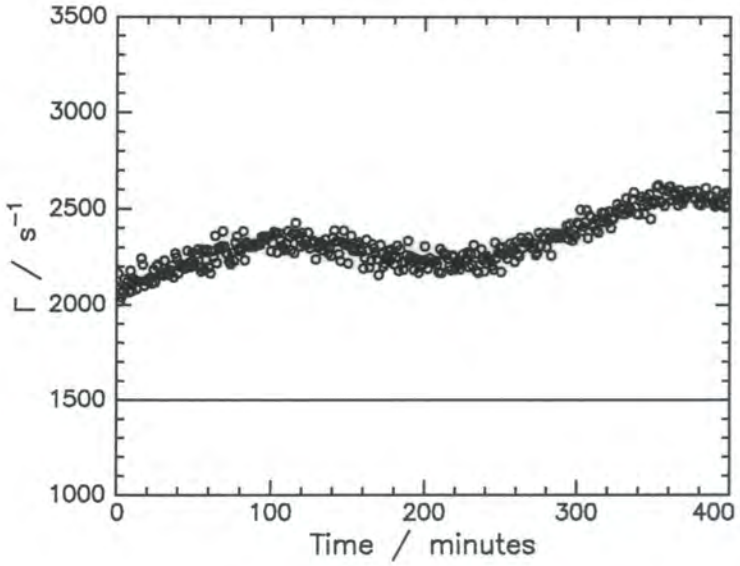

Figure 7.4.33. Capillary wave damping against time for PMMA-QP4VP on 0.1M KCl solution (circles). Γ_s = 2.0mg m^{-2}, q = 267.7cm^{-1}. Data overlayed with Γ_{water} = 1499s^{-1} (line)

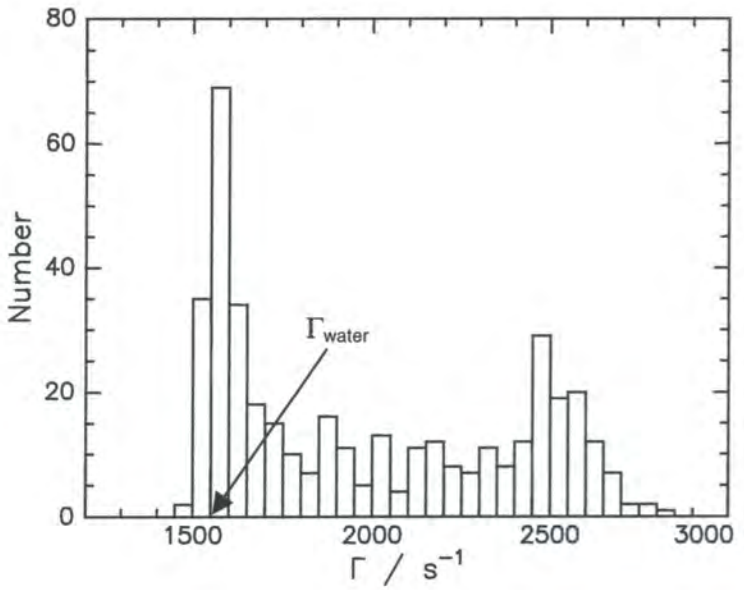

Figure 7.4.34. Histogram plot of capillary wave damping for PMMA-QP4VP on 0.1M KCl solution. Γ_s = 0.5mg m^{-2}, q = 266.9cm^{-1}. Value of Γ_{water} = 1552s^{-1} indicated by the arrow

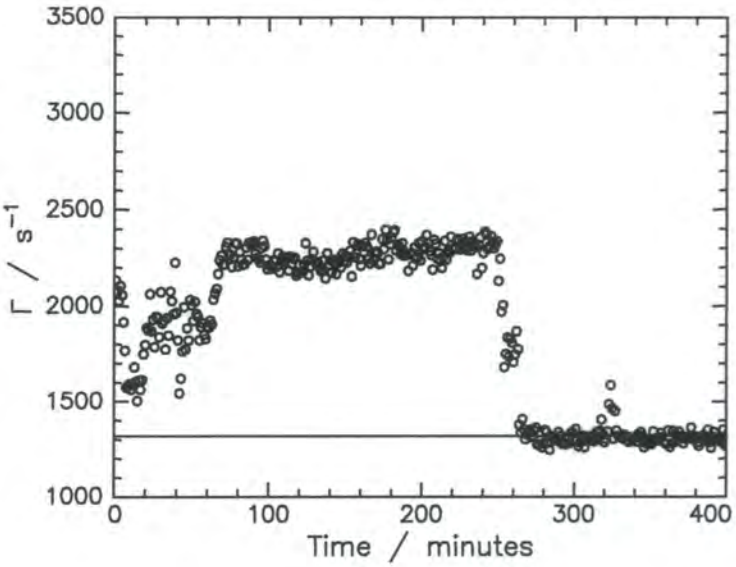

Figure 7.4.35. Capillary wave damping against time for PMMA-QP4VP on 1M KCl solution (circles). Γ_s = 0.5mg m^{-2}, q = 263.0cm^{-1}. Data overlayed with Γ_{water} = 1350s^{-1} (line)

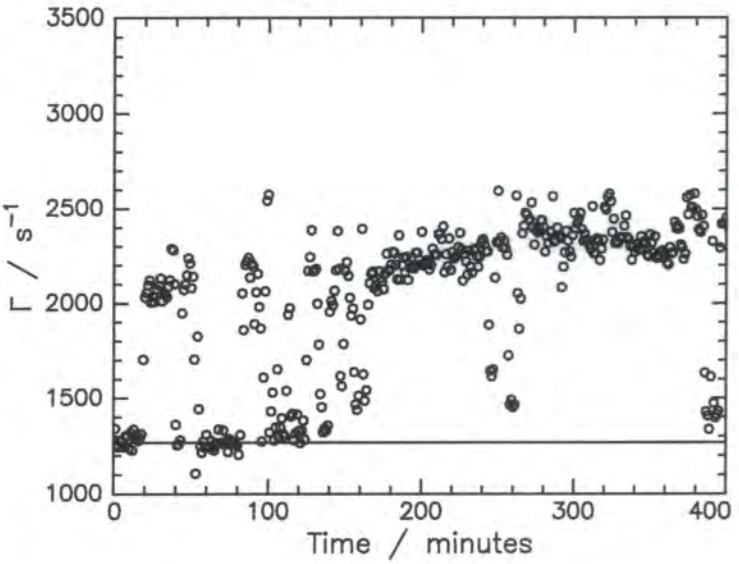

Figure 7.4.36. Capillary wave damping against time for PMMA-QP4VP on 1M KCl solution (circles). Γ_s = 1.0mg m^{-2}, q = 259.6cm^{-1}. Data overlayed with Γ_{water} = 1268s^{-1} (line)

polymer covered surface. This is confirmed by the histogram in figure 7.4.34, where it is clear that the two main peaks occur in these regions ($\Gamma \approx 1550$ and $2500s^{-1}$). The intermediate values (which are recorded with almost equal frequency) are found when the laser beam illuminates water for a portion of the time taken to record a correlation function (30s) and polymer for the remaining time. It can therefore be concluded that at this surface concentration, the film exists as a series of islands that are small and / or moving rapidly. A film of $\Gamma_s = 1.0mg\ m^{-2}$ on the same subphase shows similar characteristics, although in this instance there are only two intervals (each of approximately 30 minutes duration) where a value of $\Gamma \approx 2100s^{-1}$ is not recorded. This implies that the film still exists as a series of islands, although these are now very large. This appears to be a reasonable deduction as there is now twice the quantity of the polymer on the liquid surface. The time taken for the transition from low to high values of damping (and *vice versa*) is slightly greater in the latter case, implying that the islands are moving more slowly than those at the low surface concentration. The initial 20 minute period where the data is highly scattered is ascribed to be the region where the polymer aggregates to form these larger islands. Finally, the film of $\Gamma_s = 2.0mg\ m^{-2}$ is discussed. At this high surface concentration, it is expected that the polymer would form a complete film, as observed for a similar surface concentration on water (figure 7.3.30). Although the damping varies between the range $2000 < \Gamma / s^{-1} < 2500$, the film is assumed to completely cover the liquid surface as at no stage does the damping descend to that of pure water ($1500s^{-1}$). The effect is therefore explained by the film being non-uniform with some domains containing more material than others, affecting the recorded value of damping. Other physical effects, for instance a change in temperature during the course of the experiment, would not result in the wide range of values exhibited here.

When spread on a solution of 1.0M KCl, the polymer exhibits different behaviour than when on a lower concentration subphase. A film of $0.5mg\ m^{-2}$ records scattered values of damping for an hour before the polymer aggregates to form what appears to be a large or slow moving island. After a further period of three hours, the island moves out of the laser beam and thereafter a value of damping equivalent to that of water is recorded. A film of the higher surface concentration ($1.0mg\ m^{-2}$) appears to

exist initially in the form of small islands. As time passes, the periods where no material is in the surface region illuminated by the laser beam become increasingly short, implying that aggregation of the islands is occurring. This effect has been observed for a low concentration film of PMMA on water.[22]

In an attempt to rationalise the above results, closer attention is paid to both the distribution of the polymer on the liquid surface and the properties of the subphase. Using the structure of the copolymer determined in chapter four and assuming that all of the polymer is resident upon the liquid surface, the average surface area available to each polymer chain, A_{chain}, can be calculated. From this, the average chain separation, d_{chain} is calculable and these data are given in table 7.4.4.

Γ_s / mg m^{-2}	A_{chain} / Å^2	d_{chain} / Å
0.5	2.16	1.47
1.0	1.08	1.04
2.0	0.54	0.75

Table 7.4.4. Values of average area and separation per chain of PMMA-QP4VP calculated for three specific surface concentrations

The values are compared to the Debye lengths of the subphases, which can be calculated from equation 7.4.2:[33]

$$r_D = \left(\frac{\varepsilon RT}{2\rho F^2 I} \right)^{1/2}$$

Equation 7.4.2.

Where F is the Faraday constant, and ε and I the permittivity and ionic strengths of the solution respectively. The values of Debye length calculated from this are given in table 7.4.5, and are highly similar to those obtained experimentally in the literature.[34]

Solution	R_D / Å
Water	96
0.1M KCl	0.98
1M KCl	0.29

Table 7.4.5. Calculated Debye lengths for water and 0.1M and 1M salt solution

By comparing the data in the two tables, it can be seen that if the polymer chains on salt solutions are evenly spaced, their separation is greater than the Debye length. This indicates the charges on the polyelectrolyte are screened from one another. However, this idealised picture is unrealistic, as the polymer chain will obviously not exist in such a manner, the molecules being less uniformly distributed across the liquid surface. Nevertheless, the relative values of the Debye length can be used to explain some of the characteristics observed from these experiments. Even at low surface concentrations (0.5mg m^{-2}), the polymer spread on water exists as a continuous film. This is due to the weak screening of charges in the subphase (r_D » d_{chain}) which allows the polyelectrolyte chains to be attracted to each other, thus forming one mass of material. Moving to a film of Γ_s = 1.0mg m^{-2} on 0.1M KCl solution, this exists as almost a complete film with two incidences of islands being observed. Although the surface concentration is twice that on water, this is more than countered by the two orders of magnitude decrease in Debye length. The greater screening results in the chains exhibiting less attraction, resulting in a greater number of islands than the lowest surface concentration film on water. Increasing the salt concentration to 1M KCl enhances this effect. Due to the increased screening, the polymer originally exists as a number of small islands that only aggregate after a period of hours. It is suggested that the agglomeration is caused by the islands randomly 'floating' into one another, rather than any long-range intermolecular attraction.

7.4.4. SUMMARY

Following the investigation of the dynamic surface properties of a film of PMMA-QP4VP on a water subphase, SQELS has been used to study the same system on potassium chloride solutions of concentrations 10^{-3}M, 0.1M and 1M.

Spread monolayers of the polymer on these subphases have been found to exist as non-uniform films, even at surface concentrations of 1.0mg m^{-2}. This effect is subphase dependent, the higher the salt concentration, the more 'islands' of material are present on the liquid surface. An explanation of this has been given in terms of the screening of the charges on the polyelectrolyte chains.

Surface concentration studies have revealed that the frequency of the capillary waves changes little with subphase, although the gradient of the monotonic decrease in frequency becomes less negative with increasing subphase salt concentration. The plots of capillary wave damping are similar in shape, although the maxima occur at slightly different surface concentrations. The values of damping measured at these maxima decrease with increasing salt concentration. Extraction of the viscoelastic parameters of the systems reveals some unusual behaviour, especially for the film spread on a solution of 1M KCl, where negative dilational viscosities are recorded at high polymer surface concentrations. This is the only incidence of this phenomenon in this work. The surface tension and dilational modulus data obtained by dynamic and static methods method show similar characteristics, much more so than the data obtained on water.

A series of frequency dependence experiments have revealed that neither the Maxwell fluid nor the Voigt solid viscoelastic model can be successfully applied to a film of the polymer spread on KCl solutions. Mode mixing has been found not to occur at the surface concentrations where the maximum in capillary wave damping is revealed. Nor is it found for the surface concentrations of the film on 1M KCl solution where negative values of ε' are measured. In fact, mode mixing in this circumstance is only revealed when ε_0 drops as low as 5mN m^{-1}, well below the values of *ca.* 55mN m^{-1} obtained experimentally.

7.5. CONCLUSIONS

From SQELS experiments, the structure of the polymer films has been found to vary with surface concentration. Generally, at low surface concentrations the polymer exists as a series of islands, whereas at higher concentrations, a uniform film is observed, giving complete coverage of the liquid surface. The arrangement of the polymer at any specific surface concentration is found to vary with subphase. On water, it has been deduced that the polymer forms large agglomerations, whereas the tendency to form 'islands' is greater on salt solutions, the number of these domains increasing with salt concentration.

By studying the variation in capillary wave frequency and damping with surface concentration, trends have been revealed which are generally independent of subphase. However, the rate of change of frequency is found to decrease with increasing salt concentration. Furthermore, the maximum in damping is of a lower value and occurs at a different surface concentration. At this maximum, classical resonance between the capillary and dilational modes is found to occur on water and 10^{-3}M KCl solution, although this does not appear to be the case for the two higher salt concentration subphases. For a spread film on water, a second maximum is observed in capillary wave damping at $\Gamma_s = 1.5 mgm^{-2}$. By applying the theory of lossy coupled oscillators, this has been assigned to be a second, unidentifiable form of mode coupling.

The viscoelastic parameters of the system have been extracted by constraining transverse shear viscosity to zero. Due to the nature of the system, it was unnecessary to include either a coupling constant or a bending modulus in the dispersion equation. Comparison of this behaviour to that predicted by polymer scaling theory was carried out with varying degrees of such success. The dynamic values of surface tension and dilational modulus obtained by SQELS were compared with the static values obtained from surface pressure measurements. Here, it was found that the two data sets agreed well for films spread on salt solutions and less well for those on water. Negative values of dilational viscosity were observed for high surface concentrations of the film spread on 1M KCl solution.

The measurement of the capillary wave frequency and damping dependence upon wavenumber initially appeared to show unusual characteristics, although these were later assigned to be due to either the inflexibility of the correlator system or film inhomogeniety. Both frequency and damping scaled with wavenumber as predicted.

Extraction of the viscoelastic parameters of the system with respect to capillary wave frequency allowed the application of viscoelastic models. Neither the Maxwell fluid nor the Voigt solid model were found to represent any of the data to an adequate degree, implying that a more intricate arrangement of viscoelastic elements is required to successfully model this system.

The possibility of mode mixing has been studied. This effect is not observed in any of the systems studied here, even those where negative dilational viscosities were found. Subsequent theoretical studies showed that to observe mode mixing, smaller values of ε_o than those extracted here were required.

7.6. REFERENCES

1 J. C. Earnshaw, R. C. McGivern, A. C. McLaughlin and P. J. Winch, *Langmuir*, 1990, **6**, 650.

2 J. C. Earnshaw and R. C. McGivern, *J. Colloid Interface Sci.*, 1988, **123**, 36

3 M. Kawaguchi, M. Sano, Y.-L. Chen, G. Zografi and H. Yu, *Macromolecules,* 1986, **19**, 2606.

4 B. B. Sauer, M. Kawaguchi and H. Yu, *Macromolecules,* 1987, **20**, 2732.

5 B. B. Sauer and H. Yu, *Macromolecules,* 1989, **22**, 786.

6 M. Kawaguchi, B. B. Sauer and H. Yu, *Macromolecules,* 1989, **22**, 1735.

7 D. M. A. Buzza, J. L. Jones, T. C. B. McLeish and R. W. Richards, *J. Chem. Phys.*, 1998, **109**, 5008.

8 A. J. Milling, R. W. Richards, R. C. Hiorns and R. G. Jones, *Submitted for publication.*

9 D. Sharpe and J. Eastoe, *Langmuir*, 1995, **11**, 4636.

10 S. K. Peace and R.W. Richards, *Polymer*, 1996, **37**, 4945.

11 J. C. Earnshaw, R. C. McGivern and P. J. Winch, *J. Phys. (Paris)*, 1988, **49**, 1271.

12 F. Monroy, F. Ortega, and R. G. Rubio, *J. Phys. Chem. B.*, 1999, **103**, 2061.

13 S. K. Peace and R. W. Richards, *Langmuir*, 1998, **14**, 667.

14 J. C. Earnshaw and E. McCoo, *Langmuir*, 1995, **11**, 1087.

15 E. H. Lucaseen-Reynders and J. Lucassen, *Adv. Colloid Interface Sci.*, 1969, **2**, 347.

16 L. Kramer, *J. Chem. Phys.*, 1971, **55**, 2097.

17 A. B. Pippard, *The Physics of Vibration*, Cambridge University Press, Cambridge, UK, 1989.

18 H. Dautzenberg, W. Jaeger, J. Kötz, B. Philipp, Ch. Seidel and D. Stscherbina, *Polyelectrolytes: Formation, Characterization and Application*, Hanser, Munich, Germany, 1994.

19 J. C. Earnshaw and A. C. McLaughlin, *Proc. R. Soc. Lond. A*, 1993, **440**, 519.

20 J. C. Earnshaw, *Adv. Colloid Interface Sci.*, 1996, **68**, 1.

21 J. D. Ferry, *Viscoelastic Properties of Polymers*, John Wiley & Sons, New York, USA, 1970.

22 R. W. Richards and M. R. Taylor, *J. Chem. Soc. Faraday Trans*, 1996, **92**, 601.

23 R. W. Richards, B. R. Rochford and M. R. Taylor, *Macromolecules*, 1996, **29**, 1980.

24 N. G. McCrum, B. E. Read and G. Williams, *Anelastic and Dielectric Effects in Polymer Solids*, Dover, New York, USA, 1967.

25 D. Langevin (ed.), *Light Scattering By Liquid Surfaces and Complementary Techniques*, Marcel Dekker, Inc., New York, USA, 1992.

26 J. C. Earnshaw and A. C. McLaughlin, *Prog. Colloid Polym. Sci.*, 1989, **79**, 157.

27 J. C. Earnshaw and D. J. Sharpe, *J. Chem. Soc. Faraday Trans*, 1996, **92**, 611.

28 R. W. Richards and M. R. Taylor, *Macromolecules*, 1997, **30**, 3892.

29 C. Booth, R. W. Richards, M. R. Taylor and G.-E. Yu, *J. Phys. Chem. B*, 1998, **102**, 209.

30 M. van der Tempel and E. H. Lucassen-Reynders, *Adv. Colloid Interface Sci.*, 1993, **18**, 281.

31 M. Hennenberg, X.-L. Chu, A. Sanfeld, M. G. Velarde, *J. Colloid Interface Sci.*, 1992, **150**, 7.

32 L. E. Scriven and C. V. Sternling, *Nature*, 1996, **187**, 186.

33 P. W. Adams, *Physical Chemistry*, 4/e, Oxford University Press, Oxford, UK, 1990.

34 P. K. Weissenborn and R. J. Pugh, *J. Colloid Interface Sci.,* 1996, **184**, 550.

CHAPTER EIGHT

CONCLUSIONS & FURTHER WORK

8.1. CONCLUSIONS

The main aim of this work was to determine the organisation and surface wave dynamics of a copolyelectrolyte system, PMMA-QP4VP, when spread on water and potassium chloride solution subphases.

From the measurement of surface pressure isotherms (chapter five), it was found that the shape of the isotherm for a film of PMMA-QP4VP differed significantly from that of the unquaternised copolymer. This implies that the quaternisation of the P4VP chain to produce a polyelectrolyte system has a significant effect upon monolayer organisation. The initial rise in the surface pressure isotherm (at Γ_s = 1.2mg m^{-2}) is attributed to the interaction of the molecules on the surface and the penetration of the QP4VP chains into the liquid subphase. Comparison of the isotherm recorded on water with those on salt solutions allows the change in polymer organisation to be inferred. From the change in 'take-off' concentration of the isotherms, it is revealed that the polyelectrolyte chain becomes less stretched (and therefore adopts a more 'coiled' conformation) as subphase salt concentration increases.

Although the exact surface structure of the polymer film was not observable by Brewster angle microscopy, it was still possible to deduce a number of characteristics of the system. Complete surface coverage was not achieved until a surface concentration in the range of $1.0 < \Gamma_s$ / mg $m^{-2} < 1.5$ was reached. This correlates with the results from surface pressure measurements, where the initial increase in surface pressure was observed in this same concentration range. At higher surface concentrations, the polymer film increased in thickness.

Quantitative information on the polymer organisation had been obtained by neutron reflectometry (chapter six), the majority of data analysis being done using the kinematic approximation. Similar results were found by the optical matrix or model independent fitting methods. Although some unusual behaviour was exhibited, especially by the water self partial structure factors, a full description of the polymer organisation at the air – liquid interface was obtained. In all cases, the PMMA and

QP4VP blocks were best described by Gaussian and parabolic layers respectively. Some overlap between the two distributions was observed, and it is thought that this is due the effects of the two blocks being tethered together. This results in a small quantity of PMMA being 'dragged' into the liquid subphase by the QP4VP chains. Conversely, if any of the PMMA were to loop away from the liquid surface into the air phase, some of the QP4VP would inevitably be pulled out of the subphase. The organisation of the near surface water layer proved more difficult to determine. In the majority of the systems studied, this could best be described by a smooth hyperbolic tangent distribution, although in three cases, a double uniform water layer model was utilised.

Comparing the parameters extracted from these data, the PMMA block increases in both thickness and number density as polymer surface concentration increases. Meanwhile, the number density of the QP4VP block remains approximately constant, but gradually increase its thickness. Comparison of this increasing subphase penetration with polyelectrolyte brush scaling theory shows that the prediction of increasing brush height with surface concentration is followed. However, the experimental value of the scaling exponent, 0.50, is far greater than the predicted value of 0.33. The difference between the two values is assigned to factors such as the small brush length, the irregular grafting of the chains to the surface and the non-ideality of the bulky polyelectrolyte brush.

The results obtained for the film spread on salt solutions showed, as expected, little change in the structure of the PMMA block, the hydrophilic QP4VP block being more affected by changes in subphase salt concentration. Addition of a small quantity of KCl (10^{-3}M) causes the polyelectrolyte brush to adopt a stretched brush conformation. On higher concentration salt subphases, the chain decreases in length and increases in number density, indicative of the chain adopting a coiled structure.

This decrease in brush length is again compared with scaling theory, where the overall decrease in length generally agrees with the predicted behaviour. The scaling exponent extracted, -0.06 is again distinct from the predicted value, in this instance -0.33.

The results generally agree well with those obtained by surface pressure measurements and Brewster angle microscopy. The increase in thickness of the PMMA block with increasing surface concentration found by neutron reflectometry is mirrored by BAM. Secondly, the observation that the organisation of the PMMA

block is independent of subphase salt concentration correlates with the observation that surface pressure isotherms of PMMA homopolymer monolayers are also independent of subphase. The change in QP4VP chain length with subphase salt concentration can also be deduced from surface pressure isotherms, by comparison of the isotherm 'take-off' concentrations. In both cases, the brush length is found to initially increase upon the addition of salt and then decrease with increasing salt concentration.

Following the determination of the organisation of the polymer at the air – liquid interface, attention was then turned to dynamics of the monolayer, as investigated by surface quasi-elastic light scattering (chapter seven). The experimental data was analysed without the inclusion of a transverse shear viscosity. This is the first investigation to use this revision of the dispersion equation, therefore making comparison with the bulk of work in the literature impossible.

The resonance observed between the capillary and dilational modes of the system occur in a surface concentration range of $0.7 < \Gamma_s$ / mg $m^{-2} < 1.0$. At these concentrations, the surface pressure isotherms record a surface pressure of zero. Neutron reflectometry experiments have not been carried out at concentrations below $\Gamma_s = 1.0$mg m^{-2} because of the long data acquisition time required to explore such a system and the knowledge that only at higher surface concentrations is complete surface coverage achieved. The discovery of a second mode coupling for a film of $\Gamma_s = 1.5$mg m^{-2} on water has no obvious correlation with either the surface pressure or neutron reflectometry results.

The dynamic values of surface tension, γ_o, and dilational modulus, ε_o, obtained from SQELS were compared with the static values from surface pressure measurements. On water, there was poor agreement between the two sets of data, much less so than on KCl solution subphases. In the latter case, the dynamic and static values of γ_o showed good agreement. The two sets of ε_o values showed similar trends, although the exact values were somewhat different.

Analysis of the dependence of the viscoelastic parameters dependence on capillary wave frequency revealed that neither the Maxwell nor the Voigt viscoelastic model was applicable in this instance, implying that a more complex model was needed. An investigation into the phenomenon of mode mixing revealed that this did not

occur for any of the systems studied here, despite the observation of negative values of dilational viscosity, ε', for high concentration films on 1M KCl solutions.

8.2. Suggestions for Further Work

At the conclusion of this work, there remain some unanswered questions. Why is there such a discrepancy between the theoretical and experimentally obtained scaling exponents? This may be due to the polyelectrolyte block not being of sufficient length, a problem that could be rectified by the tailored synthesis of a polymer with longer chains. Alternatively (or in addition), it may be advantageous to select a system with a different polyelectrolytic component, as a less bulky group would result in a system closer to ideality. Furthermore, if this block could be fully deuterated, the resulting reflectometry data would be of a higher quality, allowing the surface organisation of the system to be determined with more certainty.

The knowledge of the system obtained from SQELS experiments could be increased by a further study of the viscoelastic behaviour of the system. Clearly, there is some frequency dependent behaviour exhibited by the system, which could possibly be elucidated by the development of more complex viscoelastic models. In addition, the observation of negative dilational viscosities still seems to imply that the dispersion equation used to describe polymers at the air-liquid interface is not correct. This theoretical field is another that would benefit from further development.

APPENDICES

A. Characterisation Spectra

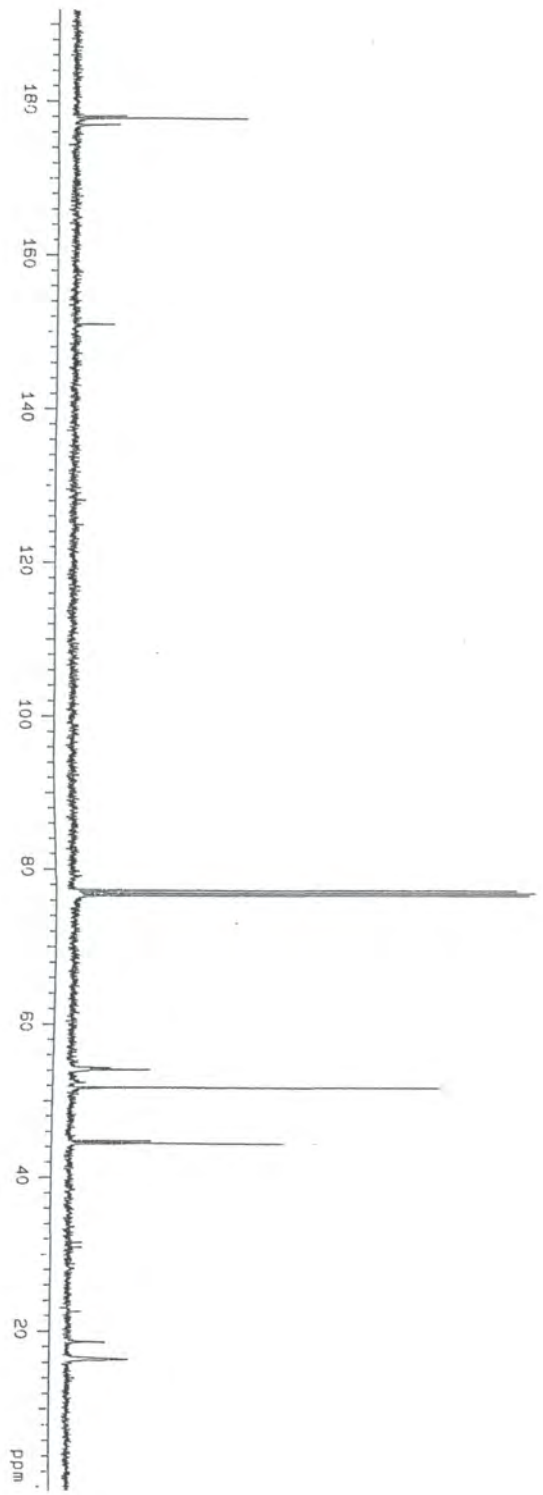

Spectrum 1. ^{13}C NMR spectrum of PMMA in DMSO

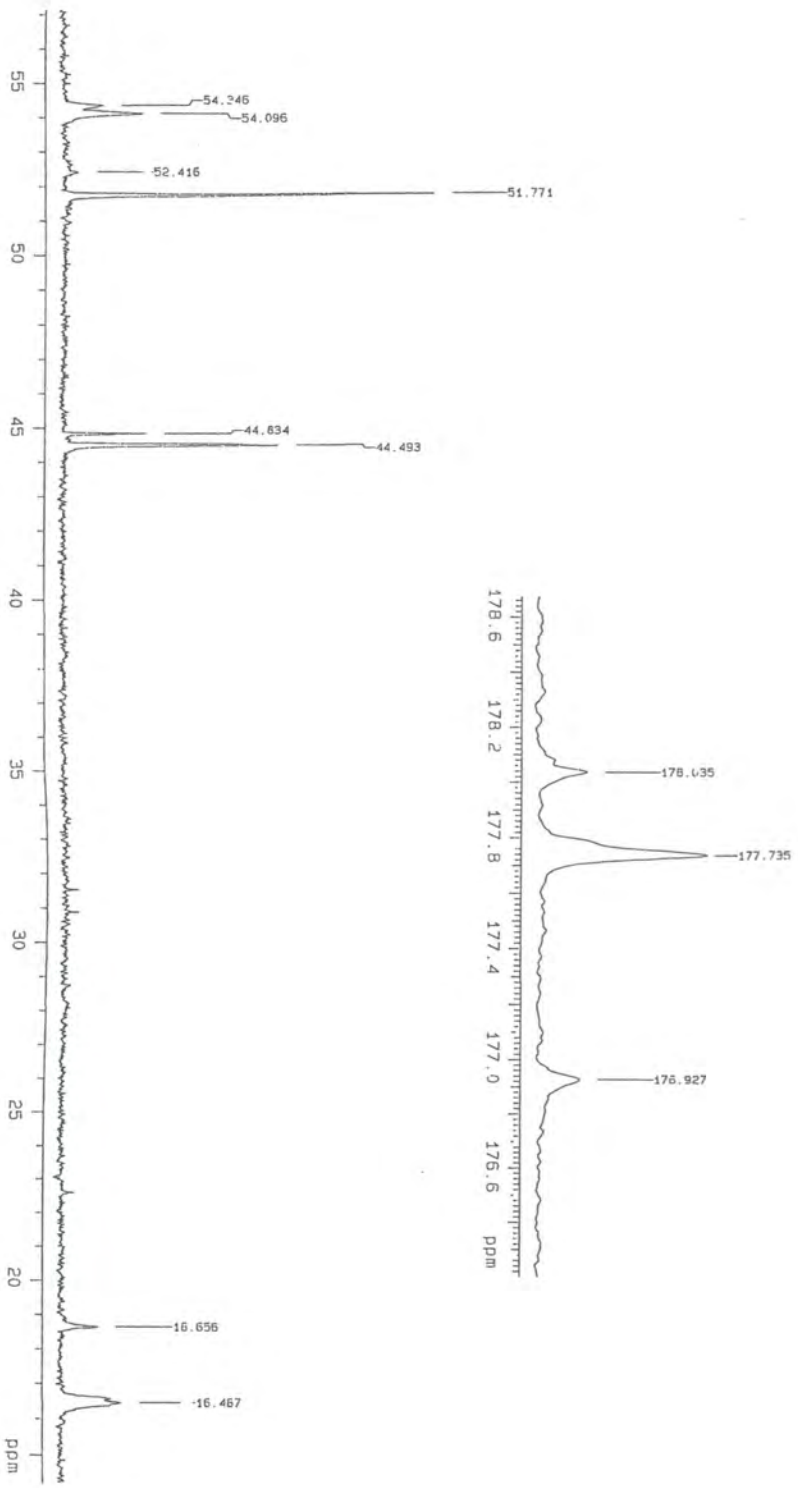

Spectrum 2. Expansion of spectrum 1 showing the regions δ = 15 to 55ppm and 176 to 179ppm

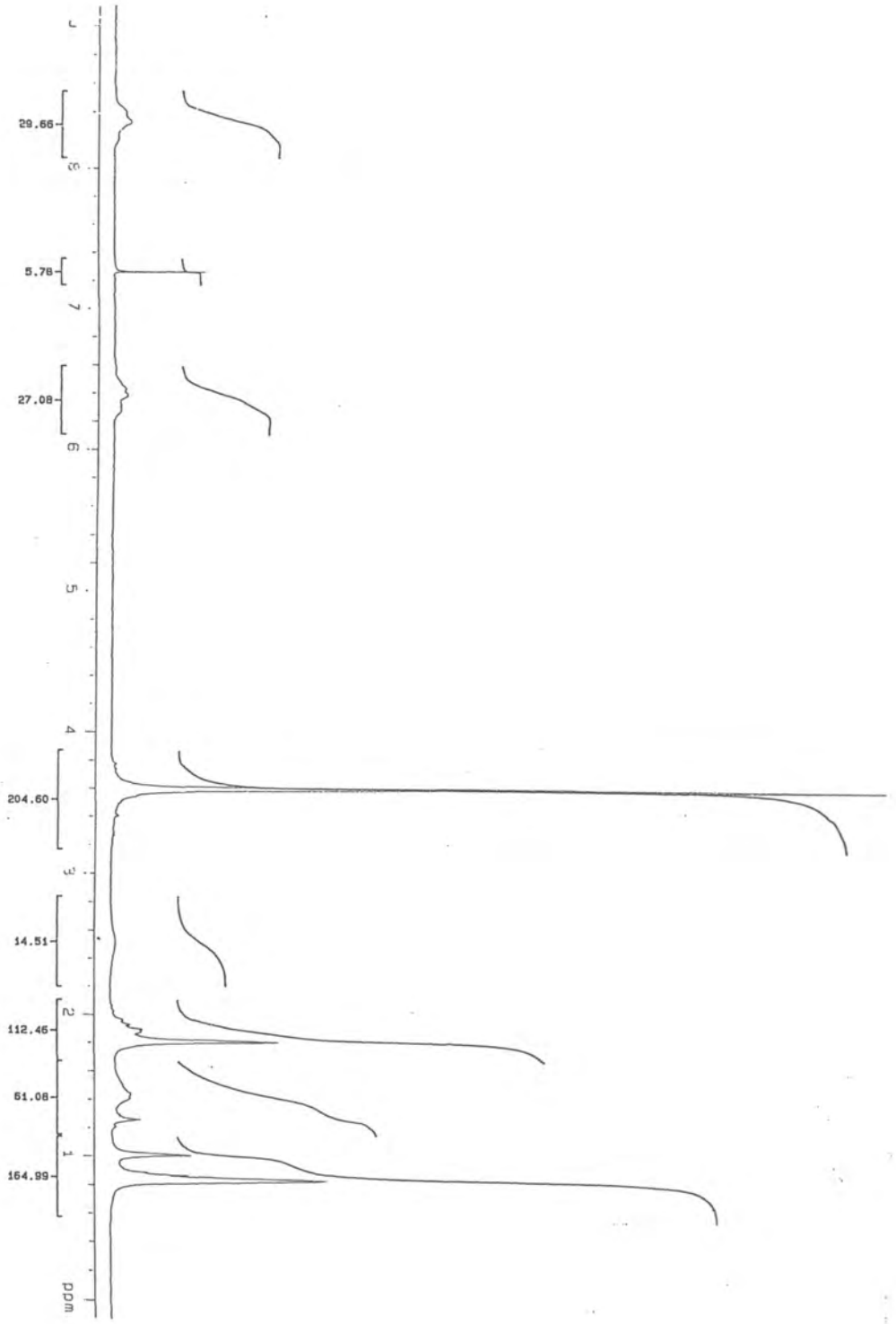

Spectrum 3. ^{1}H NMR spectrum of unquaternised HPMMA-P4VP in $CHCl_3$

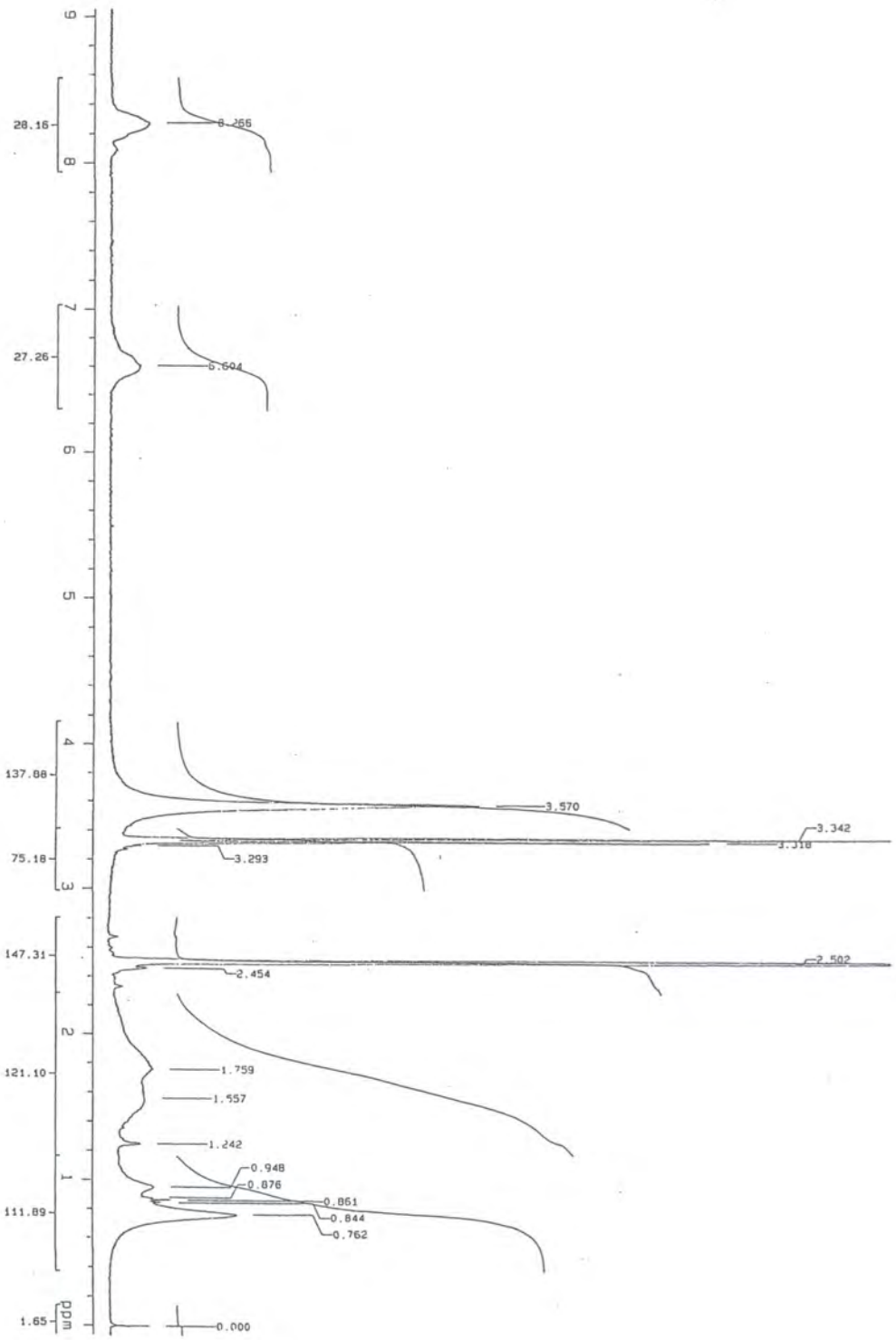

Spectrum 4. ^{1}H NMR spectrum of unquaternised HPMMA-P4VP in DMSO

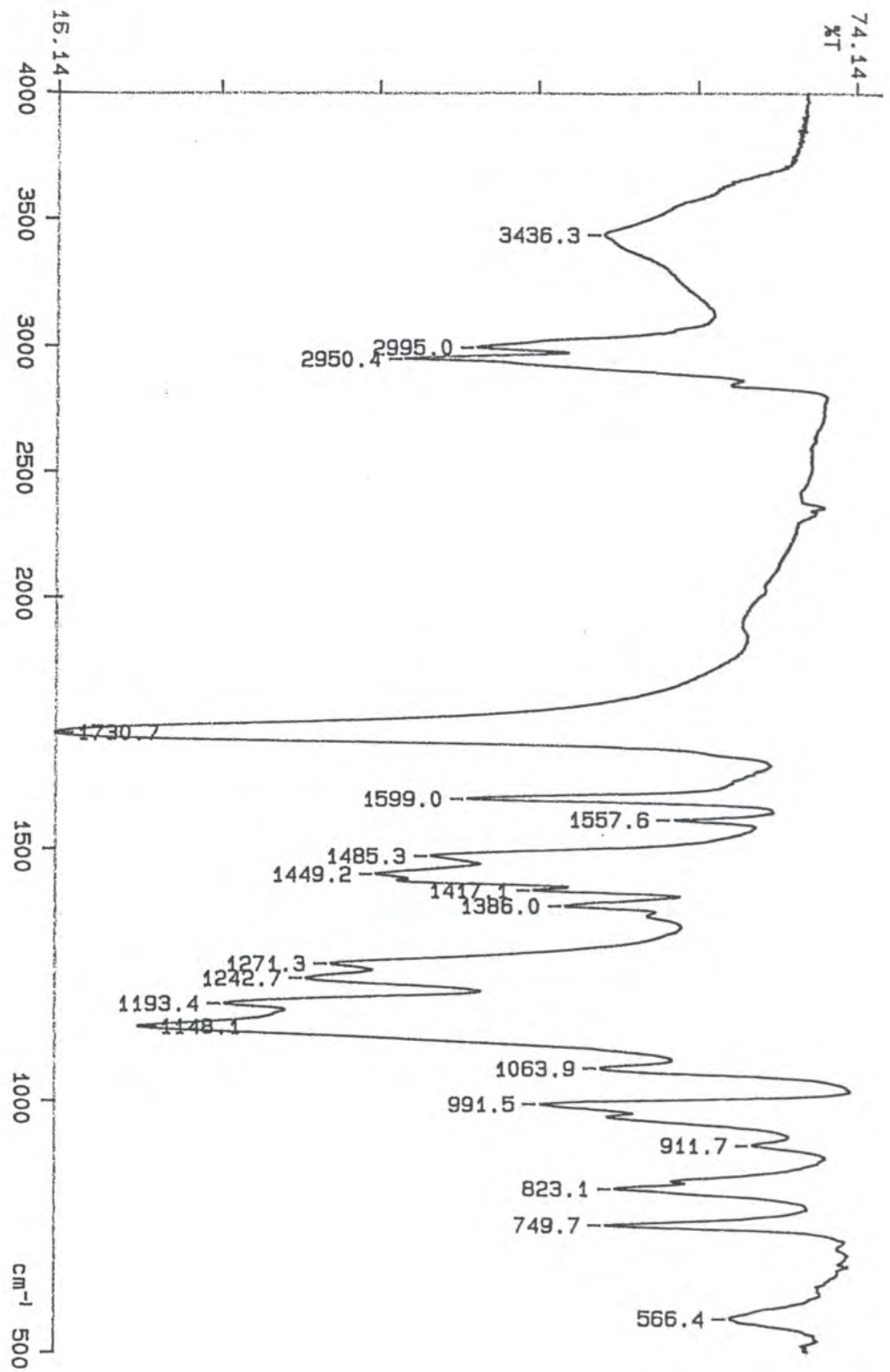

Spectrum 5. IR spectrum of unquaternised HPMMA-P4VP

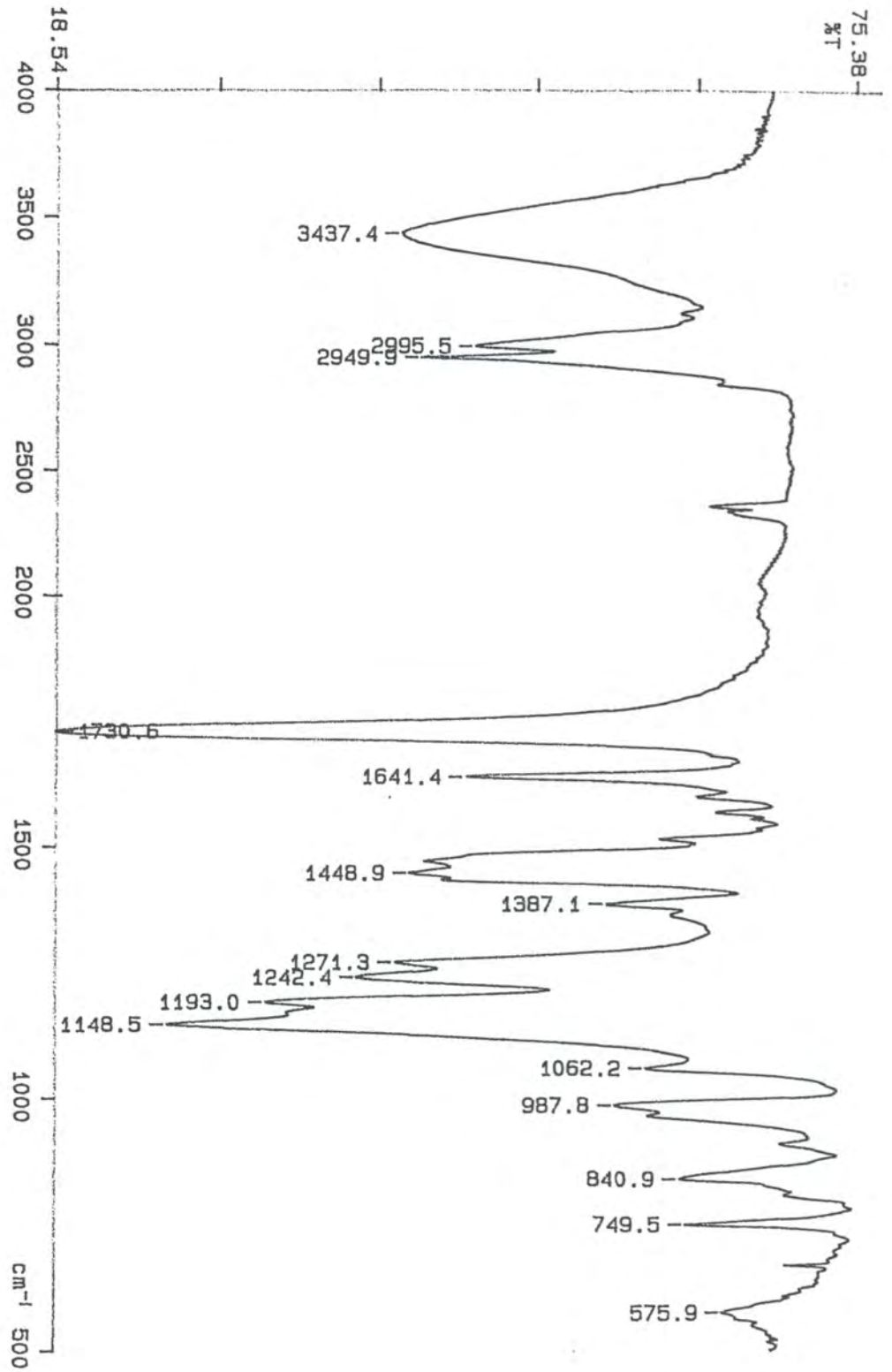

Spectrum 6. IR spectrum of quaternised HPMMA-Q(H)P4VP

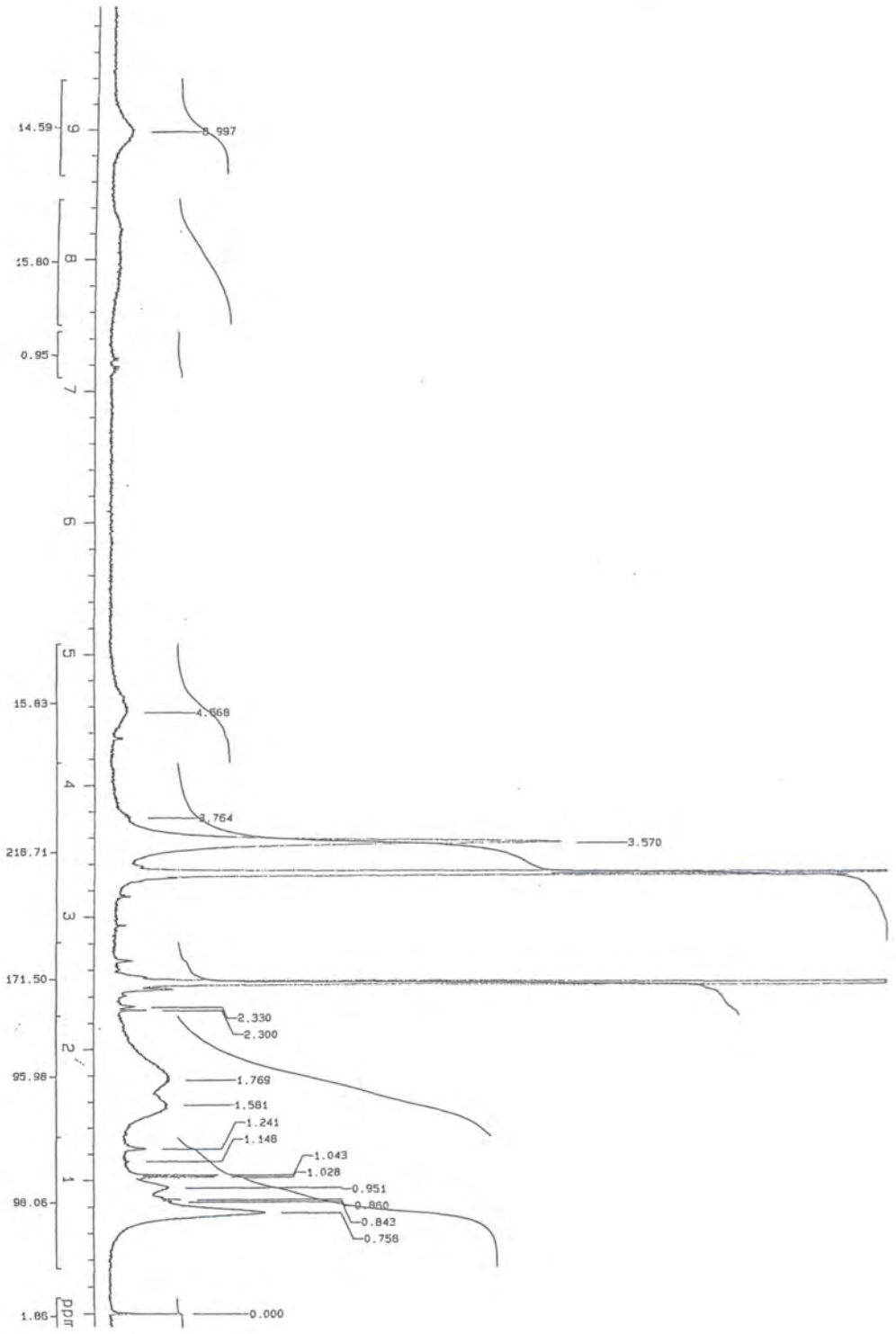

Spectrum 7. ^{1}H NMR spectrum of quaternised HPMMA-Q(H)P4VP in DMSO

B.1. LECTURES ATTENDED

B.1.1. ACADEMIC YEAR 1996/7

23 October	Prof. H. Ringsdorf, Johannes Gutenberg Universitat, Mainz, Germany Function Based on Organisation
20 November	Prof. J. Earnshaw, The Queen's University, Belfast Surface Light Scattering: Ripples and Relaxation
27 November	Dr R. Templer, Imperial College, London Molecular Tubes and Sponges
6 December	Dr A. C. Barnes, University of Bristol Application of Neutron Spectroscopy and Diffraction to Studies of Disordered Systems (Department of Physics Colloquium)
22 January	Dr N. Cooley, BP Chemicals, Sunbury Synthesis and Properties of Alternating Polyketones
26 February	Dr A. Ryan, UMIST Making Hairpins from Rings and Chains
19 March	Dr K. Reid, University of Nottingham Probing Dynamical Processes with Photoelectrons
17 April	Prof. D. Geschke, University of Leipzig, Germany NMR of Liquid Crystalline Polymers

7 May Prof. M. Harrington, Caltech, Pasadena, USA
Polymers which both Enable and Limit the Recovery of Protein Alterations in Studies Ranging from Gene Regulation to Mad Cow Disease.

13 June Prof. S. Kobayashi, Kyoto University, Japan
Synthesis of Polyesters via Enzymatic Polymerisation

13 June Prof. H. Yu, University of Wisconsin, USA
Dynamics of Macromolecular Monolayers

B.1.2. ACADEMIC YEAR 1997/8

21 October Prof. A. F. Johnson, University of, Leeds
Reactive Processing of Polymers: Science and Technology

28 October Prof. A. P. de Silva, The Queen's University, Belfast
Luminescent Signalling Systems

12 November Dr J. Frey, University of Southampton
Spectroscopy of Liquid Interfaces: from Bio-organic Chemistry to Atmospheric Chemistry

26 November Professor R. W. Richards, University of Durham
Inaugural Lecture: A Random Walk in Polymer Science

2 December Dr C. J. Ludman, University of Durham
Explosions

28 January Dr S. Rannard, Courtaulds Coatings, Coventry
The Synthesis of Dendrimers using Highly Selective Chemical Reactions

18 February Professor G. Hancock, University of Oxford
Surprises in the Photochemistry of Tropospheric Ozone

4 March Professor T. C. B. McLeish, University of Leeds
The Polymer Physics of Pyjama Bottoms

B.1.3. ACADEMIC YEAR 1998/9

7 October Dr S. Rimmer, University of Lancaster
New Polymer Colloids

27 October Professor A. Unsworth, University of Durham
What's a Joint Like this Doing in a Nice Girl Like You?

28 October Professor J. P. S. Badyal, University of Durham
Inaugural Lecture: Tailoring Solid Surfaces,

18 November Dr R. Cameron, University of Cambridge
Biodegradable Polymers

1 December Professor N. Billingham, University of Sussex
Plastics in the Environment - Boon or Bane?

10 February Dr C. Bain, University of Oxford
Surfactant Adsorption and Marangoni Flow at Expanding Liquid Surfaces

9 March Dr M. Warhurst, Friends of the Earth
Is the Chemical Industry Sustainable?

11 May Dr J. Sodeau, University of East Anglia
Ozone Holes and Ozone Hills

B.2. Conferences Attended

April 1997	Macro Group UK Spring Meeting for Younger Researchers, Queen's Hotel, Leeds
June 1997	Marangoni and Interfacial Phenomena in Materials Processing, The Royal Society, London
July 1997	Polymer Surfaces and Interfaces III, University of Durham
September 1997	Polymers and Surfactants, North-East Wales Institute, Wrexham†
September 1997	IRC Industrial Club Meeting, The Royal Armouries, Leeds.
September 1997	Neutron and Muon Beam Users' Meeting, Rutherford-Appleton Laboratory, Oxfordshire
January 1998	IRC Polymer Engineering Course, University of Bradford
January 1998	IRC Polymer Physics Course, University of Leeds
April 1998	RSC National Congress and Young Researchers' Meeting, University of Durham†
July 1998	37th IUPAC International Symposium on Macromolecules, Conrad Jupiter Hotel, Gold Coast, Australia†
September 1998	New Perspectives in Neutron and Muon Science: A Meeting for Young Researchers, Cosener's House, Abingdon†
September 1998	Neutron and Muon Beam Users' Meeting, Rutherford-Appleton Laboratory, Oxfordshire†
September 1998	IRC Industrial Club Meeting, University of Durham†
April 1999	RSC Faraday Discussion No. 112: Physical Chemistry in the Mesoscopic Regime, The Queen Hotel, Chester†

† indicates a presentation by the author

B.3. Publications

A. S. Brown, R. W. Richards, D. M. A. Buzza and T. C. B. McLeish, *Faraday Discuss.*, 1999, **112**, 309.